Source Processes and Spectral Ground Motion Models of Intermediate-Depth Vrancea (Romania) Earthquakes

---

Herdprozesse und spektrale Modelle der Bodenbewegung von mitteltiefen Vrancea (Rumänien) Erdbeben

Zur Erlangung des akademischen Grades eines

DOKTORS DER NATURWISSENSCHAFTEN

von der Fakultät für Physik der

Universität Karlsruhe (TH)

genehmigte

DISSERTATION

von

Dipl.-Geophys. Adrien Pierre Henri Oth

aus

Oberanven (Luxembourg)

Tag der mündlichen Prüfung: 7. Dezember 2007

Referent: Prof. Dr. Friedemann Wenzel

Korreferent: Prof. Dr. Karl Fuchs

– If you torture the data long enough, it will confess. –

Ronald H. Coase

Abstract

For successful assessment and mitigation of earthquake hazards, it is necessary to be able to reliably predict the level of ground shaking which has to be expected from future large earthquakes. This prediction of ground motion can be done either by using empirical relations (derived from past earthquakes) between some ground motion parameter and the source and observer location, so-called attenuation relations, or by performing numerical simulations of future earthquakes based on models of the earthquake source and the propagation medium (i.e. the Earth).

The capacity of the first option is at times rather limited, for instance if only very few large earthquakes occurred in the region of interest in instrumental times. Numerical simulations, on the other hand, cannot provide reliable results without a detailed description of the underlying source process and a thorough understanding of path and site effects.

This thesis aims at a better understanding of the source process and the spectral characteristics of the intermediate-depth Vrancea (Romania) earthquakes. Four moderate to large events are analyzed using the empirical Green's functions technique of Irikura (1983, 1986, 1999) and a genetic algorithm optimization procedure in order to derive appropriate source models which can explain the strong motion recordings obtained from these earthquakes. The results indicate that the source process of Vrancea earthquakes can be well modeled by assuming small asperities with high static stress drops (300-1200 bars) and high particle velocities at the fault (up to 5 m/s). This implies a very efficient high-frequency radiation and leads to the conclusion that the source properties of these earthquakes are inherently different from crustal ones.

For the large Vrancea earthquake which occurred on March 3, 1977 ($M_W = 7.4$), a novel approach can be used to derive a suitable source model. As only one strong motion record exists for this event, macroseismic intensity (MSK scale) information is used in the genetic algorithm optimization. The results obtained are very promising and indicate that this method could be a powerful tool to get more insights into the source parameters and the strong motion generation of large historical earthquakes, for which in many cases macroseismic maps can be inferred from historical chronicles.

Using a database composed of accelerometric recordings from many small and moderate as well as the few strong Vrancea earthquakes, the source, path and site contributions to the Fourier amplitude spectra of the S-waves are separated using the generalized inversion technique (GIT) (e.g. Castro et al., 1990). The results indicate that seismic attenuation in the area depicts strong lateral variations. Furthermore, site amplification functions and source spectra are derived for 43 stations and 55 earthquakes, revealing strong amplification at high frequencies and source spectra following the ω^{-2}-model with high corner frequencies. It is also shown that the H/V ratios are not a good estimate of site amplification in the case of Vrancea earthquakes.

Zusammenfassung

Kapitel 1: Einleitung

Neben anderen Naturkatastrophen wie Stürmen, Vulkanausbrüchen oder Überschwemmungen stellen Erdbeben eine ernst zu nehmende Gefahr in vielen Regionen der Welt dar. In den letzten Jahren hat zum Beispiel das große Sumatra Beben im Jahre 2004 (mit circa 225000 Todesopfern) gezeigt, wie hilflos unsere Gesellschaft angesichts einer solchen Katastrophe ist. Wegen der Komplexität des Erdbebenprozesses und der Tatsache, dass viele entscheidende Parameter nur mit großer Ungenauigkeit aus indirekten Beobachtungen zu bestimmen sind, ist es zumindest fraglich, ob es je möglich sein wird, Erdbeben zuverlässig vorherzusagen. Dessen ungeachtet ist es von außerordentlicher Bedeutung, verlässliche Abschätzungen der Bodenbewegung zukünftiger Erdbeben zu berechnen. Diese können zum Beispiel zur Erstellung von Bauvorschriften dienen und sind ein essentieller Bestandteil jeder Gefährdungsanalyse.

Bodenbewegungsparameter zukünftiger Erdbeben können entweder deterministisch oder probabilistisch abgeschätzt werden. Zur deterministischen Berechnung gibt es im Wesentlichen zwei Herangehensweisen. Die erste Möglichkeit ist, anhand von Aufzeichungen vergangener Beben empirische Beziehungen zwischen Bodenbewegungsparametern (z.B. der maximalen Bodenbeschleunigung) und Magnitude, Entfernung, Bruchprozess sowie Standorteffekten aufzustellen, sogenannten *Abminderungsfunktionen* (z.B. Boore and Joyner, 1981; Abrahamson and Silva, 1997; Boore et al., 1997). Solche Beziehungen stellen eine relativ einfache Parametrisierung der Bodenbewegung dar und haben unter anderem den Nachteil, dass sie stark von der verfügbaren Datenbasis instrumentell registrierter Starkbeben in der entsprechenden Gegend abhängen.

Die zweite Möglichkeit besteht in numerischen Simulationen der Bodenbewegung. Dies können Modelle der Wellenausbreitung in dreidimensionalen Untergrundmodellen sein (z.B. Olsen, 2000), die rechnerisch allerdings sehr aufwändig sind und zur Zeit noch auf relativ niederfrequente Bereiche beschränkt sind. Methoden, um die hochfrequente Bodenbewegung zu simulieren, die für ingenieurseismologische Anwendungen von großer Bedeutung ist, sind zum Beispiel die Methode der empirischen Green's Funktionen (z.B. Irikura, 1983, 1986, 1999), wo die Aufzeichnung eines kleinen Bebens als Green's Funktion verwendet wird, um ein großes zu simulieren, oder auch die stochastische Methode (Boore, 2003), die auf spektralen Modellen der Bodenbewegung beruht. Diese Methoden haben im Wesentlichen gemeinsam, dass sie alle stark von dem angenommenen Herdmodell sowie der Kenntnis der Untergrundstruktur und Standorteffekten abhängig sind. Dies bedeutet, dass gute Modelle für den Erdbebenherd, die Propagation im Untergrund sowie für die Standorteffekte vorliegen müssen, um realistische Simulationen zu berechnen.

Ziel dieser Arbeit ist es, die Herdprozesse der mitteltiefen Vrancea (Rumänien) Erdbeben sowie die spektralen Eigenschaften der von ihnen hervorgerufenen Bodenbewegung besser zu verstehen. Hier-

zu wird zum einen der Herdprozess von zwei mittelgroßen und zwei starken Vrancea Beben mittels empirischer Green's Funktionen (mit der Methode von Irikura, 1983, 1986, 1999) untersucht. Zum anderen werden anhand der seit 1997 im Rahmen des Sonderforschungsbereichs (SFB) 461 'Starkbeben – Von geowissenschaftlichen Grundlagen zu Ingenieurmaßnahmen' gewonnenen Kleinbebenaufzeichnungen sowie einiger größerer Beben spektrale Modelle der Bodenbewegung hergeleitet, die sowohl ein tieferes Verständnis der einzelen Beiträge zur Bodenbewegung (Quelle, Propagation, Standort) ermöglichen, als auch die Grundlage für stochastische Simulation zukünftiger Beben bilden können.

Für das starke Vrancea Beben vom 3. März 1977 wird eine neue Methode zur Bestimmung von Herdparametern aus der räumlichen Verteilung makroseismischer Intensitäten mit Hilfe von empirischen Green's Funktionen entwickelt. Die erzielten Ergebnisse sind vielversprechend und machen diese Methode interessant, um eventuell mehr über die Herdparameter historischer Erdbeben zu erfahren, für die des Öfteren gute makroseismische Karten aus historischen Aufzeichnungen gewonnen werden können.

Die vorliegende Dissertation lässt sich in drei Teile gliedern: Kapitel 2 und 3 behandeln die theoretischen Aspekte, die für die folgenden Kapitel wichtig sind. Kapitel 4 und 5 beschreiben Simulationstechniken zum Modellieren der seismischen Bodenbewegung (insbesonders die Methode der empirischen Green's Funktionen) sowie den genetischen Algorithmus, der verwendet wird, um in Kapitel 6 Herdmodelle für vier Vrancea Beben herzuleiten. In Kapitel 6 und 7 werden die vorher eingeführten Konzepte und Methoden schließlich angewandt, um den Herdprozess sowie die Herd-, Propagations- und Standortbeiträge zu den Amplitudenspektren der Bodenbewegung zu untersuchen.

Kapitel 2: Fundamentale seismologische Konzepte

In diesem Kapitel werden die grundlegenden Konzepte, die in dieser Arbeit Anwendung finden, eingeführt. Angefangen mit einem kurzen Abschnitt über die elastodynamische Wellengleichung werden daraufhin die theoretische Beschreibung von Erdbebenquellen sowie gängige Quellmodelle (z.B. das Haskell Modell) vorgestellt. Anschliessend wird die Beschreibung seismischer Bodenbewegung durch die Diskussion von Propagations- und Standorteffekten vervollständigt. Dieses Kapitel schließt mit einer Diskussion über die üblicherweise verwendeten Bodenbewegungsparameter, wobei die seismische Intensität eine entscheidende Rolle in Bezug auf die Herdmodellbestimmung des Vrancea Bebens vom 3. März 1977, die in Kapitel 6 durchgeführt wird, spielt.

Kapitel 3: Spannungsabfall und weitere Herdparameter

Der Spannungsabfall bei einem Erdbeben (d.h. die Differenz zwischen dem Spannungszustand auf der Bruchfläche vor und nach dem Beben) gilt in der Seismologie als einer der wichtigsten Quellparameter. Streng genommen muss jedoch zwischen statischem und dynamischem Spannungsabfall unterschieden werden. Der statische Spannungsabfall gibt Aufschluss über das Skalierungsverhalten der statischen Herdparameter (z.B. Herdgröße, Versatz) und wird häufig mit der seismotektonischen Ursache der Beben in Verbindung gebracht (so weisen tiefe Beben offensichtlich größere statische Spannungsabfälle auf als krustale, z.B. Mikumo, 1971). Der dynamische Spannungsabfall ist die Spannung, die effektiv zur Verfügung steht, um den Versetzungsprozess auf der Bruchfläche anzutreiben und bestimmt im Wesentlichen die Amplitude der hochfrequenten Bodenbewegung (z.B. Brune, 1970, 1971).

Häufig wird nicht zwischen statischem und dynamischem Spannungsabfall unterschieden und der Spannungsabfall wird oft aus der Eckfrequenz des beobachteten Spektrums (nachdem Propagations- and Standorteffekte korrigiert wurden) ermittelt. Allerdings ist es ohne weitere Informationen nicht möglich, den Spannungsabfall ohne starke Modellannahmen zu berechnen, so dass die ermittelten Werte nicht zwangsläufig mit den wirklichen Spannungen, die bei einem Erdbeben wirken, übereinstimmen. In diesem Kapitel wird dieses Problem ausführlich diskutiert. Es ist am sinnvollsten, das Spektrum nur mit Größen zu parametrisieren, die sich auch aus diesem ohne schwerwiegende Modellannahmen messen lassen. Dies sind das seismische Moment und die Eckfrequenz. Um eine physikalisch sinnvolle Aussage über den Herdprozess machen zu können, müssen neben dem Spektrum auch noch weitere Informationsquellen zur Verfügung stehen. Bei großen krustalen Beben stellt sich das Problem nicht in dieser Form, da für die meisten dieser Beben sehr gute Modelle des Versatzes auf der Bruchfläche aus den (Nahfeld-) Beobachtungen hergeleitet werden können. Daher bezieht sich die Diskussion in Kapitel 3 im Wesentlichen auf kleine bis mittelgroße Beben.

Kapitel 4: Methoden zur Simulation seismischer Bodenbewegung

Dieses Kapitel befasst sich mit der Simulation seismischer Bodenbewegung. Die drei gängigsten Techniken werden diskutiert: die Methode der empirischen Green's Funktionen, die stochastische Simulation sowie die Modellierung des Wellenfeldes eines Erdbebens mit der Methode der finiten Differenzen. Besonderer Wert wird auf die Methode der empirischen Green's Funktion von Irikura (1983, 1986, 1999) gelegt, da diese in Kapitel 6 umfassend Anwendung findet. Diese Methode beruht auf den Skalierungsbeziehungen zwischen großen und kleinen Erdbeben. In einem ersten Schritt werden die theoretischen Grundlagen aus Kapitel 2 und 3 aufgegriffen, um die Methode einzuführen und einige praktische Aspekte diskutiert. Daraufhin wird das Quellmodell, das den Simulationen zugrunde liegt (dieses wurde von Miyake et al., 2003, als 'strong motion generation area' bezeichnet), ausführlich diskutiert. Die physikalischen Größen, die zur Simulation benötigt werden, werden besprochen und eine Parameterstudie anhand eines Beispiels durchgeführt, um den Einfluss der einzelnen Parameter genauer zu untersuchen. Irikura's Methode wird schließlich kurz mit der Methode von Hutchings (Hutchings and Wu, 1990; Hutchings, 1991, 1994) verglichen, die auf anderen Grundannahmen beruht.

Zu guter Letzt werden noch die Methode der stochastischen Simulation (Boore, 2003) sowie die Finite Differenzen Methode (z.B. Olsen, 2000) angesprochen. Die in Kapitel 7 hergeleiteten spektralen Modelle der Bodenbewegung für Vrancea Erdbeben können als Grundlage zur stochastischen Simulation verwendet werden und erlauben dementsprechend die Simulation von Beschleunigungszeitreihen von Szenariobeben im rumänischen Staatsgebiet.

Kapitel 5: Parameteroptimierung mit genetischen Algorithmen

Genetische Algorithmen basieren auf evolutionären Prinzipien und sind ein sehr gut geeignetes Hilfsmittel, um nicht-lineare Inversionsprobleme zu lösen. Die Fragestellung, passende Herdparameter eines bestimmten Bebens mit der Methode der empirischen Green's Funktionen von Irikura zu bestimmen, stellt ein solches nicht-lineares Problem dar. Nach der Erstellung einer ersten Population von Testmodellen funktioniert ein genetischer Algorithmus im Wesentlichen in drei Schritten: a) Natürliche Selektion – nur die besten Mitglieder der Population überleben (die Bewertung der Modelle

findet mit einer dem Problem angemessenen Kostenfunktion statt), b) Paarung und Kreuzung – nachdem eine Population bewertet wurde, werden nach einem vorgegebenen Schema verschiedene Modelle miteinander gekreuzt, c) Mutation – an den gekreuzten Modellen werden zufällige Änderungen vorgenommen. Die resultierenden neuen Modelle bilden die nächste Population.

Zunächst werden die Grundlagen besprochen, die zur Programmierung eines genetischen Algorithmus nötig sind. Im Anschluss wird der im Rahmen dieser Arbeit entwickelte Algorithmus beschrieben. Die entscheidende Komponente des Algorithmus ist die Tatsache, dass dieser nicht dazu gedacht ist, schnellstmöglich die beste Lösung zu finden, da dies zu einer verfrühten Konvergenz in ein lokales statt in das globale Minimum der Kostenfunktion führen kann. Die den genetischen Algorithmus steuernden Parameter (dies sind vor allem Populationsgröße, Kreuzungs- und Mutationsrate sowie das Auswahlschema, das bestimmt, welche Modelle miteinander gekreuzt werden sollen) werden so gewählt, dass dieser einen ganzen Satz akzeptabler Modelle findet. Diese Herangehensweise ist hilfreich, um die Eindeutigkeit der erhaltenen Lösung überprüfen zu können, was, wie sich in Kapitel 6 herausstellt, ein sehr wichtiger Aspekt ist.

Kapitel 6: Herdparameter aus Inversion mittels empirischen Green's Funktionen

Der Herdprozess der zwei moderaten Vrancea Beben vom 27. Oktober 2004 ($M_W = 5.8$) und 14. Mai 2005 ($M_W = 5.2$) sowie der zwei großen Beben am 3. März 1977 ($M_W = 7.4$) und 30. August 1986 ($M_W = 7.1$) wird mithilfe von Irikura's Methode der empirischen Green's Funktionen (Irikura, 1983, 1986, 1999) untersucht. Dies ist die erste systematische Studie dieser Art für Vrancea Beben, wobei die größtmögliche Datenbasis an digitalen Akzelerometerdaten verwendet wird. Die Vrancea Erdbeben finden alle in einem sehr eng begrenzten Herdvolumen statt. Das Epizentralgebiet beträgt nur etwa 30×70 km^2 und die Tiefe der Beben erstreckt sich von circa $80 - 200$ km. Vier Erdbeben mit Magnituden größer als 6.5 haben sich im vergangenen Jahrhundert hier ereignet: am 10. November 1940 ($M_W = 7.7$), 3. März 1977 ($M_W = 7.4$), 30. August 1986 ($M_W = 7.1$) sowie am 30. Mai 1990 ($M_W = 6.9$). Letzteres Beben konnte in dieser Studie nicht verwendet werden, da kein passendes kleineres Beben als EGF gefunden werden konnte.

Sieben Parameter charakterisieren die sogenannte 'strong motion generation area' (SMGA, Miyake et al., 2003), die als eine rechteckige Bruchfläche mit konstantem Versatz und Anstiegszeit definiert ist: Verhältnis der Spannungsabfälle von großem (TARGET) und kleinem (EGF) Beben C, Skalierungsfaktor N, Länge L, Breite W, Anstiegszeit T_r sowie die zwei Koordinaten (entlang des Streichens und Fallens der Bruchfläche) des Hypozentrums. Um die Anzahl der freien Parameter so klein wie möglich zu halten, werden C und N aus den spektralen Verhältnissen zwischen TARGET und EGF ermittelt, d.h. die Zahl der zu invertierenden Parameter beträgt nur noch fünf. Diese Parameter werden für die vier anfangs erwähnten Erdbeben durch Inversion mittels des im vorhergehenden Kapitels entwickelten genetischen Algorithmus bestimmt. Weitere Parameter, die angegeben werden müssen, sind die Scherwellen- und die Bruchgeschwindigkeit, v_S und v_R. Der Frequenzgehalt, der für die Inversion nutzbar ist, ist zu tiefen Frequenzen durch die Anforderung eines akzeptablen Signal-Rausch-Verhältnisses der verwendeten EGF-Aufzeichnungen begrenzt. Für die Beben aus den Jahren 2004 und 2005 führt dies zu einer unteren Grenze von 0.5 Hz, für das Beben von 1986 zu 0.4 Hz. Das 2004er Beben wird wiederum als EGF zur Simulation des 1977er Bebens verwendet. Hier liegt die Untergrenze des verwendeten Frequenzbereichs bei 0.2 Hz.

Für die drei Beben von 2004, 2005 und 1986 sind genügend Akzelerogramme vorhanden, um die Inversion anhand der beobachteten Zeitreihen durchzuführen. Als Kostenfunktion wird die L2-Norm

zwischen der Einhüllenden der Beschleunigung sowie der Wellenform der Verschiebung gewählt. Auf diese Weise lassen sich sowohl hochfrequente wie auch tieffrequente Eigenschaften der Akzelerogramme beschreiben. Für das große Beben von 1977 ist eine andere Herangehensweise notwendig, da dieses Beben nur an einer einzigen Station in Bukarest aufgezeichnet wurde und es daher unmöglich ist, eine Inversion durchzuführen, die auf Wellenformen beruht. Hier wird eine andere Informationsquelle, nämlich die makroseismische Intensität, verwendet, um ein Herdmodell für dieses Erdbeben herzuleiten. Mit dem 2004er Beben als EGF werden an 33 Beobachtungspunkten synthetische Beschleunigungszeitreihen generiert. Aus diesen werden mit der Methode von Sokolov (2002) die makroseismischen Intensitäten (MSK Skala) abgeschätzt, die durch diese Zeitreihen hervorgerufen würden. Diese werden mittels der L1-Norm mit den beobachteten makroseismischen Intensitäten verglichen. Durch Minimieren dieser Kostenfunktion kann ein Herdmodell bestimmt werden, das die beobachteten Intensitäten bestmöglich erklärt. Hierbei müssen allerdings einige Annahmen gemacht werden: erstens können C und N nicht, wie bei den anderen drei analysierten Beben, aus den spektralen Verhältnissen bestimmt werden. Aus diesem Grund wird $C = 1$ gesetzt, was in Anbetracht der Ergebnisse für die anderen Beben eine vernünftige Annahme darstellt. N kann dann aus dem Verhältnis der Momente von TARGET und EGF berechnet werden. Zweitens wurde das Verhältnis von Länge zu Breite der SMGA festgehalten, da die Inversion keine Phaseninformation enthält (die Methode von Sokolov, 2002, beruht einzig und allein auf den Fourier Amplitudenspektren). Es gibt zwei Möglichkeiten, die Inversionsergebnisse auf ihre Plausibilität zu überprüfen, welche im Folgenden noch besprochen werden.

Für die drei Beben von 2004, 2005 und 1986 werden drei verschiedene Verhältnisse zwischen Bruch- und Scherwellengeschwindigkeit getestet, v_R/v_S = 0.7, 0.8, 0.9, wobei v_S = 4.5 km/s beträgt. Für jedes dieser Verhältnisse werden fünf Durchläufe des genetischen Algorithmus berechnet, jeder davon mit anderen Startmodellen. Während für die 2004er und 2005er Beben die invertierten SMGA Parameter bei allen drei Verhältnissen sehr stabil sind, ist dies nicht mehr der Fall für das 1986er Beben und v_R/v_S = 0.9. In diesem Fall gibt es mindestens drei verschiedene Lösungen mit ähnlichen Werten der Kostenfunktion. Allerdings findet sich das Modell mit dem kleinsten Wert der Kostenfunktion bei v_R/v_S = 0.7, wo keine Uneindeutigkeit auftritt, und der Wert der Kostenfunktion für dieses Modell ist um circa 10-15% kleiner als für v_R/v_S = 0.9. Diese Uneindeutigkeit beim 1986er Beben beruht vermutlich auf mehreren Faktoren: C und N lassen sich für dieses Beben sehr schwer bestimmen, die Datenbasis ist im Vergleich zu der des 2004er Bebens recht spärlich und die azimutale Verteilung der Stationen ist nicht optimal. Insbesonders die Verwendung eventuell fehlerhafter Werte für C und N kann problematisch sein, da die Berechnungen sehr sensitiv im Bezug auf diese Parameter sind.

Angesichts der Tatsache, dass die beste Lösung für das 2004er Beben bei v_R/v_S = 0.9 erzielt wurde und dieses als EGF für das 1977er Beben verwendet wird, wird die Berechnung der SMGA Parameter des 1977er Bebens mit diesem Verhältnis v_R/v_S durchgeführt. Das Längen-Breiten-Verhältnis wird einmal auf 1:1 sowie auf 1:1.5 festgelegt. Die aus der Inversion der Intensitätsverteilung erhaltenen Modelle sind in der Lage, diese recht gut zu erklären. Ausserdem werden zwei Plausibilitätsprüfungen durchgeführt. Zum einen muss das Quellmodell für diese Beben auch in der Lage sein, die einzige Aufzeichnung in Bukarest zu erklären. Dies ist in der Tat der Fall. Zum anderen müssen die Parameter des EGF-Bebens, die sich bei der Inversion ergeben, halbwegs mit denen übereinstimmen, die bei der Betrachtung des 2004er Bebens als TARGET ermittelt wurden. Auch diese Anforderung wird von der berechneten Lösung erfüllt. Dies bedeutet, dass die Ergebnisse für das 1977er und 2004er Beben konsistent sind.

Miyake et al. (2003) zeigen, dass die SMGA Parameter für krustale Beben sehr gut mit den empirischen Relationen übereinstimmen, die von Somerville et al. (1999) für die Skalierung von soge-

nannten Asperities aufgestellt wurden. Miyake et al. (2003) interpretieren die SMGA daher als Asperity innerhalb einer gesamten, größeren Bruchfläche, die aber keinen relevanten Spannungsabfall aufzeigt. Die SMGA bei krustalen Beben zeigt einen statischen Spannungsabfall von circa 100 bar. Die SMGA's der Vrancea Erdbeben zeigen zum einen sehr kleine Dimensionen, zum anderen auch sehr kleine Anstiegszeiten im Verhältnis zu den Erwartungen für krustale Beben (circa einen Faktor 2-10 kleiner). Nur das 2005er Beben zeigt ähnliche SMGA (bzw. Asperity) Dimensionen wie krustale Beben, allerdings immer noch eine deutlich kürzere Anstiegszeit. Folgt man der Interpretation von Miyake et al. (2003), so beträgt der statische Spannungsabfall für die betrachteten Vrancea Beben (ausser 2005) zwischen 300-1200 bar, und die Partikelgeschwindigkeit auf der Bruchfläche liegt im Bereich 3-5 m/s. Bei krustalen Beben hat man Partikelgeschwindigkeiten von maximal 2 m/s ermittelt (Kanamori, 1994). Dies bedeutet, dass die mitteltiefen Vrancea Beben eine sehr starke Abstrahlung hoher Frequenzen zeigen und sich physikalisch deutlich von krustalen Erdbeben unterscheiden. Insbesonders die starke Hochfrequenzabstrahlung ist eine Tatsache, die bei der Gefährdungsabschätzung berücksichtigt werden muss.

Kapitel 7: Spektrale Modelle der Bodenbewegung für Vrancea Erdbeben

Die Fourier Amplitudenspektren der seismischen Bodenbewegung lassen sich allgemein durch die Multiplikation eines Quellterms mit einem Dämpfungsterm sowie eines Standortterms parametrisieren (dies entspricht einer Konvolution der Effekte im Zeitbereich). Durch Logarithmieren lässt sich das Problem linearisieren und so ist eine Inversion mittels der Methode der kleinsten Fehlerquadrate möglich, um diese Beiträge zu trennen (z.B. Castro et al., 1990). Diese Separation ermöglicht sowohl ein besseres physikalisches Verständnis der einzelnen Effekte als auch die Erstellung von spektralen Bodenbewegungsmodellen, die zur Simulation von stochastischen Zeitreihen (Boore, 2003) zukünftiger Starkbeben (Szenariobeben) verwendet werden können.

Insgesamt werden Aufzeichnungen von 55 Beben (darunter einige moderate und 3 Starkbeben) an 43 Stationen untersucht. Die Inversion erfolgt in zwei Schritten: zunächst werden die Daten nach den Dämpfungseigenschaften der Region invertiert. Dabei stellt sich das Problem, dass es sich bei den Vrancea Beben um mitteltiefe Ereignisse handelt und daher die kleinste Hypozentralentfernung im Datensatz circa 90 km beträgt. Dies ist im Folgenden auch die Referenzentfernung, in der die Quellspektren bestimmt werden. Es zeigt sich, dass die Dämpfungseigenschaften starke laterale Variationen aufweisen. Stationen, die direkt im Epizentralgebiet bzw. im Karpatenbogen stehen, zeigen eine sehr viel stärke Dämpfung bei hohen Frequenzen als solche, die sich im Vorlandbecken oder zum Beispiel in Bukarest befinden. Die Stationen werden je nach ihren spektralen Amplituden bei hohen Frequenzen in zwei Regionen eingeteilt, für die separate Dämpfungsfunktionen invertiert werden. Dieser unterschiedliche Effekt der Dämpfung ist von fundamentaler Bedeutung für die seismische Gefährdungsabschätzung in Rumänien, da durch die sehr starke Dämpfung im Bereich des Karpatenbogens die Gefährdung für Strukturen, die hohe Eigenfrequenzen aufweisen, sehr viel geringer ist als im Vorlandbecken. Für Hochhäuser dagegen ist die Gefährdung überall in Rumänien gleichermaßen groß. Die lateralen Variationen der seismischen Dämpfung stellen auch eine wichtige Komponente zum besseren Verständnis der makroseismischen Intensitätsverteilung vergangener Beben dar.

Nach der Bestimmung der Dämpfungsfunktionen werden die Daten mit diesen korrigiert und im zweiten Inversionsschritt die Quell- und Standortbeiträge voneinander getrennt. Dabei werden zwei Stationen, die auf Festgestein stehen, als standorteffektfrei angesehen. Eine solche Randbedingung ist notwendig, um einen unbestimmten Freiheitsgrad in der Inversion zu beseitigen (Castro et al., 1990).

Bei den Standorteffekten zeigt sich, dass sowohl die horizontale wie die vertikale Komponente verstärkt werden. Insbesonders die Vertikalkomponente wird bei sehr hohen Frequenzen verstärkt. Die Quellspektren können aufgrund der Geometrie nur auf eine Entfernung von 90 km normiert bestimmt werden. Daher enthalten diese noch einen residualen Dämpfungseffekt. Um die Quellspektren interpretieren zu können, muss dieser korrigiert werden. Dies kann zum Beispiel dadurch erfolgen, dass man ein bekanntes Quellspektrum mit dem invertierten vergleicht und dadurch einen Korrekturterm für alle anderen invertierten Spektren herleitet. Dieses Referenzquellspektrum stammt in diesem Fall vom Beben vom 27. Oktober 2004 ($M_W = 5.8$), welches im vorhergegangenen Kapitel studiert wurde. Dort wurde als Eckfrequenz für dieses Beben der Wert 1,6 Hz bestimmt. Die auf diese Weise korrigierten Quellspektren folgen dem ω^{-2}-Modell (Brune, 1970, 1971) sehr gut. Sie weisen alle sehr hohe Eckfrequenzen auf, was mit den hohen Spannungsabfällen, die in Kapitel 6 ermittelt wurden, exzellent vereinbar ist. Außerdem folgen die Eckfrequenzen dem Trend, den man im Falle selbst-ähnlicher Skalierung erwartet.

Schließlich werden die ermittelten Standorteffekte noch mit den H/V Spektren verglichen, welche oft als eine Abschätzung des Standorteffekts herangezogen werden. Es zeigt sich, dass die H/V Spektren im vorliegenden Fall nicht geeignet sind, den Standorteffekt abzuschätzen, was vornehmlich an der Verstärkung der Vertikalkomponente bei hohen Frequenzen liegt. Dies ist insbesonders für die seismische Mikrozonierung von großer Bedeutung, da man bei Verwendung des H/V Spektrums zum Charakterisieren eines Standortes die Verstärkung der hohen Frequenzen stark unterschätzt.

Die ermittelten Ergebnisse werden mit bereits vorhandenen Modellen (Sokolov et al., 2004, 2005) verglichen, die auf einer etwas anderen Parametrisierung des Problems beruhen. Es zeigt sich, dass sich die beobachteten Spektren mit beiden Modellen gut erklären lassen, diese aber fundamental andere physikalische Schlussfolgerungen nach sich ziehen. Es ist daher überaus wichtig, sowohl auf die Parametrisierung (soviel Modellparameter wie nötig, so wenig wie möglich) als auch auf die verwendeten Annahmen zu achten, wenn die spektralen Modelle physikalisch interpretiert werden. Die hier hergeleiteten Modelle beruhen auf wenigen Annahmen, die sich auch physikalisch sehr gut rechtfertigen lassen. So wird zum Beispiel kein Dämpfungsmodell angenommen, sondern eines aus den vorhandenen Daten abgeleitet. Die Frage des Dämpfungsmodells ist zum Beispiel entscheidend für die Ergebnisse der Quellspektren und Standorteffekte.

Kapitel 8: Zusammenfassung und Schlussfolgerungen

In dieser Arbeit werden sowohl die Herdeigenschaften der mitteltiefen Vrancea Erdbeben als auch deren Fourier Amplitudenspektren untersucht. Bei der Inversion der Herdparameter mittels der Methode der empirischen Green's Funktionen von Irikura (Irikura, 1983, 1986, 1999) zeigt sich, dass diese Erdbeben sich ganz wesentlich von den krustalen unterscheiden. Sie zeigen wesentlich höhere Spannungsabfälle (eine Größenordnung) und ebenso deutlich höhere Partikelgeschwindigkeiten, was eine aussergewöhnlich effektive Abstrahlung hoher Frequenzen zur Folge hat. Diese Tatsache spiegelt sich auch in den sehr hohen Eckfrequenzen der Quellspektren wieder, die in Kapitel 7 bestimmt wurden. Dort wurden ausserdem die Dämpfungseigenschaften der Region untersucht sowie Abschätzungen für die Standorteffekte an 43 Stationen hergeleitet.

Die vorliegende Arbeit stellt somit eine komplette Analyse der mitteltiefen Vrancea Beben dar, die sich von einer detaillierten Studie der Herdparameter über die Bestimmung der Dämpfung bis zu den Standorteffekten erstreckt. Aus diesem Grund ist sie ein wichtiger Beitrag zum Verständnis dieser Beben und damit auch zur besseren Abschätzung des Gefährdungspotenzials dieser Ereignisse.

Contents

Chapter 1

Introduction

Among natural hazards such as floods, volcanic eruptions or storms, earthquakes pose a serious threat to many areas in the world. During the last few years, several memorable large events, such as the giant Indian Ocean earthquake with its tsunami in 2004 (death toll of about 225000, estimated economic loss of approximately 15 billion US$) or the Pakistan earthquake in 2005 (more than 87000 dead, 5 billion US$ loss) [1] have painfully shown, how vulnerable human society is to these disasters. Especially several so-called megacities are highly endangered by earthquake catastrophes. For instance, Tokyo (pop. 36 million), Los Angeles (pop. 18 million) or Istanbul (pop. 12 million) are seriously threatened by the (possibly near-) future occurrence of a large earthquake.

Ideally, one would like to be able to reliably predict the occurence of future large earthquakes. Yet, numerous attempts to predict earthquakes failed (e.g. Wyss, 1997, 2001), which led the vast majority of the seismological community to cast doubt on the feasibility of earthquake forecasting (e.g. Geller et al., 1997). If an earthquake occurs or not, depends on the highly complex interaction of various physical parameters, most of which have in common that their precise role in earthquake generation is not yet completely understood and that they can only be measured (if they can) through indirect observations. As a consequence, it is extraordinary difficult to assess the current state of a fault zone and, therefore, time, location and magnitude of a forthcoming event with acceptable uncertainty.

Regardless whether or not it will somewhen be possible to provide reliable earthquake predictions, it is necessary to assess what ground shaking has to be expected (either deterministically or probabilistically, see e.g. Kramer, 1996) from these future earthquakes. These strong motion predictions can for instance be used to define appropriate building codes and to design the infrastructure (e.g. bridges, tunnels, high rise buildings etc.) so that the latter can withstand a certain level of ground shaking without excessive structural damage, which also represents a life-saving measure.

Using the deterministic approach, strong ground motion estimates can be derived from data recorded during past moderate to large earthquakes, and these datasets are used to derive so-called ground motion attenuation relations (e.g. Boore and Joyner, 1981; Abrahamson and Silva, 1997; Boore et al., 1997; Campbell, 1997; Sadigh et al., 1997; Somerville et al., 1997; Toro et al., 1997; Campbell, 2003). Attenuation relations relate some ground motion parameters (e.g. peak ground acceleration, PGA, peak ground velocity, PGV, macroseismic intensity) to the magnitude, distance between earthquake source and observer, type of faulting and site conditions. These relations are usually updated after each

---

[1] figures from Swiss Re, 2006

1

large earthquake, when new data are available. A main drawback of these relations is the fact that they represent quite simple parameterizations of ground motion. Additionally, the data points at very close distances are generally rather sparse, which makes the predictions at small distances unreliable. In regions where no large earthquakes occurred during instrumental times (for instance, in the Dead Sea area, the last earthquake with moment magnitude higher than 6 occurred in 1927), attenuation relations from other areas in the world can be used, but there is a large degree of speculation on the resulting ground motion predictions.

The probabilistic approach estimates, based on a record of historical seismicity and appropriate strong ground motion attenuation relations (hence, these relations are commonly required both for deterministic and probabilistic seismic hazard assessment), the probability of exceedence of a certain ground motion parameter (e.g. peak ground acceleration or seismic intensity) within a specified time period (e.g. Shedlock et al., 2000; Sokolov et al., 2004; Ardeleanu et al., 2005).

In recent years, numerical simulations of ground motion have become an increasingly popular tool in order to assess the level of shaking that has to be expected from future earthquakes. With the steadily increasing computational power during the last decade, it is for instance possible to compute the full wave field in three dimensions from one or several scenario earthquakes using e.g. the finite-difference technique and to derive ground motion parameters from these simulations (e.g. Olsen, 2000; Olsen et al., 2006). Such scenario earthquakes may be, for instance, the largest earthquake observed in historical times or a 'maximum thinkable' event. The information needed as an input for these simulations is two-folded: first, an Earth model (seismic velocities and densities) as accurate as possible is required. Secondly, these simulations are only as good as the source model on which they are based. Yet, the better the subsurface structural models get, the finer the discretization must become and, as a result, the computational costs are becoming exorbitantly high. As a rule, the subsurface models are limited in their small-scale resolution, which is why these simulations are usually only performed for rather low frequencies, below the range of engineering interest.

Because, for high frequency ground motion simulations, the numerical simulations discussed above are not practicable (not yet – this situation might change in the future), two other methods are often used: the empirical Green's function (EGF) (e.g. Hartzell, 1978; Kamae and Irikura, 1998; Miyake et al., 2003) and the stochastic (e.g. Boore, 1983, 2003; Sokolov et al., 2004) techniques. The former one uses small earthquakes, collocated with the large event of interest and having a similar focal mechanism, as 'empirical' Green's functions to be summed with given time lags to simulate the rupture process. The latter one is based on the findings of Hanks and McGuire (1981) that high-frequency acceleration records can essentially be described as bandlimited, gaussian noise with certain spectral characteristics. Thus, the EGF technique is strongly dependent on the assumed source characteristics while for the stochastic technique appropriate spectral ground motion models must be available. This means to have a thorough understanding of site effects, attenuation along the path between source and receiver as well as the spectral properties of the earthquake source (in the stochastic approach, the earthquake is commonly approximated to be a point source with a given source spectrum). Both of these approaches are used with several methodological variations by different authors, and some researchers combined both ideas (e.g. the stochastic simulation of finite-fault earthquakes, Beresnev and Atkinson, 1997, 1998).

This thesis aims at a better understanding of the ground motions resulting from the intermediate-depth Vrancea (Romania) earthquakes. These events, with a maximum instrumentally measured magnitude of 7.7, pose a significant hazard to Romania and its neighbouring countries Moldova and Bulgaria (e.g. Ardeleanu et al., 2005; Mantysniemi et al., 2003). During the last century, four major earth-

quakes with magnitude higher than 6.5 occurred within the Vrancea seismic zone. Both the source processes of these earthquakes, with a particular emphasis on strong motion generation, and the spectral characteristics of ground motion are studied. This knowledge is an essential component in order to estimate the level of ground shaking that has to be expected from future Vrancea earthquakes and to compute synthetic catalogues of large events in order to assess seismic hazard.

Chapter 2 introduces the reader to the fundamental seismological concepts which are applied throughout this work. Starting with a short section on the elastodynamic equation of motion, the representation theorem and the source description of earthquakes are discussed. Popular source models, such as the Haskell and Brune models, are presented. The further discussion treats the commonly utilized empirical scaling relations for source parameters such as fault size or slip. Having completed the discussion on the earthquake source, I then focus my attention to path and site effects, which complete the description of ground motions at a given receiver location. Finally, this chapter concludes with a short summary on ground motion parameters. Especially macroseismic intensity will play an important role in this thesis, as it is used to infer a suitable source model for the 1977 large Vrancea earthquake.

In Chapter 3, I discuss earthquake source parameters (especially stress drop) and the energy budget of earthquakes. Strictly speaking, it is necessary to distinguish between static and dynamic stress drop. Static stress drop is defined as the (static) difference between the shear stress on the fault before and and after the earthquake. Whereas static stress drop is commonly viewed to be related to the origin of the event (for instance, static stress drop of deep earthquakes seems to be markedly higher than for crustal events, e.g. Mikumo, 1971) and provides hints on the scaling of the static parameters (such as source size or final displacement) characterizing an earthquake, dynamic stress drop is the stress which is effectively available to drive fault motion and, as such, a key parameter in the estimation of strong ground motion, as it influences the high-frequency level of acceleration (Brune, 1970, 1971) and can be linked to peak ground acceleration (PGA, Hanks and Johnson, 1976). Furthermore, stress drop is a typical input parameter in order to compute ground motion simulations with the stochastic technique. Yet, as I explain in Chapter 3, the spectra of seismic waves include rather little information about stress drop and source size, which are nevertheless commonly estimated from the corner frequency of the source spectrum (e.g. Allmann and Shearer, 2007).

Three techniques to compute strong motion simulations are presented in Chapter 4: the EGF technique, the stochastic approach and the finite-difference method. The two main EGF approaches are discussed: Irikura's (1983, 1986, 1999) and Hutchings' (1991,1994, Hutchings and Wu, 1990) methodology. More emphasis is put on Irikura's approach, as this technique is used in this work to derive suitable 'strong motion generation areas' (SMGA, Miyake et al., 2003) for several moderate and large Vrancea shocks (Chapter 6). The stochastic technique (Boore, 2003) is introduced in view of the spectral ground motion models which are derived in Chapter 7. Using such models, this simulation approach enables the user to perform fast and data-consistent high frequency simulations of acceleration time histories. Finally, a brief description of the finite-difference technique and a short discussion conclude this chapter.

Chapter 5 provides an introduction into parameter optimization using genetic algorithms (e.g. Goldberg, 1989) and the algorithm developed in this thesis is presented. Such algorithms are a very powerful tool to solve non-linear inverse problems. The determination of appropriate source models for Vrancea earthquakes using Irikura's EGF technique is a problem of this kind, and therefore, I will design an algorithm of the genetic type to perform these inversions. The mode of operation of genetic algorithms is introduced and a brief summary of the theoretical background is given.

Chapter 6 is, as already mentioned, devoted to the determination of appropriate SMGA (Miyake et al., 2003) source models for two moderate (2004, M_W = 5.8 and 2005, M_W = 5.2) and two large (1977, M_W = 7.4 and 1986, M_W = 7.1) Vrancea earthquakes. First, a short introduction to the seismicity of the Vrancea region as well as the database utilized is given. For the 2004, 2005 and 1986 earthquakes, enough strong motion observations are available to compute inversions by minimizing the cost (misfit) between the acceleration envelopes and displacement waveforms. However, the situation is rather different for the 1977 event, where only one single strong motion recording is available. Therefore, a novel approach is adopted to nevertheless derive a suitable source model for this earthquake: macroseismic intensity is used as an inversion criterion, as a detailed intensity map exists for this event. Using the technique of Sokolov (2002), seismic intensity is estimated from the simulated time series and the cost between observed and simulated intensities is minimized. The results are very promising and the approach could be interesting to derive source parameters of historical earthquakes, for which often quite reliable macroseismic intensity maps can be obtained from historical records.

In Chapter 7, spectral ground motion models for Vrancea earthquakes are derived. Using a least squares inversion approach usually referred to as the *generalized inversion technique* (e.g. Castro et al., 1990), the whole path attenuation, site and source contributions to the observed acceleration spectra from many small and several moderate and large Vrancea earthquakes are separated. This separation contributes to the understanding of the spectral characteristics of these earthquake sources as well as the amplification due to local site conditions, which represents an essential piece of information to adequately predict ground motions from future earthquakes. 43 sites spread over the Romanian territory are analyzed. Furthermore, the inversion provides insights into the attenuation of the seismic waves on their way from the source to the receiver, which turns out to show strong lateral variations. The site amplification functions resulting from the inversion are also compared with the commonly used H/V ratios.

Finally, with Chapter 8, the thesis ends with a summary of the results and the main conclusions.

Chapter 2

Fundamental Seismological Concepts

During the past few decades, the seismological community has made substantial advances in understanding the physics of earthquakes and the related ground shaking. The purpose of this Chapter is to briefly summarize the fundamental findings which are of importance to the work presented in this thesis. Starting with a short section on the most fundamental equation in seismology, the elastodynamic equation of motion, I will then give an introduction into the representation of seismic sources and two useful and well-known source models, namely the Haskell and Brune models. In the third section, empirical scaling relations, which are of utmost importance for the empirical Green's function technique, and stress drop will be addressed. After a short section about propagation path and site effects on seismic ground motion, this chapter will end with a section on commonly utilized ground motion parameters and seismic intensity. Especially the latter will play an important role in the source inversion presented in Chapter 6.

2.1 The Elastodynamic Equation of Motion

A large part of our understanding of the physics of earthquakes and wave propagation is based on a single fundamental equation, the equation of motion. It connects forces in a continuous medium to observable displacements. The equation of motion can be derived by applying Newton's second law (i.e. the conservation of momentum) to a continuous medium (applying physical laws to a continuous medium leads to the concept of *continuum mechanics*). Note that by considering the Earth to be a continuous body, the microscopic structure of the Earth's interior is ignored. The concept of continuum mechanics is also appreciated by many other fields of natural science, among them for instance meteorology.

The conservation of momentum within a volume V with surface S of a continuous medium subjected to a total body force $\mathbf{F}$ and surface traction vector $\mathbf{T}(\mathbf{n})$ ($\mathbf{n}$ is the normal unit vector at a given point on S) leads to the *equation of motion* (e.g. Aki and Richards, 2002):

$$\frac{d}{dt} \iiint_V \rho \frac{d\mathbf{u}}{dt}\, dV = \iiint_V \mathbf{f}\, dV + \iint_S \mathbf{T}(\mathbf{n})\, dS \ , \tag{2.1}$$

where $\mathbf{u}(\mathbf{x}, t)$ is the displacement vector within a cartesian coordinate system with position vector $\mathbf{x} = (x_1, x_2, x_3)$, ρ represents the density of the material and $\mathbf{f}$ is the body force density such that

$\iiint_V \mathbf{f} \, dV = \mathbf{F}$. The components of the traction vector can be expressed as $T_i = \sigma_{ji} n_j$, where $i, j = 1, 2, 3$. In this notation, summation is carried out over repeated indices. σ_{ij} are the nine components of the *stress tensor*. σ_{ij} is a symmetric tensor due to the conservation of angular momentum.

The derivative with respect to time t may be drawn into the integral, as the volume V is supposed to be constant with time. If the particle displacements are very small compared to the wavelength of the spatial fluctuations in displacement and stress, the total derivative $\frac{d}{dt}$ may be substituted by the partial derivative $\frac{\partial}{\partial t}$. Using Gauss's divergence theorem to transform the surface integral in equation (2.1) into a volume integral and considering the forces per unit of volume, we can rewrite the equation of motion in its most commonly cited differential form:

$$\rho \frac{\partial^2 u_i}{\partial t^2} = f_i + \frac{\partial \sigma_{ij}}{\partial x_j} \quad \text{with } i, j = 1, 2, 3 \,. \tag{2.2}$$

Equation (2.2) is the linearized *elastodynamic equation of motion* in its most general form for anisotropic inhomogeneous media. Note that ρ in equation (2.2) is constant with time, as temporal fluctuations turn out to be neglible during the linearization process, whereas u_i represents the displacement with respect to a position of equilibrium, which is assumed to equal zero.

To be exact, equation (2.2) represents a system of three 2nd-order partial differential equations. For very small deformations (which is mostly the case in seismology, as the relative length changes are of the order of 10^{-6}, see e.g. Lay and Wallace, 1995), the *strain tensor* ϵ_{ij} is given by

$$\epsilon_{ij} = \frac{1}{2} \left(\frac{\partial u_i}{\partial x_j} + \frac{\partial u_j}{\partial x_i} \right). \tag{2.3}$$

In a linear elastic medium the relation between stress σ_{ij} and strain ϵ_{ij} is given by *Hooke's law*:

$$\sigma_{ij} = c_{ijkl} \epsilon_{kl} \,, \tag{2.4}$$

with c_{ijkl} being called the *stiffness tensor*. The stiffness tensor is a 4th-order tensor containing 81 elastic moduli. As Aki and Richards (2002, Chapter 2.2) show, the stiffness tensor contains only 21 independent elements in the most general anisotropic case. For an isotropic medium, the stress-strain relation greatly simplifies and two elastic moduli, the *Lamé moduli* λ and μ, are sufficient for a complete description of the elastic properties of the medium:

$$\sigma_{ij} = \lambda \epsilon_{kk} \delta_{ij} + 2\mu \epsilon_{ij} \,. \tag{2.5}$$

Herein, δ_{ij} is the Kronecker function (i.e. $\delta_{ij} = 0$ for $i \neq j$ and $\delta_{ij} = 1$ for $i = j$). As Aki and Richards (2002, p. 67-68) outline, if the Lamé parameters are assumed to be constant throughout the considered medium, i.e. $\frac{\partial \lambda}{\partial x_i} = 0$ and $\frac{\partial \mu}{\partial x_i} = 0$, the displacement field $\mathbf{u}(\mathbf{x}, t)$ can be expressed in terms of a curl-free scalar and a divergenceless vector potential, which both obey the wave equation. This leads to the concept of P- and S-waves which propagate with velocities

$$v_P = \sqrt{\frac{\lambda + 2\mu}{\rho}} \quad \text{and} \quad v_S = \sqrt{\frac{\mu}{\rho}}. \tag{2.6}$$

The equation of motion as given by (2.2) is one of the key point for the entire development of seismological theory. The wave propagation in arbitrarily heterogeneous media can be computed by

numerically solving the equation of motion, for instance using the finite-difference technique. In general, body forces such as gravity are not relevant for seismological problems (except if very long periods are used, such as e.g. in the analysis of the Earth's free oscillations) and can be dropped from equation (2.2). However, body forces nevertheless play an important role because seismic sources may be represented in an attractive way by body force couples, as we will see in the next section.

2.2 The Earthquake Source Process

As we have seen in Section 2.1, seismic wave propagation through any medium is governed by the relationship $\rho \ddot{u}_i = \sigma_{ij,j}$ and the stress-strain relation (Hooke's law in a linear elastic medium). However, in the source region, we cannot work with the assumption of very small strain, as the earthquake represents a displacement discontinuity which can be very large. Additionally, the linear stress-strain relationship given by Hooke's law fails in the source area.

One way to circumvent these inherent difficulties is to use a kinematic source description within the framework of Green's functions. A kinematic source description is one where the displacement discontinuity across the fault surface is prescribed. As we will see, knowing the fault slip as a function of space and time enables us to compute the ground motion at any given point within the medium by integrating the Green's functions weighted by the displacement discontinuity over the fault surface and applying a temporal convolution operator (Aki and Richards, 2002, Chapter 3). Such kinematic source models have the disadvantage that the slip function is adopted intuitively to represent seismic faulting and that they do not have any direct connection to the dynamic processes in the source region.

A more physical approach is to start from an initial state of stress on the fault plane and to let the rupture evolve freely, under a given constitutive law (e.g. slip weakening) which describes the interaction between stress and slip. Such dynamic rupture models are getting increasingly popular (e.g. Aagaard et al., 2001; Aochi and Madariaga, 2003; Gottschämmer, 2002; Olsen et al., 1997) and usually techniques such as finite-differences are applied to compute the temporal evolution of the rupture process. Yet, these simulations are computationally expensive, cover a rather limited frequency range and the physical interactions during earthquake rupture are far from being completely understood.

The following discussion focuses on kinematic source models, as the empirical Green's function technique employed in this work is based on such a source description. Let us begin with the introduction of the representation theorem and the definition of the Green's function.

2.2.1 Representation Theorem and Green's Functions

The *representation theorem* for seismic sources is the most fundamental equation presented in this thesis, as it is the foundation on which the empirical Green's function technique to simulate strong ground motion is build upon. In fact, there is not one single representation theorem and there are different ways to formulate it. Here, I present it in the form given by Aki and Richards (2002, p. 39):

$$\boxed{u_n(\mathbf{x}, t) = \int_{-\infty}^{+\infty} d\tau \iint_A [u_i(\boldsymbol{\xi}, \tau)] c_{ijpq} \nu_j \frac{\partial G_{np}(\mathbf{x}, t - \tau; \boldsymbol{\xi}, 0)}{\partial \xi_q} \, dA}. \tag{2.7}$$

$u_n(\mathbf{x}, t)$ is the nth component of displacement at point $\mathbf{x}$ at time t, $[\mathbf{u}(\boldsymbol{\xi}, \tau)] = \mathbf{u}(\boldsymbol{\xi}, \tau)|_{A^+} - \mathbf{u}(\boldsymbol{\xi}, \tau)|_{A^-}$ marks the displacement discontinuity (or fault slip) through the fault surface A, where $\boldsymbol{\xi}$ is the position

vector on the fault surface and τ the time at which the displacement occurs. ν is the vector normal to the fault surface and a linear elastic medium (stiffness tensor c_{ijpq}, stress-strain relation (2.4)) is assumed. Finally, $G_{np}(\mathbf{x}, t; \xi, \tau)$ is the *Green's function*. $G_{np}(\mathbf{x}, t; \xi, \tau)$ represents the nth component of displacement observed at location $\mathbf{x}$ and time t due to a unit point force impulse in direction p at location ξ and time τ. Thus, it depends on both source and receiver coordinates and satisfies the equation of motion:

$$\rho \frac{\partial^2 G_{np}}{\partial t^2} = \delta_{np} \delta(\mathbf{x} - \xi) \delta(t - \tau) + \frac{\partial}{\partial x_j} \left(c_{njkl} \frac{\partial}{\partial x_l} G_{kp} \right), \tag{2.8}$$

with initial conditions $G(\mathbf{x}, t; \xi, \tau) = 0$ and $\partial G(\mathbf{x}, t; \xi, \tau)/\partial t = 0$ for $t \leq \tau$ and $\mathbf{x} \neq \xi$. The boundary conditions depend on the considered system. Considering the Earth, the boundary conditions are determined by the free surface with vanishing traction vector.

From equation (2.7) it is clear to see that if the displacement discontinuity as a function of space and time and the Green's function (which is, strictly speaking, a 2nd-order tensor) is known, the motion within the entire medium is uniquely determined. [$\mathbf{u}$] involves a description of earthquake source physics, whereas G_{np} represents the propagation of the seismic waves from the source to the receiver.

In (2.7) as well as in the following, it is explicitly assumed that the boundary conditions are time-independent and homogeneous. Hence, the Green's function depends on time only through the difference $t - \tau$ and the time origin can be shifted (Aki and Richards, 2002, p. 27):

$$G_{np}(\mathbf{x}, t; \xi, \tau) = G_{np}(\mathbf{x}, t - \tau; \xi, 0) = G_{np}(\mathbf{x}, -\tau; \xi, -t) = G_{pn}(\xi, t; \mathbf{x}, \tau). \tag{2.9}$$

Further assumptions made in equation (2.7) are that there are no body forces for the displacement field $\mathbf{u}$ and that there is no traction discontinuity through A, i.e. [$\mathbf{T}(\nu)$] = 0. The representation theorem has certain limitations (Anderson, 2003). In the case of very large wave amplitudes at the observation point, the assumed linear stress-strain relation can break down. These are non-linear effects on ground motion which are not accounted for. The second problem may be on the source side. Equation (2.7) clearly splits the source and the propagation effects into parts which are independent of each other. If for instance the source process itself influences the seismic wave propagation, the Green's function depends explicitly on time t and not only on $t - \tau$ anymore. Nevertheless, the representation theorem has proven to be an extraordinary useful mathematical tool in the description of seismic sources.

In a homogeneous, isotropic, unbounded medium, the Green's function can be computed analytically (Aki and Richards, 2002, p. 492) and is given by:

$$G_{np}(\mathbf{x}, t; \xi, \tau) = \frac{(3\gamma_n \gamma_p - \delta_{np})}{4\pi\rho r^3} \int\limits_{r/v_P}^{r/v_S} t' \delta(t - \tau - t') dt' + \frac{\gamma_n \gamma_p}{4\pi\rho r v_P^2} \delta\left(t - \tau - \frac{r}{v_P}\right) - \frac{\gamma_n \gamma_p - \delta_{np}}{4\pi\rho r v_S^2} \delta\left(t - \tau - \frac{r}{v_S}\right). \tag{2.10}$$

In this notation, γ is the unit vector pointing from source point ξ to observation point $\mathbf{x}$ and $r = |\mathbf{x} - \xi|$ is the distance inbetween them. Note that G_{np} contains terms decaying with r^{-1}, which are the far-field terms, whereas the first term on the right-hand side is the near-field term. For realistic media, however, the Green's function cannot be given analytically.

In view of Chapter 4, where the details of the empirical Green's functions simulation technique are addressed, I modifiy the notation of the slip vector [$\mathbf{u}(\xi, \tau)$] on the fault plane as follows:

$$[u_i(\xi, \tau)] = D(\xi, \tau) l_i, \tag{2.11}$$

where $D(\boldsymbol{\xi}, \tau)$ is the slip time function which describes the temporal evolution of the displacement discontinuity at point $\boldsymbol{\xi}$ (its value is 0 before the rupture onset and $D_{final}(\boldsymbol{\xi})$ from that time on when the final value of slip has been reached). $\mathbf{l}$ denotes the unit vector in the direction of slip. A commonly used functional form for D is a ramp function, which we will meet again when describing the Haskell source model.

Using the convolution operator ($*$) and defining the *moment density tensor* as

$$m_{pq}(\boldsymbol{\xi}, \tau) = [u_i(\boldsymbol{\xi}, \tau)]c_{ijpq}v_j = D(\boldsymbol{\xi}, \tau)l_i c_{ijpq}v_j \,, \tag{2.12}$$

equation (2.7) can be rewritten as

$$u_n(\mathbf{x}, t) = \iint_A m_{pq} * \frac{\partial G_{np}}{\partial \xi_q} \, dA \,. \tag{2.13}$$

For an isotropic body and a displacement discontinuity which is parallel to the fault plane A, equation (2.12) becomes, with $R_{pq} = (v_p l_q + v_q l_p)$ being the *radiation pattern* in cartesian coordinates:

$$m_{pq} = \mu(v_p[u_q] + v_q[u_p]) = \mu D(v_p l_q + v_q l_p) = \mu D R_{pq} \,. \tag{2.14}$$

If the fault A lies in the plane defined by $\xi_1 = 0$ and the fault slip only has a component $[u_3]$ in ξ_3-direction, the only non-zero elements of the moment density tensor are m_{13} and m_{31}. The source process from a pure shear dislocation can be represented by a system of force couples perpendicular to each other, the so-called *double couple*, distributed over the fault plane. Note that the tensor $\mathbf{m}$ is both dependent on $\boldsymbol{\xi}$ and t. The displacement $\mathbf{u}(\mathbf{x}, t)$ can be computed as a linear superposition of the contributions from the double couples at the different locations on the fault.

2.2.2 Point Dislocation Source and Moment Tensor

As yet, all the considerations have been done for a fault plane of finite extent. If the wavelength is long as compared with the linear dimension of the fault ($\lambda \gg L$) and if the observation point is at least several wavelengths away from the fault ($r \gg \lambda$), the contributions from the different parts of the fault may be approximated to be in phase, which leads to the concept of an effective *point source* (Aki and Richards, 2002, p. 51-52). The seismic waves generated by this point source may be described in terms of a double couple with *moment tensor M* equal to the integral of the moment density tensor over A:

$$M_{pq} = \iint_A m_{pq} \, dA \,. \tag{2.15}$$

Thus, for a point source, equation (2.13) simplifies to

$$u_n(\mathbf{x}, t) = M_{pq} * \frac{\partial G_{np}}{\partial \xi_q} \,, \tag{2.16}$$

and introduction of (2.14) in (2.15) leads to:

$$M_{pq} = \mu A \bar{D}(t) R_{pq} \quad \text{with} \quad M(t) = \mu A \bar{D}(t) \,. \tag{2.17}$$

$M(t)$ describes the temporal evolution of the seismic moment. $\bar{D}(t)$ represents the temporal evolution of the average slip on the fault plane [1] and A is the source area. The displacement $\bar{D}(t)$ rises from 0 to

---

[1]Remember that the slip on the entire fault plane is condensed into a single point.

the final constant value $\bar{D}(\infty)$ within the source *rise time* τ_R. When the final value of slip is reached, the total *seismic moment*

$$\boxed{M_0 = \mu A \bar{D}(\infty)}.$$ (2.18)

has been released. This value is commonly used to characterize the size of an earthquake and it is one of the most fundamental quantities in seismology.

In a homogeneous, isotropic, unbounded medium, the displacement in the far-field due to a double couple point source may be given in spherical coordinates (with the point source being the origin) by (e.g. Lay and Wallace, 1995, p. 337):

$$\boxed{\mathbf{u}(\mathbf{x}, t) = \frac{\mathfrak{R}_P^{\theta\phi}}{4\pi\rho v_P^3} \frac{1}{r} \dot{M}\left(t - \frac{r}{v_P}\right) + \frac{\mathfrak{R}_S^{\theta\phi}}{4\pi\rho v_S^3} \frac{1}{r} \dot{M}\left(t - \frac{r}{v_S}\right)}.$$ (2.19)

$\dot{M}(t) = \mu A \dot{D}(t)$ denotes the *moment rate function* (also called *source time function*), $r = |\mathbf{x}|$ and $\mathfrak{R}_P^{\theta\phi}$ and $\mathfrak{R}_S^{\theta\phi}$ are the radiation patterns for P- and S-waves in spherical coordinates given by

$$\begin{aligned}
\mathfrak{R}_P^{\theta\phi} &= \sin(2\theta)\cos(\phi)\,\hat{\mathbf{r}} \\
\mathfrak{R}_S^{\theta\phi} &= \cos(2\theta)\cos(\phi)\,\hat{\boldsymbol{\theta}} - \cos(\theta)\sin(\phi)\,\hat{\boldsymbol{\phi}},
\end{aligned}$$ (2.20)

$\hat{\mathbf{r}}$ being the radial and $\hat{\boldsymbol{\theta}}, \hat{\boldsymbol{\phi}}$ the transverse unit vectors, respectively. From equation (2.19), we see that the displacement in the far-field is proportional to the moment rate function (respectively to the slip velocity $\dot{D}(t)$) at the source. Furthermore, the radiation patterns show that the particle motion resulting from the P-waves only has a radial component, whereas the particle motion resulting from the S-waves only has a transverse component. Usually, a point source is a good approximation for small earthquakes where effects due to rupture propagation (such as e.g. directivity) are not that important. Clearly, assuming a large earthquake with a fault plane that may be as large as several hundred to thousand kilometers as a point source is only justified for long-period, teleseismic waves.

2.2.3 The Haskell Source Model and Directivity

The kinematic source model developed by Haskell (1966) is widely utilized and described in detail in most textbooks on seismology (e.g. Lay and Wallace, 1995). It consists of a rectangular fault plane of length L and width W (see Figure 2.1). The rupture propagates unilaterally in x-direction. The starting point in the derivation of this model is to subdivide the fault into small segments with width W and length dx, hence effectively considering a line source of length L. Each of these segments is considered to be a double couple point source. The displacements resulting from such a point source are given in equation (2.19). With a unilateral rupture propagation with constant rupture velocity v_r and letting $dx \to 0$, it is possible to write the displacement caused by the Haskell source model as the integral of the contributions of all the infinitesimally small segments lagged in time. Since the moment rate $\dot{M}(t)$ for each little segment may be given as $\dot{M}(t) = \mu W dx \dot{D}(t)$, where $\dot{D}(t)$ is the slip velocity of this segment, we may write the far-field P-wave displacement in spherical coordinates (the same is of course valid for the S-wave displacement):

$$u(r, t)^P = \frac{\mu \mathfrak{R}_P^{\theta\phi} W}{4\pi\rho r v_P^3} \int_0^x \dot{D}(t) * \delta\left(t - \frac{x}{v_r}\right) dx.$$ (2.21)
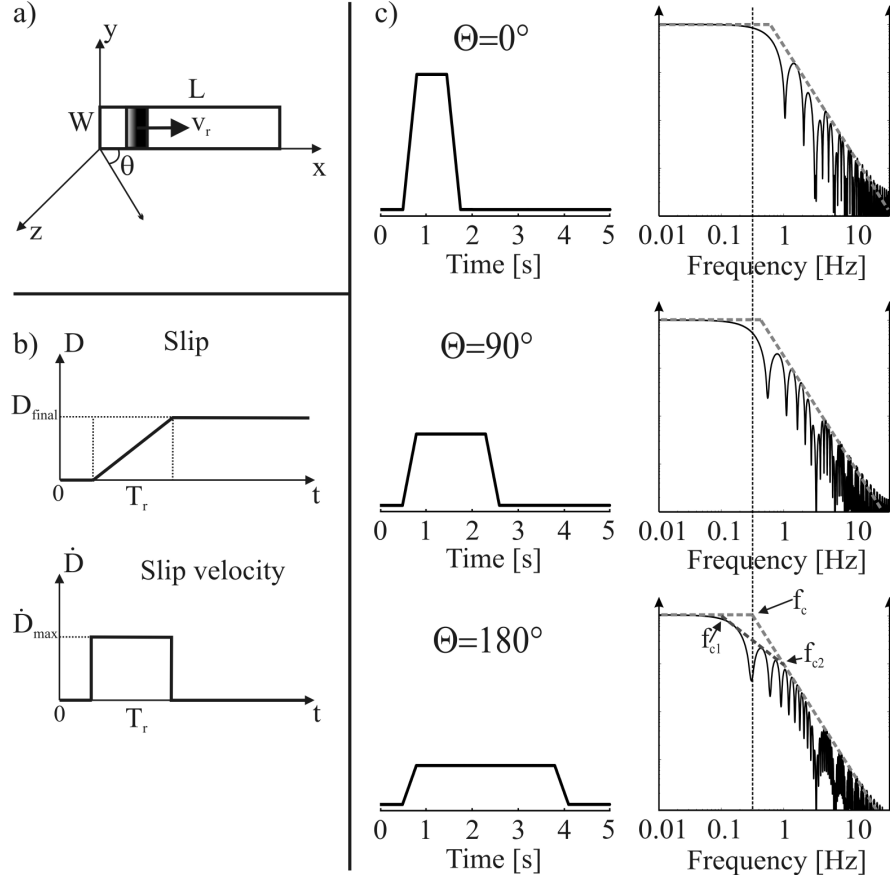
Figure 2.1: The Haskell source model. a) Sketch of the kinematic model. The fault plane of length L and width W ruptures from left to right with constant rupture velocity v_r. θ defines the angle between rupture propagation direction and observation point. b) Slip and slip velocity time functions assumed in the Haskell model for a point on the fault plane. c) Illustration of the trapezoidal source time function (left) and the corresponding source spectrum (on loglog axes) for three different θ. The directivity effect is clear to see. Further details are discussed in the text.

Herein, the sifting property of the δ-function has been used. As the slip velocity $\dot{D}(t)$ is assumed to be the same everywhere on the fault, it can be taken outside of the integral. The integral of the δ-function is the Heaviside step function, and carrying out the integration by substituting $z = t - x/v_r$ leads to:

$$\mathbf{u}(r,t)^P = \frac{\mu \mathcal{R}_P^{\theta\phi} W}{4\pi\rho r v_P^3} v_r \dot{D}(t) * B(t; \tau_c). \tag{2.22}$$

$B(t; \tau_c)$ is a boxcar of duration τ_c, the latter one being the *rupture time* of the fault. As indicated in Figure 2.1, a possible slip function $D(t)$ may be a ramp function, starting at zero slip and reaching D_{final} after the *rise time* T_r. The corrresponding slip velocity function $\dot{D}(t)$ is a boxcar of duration T_r. Hence the source time function of such an earthquake is given by the convolution of two boxcars with length T_r and τ_c, which leads to a trapezoidal shape.

The so-called *directivity* is an important consequence of such an extended source model. In fact, the rupture time is not equal to the real rupture duration (which is equal to $\frac{L}{v_r}$), but is azimuth-dependent.

This is the seismological analogy to the Doppler effect in acoustics. τ_c is given as:

$$\tau_c = \frac{L}{v_r} - \frac{L\cos(\theta)}{c}, \tag{2.23}$$

where c is the velocity of the considered wave type (Lay and Wallace, 1995). Thus, the source time function in the Haskell model is always a trapezoidal function whose overall length varies with viewing azimuth (the source time functions for three azimuths are schematically shown in Figure 2.1). As the area below the source pulse must be equal to the total seismic moment M_0 in every direction (e.g. Lay and Wallace, 1995, p. 368), the amplitude of the source time function is much larger if the rupture time is shorter. Thus, the waveforms in the direction of rupture propagation ($\theta = 0°$) will be more impulsive with higher frequency content (see Section 2.2.4) than those in the opposite direction ($\theta = 180°$). One last thing to note at this stage is that for the point source, the source rise time τ_R as defined in Section 2.2.2 is different from the rise time T_r defined here. Within τ_R, the entire seismic moment of the 'point source earthquake' is released, whereas within T_r in the finite fault model, only the contribution of one single point on the fault plane to the seismic moment is released. Only through the convolution with the boxcar describing the rupture propagation the entire seismic moment is reached.

2.2.4 The Source Spectrum

The source time function derived in the preceding section, being a convolution of two boxcars, may be rewritten as (see also e.g. Lay and Wallace, 1995):

$$S(t) = M_0(B(t; T_r) * B(t; \tau_c)). \tag{2.24}$$

As the Fourier transform of a boxcar is given by

$$F(B(t; \tau)) = \hat{B}(\omega) = \frac{\sin(\omega\tau/2)}{\omega\tau/2}, \tag{2.25}$$

where $\omega = 2\pi f$ denotes the angular frequency, and the convolution operator in time corresponds to a multiplication in frequency domain, the displacement Fourier amplitude spectrum (FAS) derived from the Haskell source is

$$\hat{S}(\omega) = M_0 \left| \frac{\sin(\omega T_r/2)}{\omega T_r/2} \right| \cdot \left| \frac{\sin(\omega \tau_c/2)}{\omega \tau_c/2} \right|. \tag{2.26}$$

The spectrum in (2.26) displays three characteristic regions: a flat portion with value M_0 for frequencies lower than $f_{c1} = 1/\pi\tau_c$, a spectral decay proportional to f^{-1} for frequencies between $f_{c1} = 1/\pi\tau_c$ and $f_{c2} = 1/\pi T_r$ and a spectral decay proportional to f^{-2} for high frequencies ($f > f_{c2}$). Commonly, the f^{-1} decay is very difficult to detect and only one *corner frequency* f_c, which is defined as the intersection between the low-frequency plateau and the f^{-2} decaying part of the spectrum, is identified:

$$f_c = \frac{1}{\pi\sqrt{\tau_c T_r}}. \tag{2.27}$$

This is the so-called f^{-2}- or ω^{-2}-model. The form of the theoretical source spectrum is indicated with the calculated source spectrum for each displacement pulse in Figure 2.1. The corner frequency is highest in the case of forward directivity (i.e. $\theta = 0°$). In the plot for $\theta = 180°$, the f^{-1} decay between f_{c1} and f_{c2} is also shown. It is much harder to identify for $\theta = 0°$, as the rupture time τ_c is shorter in

that case and closer to T_r, leading to corner frequencies which are close to each other. In such a case, the ω^{-2}-model with one corner frequency provides the best description of the spectrum.

If one wants to determine the corner frequency from the observed spectra, one has to perform some sort of spatial averaging of the spectra, as rupture propagation effects may considerably distort the spectral shape at a given location. In a general form, an ω^{-2} Fourier amplitude source spectrum can be written as:

$$|S(\mathbf{x}, f)| = M_0 \cdot \left[1 + \left(\frac{f}{f_c} \right)^2 \right]^{-1}.$$ (2.28)

Generally, the corner frequency is observed to be higher for P-waves than for S-waves (Aki and Richards, 2002).

The corner frequency plays an important role in seismology, as it is inversely proportional to the linear dimension of the fault. Brune (1970, 1971), as we will see in the next section, developed a relation between the dimension of a circular fault and the corner frequency which has been used extensively in observational seismology. However, it is disputed whether it is possible to give an exact relation (Beresnev, 2001), and this issue will be treated in more details in Chapter 3. The ω^{-2} spectral scaling has been found to explain the observed earthquake spectra best (e.g. Boore, 1986; Aki and Richards, 2002), although other source models exist which lead to different high frequency spectral decays such as e.g. ω^{-3}. For the Haskell case, if the rupture propagation would be considered to be two-dimensional, an ω^{-3} source spectrum with three corner frequencies would be expected. Note that the Haskell source model is about rupture propagation only and does not include any effects due to rupture nucleation or arrest. As Aki and Richards (2002, Chapter 10) discuss, the spectral decay at high frequencies is also largely influenced by the nucleation and stopping mechanisms.

2.2.5 The Brune Source Model

Starting from the assumption of a circular fault on which an instantaneous shear stress pulse is applied, Brune (1970, 1971) proposes a model where this stress pulse generates a shear wave which propagates through the medium. As the stress pulse is applied instantaneously, no effects of rupture propagation are considered. The far-field displacement in this model is given by:

$$u(t) = \Re^{\theta\phi} \frac{r}{R} \frac{\Delta\sigma}{\mu} v_S \left(t - \frac{R}{v_S} \right) e^{-2\pi f_c \left(t - \frac{R}{v_S} \right)}.$$ (2.29)

r/R corresponds to a geometrical attenuation term, r is the fault radius and R, $\Delta\sigma$ and μ are the source-site distance, (dynamic) *stress drop* and shear modulus respectively. $\Re^{\theta\phi}$ is the radiation pattern. The FAS of relation (2.29) becomes:

$$|\hat{u}(f)| = \Re^{\theta\phi} \frac{r}{4\pi^2 R} \frac{\Delta\sigma}{\mu} v_S \frac{1}{f^2 + f_c^2}$$ (2.30)

with

$$f_c = \frac{2.34}{2\pi} \frac{v_S}{r}.$$ (2.31)

This is the famous relation between corner frequency and source radius r. It has been used in numerous studies to estimate source dimensions from measured corner frequencies, mostly for small to moderate

earthquakes. Formula (2.31) assumes total (static) stress drop, i.e. the shear stress drops from the tectonic stress σ_0 to the frictional stress σ_f. Stress drop and the related issues are further treated in Section 2.3 and Chapter 3. From (2.30), it is easy to see that the Brune model leads to a FAS which has an ω^{-2}-shape, akin to the Haskell model presented earlier. Finally, Brune also proposes the following relation between the seismic moment and the stress drop:

$$M_0 = \frac{16}{7}\Delta\sigma r^3.$$ (2.32)

2.3 Empirical Scaling Relations

The most important quantity in earthquake scaling relations is the *stress drop*, which has been briefly introduced above. Strictly speaking, we have to distinguish between *static* and *dynamic* stress drop, and a detailed discussion concerning this distinction can be found in Chapter 3. The static stress drop $\Delta\sigma_S$ represents the difference in the state of stress on the fault plane before and after the earthquake, i.e. $\Delta\sigma_S = \sigma_0 - \sigma_1$. σ_0 stands for the tectonic shear stress on the fault before and σ_1 denotes the state of shear stress after earthquake rupture. $\Delta\sigma_S$ is proportional to the deformation on the fault plane:

$$\Delta\sigma_S = C_S\mu\frac{\bar{D}}{\tilde{L}}.$$ (2.33)

$\bar{D}$ is the average (final) slip and $\tilde{L}$ is a characteristic rupture dimension. C_S is a non-dimensional constant which is geometry-dependent, of order unity (Kanamori, 1994). The static stress drop defined by relation (2.33) represents a spatial average over the fault plane. As long as source models such as the Haskell model with uniform slip are considered, the local stress drop at a given point is identical to the average stress drop. However, as discussed further below, the displacement over the fault plane for real earthquakes can be very complex and hence, the static stress drop will not be the same everywhere either. Typical stress drop values for crustal earthquakes range between 10 to 100 bars (e.g. Kanamori, 1994). Setting $\tilde{L} = \sqrt{A}$, where A is the fault area, and using the definition of the seismic moment (2.18), we get:

$$M_0 = \frac{1}{C_S}\Delta\sigma_S A^{\frac{3}{2}}$$ (2.34)

or, logarithmically,

$$\log M_0 = \frac{3}{2}\log A + \log\left(\frac{\Delta\sigma_S}{C_S}\right).$$ (2.35)

If $\Delta\sigma_S$ is constant, (2.35) gives a linear relationship between $\log M_0$ and $\log A$ with slope 3/2. As the observations do indeed follow this trend (albeit a large scatter in the data) (see e.g. Lay and Wallace, 1995), it has been generally accepted that the static stress drop is roughly constant, ranging from 10 to 100 bars. This constant stress drop assumption leads to the well-known concept of *self-similarity* among earthquakes, which is exploited in Irikura's empirical Green's functions method. It states that the earthquake source process is scale-invariant and that events of different sizes cannot be distinguished except by a scale factor. Static stress drop values are usually subjected to large uncertainties. As $\Delta\sigma_S \propto \tilde{L}^{-3}$ for a given seismic moment, an uncertainty of factor 2 in source dimensions leads to an uncertainty of factor 8 in static stress drop.

A direct consequence of constant static stress drop is that the average slip $\bar{D}$ scales with rupture dimension, i.e. $\bar{D} \propto \tilde{L}$ and that the seismic moment scales with rupture duration τ_c such that $M_0 \propto \tau_c^3$
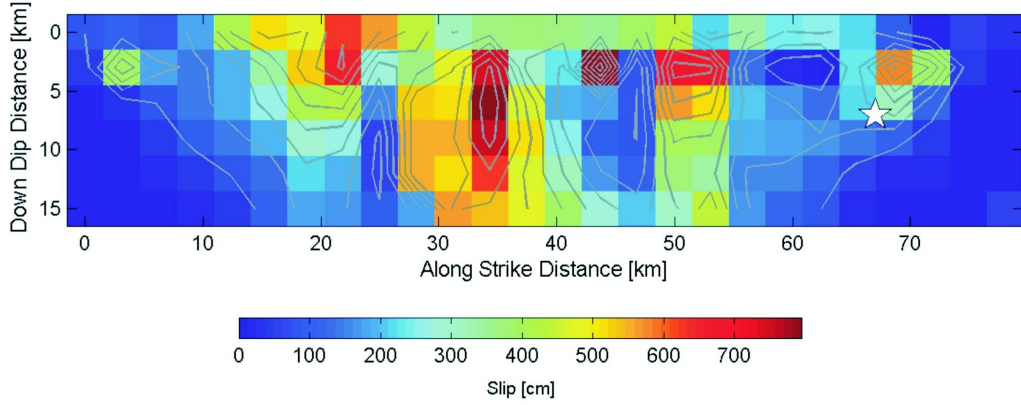
Figure 2.2: Slip distribution for the 1992 Landers, California, earthquake (Wald and Heaton, 1994, modified from http://www.seismo.ethz.ch/srcmod/). The white star marks the hypocenter and the dark red patch at approx. 35 km along strike constitutes the largest asperity.

(with constant rupture velocity v_R). These are the conditions for static similarity. The condition for dynamic similarity is that the (average) slip velocity be constant. This implies, as we will see in Chapter 3, that the dynamic stress drop is constant too and that the rise time is proportional to the average slip, i.e. $T_r \propto \bar{D}$. Then, the ω^{-2} source spectrum obeys to the following relation:

$$M_0 f_c^3 = constant\,, \tag{2.36}$$

a fact which was recognized by Aki (1967). For a rectangular fault of length L and width W, static similarity imposes that the fault aspect ratio is constant ($W \propto L$). This is the reason why self-similarity breaks down for very large crustal earthquakes which rupture through the entire seismogenic zone. In that case, the fault slip becomes independent of fault length (Scholz, 2002).

Hanks and Kanamori (1979) defined the *moment magnitude* scale, which, unlike other magnitude scales, does not saturate for very large earthquakes:

$$\boxed{M_W = \frac{2}{3} \log_{10} M_0[Nm] - 6.03}\,. \tag{2.37}$$

Other authors (e.g. Wells and Coppersmith, 1994; Somerville et al., 1999; Mai and Beroza, 2000) derived empirical scaling relations between several parameters that may be used to characterize the earthquake source, for instance between seismic moment (or M_W) and fault dimensions, which are usually only valid for crustal earthquakes within a given magnitude range. It is important to note that these relations are all build upon the condition that the self-similarity principle is valid.

Complexity of Earthquake Slip and Asperities

So far, I have only spoken about average source properties, such as average static stress drop and average slip. However, for many earthquakes worldwide, slip inversions have been performed, revealing that the slip distribution on the fault plane is in fact highly heterogeneous in space and time (e.g. Heaton, 1990; Wald and Heaton, 1994; Sekiguchi and Iwata, 2002) (a database containing many of these finite source rupture models has been compiled by P.M. Mai and can be found online at

http://www.seismo.ethz.ch/srcmod/). An example for such a model is given in Figure 2.2. These observations clearly show that a source model with uniform slip and slip velocity (e.g. the Haskell model discussed above) is a very strong simplification of the rupture process during earthquakes. The true source process may even show variability on a much smaller scale than the results of slip inversions indicate, as these studies usually utilize only long period waves.

Areas on the fault plane which show large slip relative to the average slip over the entire rupture surface are called *asperities*. In terms of the definition of the seismic moment (2.18), these regions are responsible for a large part of the moment release. This definition of an asperity characterizes the earthquake source process as a function of slip. As we will see later in this work, another option is to define an asperity in view of slip velocity, which makes sense if high frequency radiation is considered. The areas on the fault plane where very little slip occurs during the earthquake are often termed as *barriers*. Although, initially, asperities and barriers have been considered as separate models (Udias, 1999, p. 355-357), a mixture of both is necessary to explain the observed properties of earthquake rupture.

Several researchers attempted to characterize the complexity of earthquake source models in order to improve strong ground motion predictions (e.g. Somerville et al., 1999; Mai and Beroza, 2002). Whereas Mai and Beroza (2002) use spatial random fields for this purpose, Somerville et al. (1999) develop empirical scaling laws between seismic moment and asperity size, moment and rise time etc. They find for instance that the combined area of asperities occupies approx. 22% of the total fault area for crustal earthquakes.

2.4 Path and Site Effects

As the earthquake source description is of key importance for the empirical Green's functions method employed in this work, I have focussed in the preceding section on the details of the source process. However, the ground motions at a given site do not solely depend on source effects. The seismic waves that propagate from the fault plane to the site of interest are affected and, under certain circumstances, severely modified by path and site effects. Commonly, source, path and site effects are considered to be independent of each other and each of them can be represented by a linear filter. Then, the observed waveform $u(\mathbf{x}, t)$ may be expressed as (see e.g. Lay and Wallace, 1995; Stein and Wysession, 2003):

$$u(\mathbf{x}, t) = s(\mathbf{x}, t) * p(\mathbf{x}, t) * i(\mathbf{x}, t), \tag{2.38}$$

where $s(\mathbf{x}, t)$ represents the source, $p(\mathbf{x}, t)$ the propagation path, $i(\mathbf{x}, t)$ the site effect and $*$ denotes convolution. The instrument response is considered to be already corrected for in equation (2.38).

If one compares this formulation for ground motions with equation (2.13), the Green's function in the latter relation contains the path and site effects. Note however that the separation of the effects as given by (2.38) is, strictly speaking, only correct if the earthquake source may be regarded as a point source, i.e. if the observation point is in the far-field. In that case, the Green's function (and thus, the path and site effect) is in a first approximation independent of the position on the fault plane.

The convolution in time domain corresponds to a multiplication in frequency domain:

$$\boxed{U(\mathbf{x}, f) = S(\mathbf{x}, f) \cdot P(\mathbf{x}, f) \cdot I(\mathbf{x}, f)}. \tag{2.39}$$

Equation (2.39) constitutes the basis for *spectral ground motion models*, which are of central importance for Chapter 7. It is important to note that the considerations below are done in view of the

amplitude spectrum only. The frequency domain, in order to be formally equivalent to time domain, furthermore includes the phase spectrum. The issue of the phase is further treated in Chapter 4.2. Thus, in the following, only the amplitude spectra are considered.

The source term $S(\mathbf{x}, f)$ is usually supposed to follow the ω^{-2}-scaling for FAS as given by (2.28) multiplied by a constant as given later on in equation (4.31). The path term $P(\mathbf{x}, f)$ may be splitted into the effects of *geometrical spreading* and *anelastic attenuation*, whereas the site term $I(\mathbf{x}, f)$ may be divided into the *site amplification* and path-independent *high frequency diminution*. All of these different terms influence the observed ground motion and are introduced in the subsections below.

2.4.1 Path Effects

Geometrical Spreading

With geometrical spreading, seismologists refer to the fact that the amplitudes on a given wavefront decrease as the area of the wavefront increases, which is a simple consequence of the conservation of energy. Body waves (P- and S-waves) in a homogeneous medium depict spherical wavefronts, and the amplitude decay can be described by ($R(\mathbf{x})$ is the distance from source to site):

$$\boxed{G(\mathbf{x}) = \frac{1}{R(\mathbf{x})}}, \qquad\qquad (2.40)$$

Anelastic Attenuation and Scattering

Anelastic attenuation as well as the phenomenon of scattering lead to a decrease in wave amplitudes with distance and time. The former is due to the fact that the Earth is not a perfectly elastic body and energy is lost in terms of heat due to internal friction. The latter is due to the wavefield's interaction with small-scale heterogeneities. The propagating waves are refracted, reflected, diffracted and conversions from P- to S-waves and vice-versa take place at these heterogeneities. Long-period waves are rather insensitive to these effects, but high-frequency waves are strongly affected and coda waves form. Note that anelastic attenuation leads to an effective loss of energy, while scattering redistributes the energy.

Anelastic attenuation is quantitatively described by the *quality factor Q*. The inverse of Q is proportional to the ratio of energy ΔE dissipated during one cycle of oscillation with angular frequency ω to the mean energy E contained in the cycle:

$$\frac{1}{Q} = \frac{1}{2\pi} \frac{\Delta E}{E}. \qquad\qquad (2.41)$$

Typical values for Q range from several tens to several thousands in compacted rock (Lay and Wallace, 1995), i.e. attenuation is generally rather small. This may be quite different e.g. in very soft sediments. The amplitude reduction of a harmonic P- or S-wave with angular frequency $\omega = 2\pi f$ with distance is given by

$$A(\mathbf{x}) = A_0 \cdot \exp\left[-\frac{\pi f R(\mathbf{x})}{Q(f)c}\right], \qquad\qquad (2.42)$$

where c is the seismic velocity of the considered wave type and A_0 is the initial amplitude. $Q(f)$ is roughly constant for long-period waves (1000 - 1 s period). For smaller periods, it has been found

experimentally that Q increases with frequency (attenuation is larger for higher frequencies) as a power law of the form (Udias, 1999):

$$Q(f) = Q_0 \left(\frac{f}{f_0} \right)^n.$$ (2.43)

Q_0 is the value corresponding to the reference frequency f_0. To summarize, the operator accounting for anelastic attenuation may be written as:

$$E(\mathbf{x}, f) = \exp\left[-\frac{\pi f R(\mathbf{x})}{Q(f)c} \right],$$ (2.44)

with $Q(f)$ expressed through (2.43). Note that the above relations require that attenuation be linear, i.e. Q is independent of wave amplitude, and that attenuation be small, i.e. $Q \gg 1$. Very close to large earthquakes or explosions, attenuation may become nonlinear due to the large strains involved (Stein and Wysession, 2003). Q-values are usually higher for P- than for S-waves, meaning that the compressional waves are less damped than the shear waves.

2.4.2 Site Effects

Site effects may have an enormous impact on ground motion and play an important role in seismic hazard assessment. Per definition, site effects modify the seismic wavefield in the immediate vicinity of the receiver as compared with a site that shows no response. Usually, they include modifications of the waves by soft sedimentary layers, effects of local topography, water table or sedimentary basins (Anderson, 2003). By engineering seismology practice, site effects are limited to the upper 30 to few hundred meters and are commonly linked to the average shear wave velocity v_{S30} of the upper 30 m (Boore and Joyner, 1997). Note that changes in the wavefield due to large-scale tectonic structures such as deep sedimentary basins (e.g. focusing and defocusing of basin-edge induced surface waves, wave-guiding), in the strictest sense, may not be counted among site effects, as the structures causing them can be correlated over many kilometers laterally and/or in depth. Their consequences can be analyzed separately by considering two- or three-dimensional models of wave propagation (e.g. Oth et al., 2007b).

Site effects are usually assessed using observational data, such as weak and strong motion or ambient noise, or through numerical simulation of wave propagation through (mostly 1D) underground models below the site of interest (Kawase, 2003, and references therein). They are highly frequency dependent and can be non-linear (i.e. non-linear stress-strain relation). Non-linearity in soft media, as noted by Kawase (2003), tends to reduce shear rigidity and shear wave velocity, while it increases the damping factor. This results in prolongation of the predominant periods and, generally, in a reduction of amplitude.

For further discussion, I follow e.g. Boore (2003) and separate the site term $I(\mathbf{x}, f)$ into two contributions: the site amplification $H(f)$ and high frequency diminution $D(f)$. The dependency on $\mathbf{x}$ is not written explicitly anymore in the following. As part of relation (2.39), the site effect is considered to be linear, i.e. independent of wave amplitude.
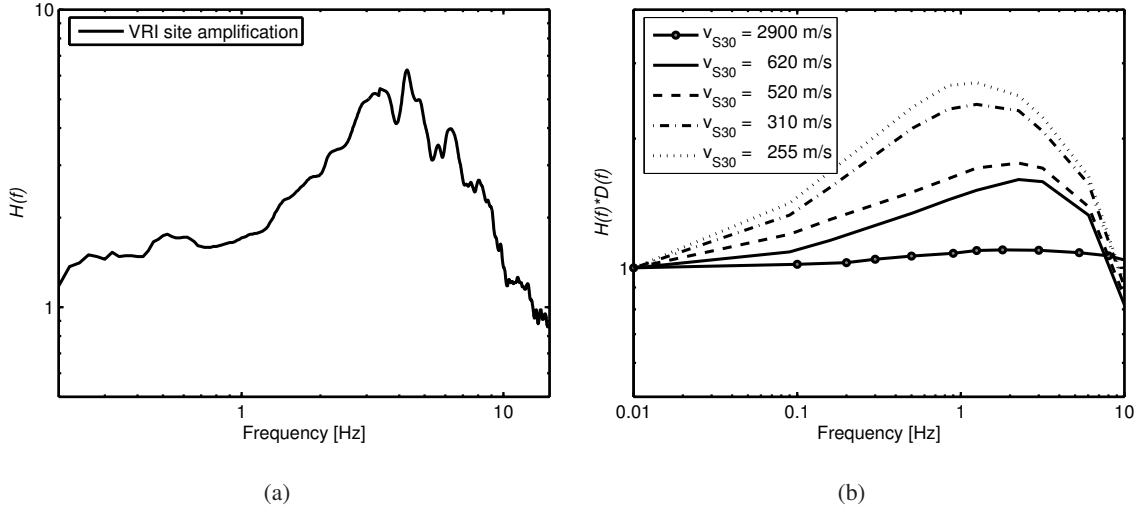
Figure 2.3: (a) Amplification spectrum $H(f)$ for station VRI (Romania) as derived by Sokolov et al. (2004). (b) Combined effect of site amplification $H(f)$ and high frequency diminution $D(f)$ for sites classified following their average shear wave velocity of the upper 30 m v_{S30} (Boore and Joyner, 1997).

Site Amplification

Seismic waves impinging on a low-velocity sedimentary layer are amplified due to the impedance contrast between this layer and the underlying bedrock. As a result of energy conservation, the amplitudes are heightened in the low-velocity layer. Moreover, the waves are trapped within the layer and bounce up and down, which leads to resonance effects. The constructive interference of these resonating waves consequently leads to further amplification (Bard, 1999).

For a 1D structure consisting of a sedimentary layer with average shear wave velocity β and bedrock below and vertically incoming SH-waves, the resonance is maximal at the frequencies:

$$f_n = (2n + 1)\frac{\beta}{4h} \quad \text{with } n = 0, 1, 2 \ldots, \tag{2.45}$$

where h is the thickness of the layer (Bard, 1999). (2.45) indicates that constructive interference takes place if the thickness of the layer is a multiple of the quarter-wavelength.

Site amplification is usually assessed in terms of *amplification spectra*. Multiplying the FAS of the bedrock motion with this amplification spectrum leads to the FAS of the ground motion at the site. The different methods to estimate site amplification have recently been reviewed and summarized by Kawase (2003, see also references therein). Most techniques are based on the separation of the different contributions to ground motion following (2.39). One way is to use a reference site close to the site of interest which may be regarded as free of site effect. As the ground motion at both sites is influenced by the same source and approx. the same propagation path effect, a simple division of the FAS gives an estimate of site amplification. However, as an appropriate reference site is rarely available, the H/V-technique has been developed. Briefly, this technique assumes that the vertical component is almost free from site influence and hence, by spectral division of the horizontal components by the vertical component, only the amplification spectrum should remain. The H/V-method has been applied both on S-wave earthquake recordings (e.g. Lermo and Chavez-Garcia, 1993; Sokolov et al.,

2005) and ambient noise (Nakamura, 1989). Sokolov et al. (2004) simulated theoretical very hard rock (VHR) spectra from Vrancea earthquakes and divided the observed spectra by the VHR spectra to obtain an estimate for site amplification.

An example for such an amplification spectrum is shown in Figure 2.3(a). Boore and Joyner (1997) compute spectral amplification functions using the quarter-wavelength approximation for different soil types classified following the average shear wave velocity of the upper 30m v_{S30} derived from borehole data. They show that the amplification spectrum may be approximated by a series of straight lines in loglog-space. Boore (2003) uses such a parameterization of site amplification in his stochastic method for simulating ground motions. The combined effect of spectral amplification and high frequency diminution (discussed below) for different site conditions (as given in Boore and Joyner, 1997) is plotted in Figure 2.3(b).

High Frequency Diminution

The ω^{-2}-model for the source spectra predicts a plateau at low frequencies if the resulting displacement spectrum is considered, as can be seen from (2.28). Then, the second derivative displays a plateau at frequencies higher than the corner frequency f_c (due to the factor $(2\pi f)^2$ when differentiating the spectrum). Yet, observations indicate that the FAS of acceleration data (even after correction for anelastic attenuation) falls off rapidly for frequencies higher than a given maximum value f_{max} (Hanks, 1982), which is usually found in the range 8 - 10 Hz. Boore (2003) summarizes that the effect may be accounted for by two types of filters: the f_{max} filter of the form

$$D(f) = \left[1 + \left(\frac{f}{f_{max}} \right)^8 \right]^{-\frac{1}{2}} , \tag{2.46}$$

or the κ filter introduced by Anderson and Hough (1984)

$$\boxed{D(f) = \exp(-\pi\kappa f)} . \tag{2.47}$$

Physically, it is not quite clear whether this high frequency diminution is related to the seismic source or to the site. Anderson and Hough (1984) for instance related the effect to high attenuation in the near-surface weathered layers. It may, however, also reflect some minimum source size. Atkinson and Silva (1997) argue that κ should be considered as a magnitude-dependent quantity, due to non-linear behavior of surface rocks.

Finally, one should note that the anelastic attenuation operator given by (2.44) also induces high frequency diminution of a very similar form. Therefore, trade-offs, especially between the κ- and Q-operators, result and it is not a trivial task to determine these parameters *uniquely*. As Anderson and Hough (1984) already noted, by setting the exponent n in (2.43) to 0.25, equation (2.44) leads to a functional form which is very similar to (2.47).

2.5   Ground Motion Parameters and Seismic Intensity

The most complete description of seismic ground motion is given by the recorded time series. From the engineering point of view, the time series itself is not very convenient to parameterize ground

motion. Rather, it is attractive to extract parameters from the time series which characterize amplitude, duration and frequency content. Common ground motion parameters which are used in some way or the other in this thesis are shortly presented below. The most important one in view of my work is seismic intensity, as it is used as a criterion of fit in the inversions presented in Chapter 6. A more detailed discussion of these parameters can be found e.g. in Kramer (1996).

2.5.1 PGA, PGV and PGD

Peak ground acceleration (PGA), *peak ground velocity* (PGV) and *peak ground displacement* (PGD) are the maximum absolute values of the acceleration, velocity and displacement waveforms. From the vector sum of the two horizontal components, the *peak horizontal acceleration* (PHA) and *peak horizontal velocity* (PHV) can be determined. PGD is more difficult to determine accurately, as integration of the records and long-period noise may pose problems in the low-frequency range.

2.5.2 Duration

The duration of strong ground motion is an important parameter, as it has a strong influence on earthquake damage. There are different definitions of duration (Kramer, 1996). The *bracketed duration* is defined by the first and last exceedence of a certain threshold in acceleration, which is often set to 0.05 g. Trifunac and Brady (1975) define the time interval in which 90 % of the acceleration-squared takes place as the duration of strong ground motion (between 5 % and 95 %).

2.5.3 Spectral Parameters

The frequency content of the observed time series is of crucial importance, both from the seismological and the engineering viewpoint. First, the frequency content may provide valuable information on the earthquake source as well as the underground structure. Secondly, the response of structures such as bridges or large buildings is very sensitive to the frequency at which they are loaded (Kramer, 1996).

Through Fourier transformation, a given time series can be *equivalently* expressed by the Fourier amplitude and phase spectra. The Fourier amplitude spectrum then directly shows the frequency content of the time series. The FAS, as shown in the previous sections, may also be parameterized in terms of corner frequency f_c, cut-off frequency f_{max}, seismic moment M_0, etc. Hence, the FAS is directly related to the characteristics of the source and wave propagation.

Another type of spectrum, the *response spectrum*, describes the maximum response of a single-degree-of-freedom system to a given exciting ground motion as a function of eigenfrequency of this system. For instance, a one- to two-storey building has an eigenfrequency of about 5 Hz. As a rule of thumb, the eigenperiod of a building can be estimated as 0.1 times the number of stories. Thus, a ten-storey building has an eigenfrequency of around 1 Hz and sensitive to lower frequency ground motion than a smaller building. There are different types of response spectra for acceleration, velocity and displacement (Anderson, 2003) and, commonly, they are computed with a damping factor of 5 %. Note that, in contrast to the FAS, the response spectrum is dependent on the duration of ground motion. For further details, I refer the reader to Kramer (1996) and Jennings (2003).
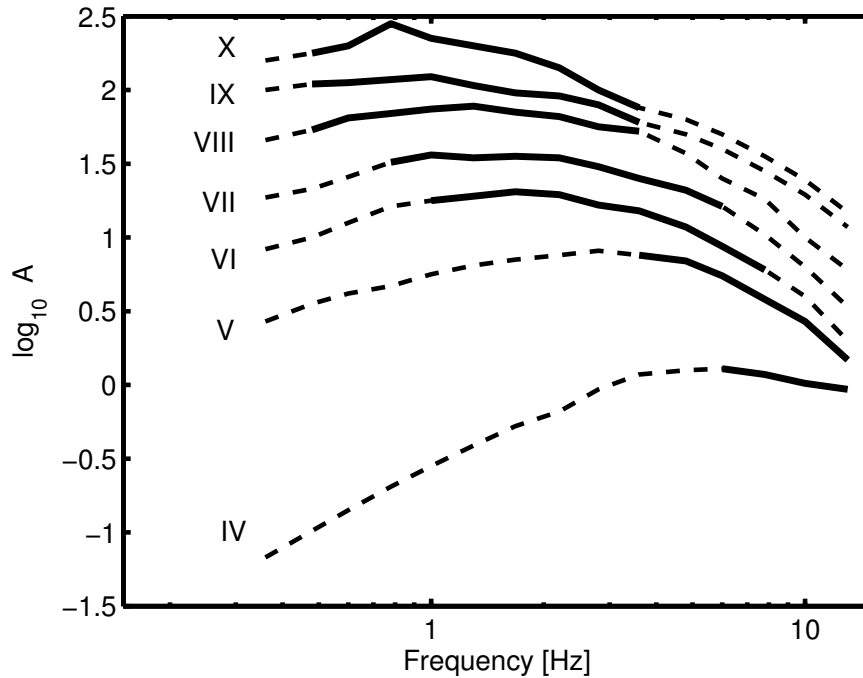
Figure 2.4: Empirical reference spectra for determining MM intensities from the FAS. For each given intensity, these spectra correspond to the logarithmic mean FAS of worldwide accelerograms at locations where this intensity level has been reported (Sokolov, 2002). The thick part of each spectrum corresponds to the representative frequency range.

2.5.4 Seismic Intensity

Seismic intensity is the oldest measure of earthquake size. Intensity if based on a qualitative description of human reaction and observed damage at a given location. If this information has been collected for many locations, an *isoseismal map* can be created for a larger area. Generally, the intensity is greatest in the vicinity of the epicenter (Kramer, 1996). Different intensity scales exists, and the most commonly utilized ones are the *modified Mercalli* (MM), *Medvedev-Spoonheuer-Karnik* (MSK), *European Macroseismic* (EMS) and *Japanese Meteorological Agency* (JMA) scales. As shown in a comparison plot in Kramer (1996), the MM and MSK scales differ only for low intensities (levels I-III) and are almost identical for higher intensities. A detailed description of the MM scale is also given in the latter reference.

As such, seismic intensity is nothing else than a quite simple quantification of earthquake damage and human behavior and many researchers have correlated intensity with peak ground motion parameters (e.g. Trifunac et al., 1975; Murphy and O'Brien, 1977; Wald et al., 1999), even though the scatter of the data is rather large. Intensity may be seen as a combined effect of amplitude, duration and frequency content of ground motion. As mentioned by Sokolov (2002), the FAS depends on all of these factors and therefore, may be better correlated with intensity than simple peak parameters.

From the FAS of about 1150 acceleration records worldwide, Sokolov (2002) links MM (or MSK) intensity to the FAS between 0.4 - 13 Hz. Each intensity value is associated with a representative frequency range, which is given by the frequency band where the variance of the logarithmically

averaged FAS is minimal (i.e., where $\sigma^2 \leq 1.3 \ \sigma^2_{min}$). Low MM intensities (III-IV) are linked to high frequency ground motion (5 - 10 Hz), while large MM intensities (VIII-IX) are mainly caused by lower frequency ground motion (0.5 - 3 Hz). Sokolov (2002) computes the probability for each intensity level between III and XII that this intensity will not be exceeded (one can then plot probability vs. intensity). The intensity value for the analyzed record is then determined either from the maximum of the first derivative of the probability function or from the intensity value whose probability not to be exceeded is 0.5. I will use the arithmetic mean of these two values. In fact, this approach tries to find the best reference spectrum for the FAS of a given record, where the reference spectrum is the logarithmically averaged FAS of all the records corresponding to a given intensity in the study of Sokolov (2002). Hence, each intensity level is associated with a reference FAS (these reference spectra are shown in Figure 2.4).

Chapter 3

Stress Drop and Other Source Parameters

As shown in Chapter 2.3, stress drop is a fundamental parameter in the description of earthquake source scaling properties. However, we have to distinguish between static and dynamic stress drop, and the reason for this differentiation and its consequences are discussed in Section 3.1. It should be emphasized right from the beginning that stress drop (as well static and dynamic) is spatially variable, but any estimate of these quantities always represents an average value over the fault (or a certain region of it) and over time (the dynamic stress drop may be highly time-dependent) (Kanamori, 1994; Scholz, 2002). In Section 3.2, I will discuss how source parameters such as stress drop or fault dimensions appear in the spectra of seismic waves and that only rather little information about the seismic source can be directly derived from these. The usual determination methods of stress drop estimates are briefly outlined in Section 3.3. This section is important in view of the physical interpretation of the inversion results presented in Chapter 6, as one has to take into account the different methodologies if different stress drop estimates from the same earthquake are compared. Finally, the energy budget of earthquakes and the consequences of the discussion on source spectra (Section 3.2) in view of the energy release are addressed in Section 3.4.

3.1 Beyond 'Stress Drop'

3.1.1 Static and Dynamic Stress Drop

Static stress drop is defined as the difference in shear stress on the fault before and after an earthquake (Chapter 2.3), and most commonly, if the parameter 'stress drop' is mentioned, it is static stress drop that is being referred to. The definition of static stress drop is (with σ_0 being the initial shear stress and σ_1 the shear stress on the fault after earthquake rupture):

$$\Delta\sigma_S = \sigma_0 - \sigma_1 = C_S\mu\frac{\bar{D}}{\tilde{L}}.$$

(3.1)

$\tilde{L}$ is a characteristic fault dimension, $\bar{D}$ the average slip and C_S is a non-dimensional constant of order unity which depends on the rupture geometry (Kanamori, 1994). This is the same definition as already

given by equation (2.33). Combining the definition of the seismic moment (2.18) with (3.1) leads to

$$M_0 = \frac{1}{C_S} \Delta\sigma_S \tilde{L}^3 \, . \tag{3.2}$$

From comparison with relation (2.32), we see that for the case of a circular fault, $C_S = 7/16$ and the characteristic rupture dimension is the radius of the fault. The range of possible values for the geometry-dependent constant C_S spans a factor of about 4 (Heaton, 1990). As the slip is usually spatially variable over the fault, the same goes for static stress drop and relation (3.1) estimates an average value.

Dynamic stress drop, on the other hand, is defined as the difference between the initial tectonic shear stress σ_0 and the frictional stress σ_f on the fault. This is the stress which is effectively available to drive fault motion and is also called the *effective stress* (Brune, 1970, 1971). Besides varying spatially, the dynamic stress drop is generally considered to be heavily time-dependent (as σ_f is not necessarily constant with time). Brune relates the dynamic stress drop to the particle velocity on the fault, and Kanamori (1994), based on Brune's work, derived the following relation between dynamic stress drop (spatial and temporal average) and average particle velocity:

$$\boxed{\Delta\sigma_D = \sigma_0 - \bar{\sigma}_f = C_D \frac{\mu}{v_S} \langle \dot{U} \rangle \quad \text{with} \quad \langle \dot{U} \rangle = \frac{\bar{D}}{2T_r}} \, , \tag{3.3}$$

where $\langle \dot{U} \rangle$ is the average particle velocity, v_S the shear wave velocity, T_r the rise time (spatial average) and C_D is a non-dimensional constant of order 2. The rise time T_r corresponds to the time span needed for the slip at a given point on the fault to reach its final value. However, as Kanamori points out, an uncertainty of at least a factor of 2 in this estimate is unavoidable, as the value of C_D varies by a factor of 2 depending on whether relation (3.3) is derived from consideraton of a rather simple macroscopic fault model (as considered by Brune, 1970, 1971) or crack theory. (3.3) also includes the assumption that the rupture propagates with a finite velocity of the order of v_S. Commonly assumed values range between 70 and 90 % of v_S.

Having introduced these definitions, we can now revisit the subject of *self-similarity* touched on in Chapter 2.3. A self-similar process is one which is scale-invariant, i.e. in terms of earthquakes, events of different sizes are indistinguishable from each other except by a scale factor. Earthquakes are characterized by their static properties (source dimensions, seismic moment, final slip) and dynamic properties (slip and rupture velocities). The conditions for self-similarity are:

- *Constancy of static stress drop*

- *Constancy of dynamic stress drop* (i.e. constancy of particle velocity).

Mathematically, these conditions can be expressed by (Kanamori and Anderson, 1975):

$$\frac{W}{L} = C_1 \text{ (aspect ratio)}, \quad \frac{\bar{D}}{L} = C_2 \text{ (strain drop)}, \quad \frac{v_R T_r}{L} = C_3 \text{ (dynamic similarity)} , \tag{3.4}$$

with constants C_1, C_2 and C_3. The condition for dynamic similarity will reappear in the relation connecting static and dynamic stress drop. The aspect ratio condition is of importance for rectangular faults. In the formulation of the similarity conditions above, $\tilde{L} = L$. Self-similarity hence implies that $\bar{D} \propto \tilde{L}$, $M_0 \propto \tilde{L}^3$, $T_r \propto \bar{D}$ and, as a consequence for spectral scaling, $M_0 \propto f_c^{-3}$ (see also equation (2.36)).

3.1.2 Relationship between Static and Dynamic Stress Drop

Static and dynamic stress drop are not independent of each other and their exact interconnection depends on the model of the earthquake source. This model dependence is discussed further below. I will now link the dynamic to the static stress drop using the definitions given above.

With (2.18) and the definition of slip velocity in (3.3), it is possible to express the dynamic stress drop as a function of M_0, $\tilde{L}$ and T_r:

$$\Delta\sigma_D = \frac{C_D}{2} \cdot \frac{M_0}{\tilde{L}^2 v_S T_r} \; . \tag{3.5}$$

Combing equations (3.2) and (3.5) yields:

$$\Delta\sigma_D = \frac{C_D}{2C_S} \cdot \frac{\tilde{L}}{T_r v_S} \cdot \Delta\sigma_S \; . \tag{3.6}$$

As C_D is of the order of 2, C_S approximately equals unity (Kanamori, 1994) and the rupture velocity v_R is of the order of the shear wave speed, we may approximate this equation to:

$$\boxed{\Delta\sigma_D \approx \frac{\tilde{L}}{T_r v_R} \cdot \Delta\sigma_S} \; . \tag{3.7}$$

Thus, the dynamic stress drop can be directly related to the static one, and the exact relation is governed by the characteristic dimension and the rise time. In fact, it is the constant C_3 in equation (3.4) (dynamic similarity) which governs the relationship above. It must be noted that the interconnection given in equation (3.7) requires that we talk about the static and dynamic stress drop averaged over the *same* region of the fault. This is of extraordinary importance, as one cannot link with these simple considerations for instance the static stress drop averaged over the entire fault to the dynamic stress drop averaged over the area of the dominant asperity.

$T_r v_R$ represents a length scale. If $T_r v_R \approx \tilde{L}$, the rise time T_r is approximately equal to the time to rupture the entire fault (or, more precisely, the region of characteristic length $\tilde{L}$ - which may for instance also be an asperity). In this case, the dynamic stress drop $\Delta\sigma_D$ is approximately equal to the static stress drop $\Delta\sigma_S$. If $T_r v_R \ll \tilde{L}$, i.e. the rise time is very short compared to the rupture time, $\Delta\sigma_D \gg \Delta\sigma_S$. An explanation for such a behavior could be the so-called abrupt-locking model (Brune, 1970, 1971; Kanamori, 1994) or the slip-pulse model (Heaton, 1990). The last thinkable possibility, $T_r v_R \gg \tilde{L}$ and, as a consequence, $\Delta\sigma_D \ll \Delta\sigma_S$, means that the slip duration is much larger than an earthquake rupture would need to propagate over the given fault area. Under these conditions, slip occurs very slowly, almost without seismic radiation.

The definitions of static and dynamic stress drop and the above considerations allow to address the question why the distinction static/dynamic stress drop has to be made. It is obvious that the static stress drop only provides the information by what amount the state of shear stress on the fault has changed (respectively, static stress drop answers the question: what is the amount of slip on a fault of a given size?). However, one key information for the evaluation of seismic radiation is missing: what is the time scale of this stress change (i.e., what is the slip velocity)? This piece of information is provided by the dynamic stress drop. It makes of course a fundamental difference if a given (static) stress change is achieved during a matter of seconds or years. In the first case, the result is an earthquake, whereas in the second case, it is aseismic creep (which would be the most extreme result of the case $T_r v_R \gg \tilde{L}$ described above). As a consequence, slip velocity (or dynamic stress drop) is a highly

important source parameter in view of the radiation of (especially, as we will see in the following section, high frequency) seismic waves. In terms of energy release, different combinations of static and dynamic stress drop lead to completely different energy budgets, as I will show in Section 3.4. It should be noted at this point that I will not discuss in detail the practical problems which arise if any parameter shall be measured from the timeseries or spectra and the resulting errors. The purpose of the further discussion is to show that even if there were no measurement errors, the spectra of seismic waves carry very little information on the seismic source.

3.2 Source Parameters and the Spectra of Seismic Waves

The source model given by Brune (1970, 1971) has already been introduced in Chapter 2.2.5. Brune proposes that the far-field FAS of shear waves are controlled by the seismic moment M_0 at low frequencies and by the dynamic stress drop $\Delta\sigma_D$ at high frequencies. He then constrained a relationship between corner frequency f_c and source radius r of the circular fault to be (2.31) under the explicit assumption that the static stress drop is equal to the average dynamic stress drop. Noting that the static stress drop in several previous studies seemed to be only a fraction of the dynamic stress drop, Brune finally proposes the abrupt-locking model as an explanation. After the passage of the rupture front, the fault plane may lock itself abruptly and the rupture can travel large distances (thus reducing the static stress drop) which are not determined by the dynamic stress drop. This is also the principal idea of the slip-pulse model presented by Heaton (1990). In that case, an intermediate slope with ω^{-1} is expected to appear in the spectrum, although it may be difficult to identify in practice.

Brune's theory is based on a simple dislocation model which does not include rupture nucleation or stopping effects. Madariaga (1976) performed dynamic finite-difference simulations for a circular shear crack nucleating at its center and propagating at a constant rupture velocity until it suddenly stops at a given radius. He finds that the slip at the center of the crack overshoots the slip expected from the static solution, which means that the static stress drop is larger than the average dynamic stress drop. The displacement amplitude spectra from Madariaga's model also show a decay of roughly ω^{-2}, but the corner frequencies are a factor of two smaller than expected from Brune's considerations. This means that for a given corner frequency, the expected source radius is half of that determined from Brune's model and hence, the static stress drop would be eight times larger. This conclusion also implies severe differences from the energetic point of view between Brune's and Madariaga's reasoning (Section 3.4). As Aki and Richards (2002, Chapter 10) summarize, the proportionality constant in the relation between corner frequency and source dimension is different for each model (another kinematic model which is often referred to is the one of Sato and Hirawasa, 1973). Source dimensions and other parameters derived from the corner frequency of the spectrum are consequently strongly model-dependent, as I will discuss in detail below.

The spectral theory in the form given by Brune has been extensively applied, especially for the determination of source parameters from small to moderate-size events (e.g. Abercrombie, 1995; Abercrombie and Rice, 2005; Allmann and Shearer, 2007), for which the simplicity of the source as presumed in this model is an acceptable assumption. The application to large earthquakes is not that common. Oncescu (1989) for instance used Brune's theory to compute an estimate of the asperity stress release from the large intermediate-depth Vrancea earthquake in 1986, an event which is also studied in this work.

The issue of model-dependency and the question what parameters can reliably be derived from the spectra of seismic waves is taken up by Beresnev (2001, 2002). As the spectrum of shear wave

radiation shall present an ω^{-2}-shape, the displacement on the dislocation that leads to such a spectrum in the far-field may *ad hoc* be given by:

$$D(t) = \bar{D}\left[1 - \left(1 + \frac{t}{\tau}\right)e^{-t/\tau}\right]. \tag{3.8}$$

$\bar{D}$ is the final value of displacement and τ is a quantity which determines how fast the final value is reached. The far-field displacement and acceleration spectra are in this case proportional to:

$$\hat{U}(f) \propto M_0\left[1 + \left(\frac{f}{f_c}\right)^2\right]^{-1} \quad \text{and} \quad \hat{A}(f) \propto (2\pi f)^2 M_0\left[1 + \left(\frac{f}{f_c}\right)^2\right]^{-1}, \tag{3.9}$$

where $f_c \equiv 1/2\pi\tau$ is the corner frequency of the spectrum. The displacement spectrum $\hat{U}_{LF}$ at low frequencies and the acceleration spectrum $\hat{A}_{HF}$ at high frequencies are constant and proportional to M_0 and $M_0 f_c^2$ respectively. The time derivative of (3.8) gives the slip velocity, which has its maximum at $t = \tau$:

$$\dot{D}_{max} = \frac{\bar{D}}{e\tau}. \tag{3.10}$$

Note the similarity between (3.10) and the average particle velocity defined in (3.3). As the corner frequency is defined to be $f_c \equiv 1/2\pi\tau$, we may thus link f_c to the maximum slip velocity:

$$f_c = \frac{e}{2\pi} \cdot \frac{\dot{D}_{max}}{\bar{D}}. \tag{3.11}$$

Beresnev (2001, 2002) concludes that in view of equation (3.11) and the fact that $\hat{A}_{HF} \propto M_0 f_c^2$, slip velocity is the parameter that is directly obtainable from the high-frequency spectrum. This, however, is only conditionally true, as I will outline now. The key question in order to assess the amount of source information carried by the spectra is in fact: what parameters can be derived from them *without* any information from other origins and *without* making any restrictive model assumptions?

Theoretical Considerations

Let us assume that we have obtained an estimate for $\hat{U}_{LF}$ and $\hat{A}_{HF}$ from the observed spectrum of seismic ground motion (although a direct estimate may be difficult in practice, as one has to correct for anelastic attenuation, site effects, geometrical spreading and radiation pattern). In the following discussion, the path and site effects shall be perfectly known and have been corrected and we assume that we have averaged the spectra of several stations at different azimuths to average out directivity and radiation pattern effects. Thus we are talking about the source contribution only (of course, the assumption of perfectly known path and site effects is not true in reality and further complicates the problem of non-uniqueness). Then, the low frequency plateau of the displacement spectrum reduces to $\hat{U}_{LF,source} = M_0$ and the high frequency plateau in acceleration to $\hat{A}_{HF,source} = 4\pi^2 M_0 f_c^2$. As yet, no special assumption about the source has been made except that it can be represented by a dislocation whose spectrum shows an ω^{-2}-shape. Thus, the parameters which are *directly* obtainable from the source spectrum are the seismic moment M_0 (which has a clear physical meaning) and corner frequency f_c (which, up to now, is a purely empirical parameter describing the spectrum). In view of the definition of $f_c \equiv 1/2\pi\tau$, we may of course restate the problem and come to the conclusion that the parameter govering the speed of the dislocation rise, τ, can be estimated from the spectrum. Hence the corner frequency indeed carries some information about the slip velocity.

Using equation (3.11) and the fact that now $\hat{A}_{HF,source} = 4\pi^2 M_0 f_c^2$, we get:

$$\hat{A}_{HF,source} \propto M_0 \left(\frac{\dot{D}_{max}}{\bar{D}}\right)^2 . \tag{3.12}$$

As above-mentioned, Beresnev (2001, 2002) states that slip velocity can be directly obtained from the corner frequency of the spectrum and that it is the true physical parameter which determines the strength of high-frequency radiation. However, to retrieve $\dot{D}_{max}$ *directly* from the spectrum, we must simply know the final displacement $\bar{D}$. It is in fact not slip velocity alone which controls the level of the high-frequency acceleration spectrum, but it is the ratio $\dot{D}_{max}/\bar{D}$. A given f_c can be explained by either low $\dot{D}_{max}$ and low $\bar{D}$ or by high $\dot{D}_{max}$ and high $\bar{D}$.

In his article published in 2002, Beresnev indeed acknowledges this problem. He argues that, as M_0 (which is the source parameter measurable from the spectrum) is directly related to $\bar{D}$ via (2.18), we can obtain an estimate for $\bar{D}$ when the source size is determined e.g. from the aftershock distribution. The key point that must be made here is that, without further knowledge from other origins than the spectra or model assumptions, it is not possible to determine either slip velocity, slip or source dimensions from the spectra. The factor controlling the strength of high-frequency radiation is their combination.

The parameter τ used in equation (3.8) governs the speed of the dislocation rise. Yet, although it is related to $\dot{D}_{max}$ and $\bar{D}$ by equation (3.10), τ is simply a mathematical parameter within the function given by (3.8). We may however link τ (or f_c) to the rise time T_r, which was defined in Chapter 2 and when giving the definition of dynamic stress drop (3.3) as the time during which the slip at a given point of the fault rises to its final value. For the slip function given in (3.8), it is not possible to define the rise time this way, as it would be formally infinite due to the exponential function. If we set the rise time as the time necessary to reach for instance 95% of the final slip, which is reasonably close to the definition given earlier, the following relation is obtained between f_c and T_r:

$$f_c \approx \frac{4.75}{2\pi} \cdot \frac{1}{T_r} . \tag{3.13}$$

Beresnev uses for instance 50% (2001) or 90% (2002). Let now the corner frequency be linked to the rise time by equation (3.13). From a given source spectrum, M_0 and f_c have been derived. These two observables can be explained by a given combination of slip $\bar{D}$, source area A and rise time T_r. If the linear source dimension is halved, the source size A diminishes by a factor 4. As we wish to keep M_0 constant, it is necessary to enlarge $\bar{D}$ by a factor of 4. If we keep T_r constant, the corner frequency will not change either, as is evident from (3.13). In summary, this means that we expect to observe exactly the same source spectrum, even though the static stress drop $\Delta\sigma_S$ was heightened by a factor 8 and the dynamic stress drop $\Delta\sigma_D$ by a factor 4. This would be a physically completely different earthquake, but without further constraints either on slip or source size, it is impossible to discriminate between these events from the source spectrum.

To remove this indetermination, there are only several possibilites:

- **Option 1:** Express the rise time T_r (or, alternatively, τ, as τ and T_r are linked via (3.13)), either as a function of source dimensions or static displacement. That means, make model assumptions. For instance, one could assume that the rise time is of the same order as the rupture time of the fault, i.e. $T_r = r/v_R$. Note that this assumption is in fact equivalent to the

assumption that the static stress drop is equal to the average dynamic one, as can be easily seen from equation (3.7). Beresnev (2001) shows that under this condition, with relation (3.13) and assuming that the rupture velocity is a given fraction of the shear wave speed, we receive a relation of the form:

$$f_c = C \cdot \frac{v_S}{r}, \tag{3.14}$$

with $C = 2.34/2\pi$ in Brune's (1970, 1971) model. Beresnev (2001) obtains a value of $C = 0.67/2\pi$ using his set of assumptions. He points out that any particular value of C has no physical meaning, as with a different set of assumptions, a different value is obtained. The key assumption in order to link f_c to r is the connection chosen between T_r and r. For a given M_0, this assumption determines the relation between static and dynamic stress drop and thus, the energy budget of the considered earthquake, as shown in Section 3.4.

Indeed, if the principle of self-similarity is considered to hold, there must also exist a relation of form (3.14). By keeping T_r constant when modifying source size, as I did in the thought experiment above, I modify in fact the proportionality constant C, which is hence model-dependent. In terms of stress drop, if the source size is changed and T_r is kept constant, the relation between $\Delta\sigma_S$ and $\Delta\sigma_D$ is altered. Thus, although it is clear that the corner frequency must be inversely proportional to the linear dimension of the fault, it is not possible to provide an *exact* relationship between f_c and linear source dimension just by using the spectrum. Particularly in terms of stress drop, this conclusion has important consequences. As an estimate of static stress drop requires an estimate of source size, it is consequently also impossible to obtain an estimate of static stress drop from the corner frequency which would not be highly model-dependent.

- **Option 2:** Gather further knowledge about the earthquake source apart from the spectrum. Beresnev (2002) proposes to infer the source dimensions e.g. from the occurrence of after-shocks. If the source size is known, there is no indetermination in equations (3.11) and (3.12). In this case, it is possible to *uniquely* determine $\bar{D}$ and $\dot{D}_{max}$, and for a given slip, the corner frequency and high-frequency spectral level are indeed controlled by the slip velocity respectively the rise time.

- **Option 3:** If enough data (possibly including near-field observations) are available, a slip inversion can be performed, resulting in a finite-fault rupture model (see also short description in the following section). In such a case, the problem of determining source parameters solely from the spectra of course vanishes. One may then even try to combine the different sources of information, which are slip inversion, far-field spectra and aftershock distribution. However, this luxury situation is usually only given for large crustal earthquakes.

Practical Consequences

The second option sounds simple, but it is not necessarily evident to estimate the source size of especially small or moderate-size events with a method other than the one described under option 1 above, namely using a specified model and determining source dimensions from the spectrum. Concerning the aftershocks, it may be difficult to assess the source size of a small earthquake by the occurrence of its (even smaller) aftershocks, as most of these may be lost in the noise and impossible to properly detect or difficult to distinguish from the natural background seismicity. It has become widespread practice to determine source dimensions and static stress drop from the spectrum just because it is not easily feasible to derive these parameters from other sources. Furthermore, as the

aftershock area expands further and further with progressing time (aftershocks may also be triggered outside of the main shock fault area due to stress transfer), it is a question of definition what time span is being considered (usually one day, Mogi, 1968), and such a definition is always subject to a certain degree of arbitrariness.

For large earthquakes, the aftershocks may indeed be an option to get a quite reliable estimate of the overall source dimensions. However, the observed strong ground motion, especially at higher frequencies, is dominated to a large extent by the radiation from the asperities, as follows e.g. from the simulation results of Miyake et al. (2003). Das and Kostrov (1986) for instance show that at high frequencies, the radiation from a single asperity within a larger background area (which is allowed to slip, but shows practically no stress release) displays the same spectral amplitude than that of a crack of the same size as the asperity, whereas it is larger than that of the crack at low frequencies, due to the slip existence on the stress-free field in the asperity model. This means that the corresponding high-frequency spectra depend on the slip velocity and slip averaged over the asperity area rather than the entire fault. The aftershock distribution, however, provides an estimate of the total rupture area rather than asperity area (for instance, Kanamori, 1994, notes that the aftershocks tend to occur outside of the areas of large slip, i.e. outside the asperities).

The problem is non-existant for many large crustal earthquakes, as slip inversions can be performed (option 3) and the databases to do so are quite extensive in some cases. The discussion regarding the determination of source parameters from the spectra is therefore most relevant for small to moderate size earthquakes, for which option 3 is usually impracticable.

The theoretical considerations above also imply an important consequence for stochastic ground motion simulations which are based on the ω^{-2}-model. This simulation technique is presented in more details in Chapter 4.2. It is widespread practice to use a source implementation of the form of equation (3.9) (either as a subfault for a finite-fault scenario or as a point source) and compute the corner frequency f_c from an assumed stress parameter $\Delta\sigma$ for instance with:

$$f_c = 4.9 \cdot 10^6 v_S \left(\frac{\Delta\sigma}{M_0} \right)^{\frac{1}{3}} . \tag{3.15}$$

where v_S is given in km/s, $\Delta\sigma$ in bar and M_0 in $dyn \cdot cm$ (e.g. Boore, 2003; Sokolov et al., 2005). Expression (3.15) is derived directly from the Brune (1970, 1971) model and $\Delta\sigma$ is usually viewed as an estimate of static (and dynamic, as they are supposed to be the same in this model) stress drop. The ultimate goal of such an approach is to perform data-consistent simulations. In that sense, no objection is necessary to this procedure if this aim is acheived. However, as Beresnev (2001, and references therein) likewise notes, it must be emphasized that there is no physical meaning behind the parameter $\Delta\sigma$. Equation (3.15) shows that $\Delta\sigma$ is a proxy for the corner frequency f_c and we could use a relation with another coefficient than in (3.15) as well. f_c, on the other hand, depends on the ratio $\dot{D}_{max}/\bar{D}$, as shown earlier. This leads again to the ambiguity discussed above. Thus, $\Delta\sigma$ should be seen as a plain modeling rather than physical parameter, which simply determines the strength of high-frequency radiation in the simulations, as it determines the position of the corner frequency and the height of the high-frequency plateau in acceleration (and might indeed do perfectly well to perform realistic simulations). In other words, $\Delta\sigma$ computed from a given f_c is not necessarily related in any way to the real stresses acting during an earthquake and its usefulness in understanding earthquake source physics is severly limited.

Summarizing this section, the main conclusion is that there is only one physically meaningful parameter which can be obtained directly from the source spectrum of seismic ground motion: the seismic

moment M_0. This parameter is affected by measurement errors and possible errors due to the imperfect knowledge of path and site effects, which might be quite large too, but not by systematic errors resulting from model assumptions regarding the source. The estimation of other relevant source parameters such as source dimensions, slip velocity or stress drop either requires additional knowledge apart from the spectrum or the adoption of more or less arbitrary and severe model assumptions. As such, the corner frequency f_c is a purely empirical parameter describing the spectrum. Self-similarity among earthquakes does require a link between f_c and some length scale characterizing the earthquake of the form (3.14). In that regard, it is clear that if we halve this characteristic length, we double the corner frequency. But the *exact* connection remains an unclear matter and may of course also be different for different seismogenic areas.

Nevertheless, the corner frequency is a parameter of extraordinary importance in seismology. The self-similar scaling of earthquake source spectra, which can be expressed in the form $M_0 f_c^3 = constant$, as recognized by Aki (1967), is an observational fact (and as such model-independent) and a well-accepted finding. This fact can be exploited without necessarily linking f_c directly to any source parameter. One example is the empirical Green's functions technique of Irikura (1983, 1986, 1999), which is discussed in detail in Chapter 4.1. In this technique, the seismic source is implemented as an extended, rectangular rupture area with constant slip and slip velocity and combined with the spectral scaling characteristics of the ω^{-2}-model, but without linking f_c directly to other parameters such as size or rise time. Even though this is still a simplified source model of the Haskell type, the source parameters derived using this technique do not suffer from the severe restrictions which apply to those derived from the spectra alone and are more likely to reflect real source physics.

Finally, before moving on to the next section, it is important to note that the above discussion results from very simple kinematic considerations based on (point source) dislocation theory, only valid in the far-field. A problematic issue is that, in principle, as both P- and S-waves result from the displacement discontinuity as given by (3.8), both wave types are expected to display the same spectral shape (which is indeed observed) and the same corner frequency (which is in contradiction to observations, e.g. Prieto et al., 2004). For instance, the dynamic crack model of Madariaga (1976) or Sato and Hirawasa's (1973) kinematic model are more appropriate in that sense, as they predict higher P- than S-corner frequencies. Nevertheless, it should always be borne in mind that any model (either kinematic or dynamic) has certain advantages and limitations and that the actual earthquake source process is, at all resolvable scales, more complicated than any of these simplifying models predicts.

3.3 Importance of Stress Drop and Usual Estimation Methods

Stress drop is commonly viewed as an interesting source parameter because it provides hints on the scaling properties of earthquakes (as seen above, constant static and dynamic stress drop means self-similar scaling). $\Delta\sigma_D$ also is a key parameter in the estimation of strong ground motion, as it controls the level of peak ground acceleration (Hanks and Johnson, 1976). Furthermore, it has been shown that static stress drop seems to be related to the origin of the considered events (for instance, several studies have shown that intermediate-depth and deep earthquakes along subduction zones often depict high static stress drops, e.g. Mikumo, 1971; Garcia et al., 2005). Kanamori (1994) summarizes that for crustal earthquakes, the static stress drop is approximately constant, ranging from 10 - 100 bars, and that particle velocity seems to be bound at about 1 - 2 m/s. Such a particle velocity corresponds to a dynamic stress drop of about 100 - 200 bars. Thus, static and dynamic stress drop seem to show the same order of magnitude for crustal events. However, as I will outline in Section 3.4, different

models for earthquake stress release exist, some with high $\Delta\sigma_D$ and low $\Delta\sigma_S$ (abrupt-locking, e.g. Brune, 1970, 1971) and others with low $\Delta\sigma_D$ and high $\Delta\sigma_S$ (overshoot, e.g. Madariaga, 1976).

The determination of stress drop and especially the differentiation between static and dynamic stress drop is not an easy task. First, the estimation of static stress drop is always related to the estimation of source dimensions. The estimate of source dimensions strongly depends on the methodology being used, and deducing them for instance from the spectra always involves more or less severe assumptions about the source, as discussed in Section 3.2. They also represent the largest source of errors, as the seismic moment can be computed quite accurately nowadays (for earthquakes with M_W larger than approximately 5.5, moment tensor inversions are routinely performed e.g. by the Harvard CMT group) and $\Delta\sigma_S \propto \tilde{L}^{-3}$. Secondly, it is difficult to obtain the slip velocity time function (and consequently dynamic stress drop), as an observed seismogram is the convolution of source and wave propagation effects, which have to be separated. In order to correct for the propagation and site effects, it is in general necessary to make highly simplifying assumptions about the medium (e.g. damping structure) and site conditions. These may severely influence the obtained slip velocities.

The most commonly utilized methods to determine the source dimensions and, consequently, static stress drop, are summarized below (see also Kanamori, 1994, and references therein).

- *Aftershock distribution*. The extent of the aftershock area is usually considered to correspond approximately to the total rupture area. Thus, static stress drops estimated derived using these dimensions represent an average value over the entire fault.

- *Surface breakage and geodetic data*. For large crustal earthquakes which also rupture the surface of the Earth, the extent of the fault plane can be estimated from the surface breakage. However, this only allows to estimate the length, and the width of the rupture zone must be estimated using other techniques such as aftershock locations. Again, as the dimensions received this way correspond to the total rupture area, the static stress drop computed from these estimates is an average over the entire fault plane.

- *Finite-source rupture models*. This is probably the most powerful method for large crustal earthquakes and has already been introduced in Chapter 2.3 (a recent review on this type of studies is given by Ide et al., 2005). It provides not only hints on source size, but also on the spatial distribution of slip (and hence static stress drop) and rise time (and thus, in combination with slip, of slip velocity). This heterogeneous distribution of source characteristics is of extraordinary importance especially for understanding the physics of large earthquakes and cannot be derived from the far-field spectra, which have been discussed above. For such events, the circular fault approximation and other assumptions involved in simple spectral models such as the one of Brune (1970, 1971) are at best highly questionable. Of course, such rupture models are also subject to uncertainties and the problem of non-uniqueness, mainly due to the large number of free parameters and insufficient databases (see e.g. Beresnev, 2003, for a discussion on this issue). Another shortcoming of this approach is that these models are derived using frequencies usually lower than about 1 Hz.

- *Corner frequency analysis*. This methodology and its severe shortcomings have been amply treated earlier in this chapter. Using relation (3.14), the source size can be estimated from the corner frequency and as a consequence, an estimate for the static stress drop of the earthquake may be computed. This approach is usually applied to smaller earthquakes (e.g. Abercrombie, 1995; Abercrombie and Rice, 2005).

There are also different approaches in order to estimate the dynamic stress drop, which I briefly list below. It might be interesting to note at this point that Boatwright (1984) shows that the stress drop estimate from the corner frequency using Brune's (1970, 1971) model seems to be rather correlated with dynamic stress drop estimates using some of the methods cited below than with average static stress drop estimated from the aftershock distribution. This would mean that the Brune stress drop represents an estimate of the dynamic rather than the static stress drop, in accordance with the initial formulation of his model before deriving a relation between corner frequency and source dimension.

- *Direct estimate from the particle velocity*. To follow this approach, it is of course necessary to get an estimate of the average particle velocity first, which is in general very difficult to obtain. One possibility is to use again the results of slip inversions. If both final slip and rise time are provided, the average slip velocity can be computed. However, as the frequency content analyzed in these studies is usually restricted to frequencies below about 1 Hz, the rise time determined this way should be regarded as an upper bound (Heaton, 1990), which means that the slip velocity should be regarded as a lower bound if the slip value is considered to be unbiased. For crustal earthquakes, it seems that the particle velocity is bound at about 2 m/s (Kanamori, 1994).

- *Initial slope technique*. Boatwright (1980) developed a methodology to determine the average dynamic stress drop from the initial slope of the far-field velocity waveform of S-waves. The underlying assumption is that the rupture grows circularly. This estimate of dynamic stress drop is only characteristic for the stress release within the first part of the rupture process and, as Boatwright notes, this technique is intended for small to moderate-size earthquakes with simple source process.

- *Root-mean-square acceleration*. Hanks and McGuire (1981) relate the root-mean-square acceleration (a_{rms}) to the dynamic stress drop. a_{rms} is defined by:

$$a_{rms} = \sqrt{\frac{\int_{t_1}^{t_2} a(t)^2 dt}{\Delta t}},$$ (3.16)

where t_1 and t_2 represent the beginning and the end of the considered time window, Δt is the length of the window and $a(t)$ denotes the acceleration time series. The dynamic stress drop may then be estimated by (see also Hanks and McGuire, 1981):

$$\Delta \sigma_D = \frac{106 \rho R}{2(2\pi)^2 \mathfrak{R}^{\theta\phi}} a_{rms} \sqrt{\frac{f_c}{f_{max}}},$$ (3.17)

where f_{max} is the maxium frequency of the acceleration spectrum, $\mathfrak{R}^{\theta\phi}$ denotes the average radiation pattern, ρ is the density and R the hypocentral distance.

As above-mentioned, for crustal earthquakes, $\Delta \sigma_S$ and $\Delta \sigma_D$ seem to cover a similar range of values. Oncescu (1989) for instance applied the initial slope and the root-mean-square techniques to the large intermediate-depth Vrancea earthquake in 1986 and obtained $\Delta \sigma_D$ values of about 1 kbar. Among other Vrancea earthquakes, this event is further treated in Chapter 6, and the results of the analysis presented in this thesis clearly indicate that both static and dynamic stress drop seem to be about one order of magnitude larger for these intermediate-depth events than for crustal earthquakes.

Finally, it should be noted that it makes of course a strong difference whether stress drop averaged over the asperity area or stress drop averaged over the entire fault plane is considered. Kanamori and Heaton (2000) mention that the static stress drop can be locally very high (up to 25 kbar around small asperities, Nadeau and Johnson, 1998). As Madariaga (1979) shows in a theoretical analysis, the stress drop averaged over the entire fault plane underestimates the stress drop on the asperities by a factor of r/R, where r is the radius of the asperity and R the total fault radius. The differentiation between asperity stress drop and average stress drop over the entire fault will play a key role in the physical interpretation of the results presented in Chapter 6.

3.4   Stress Drop and the Energy Budget of Earthquakes

In this section, I will first present the common simplified mathematical description for the energy budget of earthquakes. In a second step, the implications of different combinations of static and dynamic stress drop for the energy budget are discussed.

In the following considerations, I mainly follow the ideas presented by Kanamori (1994) and Kanamori and Heaton (2000). An earthquake can be viewed as a stress release process on a surface A. Due to tectonic loading, the shear stress on a pre-defined fault plane continuously builds up until it reaches a critical value at which the fault becomes unstable and begins to slip (see e.g. Scholz, 2002). Before slippage, the initial value of shear stress is σ_0. After slip motion has stopped, the shear stress has reached its final value σ_1 and the average slip (or offset) is $\bar{D}$. During slippage, work is done against the frictional stress σ_f. With these notations, the static stress drop is $\Delta\sigma_S = \sigma_0 - \sigma_1$ and the dynamic stress drop is given by $\Delta\sigma_D = \sigma_0 - \sigma_f$. The dynamic stress drop is thus the stress which is effectively available to drive fault motion.

During this process, the potential energy (strain and gravitational energy) of the system W is lowered by the value ΔW:

$$\Delta W = E_R + E_H + E_G, \qquad (3.18)$$

where E_R is the energy radiated in form of seismic waves, E_H is the frictional energy loss in form of heat and E_G is the energy expended to create new fault surface, also called *fracture energy*. These different contributions are schematically shown in Figure 3.1. In the model presented there, the frictional stress σ_f gradually drops with increasing slip to a constant level σ_{f0}, which is reached with the critical slip D_c. Usually, it is assumed that at the beginning of slip, the stress rises to a somewhat higher value than σ_0, which is called the *yield stress*. This rise has however little effect on the overall energy budget and is therefore neglected. This is the so-called *slip-weakening* model. The final state of shear stress σ_1 is not necessarily equal to σ_{f0}. In Figure 3.1, σ_1 is a bit higher than σ_{f0}, which results in a somewhat larger average dynamic ($\Delta\sigma_D$) than static stress drop ($\Delta\sigma_S$).

Figure 3.1: Schematic illustration of the slip-weakening model. Further explanations are given in the text.

However, instead of diminishing gradually, σ_f may also depict a drastic drop at the beginning of slippage and later resume to a larger value. I will consider this and other possible situations below

(see also Figure 3.2). Kanamori and Heaton (2000) show from a crack physics argument that, at least for large crustal earthquakes, E_G may be negligible compared to E_R and E_H. In the following, I will also assume that E_G can be neglected. In any case, it has to be borne in mind that the energy budget discussion is always based on rather simplistic models.

With the average friction $\bar{\sigma}_f$ given by the definition

$$\bar{\sigma}_f = \frac{1}{\bar{D}} \int_0^{\bar{D}} \sigma_f(D)dD \,, \tag{3.19}$$

the frictional energy loss is:

$$E_H = \bar{\sigma}_f \bar{D} A \,. \tag{3.20}$$

The seismically radiated energy may then be written as:

$$E_R = \frac{\sigma_0 + \sigma_1}{2} \bar{D} A - \bar{\sigma}_f \bar{D} A \,. \tag{3.21}$$

As $M_0 = \mu A \bar{D}$, $\Delta\sigma_S = \sigma_0 - \sigma_1$ and $\Delta\sigma_D = \sigma_0 - \bar{\sigma}_f$ (average dynamic stress drop), (3.21) gets:

$$\boxed{E_R = M_0 \frac{2\Delta\sigma_D - \Delta\sigma_S}{2\mu}} \,. \tag{3.22}$$

Equation (3.22) is the key relation for interpreting the energy release models presented in Figure 3.2. Classically, it is assumed that $\Delta\sigma_S \approx \Delta\sigma_D$ (see e.g. Kanamori, 1994, and references therein). Relation (3.22) then becomes:

$$E_R \approx M_0 \frac{\Delta\sigma_S}{2\mu} = \frac{\Delta\sigma_S}{2} A \bar{D} \,. \tag{3.23}$$

This situation can be represented by Case I in Figure 3.2, with constant σ_f. Case II is rather extreme: here, $\Delta\sigma_D = 0$. There is no seismic radiation in this case, and the entire energy is expended as heat (if fracture energy is neglected). Thus, this graph is a representation of aseismic creep. Case III is a graphical representation of the *abrupt-locking* model as introduced by Brune (1970, 1971) or the *slip-pulse* model proposed by Heaton (1990). In this case, a large effective stress is available for fault motion due to a sudden drop in friction. Heaton (1990) proposes that friction depends on slip velocity, i.e. friction drops drastically at the time slippage begins and resumes quickly to a higher level as soon as the fault motion gets slower, which leads to a self-healing slip pulse traveling over the rupture plane. Such a model involves a larger dynamic than static stress drop and, consequently, a higher E_R. Case IV represents less wave radiation than Case I. Here, the average dynamic stress drop is lower than the static stress drop. This model is often referred to as the *overshoot* model (e.g. Madariaga, 1976). Finally, Case V is a mixture of Cases III and IV. Friction drops drastically and stays small only for a small amount of time compared to the entire rupture time. This drastic drop does not necessarily have to occur at the beginning of rupture, but may actually happen at any time during the rupture process.

There are some interesting remarks in view of the discussion on the source spectrum in Section 3.2 that can be made at this point. If we have determined a certain M_0 and f_c from the spectrum, it is actually impossible to discriminate between any of the cases depicted in Figure 3.2 if no additional knowledge on the source is available. Remember that, in order to get relation (3.14), we have to make an assumption concerning the rise time T_r. Together with equation (3.7), different assumptions lead to different combinations of $\Delta\sigma_S$ and $\Delta\sigma_D$ and hence, to completely different energy budgets. Of course, if it is possible to perform a slip inversion (including near-field data), there is no difficulty to
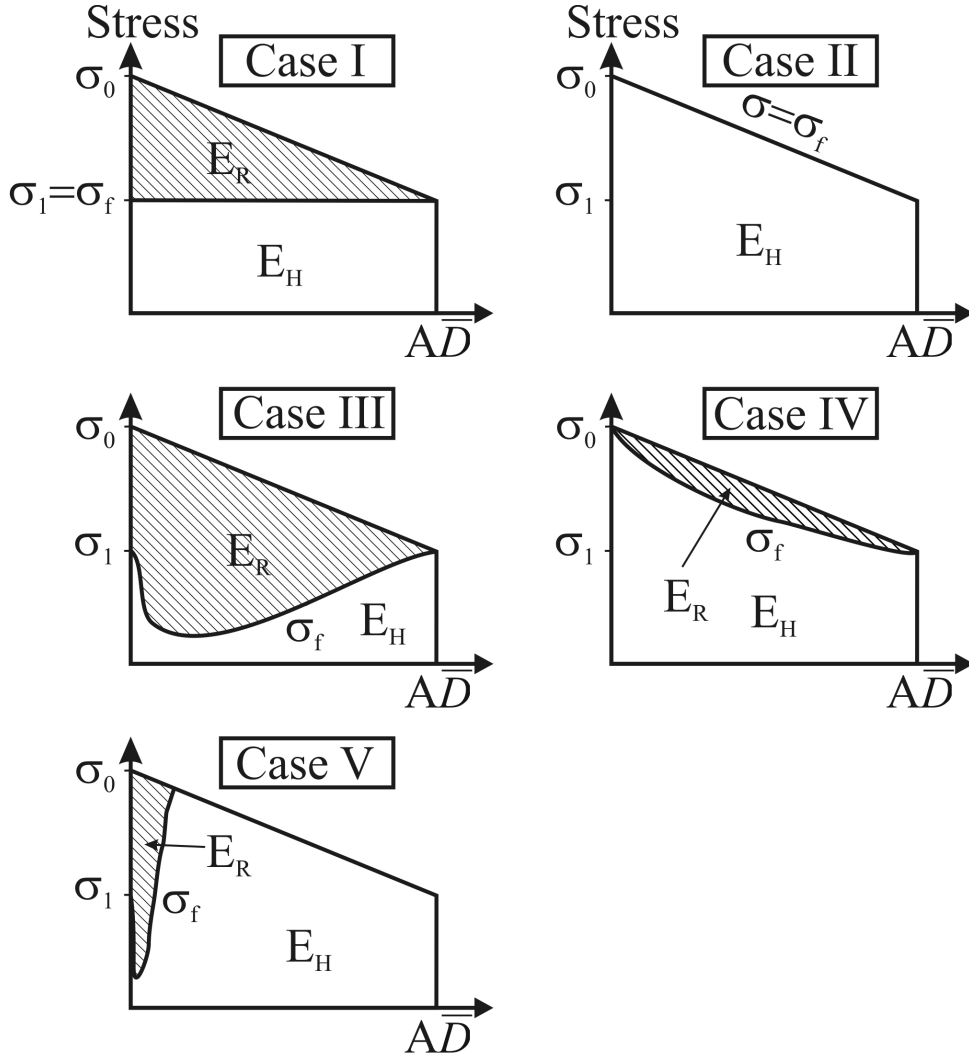
Figure 3.2: Different stress release models for earthquakes after Kanamori (1994). Further explanations are given in the text.

that respect. Again, I wish to point out a fundamental problem for the case that there is no other good source of information except the spectra from far-field observations, which is a common situation for small to moderate earthquakes (e.g. Allmann and Shearer, 2007).

Radiated energy E_R can be determined directly from velocity records by performing an integration of the squared amplitude (Kanamori, 1994), even though an accurate estimate is difficult in practice. Equation (3.22) can be rewritten as:

$$2\mu \frac{E_R}{M_0} = 2\Delta\sigma_D - \Delta\sigma_S \,. \tag{3.24}$$

The left-hand side features the directly measurable quantities E_R and M_0. From the above equation, it is possible to evaluate the difference between $2\Delta\sigma_D$ and $\Delta\sigma_S$, but not their absolute values. The corner frequency of the source spectrum, due to the reasons discussed in this chapter, is not providing any further information to solve this problem. Once more, the only ways to compute an estimate for

these two quantities are either model assumptions or further data (e.g. a reliable estimate of the source size). By comparing the ratio E_R/M_0 for different earthquakes (Kanamori, 1994), it is possible to say that one earthquake has radiated more energy with respect to its seismic moment than another one. This way, one can to a certain extent discriminate between the different cases depicted in Figure 3.2. However, the absolute values of stress release cannot be estimated without further information. Using a certain model (e.g. $\Delta\sigma_D = \Delta\sigma_S$), it is possible to give an interpretation of the above equation in terms of absolute values of stress drop, but it must be emphasized that this is only an interpretation with respect to a given source model.

In conclusion, one may rephrase the problem regarding the source spectrum like this: there is one undetermined degree of freedom which must be fixed. This may be either source dimensions, slip or slip velocity. Brune (1970, 1971) for instance fixed this degree of freedom by assuming $\Delta\sigma_S = \Delta\sigma_D$. Therefore, as stand-alone information, the spectra are only of very limited use if parameters such as source size or stress drop shall be determined. The source spectra should only be characterized by parameters which are actually directly measurable from them without further assumptions. These are seismic moment M_0 and corner frequency f_c. A further directly measurable quantity is radiated energy E_R. Alternatively, if f_c is expressed in terms of the stress parameter $\Delta\sigma$, the utilized model *must* always be clearly stated and the enormous ambiguity has to be borne in mind when using such an interconnection in the further physical interpretation of earthquake phenomena.

Chapter 4

Ground Motion Simulation Techniques

This chapter is devoted to ground motion simulation techniques. I will present the three most commonly utilized methods: the *empirical Green's functions* technique, the *stochastic simulation* of ground motion and, very briefly, the *finite-difference* technique (which is not further used in this work).

There are two main empirical Green's functions simulation approaches, which are, on one side, the approach based on earthquake scaling laws (such as the technique of Irikura, 1983, 1986, 1999) and, on the other side, the approach based on the usage of events so small that their source time function can be regarded as impulse-like over the frequency range of interest. Here, the method developed by Hutchings (Hutchings and Wu, 1990; Hutchings, 1991, 1994) has to be mentioned. In Section 4.1, I will present both approaches (with much more emphasis on the method of Irikura, as the other technique is not used in this thesis) and shortly discuss their advantages and drawbacks. As already mentioned in the previous chapter, the most interesting feature of Irikura's technique is that it uses the ω^{-2} spectral scaling without directly linking the corner frequency to any source parameter. Source dimensions and rise time as well as rupture starting point can be determined by fitting simulations to observations, as presented in Chapter 6 for several intermediate-depth Vrancea earthquakes.

Section 4.2 gives an overview over the stochastic method (e.g. Boore, 2003). This technique is extremely powerful, as it allows the fast and efficient computation of many strong motion simulations and does not require a sufficient number of recordings of any kind (for the empirical Green's functions method to be useful, there must of course exist an appropriate database of small event recordings). Finally, I will briefly introduce the finite-difference technique in Section 4.3, whose main attractivity consists in the fact that one can compute the full wavefield solution in complex underground structures and analyze their influence on ground motion. A short discussion will conclude this chapter.

4.1 The Empirical Green's Functions Technique

As shown in Chapter 2.2, the representation theorem allows to compute the displacements resulting from an earthquake if the slip on the fault plane is known. However, there is a fundamental problem in this regard. In order to make use of the representation theorem, the Green's function must also be known. Remember that the Green's function is the ground motion resulting from an impulsive point source, thus capturing the propagation path (and site) effects only. For very simple media, it can

be computed analytically. If the considered medium is complex, as is the Earth's interior, numerical solutions can be derived. Yet, the frequency range for which such solutions can be derived depends on how well the subsurface structure is known. Moreover, site effects can have a very strong influence on ground motions and are extremely difficult to incorporate into the numerical calculations.

Therefore, Hartzell (1978) was the first to propose using the recordings of small earthquakes as 'empirical' Green's functions and can consequently be viewed as the founding father of this technique. The basic idea is that the source time function of small earthquakes can be regarded as impulse-like and therefore, the record of a small earthquake primarily captures the propagation path and site effect. Thus, the recording of the small earthquake can be used, by applying a summation scheme, as a Green's function in order to simulate a large earthquake occurring at approximately the same location and recorded at the same station as the small event.

The main drawback of the original formulation of the technique is that only frequencies lower than the corner frequency of the empirical Green's function can be used. A δ-pulse in time domain has a flat FAS. As the ω^{-2}-model of the earthquake source spectrum predicts a plateau only for frequencies lower than f_c, an earthquake can be regarded to have a δ-pulse like slip velocity time function only in this frequency range. Furthermore, the assumption of a coherent rupture front for the large earthquake to be simulated can lead to artifical peridocities, as I will discuss in the framework of Irikura's technique below. These problems have been solved by different researchers using different approaches, and nowadays, it is possible to simulate ground motions over the entire frequency band of interest to earthquake engineering.

4.1.1 The EGF-Method of Irikura

As above-mentioned, Irikura's technique (1983, 1986, 1999) is based on the earthquake scaling relationships resulting from the self-similarity principle (see Chapters 2.3 and 3). Another representant of this type of empirical Green's functions technique are for instance Bour and Cara (1997). An overview over the different techniques is provided by Treml (2000). Starting from the representation theorem as given by (2.13) and the definition of the moment density tensor (2.14), the displacement resulting from the small (EGF) respectively large (TARGET) earthquakes can be expressed as:

$$e_n(\mathbf{x}, t) = \iint_{A_E} m_{pq}^E(\boldsymbol{\xi}, t) * \frac{\partial G_{np}(\mathbf{x}, t; \boldsymbol{\xi})}{\partial \xi_q} \, dA \quad \text{with} \quad m_{pq}^E(\boldsymbol{\xi}, t) = \mu d(\boldsymbol{\xi}, t) r_{pq} \tag{4.1}$$

and

$$u_n(\mathbf{x}, t) = \iint_{A} m_{pq}^T(\boldsymbol{\xi}, t) * \frac{\partial G_{np}(\mathbf{x}, t; \boldsymbol{\xi})}{\partial \xi_q} \, dA \quad \text{with} \quad m_{pq}^T(\boldsymbol{\xi}, t) = \mu D(\boldsymbol{\xi}, t) R_{pq} \, . \tag{4.2}$$

A_E and A are the fault areas, $d(\boldsymbol{\xi}, t)$ and $D(\boldsymbol{\xi}, t)$ the slip functions, r_{pq} and R_{pq} the radiation patterns of the EGF and TARGET earthquakes. Self-similarity among earthquakes requires constant static and dynamic stress drop and leads to the following relations for a rectangular rupture area with uniform slip and slip velocity (Irikura, 1999, following Kanamori and Anderson, 1975):

$$\frac{L}{l} = \frac{W}{w} = \frac{T_r}{t_r} = \frac{\bar{D}}{\bar{d}} = N \, , \tag{4.3}$$

where L, W, T_r and $\bar{D}$ represent length, width, rise time and average slip of the TARGET earthquake and l, w, t_r and $\bar{d}$ are the same parameters of the EGF event. In terms of seismic moments, this means:

$$M_0 = \mu A \bar{D} = \mu \cdot L \cdot W \cdot \bar{D} = \mu \cdot Nl \cdot Nw \cdot N\bar{d} = N^3 m_0 \, . \tag{4.4}$$

Thus, as the small event is assumed to have a non-zero rise time, it is explicitly assumed in this technique that the EGF event does not show an impulse-like source time function. The source time function of the EGF is in fact scaled up to the one of the TARGET event, as discussed further below. Moreover, as Irikura (1983, 1999) notes, the scaling relationships may not be valid for very small earthquakes, even though it is not quite clear whether or not there is a breakdown in self-similarity towards very low magnitudes (e.g. Abercrombie and Rice, 2005). Due to these reasons, Irikura's technique should be applied to EGF earthquakes with approximately $M_W \geq 3.5$. Such EGF earthquakes commonly have the advantage of a better signal-to-noise ratio than even smaller earthquakes.

Irikura (1999) notes that often some more or less significant deviations from the strict self-similar earthquake scaling are observed. As a consequence, it is useful to allow for a little more flexibility in that regard, i.e. to allow for differences in stress drop (static and dynamic) between EGF and TARGET earthquakes. In that case, equations (4.3) and (4.4) become (Irikura, 1999; Miyake et al., 2003):

$$\frac{L}{l} = \frac{W}{w} = \frac{T_r}{t_r} = N \,, \quad \frac{\bar{D}}{\bar{d}} = CN \tag{4.5}$$

and

$$M_0 = \mu A \bar{D} = \mu \cdot L \cdot W \cdot \bar{D} = \mu \cdot Nl \cdot Nw \cdot CN\bar{d} = CN^3 m_0 \,. \tag{4.6}$$

Herein, C denotes the stress drop ratio between TARGET and EGF events. This formulation assumes that static and dynamic stress drop vary by the same factor C from small to large earthquake. Using proper values for the scaling parameters N and C is essential in order to obtain sensible simulations. In Chapter 6, rather than additionally inverting for these two parameters, they are determined from the spectral ratios between TARGET and EGF events (see oncoming subsection).

Following equation (4.5), the fault plane of the TARGET earthquake can be constructed from N^2 subfaults with the dimensions of the EGF event (Figure 4.1). A further constraint, besides the fact that both events should be as closely located to each other as possible, is that their radiation patterns should be very similar, i.e.:

$$R_{pq} \approx r_{pq} \,. \tag{4.7}$$

If this is not the case, one can simply multiply the small event's recordings by R_{pq}/r_{pq}, thus correcting the radiation pattern. However, such a correction assumes that the differences in radiation pattern map linearly into the observed ground motion amplitudes, which is only true for a homogeneous halfspace. Scattering effects cause an efficient redistribution of energy, both in time and space (waves that are scattered at some heterogeneities arrive from different azimuths at the station than directly from the source, thus smearing out the radiation pattern, especially at higher frequencies). For instance, the studies by Castro et al. (2006) and
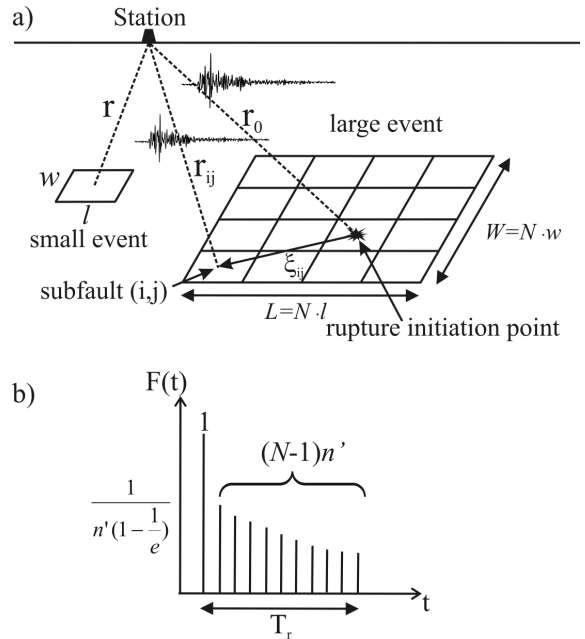
Figure 4.1: Illustration of the EGF-method of Irikura (modified after Miyake et al., 2003). Part (a) schematically shows the faults of the TARGET- and EGF-events, part (b) illustrates the shape of the filtering function.

Takenaka et al. (2003) show that the influence of the radiation pattern on ground motion amplitudes is limited to low frequencies. Castro et al. (2006) recognized the influence for frequencies lower than 0.5 Hz, while Takenaka et al. (2003) recognized the radiation pattern for frequencies lower than 1 Hz while they did not for frequencies higher than 2 Hz. As a result, the application of this simple correction can lead to unrealistic changes in amplitude and hence, it is not applied in this thesis. Care was taken that the radiation patterns of the chosen events are very similar to each other. In the case where the first motion polarities of the two radiation patterns differ (which can happen if the station is located close to the nodal plane of one focal mechanism and if the nodel plane of the other is shifted a bit relative to the first one), the polarity is corrected.

The treatement of the slip time function in Irikura's method is now explained using the simplified model of a ramp function, as it is also commonly assumed in the Haskell model (Haskell, 1966, see also Chapter 2.2.3). Both EGF and TARGET event are assumed to show such a slip time function:

$$d(\boldsymbol{\xi}, t) = \begin{cases} 0 & \text{for } t < 0 \\ \bar{d} \cdot \frac{t}{t_r} & \text{for } 0 \leq t \leq t_r \\ \bar{d} & \text{for } t > t_r \end{cases} \tag{4.8}$$

and

$$D(\boldsymbol{\xi}, t) = \begin{cases} 0 & \text{for } t < 0 \\ \bar{D} \cdot \frac{t}{T_r} & \text{for } 0 \leq t \leq T_r \\ \bar{D} & \text{for } t > T_r \end{cases} . \tag{4.9}$$

Thus, the ramp function of the TARGET earthquake can be constructed by summing N times the ramp function of the EGF event with time shifts of t_r:

$$D(\boldsymbol{\xi}, t) = \sum_{k=1}^{N} d(\boldsymbol{\xi}, t) * \delta(t - (k-1)t_r) . \tag{4.10}$$

In terms of moment density tensor and using (4.7), this results in:

$$m_{pq}^T(\boldsymbol{\xi}, t) = \sum_{k=1}^{N} m_{pq}^E(\boldsymbol{\xi}, t) * \delta(t - (k-1)t_r) . \tag{4.11}$$

In (4.2), the integral of the source area A of the target earthquake is now replaced by a discrete summation over the N^2 subfaults with areas ΔA^i, where each point on a given subfault starts slipping at the rupture onset time $\tau_R^i(\boldsymbol{\xi})$:

$$u_n(\mathbf{x}, t) = \sum_{i=1}^{N^2} \iint_{\Delta A^i} m_{pq}^T(\boldsymbol{\xi}, t) * \delta(t - \tau_R^i(\boldsymbol{\xi})) * \frac{\partial G_{np}(\mathbf{x}, t; \boldsymbol{\xi})}{\partial \xi_q} dA . \tag{4.12}$$

Introducing (4.11) in (4.12) leads to:

$$u_n(\mathbf{x}, t) = \sum_{i=1}^{N^2} \sum_{k=1}^{N} \iint_{\Delta A^i} m_{pq}^E(, \boldsymbol{\xi}, t) * \delta(t - \tau_R^i(\boldsymbol{\xi}) - (k-1)t_r) * \frac{\partial G_{np}(\mathbf{x}, t; \boldsymbol{\xi})}{\partial \xi_q} dA . \tag{4.13}$$

Finally, by comparison with (4.1) and expressing relation (4.13) as the time lagged summation of small events with rupture areas ΔA^i, we yield the formula:

$$u_n(\mathbf{x}, t) = \sum_{i=1}^{N^2} \sum_{k=1}^{N} e_n^i(\mathbf{x}, t - \tau_R^i - (k-1)t_r) , \tag{4.14}$$

where τ_R^i is the rupture time for the subfault ΔA^i, which is defined as the time when the rupture front reaches the center of the subfault. The rupture is assumed to spread circularly at constant rupture velocity v_R over the rupture plane. One attractive feature of the above formulation is that it does not require the assumption of a point source for the EGF event. Rather, the EGF recording can be regarded to contain the rupture dynamics of the small earthquake and, as a result, these effects are also contained in the simulation. As equation (4.14) is in principle valid for near- and far-field, there is no formal need to require the observer to be located in the far-field.

In practice, Irikura's methodology uses only one EGF event for the entire fault plane of the TARGET earthquake, which in turn leads to some restrictions of its applicability. By using one EGF only, the method can already be applied even with a moderate to sparse database. Yet, in this case, it is necessary to assume that the Green's function is roughly identical for all parts of the TARGET fault plane. This approximation is only acceptable if the observation point is several times the linear fault dimension away from the source, i.e. in the far-field. In the near-field, it would be necessary to have appropriate EGF earthquakes for each subfault in order to use the technique, which is usually not the case. It should also be mentioned at this point that what I call here 'EGF' is of course not the true Green's function. The Green's function is implicitely included in the small event's recording.

The application of formula (4.14) leads to several problems. First, as Irikura (1983, 1986) discusses, this formulation leads to artifical periodicities at frequency $1/t_r$ and its multiples, which are due to the fact that the summation for the slip time function is performed with time lag t_r. Second, Irikura (1983) also observes that the simulated ground motions are deficient in high frequencies compared to observations, which usually depict an ω^{-2} behavior. Irikura (1983) attributes this to the fact that the source model is of the Haskell (1966) type with rupture propagation in two dimensions (along strike and dip), which leads to an ω^{-3} source spectrum. Thus, in practice, the utility of this summation scheme is restricted to frequencies lower than the corner frequency of the EGF event. Initially, Irikura (1983) tries to overcome this problem by modifying the summation scheme such that each subfault is allowed to rupture several times, which, as Boatwright (1988) discusses, leads to an overestimation of the high frequency spectrum as expected from the ω^{-2}-model by the square root of the multiplicity.

As a remedy to these problems, Irikura (1986, 1999) introduces different filters which replace the plain summation (with index k in (4.14)) to correct for the difference in slip time function between EGF and TARGET earthquakes. The filter given in (4.16), following Irikura and Miyake (personal communication, 2003), leads to the best results. It has also been recently used by Miyake et al. (2003). With this modification, Irikura's final summation scheme reads as follows:

$$u_n(\mathbf{x}, t) = \sum_{i=1}^{N} \sum_{j=1}^{N} \frac{r}{r_{ij}} F(t) * (C \cdot e_n(\mathbf{x}, t)),$$

(4.15)

with filtering function $F(t)$ (Figure 4.1)

$$F(t) = \delta(t - t_{ij}) + \frac{1}{n'(1 - \frac{1}{e})} \sum_{k=1}^{(N-1)n'} \left[\frac{1}{e^{\frac{k-1}{(N-1)n'}}} \delta\left\{ t - t_{ij} - \frac{(k-1)T_r}{(N-1)n'} \right\} \right],$$

(4.16)

where

$$t_{ij} = \frac{r_{ij} - r_0}{v_S} + \frac{\xi_{ij}}{v_R}.$$

(4.17)

The different parameters in this formulation are schematically shown in Figure 4.1. r/r_{ij} corrects for differences in geometrical spreading due to differences in location of the EGF earthquake and the considered subfault. t_{ij} represents the time difference between the contribution from the assumed rupture

initiation point and the one from subfault (i, j), which includes rupture and wave propagation. As Irikura (1999) notes, with this summation scheme, the low frequency motions are coherently summed and amplified by CN^3, whereas the high frequency motions are incoherently summed (Joyner and Boore, 1986) and amplified by CN. How C and N can be determined is discussed further below. The filtering function has two main effects. The first one is that it shifts the artifical periodicities to frequencies higher than the ones of interest (by shortening the summation time step, which can be viewed as a kind of smoothing) and the second one is that the high frequencies are scaled as above-mentioned, which leads to a high frequency content of the simulated time series in accordance with the ω^{-2} model.

Determination of the Scaling Parameters C and N

As mentioned earlier, the determination of the correct scaling parameters C and N is essential for the successfull simulation of strong ground motion with this technique. The basic assumption underlying the method described below is that the source spectra of both EGF and TARGET earthquakes display the ω^{-2} shape. Assuming linear filters, the observed waveform $u(t)$ is a convolution of the source effect $S(t)$, the propagation path effect $P(t)$ and the site effect $I(t)$. For the TARGET $[u(t)]$ and EGF $[e(t)]$ waveforms, this means, as already given by relations (2.38) and (2.39):

$$u(t) = S(t) * P(t) * I(t) \Rightarrow U(f) = S(f) \cdot P(f) \cdot I(f) \qquad (4.18)$$

respectively

$$e(t) = s(t) * p(t) * i(t) \Rightarrow e(f) = s(f) \cdot p(f) \cdot i(f). \qquad (4.19)$$

Now we may assume that $P(f) \approx p(f)$, because the two events are chosen such that their hypocenters are as close as possible to each other, and $I(f) \approx i(f)$, which is reasonable only if linear soil behavior can be presumed. None of the acceleration records used in Chapter 6 shows a PGA value larger than about $0.3\,g$. As non-linearity is commonly related to peak accelerations larger than this threshold (e.g. Anderson, 2003; Su et al., 1998), the assumption of linear site effects is regarded to be acceptable for the rest of this work. With these approximations, by computing the ratio between the FAS of the TARGET and EGF record, one gets:

$$\frac{u(f)}{e(f)} \approx \frac{S(f)}{s(f)}. \qquad (4.20)$$

As yet, no assumption has been made on the parametric shape of the source terms. If both TARGET and EGF earthquake follow the ω^{-2} shape, as given by (2.28), (4.20) can be rewritten as:

$$\frac{S(f)}{s(f)} = \frac{M_0}{m_0} \cdot \frac{1 + \left(\frac{f}{f_{c,E}}\right)^2}{1 + \left(\frac{f}{f_{c,T}}\right)^2}. \qquad (4.21)$$

This spectral ratio displays a plateau with spectral level M_0/m_0 at frequencies lower than the corner frequency of the TARGET event, $f_{c,T}$, and a plateau of value $(M_0/m_0)(f_{c,T}/f_{c,E})^2$ for frequencies higher than $f_{c,E}$, which is corner frequency of the EGF earthquake.

From (4.6), it follows (with U_0 and u_0 being the plateaus at low frequencies for TARGET and EGF events and A_0 and a_0 the acceleration high frequency plateaus, as shown in Figure 4.2):

$$\frac{U_0}{u_0} = \frac{M_0}{m_0} = CN^3, \qquad (4.22)$$
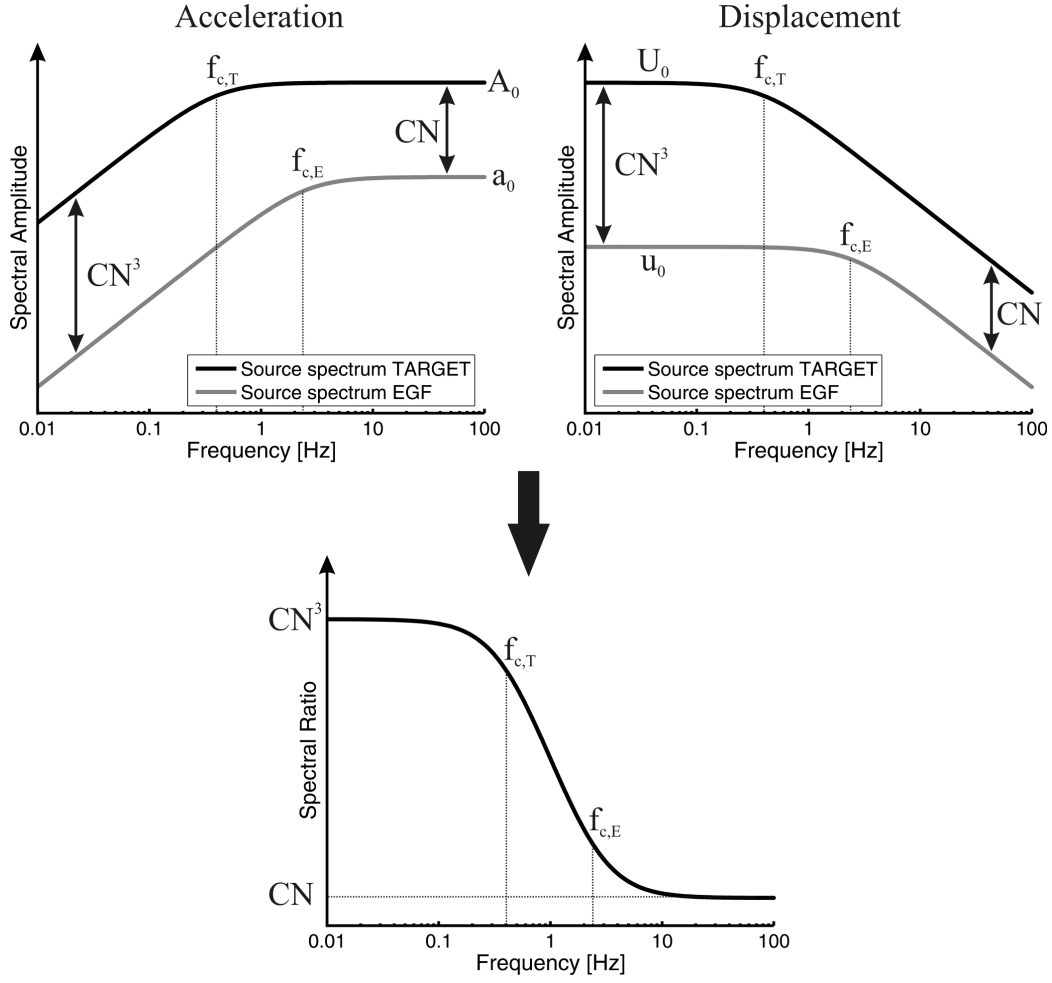
Figure 4.2: Schematic illustration of the determination of the scaling factors C and N. Top: acceleration (left) and displacement (right) source spectra (loglog plots) of the TARGET and EGF-events displaying the Brune (1970, 1971) shape. In order to get from the EGF- to the TARGET spectrum, the low frequencies have to be amplified by CN^3, whereas the high frequencies must be amplified by CN. The spectral ratio (bottom) displays a constant level with value CN^3 at frequencies lower than $f_{c,T}$ and a constant level at frequencies higher than $f_{c,E}$ with value CN. More explanations are given in the text.

and, due to self-similarity,

$$\frac{A_0}{a_0} = \frac{M_0}{m_0} \cdot \left(\frac{f_{c,T}}{f_{c,E}}\right)^2 = CN \,. \tag{4.23}$$

Therefore, from the spectral ratio, by obtaining an estimate of M_0/m_0, $f_{c,T}$ and $f_{c,E}$, it is possible to compute the scaling parameters C and N as:

$$N = \frac{f_{c,E}}{f_{c,T}} \tag{4.24}$$

$$C = \frac{M_0}{m_0} \cdot \left(\frac{f_{c,T}}{f_{c,E}}\right)^2 \,. \tag{4.25}$$

This procedure has also been used for instance by Miyake et al. (2001, 2003) and Kohrs-Sansorny et al. (2005). A simulation example using Irikura's technique is shown in Figure 4.3. The parameters used to generate this example are those inverted for TARGET-A in Chapter 6 with EGF earthquake EGF200209. Note the change in frequency content between the EGF record (top) and simulation (bottom). The enhanced low frequency part of the simulation is due to the summation procedure. It is important to use only frequencies for which the signal-to-noise ratio of the EGF recording is acceptable, as otherwise, only noise is being scaled up. For the example shown, the lowest frequency analyzed is 0.5 Hz.

Some Remarks On Irikura's Source Model

At this point, I discuss in a few more details the source model which Irikura's technique is based upon. It consists, as aforementioned, of a rectangular rupture area with uniform slip and rise time (and thus, uniform slip velocity). The rupture is assumed to propagate with a constant speed radially over the fault, starting at the rupture initiation point. It can be regarded as a Haskell type model, even though it is a bit more complicated due to the radial rupture propagation.

Figure 4.3: EGF recording and example simulation at station BVC in Bucharest. The transverse S-wave component (SH) of acceleration is shown.

If seismic moment, source dimensions and rise time are given, static and dynamic stress drop as well as average slip and particle velocity can be easily computed using relations (2.18), (3.1) and (3.3). The geometry-dependent coefficient of proportionality in (3.1) may vary within the range of a factor 4 and is usually not well known. Furthermore, it is a question of definition which source dimension (length or width) should be taken as characteristic rupture length $\tilde{L}$. Therefore, it is common practice to estimate the stress drop from an equivalent circular rupture area using (2.32).

Miyake et al. (2003) called the source implementation used in Irikura's technique the *strong motion generation area* (SMGA), as they try to explain the strong ground motion time histories over a broad frequency range as the result of (homogeneous) slip on such a rectangular fault plane. Indeed, this approach has proven to generate data-consistent time series. Miyake et al. (2003) use the frequency range between 0.2 and 10 Hz, and in this work, I will use frequencies between approximately 0.5 and 15 Hz.

As Miyake et al. (2003) point out, the SMGA size is usually smaller than the rupture areas determined e.g. from low-frequency finite source rupture models. It should be noted here that the size and rise time of such a simple source model are in fact dependent on the considered frequency range. The idea behind the SMGA is to explain both high frequency and low frequency (with, however, a tendency to higher frequencies, due to signal-to-noise ratio constraints at the low frequency end) components of ground motion. Thus, there is an obvious discrepancy between the results from low frequency slip inversions and the SMGA concept. Furthermore, the assumption of homogeneous slip clearly opposes the well-accepted finding that slip is distributed very heterogeneously over the fault plane, at least for large earthquakes (Somerville et al., 1999). Based on an analysis of twelve crustal earthquakes in
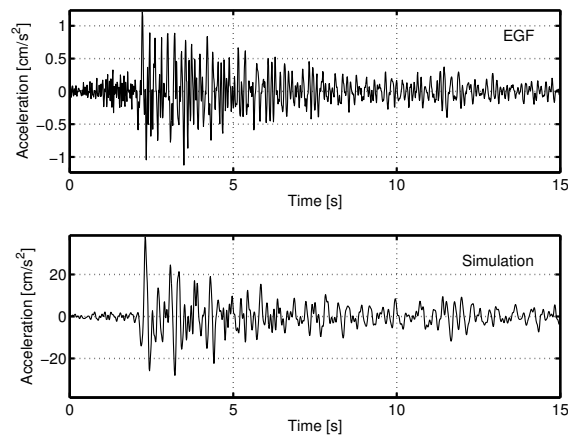
Japan, Miyake et al. (2003) come to the conclusion that the SMGA size is equivalent to the combined area of asperities as determined from low-frequency slip inversions, as both SMGA size and rise time are compatible with the scaling relations of Somerville et al. (1999).This means that seismic radiation within the frequency range used for the determination of the SMGA parameters is to a large extent dominated by the asperities.

It makes a fundamental difference in stress drop estimation whether the SMGA is considered to be an aspertity within a larger background rupture area or a crack releasing the complete seismic moment of the earthquake. Following Madariaga (1979) and Boatwright (1988), the static stress drop within a single asperity in the stress-free field is given by:

$$\Delta\sigma_{asperity} = \frac{7}{16} \cdot \frac{M_0}{Rr^2} , \qquad (4.26)$$

where r is the radius of the asperity and R is the radius of the total fault plane if they are assumed to be circular. In contrast, the static stress drop for a crack of the same size as the asperity is:

$$\Delta\sigma_{crack} = \frac{7}{16} \cdot \frac{M_0}{r^3} , \qquad (4.27)$$

Thus, the static stress drop within the asperity can actually be computed with the same formula as the one of the crack, but with a seismic moment reduced by a factor r/R due to the existence of slip on the background fault area which is supposed to show no stress release. Das and Kostrov (1986) point out a factor of $(r/R)^2$, which is due to a difference in the assumptions made for the derivation. Whereas Madariaga (1979) and Boatwright (1988) use the average slip of the crack in the reciprocal theorem, assuming the asperity to be located at an arbitrary place in the background fault plane, Das and Kostrov (1986) use the maximum slip of the crack and the assumption that the asperity is located in the center of the background fault plane. If the SMGA is equivalent to the asperity only, one should expect that at high frequencies the simulations match the observed spectra well whereas they should underestimate them at very low frequencies. I will discuss the results of the study in Chapter 6 in light of these interpretations.

Finally, the effects of variations in the parameters characterizing the SMGA (length, width, rise time, rupture initiation point) are illustrated in Figure 4.4. As can be seen from (a), reducing the size of the SMGA leads to an increase in amplitude, whereas it is the opposite when the size is increased. The same observation applies to changes in the rise time. There are also some changes in the phase of the signals. Another issue is the aspect ratio of the SMGA. Modifications in the aspect ratio can lead both to changes in amplitude and phase. Part (b) of Figure 4.4 shows that a change in the rupture initiation point can have a very strong impact on the results. Thus, directivity effects are as important in the simulations as the matter of dimensions and rise time. Therefore, a good azimuthal coverage is needed in order to perform inversions as presented in Chapter 6. For a given rupture velocity, reducing the size of the SMGA simply means that the time lags as given by (4.17) get shorter. Therefore, the simulated waveforms generally get more impulsive. If the dimensions are chosen excessively large, the contributions of the different subfaults will finally be put one after the other and no interference will take place anymore. Part (c) illustrates how important proper estimates of C and N are. Here, the SMGA dimensions, rise time and rupture initiation point have been kept constant and only C and N have been varied (in a way that the moment ratio as given by (4.6) is always the same – thus the seismic moment of the simulation is kept constant). Different combinations of C and N yield different high frequency plateaus of the simulations, which is clear to see from the very large changes in acceleration amplitude.

(a) Different sizes and rise times

(b) Different rupture initiation subfaults

(c) Different scaling factors C and N
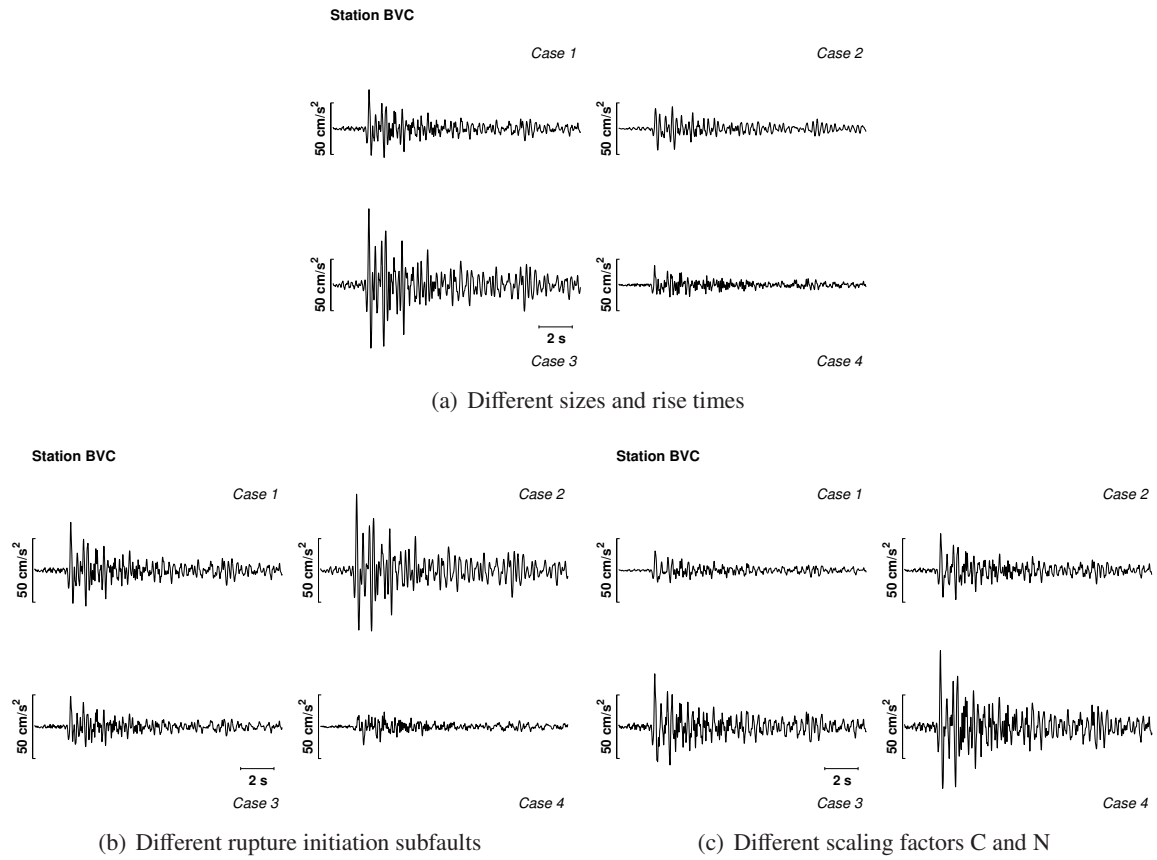
Figure 4.4: Example EGF simulations (acceleration) with different modeling parameters at station BVC. **(a)** *Case 1*: dimensions L_1 and W_1, rise time $T_{r,1}$; *Case 2*: $L_2 = 3L_1$, $W_2 = 3W_1$, $T_{r,2} = T_{r,1}$; *Case 3*: $A_2 = 1/3L_1$, $W_2 = 1/3W_1$, $T_{r,2} = T_{r,1}$; *Case 4*: $L_2 = L_1$, $W_2 = W_1$, $T_{r,2} = 3T_{r,1}$. The rupture initiation point, aspect ratio as well as C and N are kept constant. **(b)** *Case 1*: rupture initiation point $(2, 3)$; *Case 2*: $(1, 5)$; *Case 3*: $(3, 3)$; *Case 4*: $(5, 5)$. The scaling factors are $N = 5$ and $C = 1.7$ and the SMGA dimensions L and W as well as the rise time τ_r are kept constant. **(c)** *Case 1*: $C = 0.4$; $N = 8$; *Case 2*: $C = 1$; $N = 6$; *Case 3*: $C = 3$; $N = 4$; *Case 4*: $C = 8$; $N = 3$. The SMGA dimensions and rise time are kept constant. All these combinations of C and N reach an identical moment ratio.

The parameter study depicted in Figure 4.4 illustrates how important the correct choice of simulation parameters is in order to model realistic time series. The quantities that have to be given to compute a simulation are stress drop ratio C, scaling factor N, length L (or l), width W (or w), rise time T_r (or t_r), rupture initation point along strike and dip and shear and rupture velocity (see overview in Table 4.1). If the SMGA parameters for a given TARGET earthquake will be derived (for which waveform observations exist), C and N (as well as the corner frequencies $f_{c,T}$ and $f_{c,E}$) can be determined from the FAS of the records, as described earlier in this chapter. The other parameters have to be chosen in such a way that the observed time histories are matched as well as possible. This is a highly non-linear inverse problem, and inverting for the SMGA parameters requires the usage of a global search technique. The algorithm I employ for this purpose is a genetic one and is explained in Chapter 5.

Care has to be taken if the methodology is intended to be used to synthesize a catalogue of scenario earthquakes. Obviously (see Figure 4.4), choosing sensible SMGA parameters (respectively constraining a reasonable scaling behavior of these) is the key to success. First of all, unless a specific

Parameter	Description	Remarks
C	stress drop ratio	from spectral ratios, if TARGET waveforms exist, otherwise an assumption must be made (e.g. $C = 1$)
N	scaling factor	from spectral ratios, if TARGET waveforms exist, otherwise from moment ratio with assumed C
L	fault length	linked to l through N, implicitly linked to $f_{c,E}$
W	fault width	linked to w through N, implicitly linked to $f_{c,E}$
T_r	rise time	linked to t_r through N, implicitly linked to $f_{c,E}$
POS_{strike}	rupt. init. subfault along strike	important for directivity
POS_{dip}	rupt. init. subfault along dip	important for directivity
v_S	shear wave velocity	usually approximated from structural information
v_R	rupture velocity	v_R/v_S usually chosen between 0.7 and 0.9

Table 4.1: Overview of the simulation parameters needed for Irikura's EGF technique.

TARGET event shall be modeled, C and N cannot be estimated as outlined above and have to be derived using reasonable assumptions (for instance, if pure self-similarity is assumed, C would be set to 1). In terms of amplitude spectra, looking for the optimal SMGA parameters means to look for a set of parameters which can explain the corner frequencies of the EGF and TARGET events. In principle, the corner frequency $f_{c,E}$ of the (observed) EGF record can be measured. For a given N, the corner frequency of the simulated record is connected to $f_{c,E}$ by equation (4.24). However, the question is then what dimensions, rise time and further parameters listed above must be chosen. As discussed in Chapter 3, the source size and rise time of the EGF (and TARGET) are connected to the corner frequency. Therefore, they must be compatible with the corner frequency of the EGF earthquake. A (minimal) check whether one's assumptions are entirely wrong or not can be done by determining, in addition to $f_{c,E}$, the corner frequency of the synthetic record. If the SMGA parameters are chosen correctly, the corner frequency of the simulated record must be approximately equal to $N \cdot f_{c,E}$. However, the determination of $f_{c,E}$ is strongly dependent on the correction of path and site effects, which makes it a difficult parameter to accurately estimate and hence, this check may also be difficult to perform.

Thus, a proper calibration using at least several TARGET earthquakes for which the SMGA parameters are inverted is necessary. The scaling behavior of the parameters of these calibration events can then by used to infer reasonable SMGA parameters for further simulations. Otherwise, it is rather dangerous to use this methodology to compute synthetic scenario earthquake recordings. One can easily make assumptions which are incompatible with the EGF recordings utilized and the number of controlling parameters which have to be set (nine) is large.

4.1.2 The EGF-Method of Hutchings

As this technique is not used in this work, I will only provide a brief summary for completeness. Hutchings and Wu (1990) and Hutchings (1991, 1994) follow a somewhat different approach to the problem. As mentioned at the beginning of this chapter, the empirical Green's functions summation in the classical sense (i.e. assuming a pulse-like source time function) is only valid for frequencies lower than the corner frequency of the small event used as EGF. Irikura (1986, 1999) solved this problem by combining the empirical scaling relations of Kanamori and Anderson (1975) with the spectral scaling characteristics of the ω^{-2} spectral model (Brune, 1970, 1971).

Hutchings, as opposed to Irikura, considers the EGF event to be a point source (in the far-field) with impulse-like slip velocity time function. Following (2.16) together with (2.17), we get the EGF event's displacement as:

$$e_n(\mathbf{x}, t) = M_{pq} * \frac{\partial G_{np}(\mathbf{x}, t; \boldsymbol{\xi})}{\partial \xi_q} \, . \tag{4.28}$$

The slip time function is a step dislocation, as the slip velocity time function is assumed to be a δ-pulse. M_{pq}, as defined by (2.17), includes this time dependence. The summation scheme followed by Hutchings and Wu (1990) and Hutchings (1991, 1994) can be written as follows:

$$u_n(\mathbf{x}, t) = \sum_{i=1}^{M} \frac{\mu \Delta A^i D^i(t_i')^*}{m_0^i} * e_n^i(\mathbf{x}, t_i' - \frac{|\boldsymbol{\xi}^i - \boldsymbol{\xi}^0|}{v_R}) \, . \tag{4.29}$$

Herein, M is the number of subfaults, m_0^i is the seismic moment of the EGF earthquake located at subfault i, ΔA^i is the size of the i-th subfault and t_i' is time relative to the origin time of the small event located at the i-th subfault. $\boldsymbol{\xi}^0$ denotes the location of the hypocenter, v_R the rupture velocity and $D^i(t_i')^*$ is the desired slip function (e.g. ramp function) of the TARGET event deconvolved with a unit Heaviside step function, i.e. differentiated with respect to time. Note that the slip time function can, as opposed to Irikura's approach, be variable over the fault.

In order to be able to simulate high frequency ground motions covering the entire frequency range of interest to earthquake engineering, Hutchings exploits the f_{max} effect (Hanks, 1982), which I discussed in Chapter 2.4, by using small earthquakes fulfilling the criterion $f_c \geq f_{max}$. Therefore, Hutchings and Wu (1990) use only earthquakes with $M_0 \leq 10^{14} Nm$, which corresponds to a maximum magnitude of about $M_W \approx 3.5$. This way, the source spectrum of the EGF event is flat for the entire frequency range up to approximately 8-10 Hz, where f_{max} is usually found. Thus, the EGF earthquake can be viewed as a step-like source (that is why the Heaviside step function is deconvolved in equation (4.29)) over the entire frequency range. In that sense, the finite rise time is masked by the f_{max} effect.

4.1.3 Comparison of these Techniques

Depending on the problem and especially on the available database, it is advisable either to choose one or the other technique. Irikura's (1983, 1986, 1999) methodology has the advantages that one does not have to know the explicit shape of the slip time function, and, as the EGF earthquakes should have a magnitude larger than approximately 3.5, they are usually fine regarding their signal-to-noise ratio. The main attraction of this technique is its simplicity, and it is possible to generate astonishingly data-consistent time series with a very simple source model, as I will show in Chapter 6. However, its strong dependence on the correct choice of the scaling factor C and N requires a good calibration with observations before computing synthetics that shall be used e.g. for seismic hazard assessment purposes.

The technique of Hutchings (Hutchings and Wu, 1990; Hutchings, 1991, 1994) has the advantage that it does not rely on the validity of the scaling relations among earthquakes. This is clearly an advantage, as there is a breakdown of similarity towards very large magnitudes (e.g. Scholz, 2002) and it is still not clear whether or not there is a breakdown in similarity towards lower magnitudes (e.g. Abercrombie and Rice, 2005). Yet, a drawback of the method is that the shape of the slip time function has to be arbitrarily assumed and there might be more problems finding EGF earthquakes with

acceptable signal-to-noise ratio. Furthermore, it is usually necessary to have recordings of different EGF earthquakes for different parts of the fault.

What is the better choice for the Vrancea intermediate-depth earthquakes treated in this thesis? Mostly, the data quality of records from Vrancea earthquakes is only acceptable for events with $M_W \geq 4$. This is mainly attributable to the fact that the hypocentral distances are mostly larger than 100 km (and never shorter than about 70 km). Therefore, the technique of Irikura is preferred in this thesis to the one of Hutchings.

4.2 Stochastic Simulation of Ground Motion

The findings of Hanks and McGuire (1981), who came to the conclusion that the observed high-frequency ground motions can be well described by bandlimited finite-duration Gaussian noise with a characteristic amplitude spectrum, paved the way to the stochastic simulation technique, which has been used extensively in the seismological community since the early work of Boore (1983). The stochastic method is highly attractive, since it enables the fast computation of large numbers of realistic acceleration time histories and, in contrast to the EGF technique, is not limited by the availability of appropriate databases. Nevertheless, one needs to be cautious with respect to the seismological models used, especially if the technique shall be applied in an area where there are no observational data to calibrate the simulations.

The stochastic technique has been applied by many authors in almost any part of the world and a comprehensive review on the method is given by Boore (2003, see also references therein). Originally, the method was designed to simulate ground motions resulting from an effective point source, but it can also be used to simulate ground motions from a finite-fault (as with the FINSIM code developed by Beresnev and Atkinson, 1997, 1998) simply by using the stochastic method to compute the ground motions resulting from each subfault and performing a summation procedure similar or even identical to the ones described in the discussion on empirical Green's functions methods above.

4.2.1 Spectral Ground Motion Models

In Chapter 2.4, the basic features of the convolutional model of seismic ground motion have been outlined. In terms of amplitude spectra, the ground motions at a given site can be expressed as the multiplication of the source $S(M_0, f)$, path $P(R, f)$ and site $I(f)$ contributions. I will discuss the classical spectral ground motion model with respect to S-waves (and surface waves), but the same considerations generally also apply to P-waves.

Following Boore (2003), the acceleration amplitude spectrum can then be given by

$$A(M_0, R, f) = (2\pi f)^2 CS(M_0, f)P(R, f)I(f). \tag{4.30}$$

The constant C is (for S-waves):

$$C = \frac{\langle \mathfrak{R}^{\theta\phi} \rangle VF}{4\pi\rho_0 v_{S,0}^3 R_0}. \tag{4.31}$$

Herein, $\langle \mathfrak{R}^{\theta\phi} \rangle$ denotes the average radiation pattern, V is a factor accounting for the separation of shear wave energy into two horizontal components $(1/\sqrt{2})$, F accounts for the free surface and is

commonly set to a value of 2^1. ρ_0 and $v_{S,0}$ represent the density and shear wave velocity in the vicinity of the source and R_0 is the reference distance, which is usually set to 1 km.

In most applications, the source contribution is regarded to be of the ω^{-2} type (Brune, 1970, 1971):

$$S(M_0, f) = M_0 \left[1 + \left(\frac{f}{f_c} \right)^2 \right]^{-1}. \tag{4.32}$$

However, as Boore (2003) notes, there are also other possibilities (as used e.g. by Atkinson and Boore, 1995). It should be emphasized at this point that the formulation given above represents an isotropic point source, as only the average radiation pattern is considered. f_c is usually calculated from an assumed stress parameter as given by (3.15), but the severe ambiguities discussed in Chapter 3.2 have to be kept in mind.

The path contribution is composed of the geometrical spreading effect and the intrinsic damping structure along the propagation path and is accounted by

$$P(R, f) = G(R)E(R, f) = G(R) \exp \left[-\frac{\pi f R}{Q(f) v_S} \right]. \tag{4.33}$$

Herein, the quality factor Q is generally assumed to depict a frequency dependence of the type (2.43) and the geometrical spreading function $G(R)$ is usually modeled as a series of n straight lines in loglog space (Boore, 2003):

$$G(R) = \begin{cases} \frac{R_0}{R} & \text{for } R \leq R_1 \\ G(R_1) \left(\frac{R_1}{R} \right)^{p_1} & \text{for } R_1 \leq R \leq R_2 \\ \vdots \\ G(R_n) \left(\frac{R_n}{R} \right)^{p_n} & \text{for } R_n \leq R \end{cases} . \tag{4.34}$$

In a homogeneous halfspace, the geometrical spreading is described by $G(R) = 1/R$. However, if the medium is layered, a function of the form (4.34) can account for the joint arrivals of e.g. direct waves and reflections of the Moho and/or other interfaces as well as surface waves, which in theory show a geometrical spreading $G(R) = 1/\sqrt{R}$. In applications, it is important to specify what distance is used. This may be the shortest distance to the vertical projection onto the Earth's surface (the Joyner-Boore-distance r_{jb}, Boore et al., 1997) or, as used in Chapter 7 in the case of the Vrancea intermediate-depth earthquake, simply the hypocentral distance.

Finally, the site effect, which is independent of distance, can be given by

$$I(f) = H(f)D(f) = H(f) \exp(-\pi \kappa f), \tag{4.35}$$

which includes the effects of site amplification, $H(f)$, and high frequency diminution, $\exp(-\pi \kappa f)$. The main appeal of such spectral models are their simplicity. It is very easy to compute such theoretical amplitude spectra, but one question remains: what about the phase and how to obtain realistic time histories of ground motion, which are needed to estimate interesting time domain parameters such PGA?

---

[1]which is, strictly speaking, only valid for SH-waves

4.2.2 From Amplitude Spectra to Time Histories

In order to obtain realistic acceleration time series, the earlier mentioned findings of Hanks and McGuire (1981) are used, namely that the phase of acceleration ground motions can essentially be viewed to be random. Therefore, the computation of time histories is usually performed in several steps (Boore, 2003):

1. Generation of gaussian (white) noise $u_{noise}(t)$ for the assumed duration of ground motion T_d.

2. The noise is windowed with a shaping window as described further below to get $u_{noise,win}(t)$.

3. Transformation of $u_{noise,win}(t)$ into frequency domain via Fourier transform:

$$\hat{U}_{noise,win}(f) = \int_0^{T_d} u_{noise,win}(t)e^{-i2\pi ft}dt \, . \tag{4.36}$$

4. Normalization of $\hat{U}_{noise,win}(f)$ by the square root of the mean of its squared amplitude spectrum

5. Multiplication of the normalized spectrum by the desired acceleration amplitude spectrum $A(M_0, R, f)$.

6. Transformation back to time domain to obtain the final time history.

The shaping window usually employed is based on the work of Saragoni and Hart (1974) and can be written as follows:

$$w(t; \epsilon, \eta, t_\eta) = a\left(\frac{t}{t_\eta}\right)^b \exp\left[-c\frac{t}{t_\eta}\right] , \tag{4.37}$$

with

$$
\begin{aligned}
a &= (\exp(1)/\epsilon)^b \\
b &= -\epsilon \ln \eta \cdot [1 + \epsilon(\ln \epsilon - 1)]^{-1} \\
c &= b/\epsilon \\
t_\eta &= f_{Tg} \cdot T_d
\end{aligned}
\quad . \tag{4.38}
$$
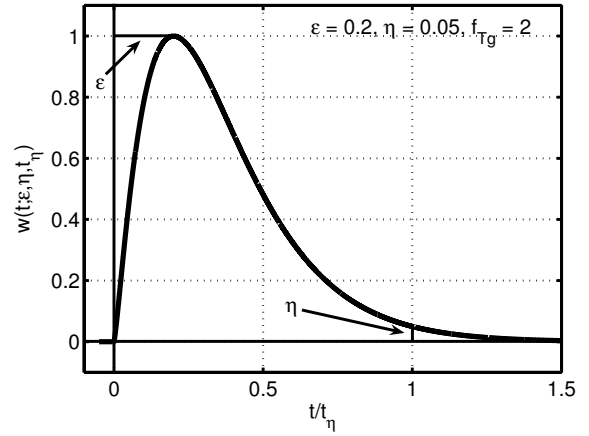
Figure 4.5: Shaping window for the stochastic simulations after Saragoni and Hart (1974).

The typical shape of the window is graphically displayed in Figure 4.5 and the different steps described are illustrated in the simulation example shown in Figure 4.6. Finally, it remains to note that the stochastic method can reproduce a given amplitude spectrum *on average* over many simulations. Each realization can markedly differ from the desired model spectrum, as Boore (2003) points out. As a result, parameters such as PGA or response spectra should only be compared to observations using averages over many different realizations. Furthermore, the stochastic method as presented above is not able to capture any kind of directivity or phase effects resulting from rupture propagation.
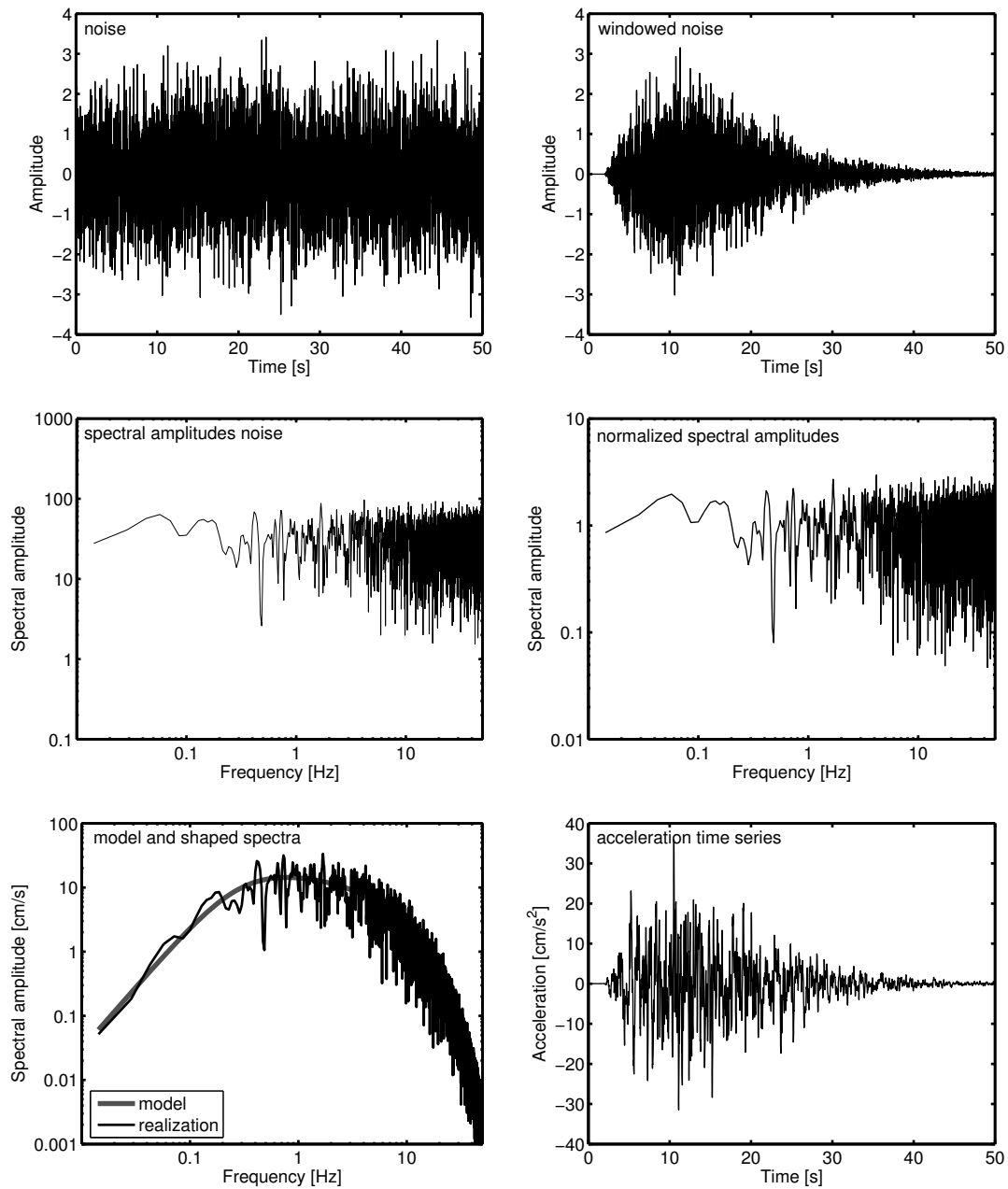
Figure 4.6: Different steps of the stochastic method (after Boore, 2003). In a first stage, gaussian noise is computed (top left). After applying the shaping window to the noise (top right), the windowed noise is transformed to the frequency domain (center left). The spectral amplitudes are normalized (center right) and multiplied with the desired spectral model (bottom left). Finally, the ground motion time series is obtained by transformation to time domain (bottom right). The simulation shown here as an example is from an $M_W = 7$ (with corner frequency $f_c = 0.3$ Hz) earthquake occuring 100 km away from the site of interest and a frequency independent site response equal to unity (very hard rock). The assumed Q-model is $Q(f) = 100f^{0.8}$ and κ was chosen as $\kappa = 0.05s$.

4.3   The Finite-Difference Method

A completely different type of ground motion simulation techniques are those computing full wave-field solutions in complex media, and the main technique used is the finite-difference method. A vast number of publications have been released during the last decade (some examples include Aochi and Madariaga, 2003; Furumura et al., 2002; Furumura and Chen, 2005; Furumura and Kennett, 2005; Furumura and Hayakawa, 2006; Furumura et al., 2006; Gottschämmer et al., 2002; Miksat et al., 2005; Miksat, 2006; Olsen et al., 1995; Olsen, 2000; Olsen et al., 2006; Oth et al., 2007b) and I refer the reader to these for thorough theoretical discussions and practical examples. Another technique of this type which emerged a few years ago is the spectral element method (Komatitsch, 1999). In brief, regarding the finite-difference method, the medium is discretized into a grid and a numerical solution of the equation of motion (2.2) is computed at each grid point by replacing the derivatives with respect to time and space with finite difference operators.

Such computations, in contrast to the EGF and stochastic techniques, are very expensive and time consuming to perform. Their main advantage is the fact that they allow to analyze all wave propagation effects including P-, S- and surface waves as well as conversions between the wave types, wave-guiding effects, reflections and refractions from different interfaces, ... However, there are also some severe drawbacks. The first one is that, due to the imperfect knowledge of the subsurface structure, the finite-difference technique is mostly applicable only for very long period ground motions ($< 0.5 - 1$ Hz), which are generally not the ones of primary interest to earthquake engineering. Furthermore, even if the structural models were perfectly known, in order to achieve simulations of ground motions in 3D up to about 10 Hz, enormous computational resources would be required. If such simulations shall be used to compute ground motion scenarios for earthquake engineering purposes, a careful calibration, both in view of the structural model and the source implementation, is required.

4.4   Discussion

Summarizing this chapter, a general remark regarding all ground motion simulation techniques is that the greatest possible effort should be undertaken to verify their validity and calibrate them with observational data before using them to compute vast numbers of theoretical scenario earthquakes. Each method has distinct advantages and drawbacks, and the way to go in the future will certainly be to combine them into hybrid applications (e.g. Kamae et al., 1998; Pulido et al., 2004), as they are complementary in many aspects. The stochastic and EGF techniques as described above are for instance suited for rather high-frequency simulations. The random phase assumed in the stochastic method is not a good approximation at frequencies much lower than the corner frequency, where the phase is rather deterministic. The EGF approach, on the other hand, is usually limited by signal-to-noise ratio constraints to lower frequencies. In view of this problem, the finite-difference technique becomes very interesting to fill that low frequency gap.

Chapter 5

Parameter Optimization Using Genetic Algorithms

One of the standard problems in seismology is the inverse problem, i.e. to infer a set of physical model parameters from a set of observations. The location of earthquakes is a good example for such an inverse problem. From the arrival time differences between P- and S-waves, we want to locate the earthquake in space and time. The spatial coordinates and the origin time are the model parameters, whereas the arrival time differences are the observations. Many books have been written on inverse theory (e.g. Tarantola, 1987; Menke, 1989). Ideally, an inverse problems should be *well-posed* (i.e. the solution is insensitive to small random errors in the data) and its solution *unique*, but in many cases, these requirements are not fulfilled. Furthermore, the solution to a given inverse problem depends upon the parameterization.

For any *inverse problem*, an according *forward problem* must be defined. This forward problem describes the theoretical dependencies of the observations on some model parameters. In terms of earthquake location, the forward problem consists in calculating the travel times of P- and S-waves through a theoretical velocity model. The inherent difficulty in solving such inverse problems can already be seen from this simple example. First, the outcome of the inversion is strongly dependent on the parameterization of the physical model which is utilized in the forward computation. The better the velocity model (i.e. the closer to reality), the better the location. Thus, care has to be taken that the parameterization of the forward model is reasonable. Secondly, as a rule, the model parameters give rise to trade-offs and several very different sets of parameters may explain the observations equally well (*non-uniqueness* of the inverse problem). The observations are also subjected to errors (e.g. noise in the seismograms), which usually aggravate the problem of non-uniqueness.

The ultimate goal of any inversion effort is to find the optimum parameters for a certain forward problem such that the residuals between modeled data and observations are minimal. In that sense, the term *parameter optimization* is also often employed. The function which has to be minimized is also called *cost function* or *misfit function*. Throughout the rest of this thesis, I will employ the term *cost function*. Let the vector $\mathbf{d} = [d_1, d_2, \ldots, d_N]^T$ contain a dataset of N discrete observations (e.g. wave arrival times) and the forward model be parameterized by the model vector $\mathbf{m} = [m_1, m_2, \ldots, m_M]^T$ (e.g. seismic velocities of the subsurface model). Usually, some norm of the following form is mini-

mized during the inversion process:

$$L_p-\text{norm}: \quad \|\mathbf{e}\| = \left[\sum_{i=1}^{N} |e_i|^p \right]^{\frac{1}{p}}. \tag{5.1}$$

Herein, the vector $\mathbf{e} = \mathbf{d_{obs}} - \mathbf{d_{syn}}$ contains the residuals between observations $\mathbf{d_{obs}}$ and synthetics $\mathbf{d_{syn}}$ generated using the physical model $\mathbf{m}$. The most frequently used norms are the L_1- and L_2-norms.

There are many ways to tackle geophysical inverse problems. The most trival is simple trial and error modeling. Different combinations of the model parameters are tested and evaluated. Explicitly linear or linearizable problems can be solved e.g. by the least squares or maximum likelihood method. For linear problems, the minimization of the L_2-norm leads to the least squares technique. However, there are numerous inverse problems whose forward problems show a strongly non-linear behavior. These are usually characterized by highly complex cost functions in the multi-dimensional parameter space. Here, steepest gradient descent may for instance be used to find a minimum, but this approach does not give a clue whether the solution found is the global or only a local minimum. Yet, in many cases, the cost function is noncontinuous or analytical expressions for the derivatives are unknown, which makes it impossible or at least difficult to apply inversion schemes which need the derivatives of the cost function. Several new techniques to solve such problems have emerged during the last 30 years, the most prominent of these being *simulated annealing* and *genetic algorithms* (GA). These techniques mimic optimization of natural phenomena and have been highly successfully applied to numerous problems.

As the discussion of all the different inversion techniques is beyond the scope of this text, I will restrict myself to the method used throughout this work, namely the genetic algorithms. Section 5.1 gives an overview on the mode of operation of GAs and Section 5.2 shortly introduces the theoretical background. Finally, in Section 5.3 I describe the algorithm developed to invert for earthquake source properties with empirical Green's functions.

5.1 The Mode of Operation of Genetic Algorithms

Holland (1975) and Goldberg (1989) can be referred to as the founding fathers of the GA technique in numerical optimization. They also give a comprehensive introduction to biological optimization, which is the process that these types of algorithms try to mimic. Starting from a randomly chosen initial population of individuals (i.e., in terms of model vectors, from an initial set of different $\mathbf{m}$), GAs allow the population to evolve under certain specified conditions to a state where the cost is minimal. The cost function determines the *fitness* (maximum fitness equals minimum cost) of the individuals. Each model parameter vector $\mathbf{m}$ is called a *chromosome*. Commonly, the model parameters are encoded as binary strings, and within a certain chromosome, each bit (either 0 or 1) is termed a *gene*. As pointed out in Haupt and Haupt (1998), it is also possible to use real-valued parameters without encoding them.

5.1.1 Parameter Encoding

Binary coding is the most commonly used parameter representation in GA applications. As an example, consider a problem which depends on two real-valued variables, say x and y. Each of these

parameters is now represented by a binary string of length l. Thus, x and y can take 2^l discrete values. The higher the number of bits l, the finer the discretization will be. For $l = 5$, the binary encoded chromosomes will have the form:

$$chromosome = \left[\underbrace{10110}_{x} \underbrace{01011}_{y} \right] = \left[gene_x[1] \; gene_x[2] \ldots gene_y[1] \; gene_y[2] \ldots \right].$$

Hence, in this example, one combination of x and y is coded with a single binary string of length 10. x and y do not necessarily need to have the same number of bits. Of course, in order to evaluate the cost function, the binary representations have to be converted to their corresponding real-valued quantities, as the vast majority of cost functions is real-valued. This process works as follows: in a first step, the part of the binary string corresponding to a certain parameter (e.g., the first 5 bits for x) is converted into an integer I with

$$I_x = \sum_{m=1}^{N_{genes}} gene_x[m] \cdot 2^{N_{genes}-m}.$$

Thus, for x, we get $I_x = 1 \cdot 2^4 + 0 \cdot 2^3 + 1 \cdot 2^2 + 1 \cdot 2^1 + 0 \cdot 2^0 = 22$. For a search range $x_{low} \leq x \leq x_{high}$, the integer I_x is mapped onto this interval by (e.g. Coley, 1999)

$$x = \frac{(x_{high} - x_{low})}{2^l - 1} \cdot I_x + x_{low}.$$

The number of bits for each parameter must be chosen in a way that the desired resolution is reached, but a representation longer than necessary should be avoided as it slows down convergence, especially in the case of a large number of free parameters, which consequently leads to very long bitstrings.

Besides binary encoding, other options exist. An increasingly popular variant of binary coding is gray coding. In the binary representation discussed above, changing one single bit may result in a completely different integer value (and thus real-valued parameter) while decoding. Thus, a crossover operation can lead to diverging instead of converging offspring with respect to their parent's values. A gray code is a binary code where two neighbouring integer values differ by one single bit. The benefical effect of gray codes is however disputed (Haupt and Haupt, 1998).

Another option is to use the real-valued parameters without encoding. This type of GA is called the *continuous parameter GA* and requires the introduction of some special features during the reproduction step, which are well discussed by Haupt and Haupt (1998).

5.1.2 From Natural Selection to Reproduction

After the creation of an initial population and its evaluation using the cost function, GAs work in three main steps:

1. Natural selection

2. Mating and Crossover

3. Mutation
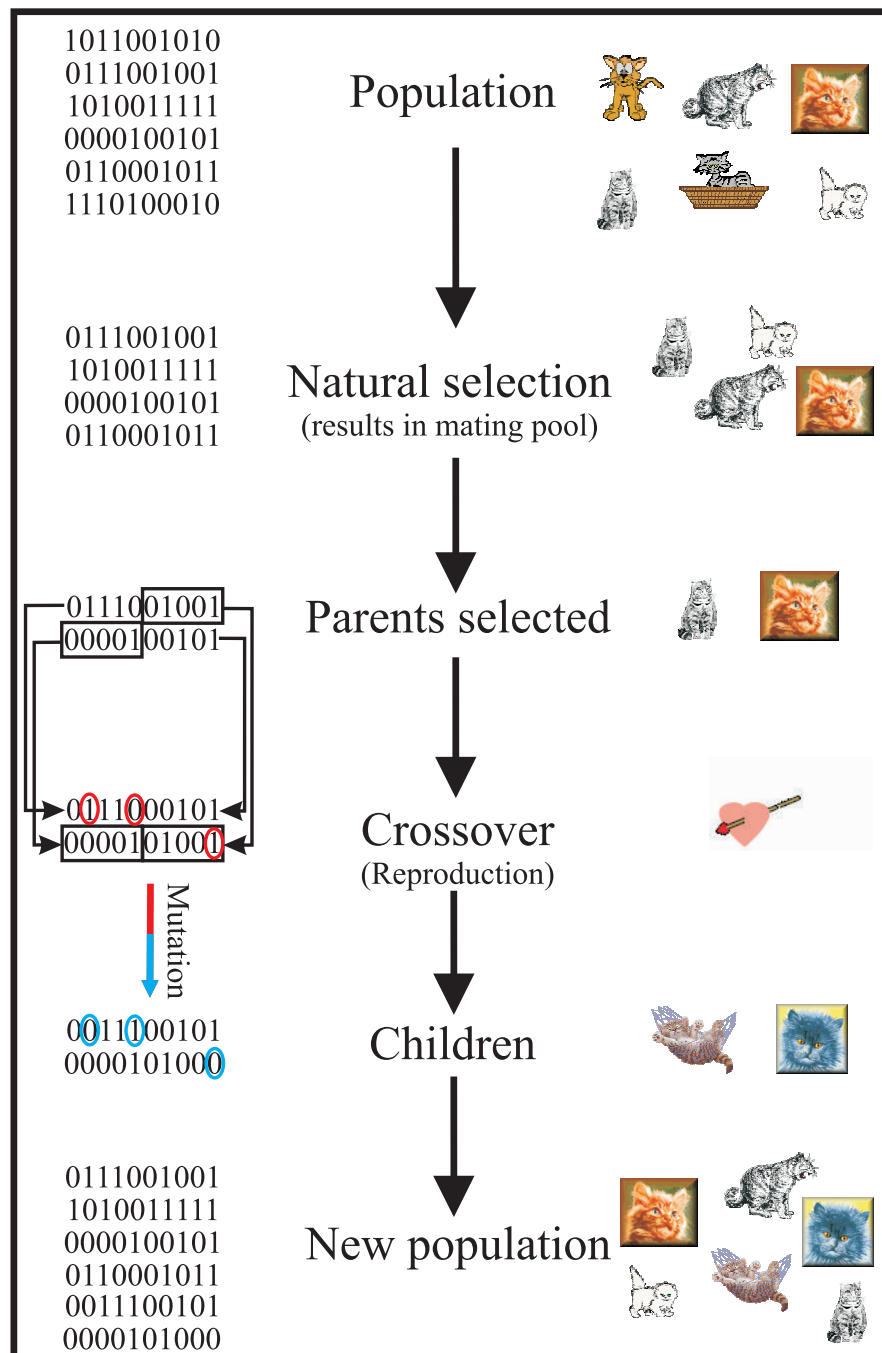
Figure 5.1: Schematic illustration of the mode of operation of the binary GA and analogy between a binary GA (left) and biological genetics (right). In this example, each population consists of six individuals. The four best of these are allowed to mate, whereas the two worst die off. Two parents are chosen, then crossover and mutation are performed, resulting in two children. In this example, the two parents also proceed unchanged to the next generation, as they represent individuals of high fitness.

Each of these steps is treated separately below. Figure 5.1 shows the different steps during the creation of a new population and the analogy between a numerical GA and biological optimization. Natural selection is performed (in this simple example, each population consists of six chromosomes, four of which may reproduce) and two parents are randomly chosen from the mating pool. Crossover and mutation result in two children. The new population contains these children and, in this case, the parents as well. Keeping the fittest parents from generation to generation is called *elitism*.

Once an initial population is created and evaluated, it is time to decide which chromosomes are fit enough to survive and, possibly, replicate themselves in the next generation.

Natural Selection and Elitism

Let the number of chromsomes (i.e. individuals) in the initial population be N_{init}. As a first step towards selection, the chromosomes are ordered from lowest to highest cost (or highest to lowest fitness). Only the $N_{pop} \leq N_{init}$ fittest individuals are allowed to mate and the population size for the rest of the iterations of the algorithm is N_{pop}. The larger initial population ensures a thorough sampling of the parameter space, which is an important condition for the GA to be able to find the global minimum. The process of natural selection may either be repeated after each iteration, choosing the fittest $N_{selected}$ chromosomes to mate, or executed only after the initial population.

In practice, it is difficult to say what fraction of the population shall be deemed fit enough to replicate. If only few chromosomes may reproduce, the diversity of the population will rapidly decrease and the algorithm may get stuck in a local minimum. If, on the other hand, the selection is not tough enough, the convergence is slowed down considerably. Following Haupt and Haupt (1998), it is rather common to keep half of the chromosomes in the mating pool.

In most algorithms, two parents produce two offspring, as we will see in the next subsection. Thus, if the mating pool does not include all individuals in the population (i.e. $N_{selected} \leq N_{pop}$), population size would decrease unless some of the chromosomes pass unchanged in the next generation. Usually, after the reproduction step, which leads to $N_{selected}$ children, the remaining $N_{pop} - N_{selected}$ are filled with the fittest chromosomes from the earlier generation. This is the above-mentioned elitism. If the population diversity shall remain high, one may also fill these positions with randomly chosen individuals, thus increasing the chance of survival of less fit chromosomes.

Mating and Crossover

After the mating pool has been chosen, it is time to pass to the reproduction step. In simple words, the general idea is that the fittest chromosomes shall share their genome hoping for improved offspring with even better fitness. This is the same principle followed by breeders who wish to breed animals or plants with certain properties. During many generations of mixing the genome of individuals who show the desired features to a certain extent, these properties are continuously enhanced and the diversity is reduced.

Returning to the binary GA, we first choose a defined number of parents, which pair in some random fashion. In most applications, two parents produce two offspring that contain the genetic (in terms of bits) traits of their parents. If elitism is desired and the parents belong to the chromosomes of highest fitness, they will, in addition to their children, proceed unchanged to the next generation. There are

Single-point crossover

Two-point crossover
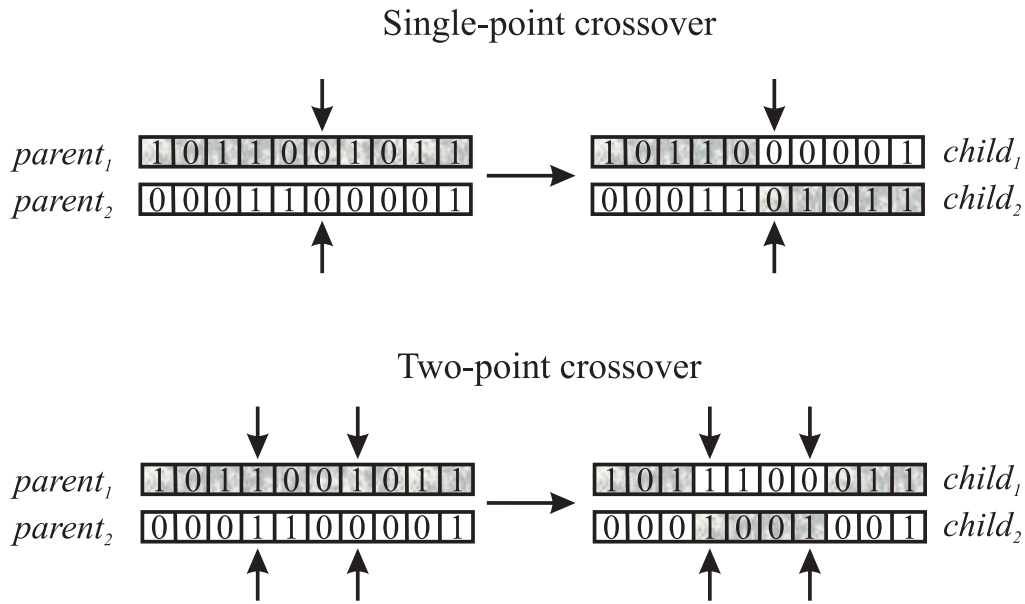
Figure 5.2: Single-and two-point crossover schemes. The vertical arrows mark the crossover points.

numerous ways to pair the chromosomes, but I will restrict the discussion on the fundamental ones. These are *single-point crossover* and *two-point crossover*.

A crossover is performed with a certain probability, which is called hereinafter the probability of crossover P_c. Typical values for P_c range from 0.6 to 1. If crossover is rejected, the two parents either proceed unchanged into the next generation or are rejected, depending on the programmer's wish. An example for single-point and two-point crossover is shown in Figure 5.2. For single-point crossover, one crossover point is randomly chosen between the first and last bit. $parent_1$ passes its binary code to the left of this crossover point to $child_1$ and $parent_2$ its binary code to the right of this point to $child_1$. $child_2$ is generated in the same way, such that $parent_2$ passes its binary code to the left of this crossover point to $child_2$ and $parent_1$ its binary code to the right of the crossover point to $child_2$. Two-point crossover works in a very similar way. The only difference is that instead of one, two crossover points are chosen and the bitstring inbetween these points is swapped (see Figure 5.2). Two-point crossover shows a consistently better performance than single-point crossover, especially when the binary representation is rather long (Haupt and Haupt, 1998). Therefore, I will use this crossover scheme in the algorithm described in Section 5.3. Other crossover techniques may e.g. involve three parents and two crossover points. With this combination, it is possible to create up to 18 children. There is no conclusive rule on how to perform the crossover operation, and the only limiting condition in inventing such operators is that it should be able to pass on desirable traits from one generation to the next.

The choice of the parents that shall undergo the crossover is another important feature in a GA. Usually, the chromosomes in a given population are weighted following their fitness and the choice of the chromosomes that replicate themselves is biased towards the fittest. This means that the fittest chromosomes from the mating pool undergo a crossover more often than less fit chromosomes. A random number then determines which chromosome is chosen. This technique is called *weighted roulette wheel*. The weighting problem will be discussed in more detail in Section 5.3.

```
┌─────────────────────────┐
│      Parameterization    │
│    Define cost function  │
└─────────────────────────┘
            │
            ▼
┌─────────────────────────┐
│     Encode parameters    │
└─────────────────────────┘
            │
            ▼
┌─────────────────────────┐
│     Create population     │
└─────────────────────────┘
            │
            ▼
┌─────────────────────────┐
│      Evaluate cost        │
└─────────────────────────┘
            │
            ▼
┌─────────────────────────┐
│       Select pairs        │
│        to mate            │
└─────────────────────────┘
            │
            ▼
┌─────────────────────────┐
│   Reproduce/Crossover     │
└─────────────────────────┘
            │
            ▼
┌─────────────────────────┐
│        Mutate             │
└─────────────────────────┘
            │
            ▼
┌─────────────────────────┐
│ Check stopping criterion  │
└─────────────────────────┘
            │
            ▼
┌─────────────────────────┐
│         Stop              │
└─────────────────────────┘
```
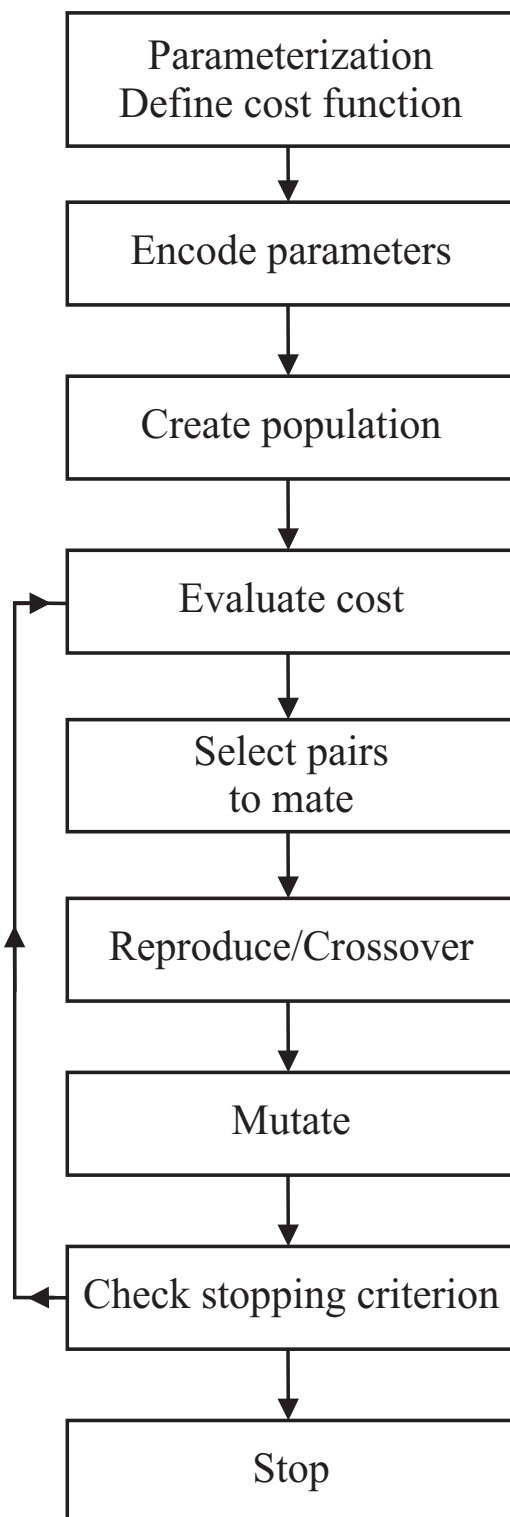
Figure 5.3: Flowchart of a typical genetic algorithm.

Mutation

Mutation, in contrast to crossover, is designed to increase the diversity of the population and hence opposes to the convergence of the GA. The step of mutation is not absolutely necessary and a GA may perfectly find the optimal solution without mutations. However, experience has proven that the mutation operator is indeed useful. After crossover, a randomly chosen small percentage of the offspring's bits are subjected to mutations. If a specific bit is chosen to be mutated, it is either changed from 0 to 1 or vice-versa (see also Figure 5.1). Thus, the mutation operator leads to random jumps within the parameter space, which helps to further explore areas which have not been visited before. The main purpose of this process is to avoid the convergence of the algorithm into a local minimum. Mutation enables the GA to randomly jump out of the actual minimum it is converging into and check whether an even deeper minimum in the cost surface might exist. Under this point of view, the mutation operator is an important part of the GA. The probability of mutation, hereinafter P_m, defines the number of bits that are mutated. In general, mutation rates of $P_m = 0.01 - 0.1$ work well. If the mutation rate is too high, too much desirable information gained through the crossover operator is destroyed and the algorithm may not converge properly anymore.

To finalize this section, the flowchart of a typical GA is depicted in Figure 5.3. The stopping criterion mentioned in this figure may be defined in different ways. The simplest variant is to stop the algorithm after a fixed number of iterations. Another way of deciding when to stop is to perform a statistical analysis after each generation in order to see whether there has been an improvement in the solution. If not, the algorithm is stopped. However, it is not uncommon that a GA does not show any improvement of the solution during a large number of iterations and then, either through lucky crossover or mutation, jumps into a lower minimum.

One rather unsatisfactory feature of GAs is the fact that they have to be tuned in view of the problem to be solved. This tuning includes a certain degree of subjective and problem-dependent decisions for which a general rule is difficult to provide. The optimal values for parameters such as population size, search ranges, crossover and mutation rates, mating

and crossover scheme, etc. are usually a bit different for each problem and their choice may seem somewhat arbitrary. Yet, GAs have proven their enormous power and utility in many applications, especially in the case of large parameter spaces and complicated cost surfaces, where Monte Carlo (random search) or direct inversion methods often fail.

5.2 The Question of Convergence

The most important issue in such a minimum-seeking algorithm is the question of convergence. A first point which must be emphasized at this stage is the fact that there is no mathematical proof of convergence for GAs and no guarantee can be given that the global minimum is indeed found. This is the reason why several researchers use GAs which shall find a set of good solutions rather than 'the optimum solution' (e.g. Lomax and Snieder, 1994; Scherbaum et al., 2006). The algorithm used in this thesis has also been designed in that direction. Before however addressing the exact algorithm, some theoretical aspects will be outlined in this section.

Although no strict mathematical proof of convergence exists, Holland (1975) introduced a theorem which explains the convergence, called the *schema theorem*. A schema is a bitstring consisting of 1's and 0's and wildcards $*$ which mark open spaces that may be filled either with a 1 or a 0. An example would be the schema $H = 1 * 10 * *$. Thorough discussions can be found in Goldberg (1989), Coley (1999) or Haupt and Haupt (1998), who phrase the theorem like this:

> Short schemata with better than average costs occur exponentially more frequently in the next generation. Schemata with costs worse than average occur less frequently in the next generation.

Two important parameters characterize a schema. The *order o* is defined by the number of fixed string positions, i.e. the schema H given above has the order $o(H) = 3$. The *defining length δ* is given by the distance of the first and last fixed string position, such that for our example $\delta(H) = 3$. Without going through the details of the derivation (see e.g. Goldberg, 1989), a mathematical expression for the schema theorem can be given in the form:

$$m(H, t + 1) \geq m(H, t)\frac{f(H)}{\bar{f}}\left[1 - P_c\frac{\delta(H)}{l - 1} - o(H)P_m\right]. \tag{5.2}$$

Herein, $m(H, t)$ is the number of occurrences of schema H within the population $\mathbf{P}(t)$ at a given timestep t. $f(H)$ represents the average fitness of the chromosomes representing the schema H at time t and $\bar{f}$ denotes the average fitness of the entire population. P_c and P_m are the probability of crossover and mutation, respectively. Finally, $l - 1$ is the number of possible crossover points within a given bitstring of length l. Equation 5.2 means that the number of individuals that represent schemata of low order and short defining length of above-average fitness grows exponentially from generation to generation. If $f(H)$ is expressed as $f(H) = (1 + c)\bar{f}$, with c being a positive constant, and we start at $t = 0$, the following proportionality arises:

$$m(H, t) \propto m(H, 0)(1 + c)^t.$$

In summary, a genetic algorithm converges to solutions which represent low-order, short schemata with above-average fitness. Note however that, strictly speaking, the convergence of continuous parameter GAs cannot be explained with the shema theorem, as they are not encoded in a way where such schemata emerge. Remarkably, their applications clearly show that they nevertheless work as well as their binary counterparts.

5.3   The Algorithm Used in this Thesis

Now that the most important thoughts and concepts about genetic algorithms have been addressed, I will describe in more detail the algorithm designed to solve the earthquake source inverse problems in Chapter 6. GAs get increasingly popular in the geophysical community and a large list of publications exists (some examples are Miyake et al., 2003; Lomax and Snieder, 1994; Sambridge and Drijkoningen, 1992; Scherbaum et al., 2006). Up to this point, GAs were discussed as a means of finding the optimum solution to a given problem. Yet, geophysical inverse problems may have several (or even numerous) distinct solutions of equivalent quality (i.e. of comparable cost). Mostly, GAs are configured for fast convergence and may consequently end up in a local rather than in the global minimum, especially if the cost surface displays several minima of similar depth. Such a *premature convergence* should be avoided by all means. It is therefore important to carefully balance the convergent and divergent features treated in the previous sections. Moreover, several runs of the algorithm with different initial populations should always be performed in order to check the stability and get a better idea of the solution space. For instance, a tough natural selection and strong elitism result in highly convergent tendencies, whereas a high mutation rate increases the divergence.

I decided to use a binary encoded GA, with a resolution of two digits after the decimal point for distance in km and two digits for time in s. To ensure a good initial sampling of the parameter space, the initial population is chosen to be larger than the subsequent populations. Natural selection is performed only following the first iteration of the algorithm, where the fittest two-third of the chromosomes are allowed to mate. For instance, the initial population is composed in most cases of 150 individuals, and after their evaluation, the population size is reduced to 100 for the rest of the run. This way, the cost surface is densely sampled right at the beginning and the algorithm concentrates on the most promising regions during the remaining generations. However, this does not mean that only these regions are walked through after the first generation. There is also a continuous sampling of new areas on the cost surface, primarily due to the mutation operator.

As I would like to find a set of acceptable solutions rather than one best solution, only a very weak form of elitism is implemented. The best 2% of the chromosomes pass unchanged to the next generation, and the fittest 98% of the individuals form the mating pool. Hence, the population diversity reduces only very slowly. The crossover probability and the mutation probability can be used to influence the convergence speed as well. I use rather low values, namely $P_c = 0.6 - 0.7$ and $P_m = 0.03 - 0.05$. The two-point and uniform crossover operators are implemented in the algorithm. For the inversions presented in Chapter 6, the binary representation leads to rather short bitstrings for which two-point crossover is an adequate crossover scheme.

Another decisive feature of a GA is the weighting scheme utilized in the selection of the parents from the mating pool. As mentioned earlier, the primarily used schemes are cost weighting and rank weighting. In the cost weighting scheme, the chromosomes are simply weighted following the value of their cost. Rank weighting, on the other hand, weights the chromosomes relative to each other, thus only deciding that a given chromosome is fitter than an other one, but not how much fitter it is. The principle of rank weighting is very easy. After each generation, the chromosomes are ordered from highest to lowest fitness. Their ranks are simply given by their positions in the list. The i-th chromosome is assigned the following probability to be chosen:

$$P_i = \frac{N_{selected} - i + 1}{\sum_{i=1}^{N_{selected}} i}.$$

The sum of these probabilities is, as required, 1. The cumulative probability $\sum_{j=1}^{i} P_j$ is calculated for each i-th chromosome and a random number in the interval [0, 1] is drawn from a uniform distribution. Starting from the top of the list, the first chromosome with a cumulative probability larger than the random number is chosen to be paired.

Rank weighting is used in this work, as cost weighting may put too much emphasis on some specific chromosome. Somewhen during the run, an individual with much lower cost than the rest may suddenly appear. If pure cost weighting is used, this individual is excessively weighted and the algorithm may converge into the local minimum defined by this extraordinary fit chromosome simply because the other chromosomes are not pairing often enough to contribute their genome to the next generations. Rank weighting, on the other hand, still causes the desired bias towards the fittest chromosomes, but gives the less fit individuals a chance. This results in a larger diversity in the population and thus a better sampling of the search space. An alternative to rank weighting would be scaling the fitness before choosing the parents such that excessive differences in the fitness are reduced (Sambridge and Drijkoningen, 1992).

An additional feature that is implemented is that the best individuals found during each run of the algorithm are stored in a separate array. This helps to examine the diversity of the lowest cost solutions and to get an overview over the acceptable solution space. Further details as well the cost functions utilized will be given in the respective sections to come. Especially the definition of the cost function plays the most important role, as it represents the property that shall be optimized. For instance, an unsuitable crossover scheme or population size may reduce the performance of the algorithm, but it does not change the solution that shall be retrieved, even though it may take more generations or several runs to find it. In contrast, an unsuitable cost function has a much more fundamental impact, as it modifies the definition of what is a 'fit' chromosome.

In order to check whether the developed algorithm works properly, several validation runs have been performed. A given set of parameters was used to synthesize strong motion simulations using the empirical Green's functions method of Irikura as presented in Chapter 4.1. The GA was then used to retrieve the known parameters. Two examples of these validation runs are discussed in more detail in Appendix A.

Chapter 6

Earthquake Source Inversion using Empirical Green's Functions

In this Chapter, I will use the empirical Green's functions method of Irikura (1983, 1986, 1999), which is described in Chapter 4.1, in combination with the genetic algorithm introduced in Chapter 5.3, to derive suitable models for the strong motion generation areas (SMGA) of four intermediate-depth Vrancea earthquakes. Two of these are of moderate size and occurred in recent years (October 27th, 2004 – M_W = 5.8 and May 14th, 2005 – M_W = 5.2). The other two discussed events are the large earthquakes which occurred on March 4th, 1977 (M_W = 7.4) and on August 30th, 1986 (M_W = 7.1). This is the first systematic source study of this type performed for Vrancea earthquakes, and the database used represents by far the largest high-quality strong motion database ever used to infer source properties of Vrancea earthquakes.

In a first step, I will give a short introduction to the seismicity and tectonics related to the Vrancea seismogenic zone (Section 6.1). Section 6.2 contains a description of the database used, followed by an analysis of the spectral ratios in order to determine the scaling factors needed for Irikura's technique (Section 6.3). The core of this study is the inversion procedure presented in Section 6.4. For the 2004, 2005 and 1986 earthquakes, it is based on waveforms, whereas for the 1977 event, due to a lack of appropriate waveform data, a novel approach is adopted, which is based on macroseismic intensities and provides encouraging results. Finally, the obtained source models and their physical meaning are discussed in Section 6.5, which concludes this Chapter.

6.1 Seismicity and Tectonics of SE-Romania

The Vrancea district, located in the South-Eastern part of the Carpathian arc, is affected by the occurrence of frequent and strong intermediate-depth earthquakes. The peculiarity regarding these earthquakes is the fact that they are all generated within a narrowly confined focal volume, whose epicentral area is limited to an extent of approximately 30×70 km^2. The depth range is limited to a vertical stripe ranging from around 80 to 200 km. Figure 6.1(a) shows the spatial distribution of the epicenters of Vrancea earthquakes. It is obvious to see that the epicenters are strongly clustered within a very small area. The observed focal mechanisms of Vrancea earthquakes (e.g. Oncescu and Bonjer, 1997; Radulian et al., 2000) as well as the results of a stress inversion by Plenefisch (1996) indicate a

(a) Seismicity

(b) Sketch of the present tectonic settings and geology
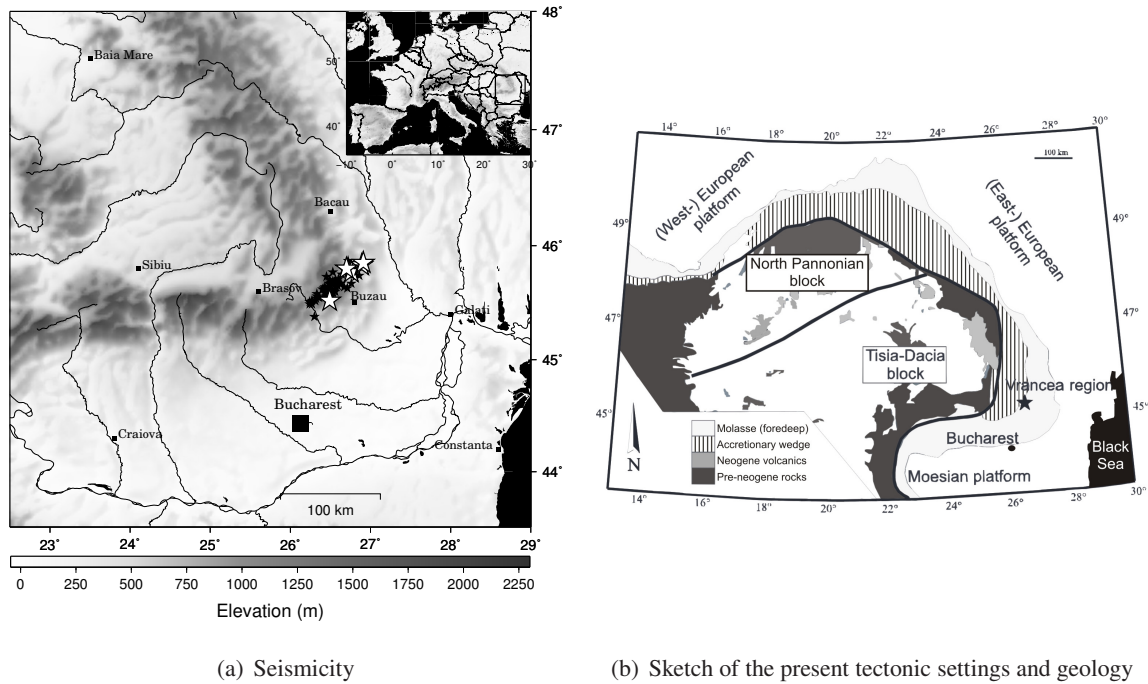
Figure 6.1: (a) Seismicity of the Vrancea Region. Displayed are all earthquakes with moment magnitudes larger than 4.0 and depth larger than 70 km during the time period 1997-2004 (small black stars) and the five large shocks (large white stars) that occurred in 1940, 1977, 1986 and 1990 (2 events, $M_W = 6.9$ and $M_W = 6.4$). (b) Sketch of the present tectonic settings and geology of the Vrancea region (simplified after Sperner et al., 2001). It is assumed that the subducting slab is at the last stage of its break-off beneath the Vrancea region (marked by a star), while it is completely detached along the rest of the Carpathian arc.

thrust regime with vertical extension and horizontal compression. Two types of fault mechanisms are observed. The prevalent type is characterized by a NE-SW striking fault plane and perpendicular maximum compression. All Vrancea events with $M_W \geq 7$ which occurred during the last century show this kind of mechanism. Fewer events have a NW-SE striking fault plane with maximum compression in the NE-SW direction.

The present tectonic setting of the Vrancea region is illustrated in Figure 6.1(b). It has been interpreted by Sperner et al. (2001) as the result of a previous subduction of oceanic lithosphere with subsequent soft continental collision and slab roll back. Continuous subduction occurred along the Alpine-Carpathian system, which was first terminated in the Alps by continent-continent collision during the Mid-Eocene, but continued in the embayment of the European continental margin in the East between Western Europe and the Moesian platform. At this time the embayment was occupied by oceanic lithosphere. During the Mid-Miocene the North-Pannonian- and the Tisia-Dacia-block migrated into this embayment due to a gradual slab retreat. The subduction process finally stopped due to the continent-continent collisions at the edges of the embayment, first at the northern and eventually at the southern rim, which forms the Vrancea region nowadays. Here the collision stopped about 8 Ma years ago. The Carpathian mountain range as well as the foredeep basins filled with molasses from the mountain arc formed as a result of the continent-continent collision.

The strong seismicity at intermediate-depth beneath Vrancea is associated with a subducted and partially detached slab. The break-off of the subducted lithosphere presumably started first in the North and continued progressively towards the South and South-East. The Vrancea earthquakes are then interpreted as events within a not yet completely detached slab segment, in a vertical position. This interpretation is compatible with the observed thrust fault mechanisms and is strongly supported by a recent regional tomography study by Martin et al. (2006), which images the slab and shows clear indications that the seismicity is confined to the slab. Wenzel et al. (1999) show that the seismic energy release rate of the Vrancea seismogenic zone is the fourth highest in Europe and comparable to the one of Southern California. Four major shocks with moment magnitudes larger than 6.5 occurred during the last century, namely on November 10, 1940 (M_W = 7.7), March 4, 1977 (M_W = 7.4), August 30, 1986 (M_W = 7.1) and May 30, 1990 (M_W = 6.9). Especially the former two led to disastrous consequences on Romanian territory. The 1977 earthquake caused large damages to the city of Bucharest, where 1570 people were killed and 11300 injured (Cioflan et al., 2004). The Bucharest metropolitan area was affected by seismic intensities of VIII and VII during the 1977 and 1986 earthquakes, respectively.

6.2 Analyzed Earthquakes and Database

All the records from the small earthquakes used as EGF events as well as from the two considered mainshocks which occurred in 2004 and 2005 (the two moderate ones) were gathered by the accelerometer network installed by the Collaborative Research Center 461 (CRC 461) 'Strong Earthquakes: A Challenge for Geosciences and Civil Engineering' of the University of Karlsruhe in cooperation with the National Institute of Earth Physics (NIEP) in Bucharest. The network (Bonjer and Grecu, 2004) is operative since 1997 and consists of 44 digital Kinemetrics K2 instruments, mostly located in free-field conditions. The recordings from the 1986 earthquake as well as from the 1977 event (one recording only) are analogue observations from an SMA-1 network operated by NIEP (Oncescu et al., 1999a) which have been digitized. The database from each earthquake is treated separately further below.

In total, acceleration data from six EGF events ($4.0 \leq M_W \leq 5.0$) are used to model the 1986, 2004 and 2005 TARGET earthquakes. The 2004 event is itself used as EGF in order to simulate the 1977 TARGET earthquake. The hypocentral coordinates, origin times and depth information of the EGF earthquakes as well as of the TARGET events is listed in Table 6.1. The October 2004 earthquake is referred to as TARGET-A, the August 1986 event as TARGET-B, the 1977 one as TARGET-C and, finally, the May 2005 earthquake as TARGET-D. The EGF earthquakes were chosen following the conditions that the focal mechanisms should be as similar as possible to the one of the TARGET and they should be located at approximately the same depth.

Figure 6.2 shows the epicenters and the locations of the stations used in this study. Additionally, the focal mechanisms of all earthquakes are displayed. Each analyzed TARGET earthquake is marked by a large star, and the focal mechanisms of the EGF event(s) associated with it are lined up in a column with the TARGET's focal mechanism. The fault plane solutions of the main shocks are taken from the Harvard CMT catalogue, whereas those of the EGF earthquakes are from the ROMPLUS catalogue (Oncescu et al., 1999b). The data recorded from the K2-network have been sampled with 200 samples/s, whereas the analogue SMA-1 recordings were digitized with a sampling rate of 100 samples/s. As a part of the digitization process, the SMA-1 recordings have been Ormsby filtered (for most stations between 0.125-24 Hz, but for some, as e.g. CFR, only between 0.125-15 Hz). Thus, in
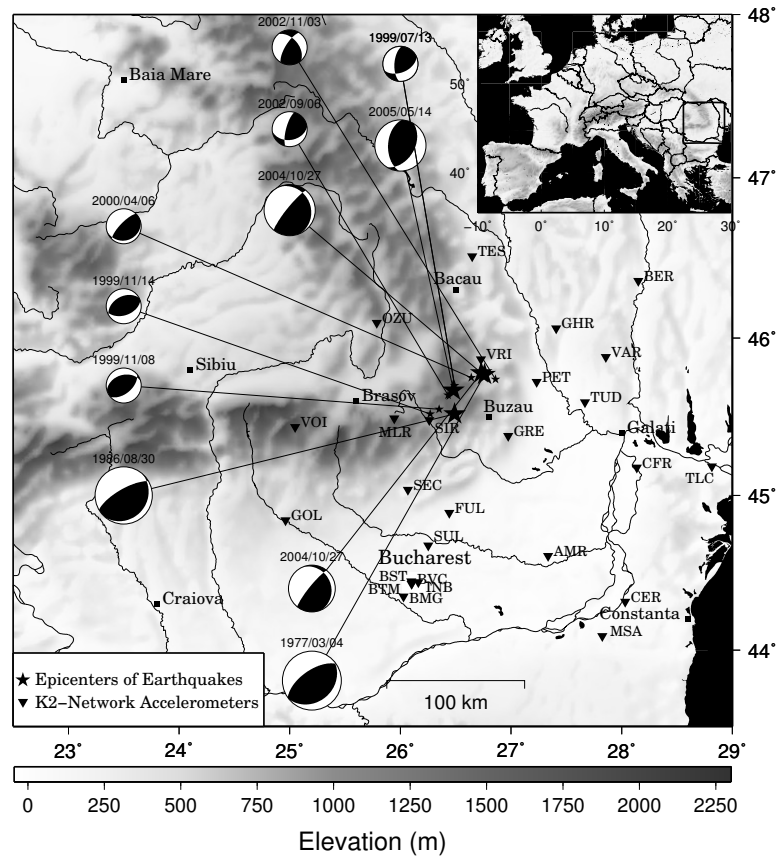
Figure 6.2: Topographic map of the Carpathian area. The epicenters of the earthquakes utilized in this study are depicted by stars (large stars: TARGET events) and the corresponding focal mechanisms are shown. The focal mechanisms of the EGF-events are lined up in columns with respect to their associated main shock. The K2- and SMA1-accelerometers which provided data from at least one EGF- and the corresponding TARGET-event are marked by inverse triangles.

view of the frequency constraints imposed by the digitization process, any analysis performed with the SMA-1 data is restricted to frequencies lower than 12-15 Hz. In order to create a consistent database, the digital K2-recordings are downsampled to a sampling frequency of 100 Hz.

Only the horizontal components of the S-wave are used, as the strongest part of the shaking is usually found there. The data are rotated and, for the inversions, I finally use 15s SH-wave signal windows that start 2 s before the S-wave onset, the latter one being picked on the velocity traces. A key point in using small earthquakes as EGFs to simulate larger ones is their signal-to-noise (SN) ratio, as only a frequency range with acceptable SN-ratio should be used in order to avoid scaling up noise instead of signal energy. An example for the evaluation of the SN-ratio of the EGF earthquake recordings is shown in Figure 6.3, where 10 s signal and noise windows have been used. The first and last 5% of the time series are tapered with a cosine window and the FAS of the records are smoothed with a 0.2 Hz wide moving average window. The SN-ratio of the K2-data is, as a rule, larger than two up to frequencies between 20-25 Hz, although the most relevant part of the signal energy is associated with frequencies smaller than about 12 Hz. Records with unclear S-wave onset or unacceptable SN-ratio are removed from the dataset. Regarding the SMA-1 digitized data, no SN-ratio analysis is feasible, as these records do not include any relevant pre-event noise.

Event ID	Date	Origin Time	Latitude [°]	Longitude [°]	Depth	M_W
EGF-A200209	2002/09/06	05:04:02	45.64	26.43	105	4.1
EGF-A200211	2002/11/03	20:30:23	45.74	26.86	90	4.0
EGF-B19991108	1999/11/08	19:22:52	45.55	26.35	138	4.6
EGF-B19991114	1999/11/14	09:05:59	45.52	26.27	132	4.6
EGF-B200004	2000/04/06	00:10:39	45.75	26.64	143	5.0
EGF-C200410	2004/10/27	20:34:36	45.78	26.73	99	5.8
EGF-D199907	1999/07/13	13:10:58	45.70	26.49	132	4.0
TARGET-A	2004/10/27	20:34:36	45.78	26.73	99	5.8
TARGET-B	1986/08/30	21:28:37	45.52	26.49	132	7.1
TARGET-C	1977/03/04	19:21:54	45.77	26.76	94	7.4
TARGET-D	2005/05/14	01:53:21	45.68	26.54	140	5.2

Table 6.1: Hypocentral coordinates, moment magnitudes and origin times of the events used in this study. The small earthquakes used to generate the synthetics are characterized by the identification code EGF whereas the respective mainshock is referenced as TARGET. The information shown in this table was gathered from the ROMPLUS (Oncescu et al., 1999b) and the Harvard CMT catalogues.
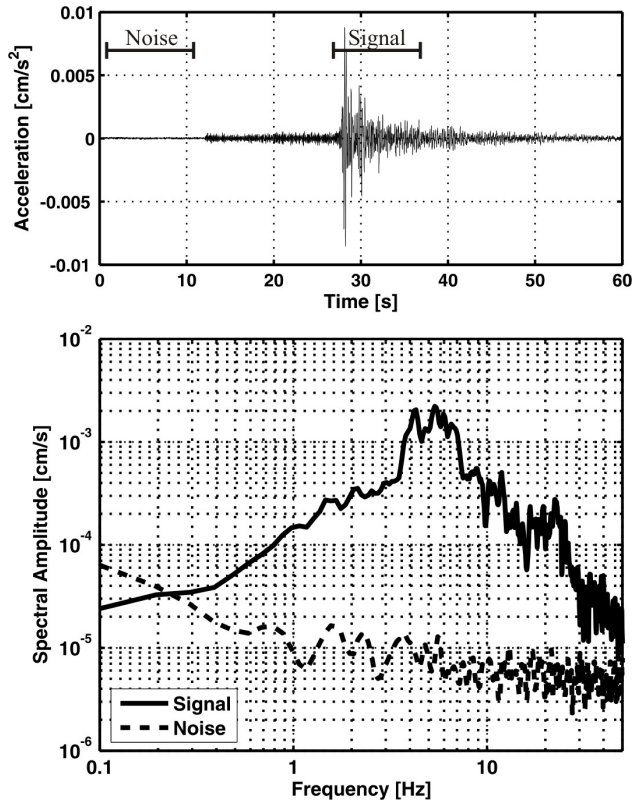
Figure 6.3: Example for the evaluation of the signal-to-noise ratio. The signal shown is the transverse component at station BER from EGF-A200211. Top: acceleration time series, where the respective signal and noise windows are indicated. Bottom: FAS of signal and noise windows.

The October 2004 Earthquake – TARGET-A

This is the event with by far the most extensive database treated in this work. Two EGF earthquakes are used, and a total of 22 recordings (12 from EGF-A200209 and 10 from EGF-A200211) at 14 stations are included in the inversion. The frequency range considered in the spectral scaling analysis is 0.5-20 Hz and, as the largest part of the signal energy is contained in the frequency band lower than approximately 12 Hz, the frequency range of the inversion is 0.5-12 Hz. Using up to 20 Hz in the determination of the spectral scaling factors helps to better constrain the high-frequency plateau, as we will see further below.

The August 1986 Earthquake – TARGET-B

For this earthquake, the database available for the study with empirical Green's functions is rather sparse. This due to the fact that most K2-accelerometers are not located at the same positions than were

the analogue SMA-1 instruments. Therefore, only six stations could be included in the spectral scaling analysis and inversion process. This sparcity of data seems to reflect in the ambiguous results for this earthquake, as discussed later in this Chapter. As a bit larger EGF earthquakes are being used here ($M_W \geq 4.5$), the frequency range which can be used for the inversion, namely 0.4-12 Hz, is a bit wider to lower frequencies. The same frequency range is used for the spectral scaling analysis. Three appropriate EGF earthquakes were selected and 14 recordings are used (5 from EGF-B19991108, 5 from EGF-B19991114 and 4 from EGF-B200004).

The March 1977 Earthquake – TARGET-C

Here, only one single SMA-1 strong motion recording at station Incerc, located in the city of Bucharest, exists. The best digitization of this recording has been performed at the Building Research Institute of the Ministry of Construction in Japan. A peculiar feature of this observation is that the EW-component depicts a strikingly different frequency content than the NS-component, the latter one being dominated by a strong peak at about 0.5 Hz. With regard to this fact, the NS-component is not used in this work. In any case, neither a representative spectral scaling analysis nor an inversion for the SMGA parameters would be sensible using one single record.

Therefore, I adopt a different approach to this problem. As, in contrast to waveform data, enough macroseismic information of the 1977 earthquake is available (Radu et al., 1979), I use the methodology of Sokolov (2002) to estimate instrumental intensities from the simulated recordings and minimize the residuals between simulated and observed intensity. The available record at station Incerc in then used to check whether or not it can be explained with the SMGA model inverted from the macroseismic intensity distribution. As EGF earthquake, the October 2004 earthquake (TARGET-A and EGF-C200410) is very well suited, especially as it has been recorded at more than 30 stations. Intensities at 33 locations are estimated for the inversion of TARGET-C's SMGA parameters. The frequency range utilized is 0.2-12 Hz.

The May 2005 Earthquake – TARGET-D

For this TARGET event, only one EGF earthquake fulfilling the necessary criteria was found in the database, and six records are utilized in the inversion. For the spectral ratio analysis, stations TUD and SUL are not considered, as their spectral ratios show some peculiar features in the intermediate-frequency range which lead to problems in correctly fitting the low and high frequency plateaus with the theoretical function. As it is more important to correctly catch the plateaus, these two stations are not used to evaluate C and N. Identically to TARGET-A, the frequency range for the spectral ratio analysis is 0.5-20 Hz and 0.5-12 Hz during the inversion.

6.3   Spectral Analysis and Scaling Factor Determination

As discussed in Chapter 4.1, in order to get realistic simulations and sensible inversion results, it is highly important to estimate the correct scaling factors C (stress drop ratio) and N (number of subfaults along strike and dip). One could of course invert for these two parameters too, but it is preferable, if possible, to estimate them from another source so that the number of free parameters during the inversion is kept the lowest possible.

The procedure to compute these two parameters, based on the spectral ratios between TARGET and EGF earthquakes, has been presented in Chapter 4.1. A theoretical spectral ratio of the form (4.21) is fitted to the logarithmic average of the observed ones. To do so, the FAS of the TARGET record and

Event ID	$\frac{M_0}{m_0}$	$f_{c,T}$ [Hz]	$f_{c,E}$ [Hz]	N	C	Number of stations
TARGET-A/EGF-A200209	211	1.7	8.3	5	1.7	12
TARGET-A/EGF-A200211	651	1.6	10.8	7	1.9	10
TARGET-B/EGF-B19991108	8144	0.3	4.0	16	2.0	5
TARGET-B/EGF-B19991114	7134	0.3	4.9	17	1.5	5
TARGET-B/EGF-B200004	914	0.3	3.1	11	0.7	4
TARGET-D/EGF-D199907	57	1.1	3.4	3	2.1	4

Table 6.2: Ratio of seismic moments M_0/m_0, corner frequencies ($f_{c,T}$ for TARGET-event, $f_{c,E}$ for EGF-event) and scaling factors (N and stress drop ratio C) computed from the spectral ratios shown in Figures 6.4 (TARGET-A), 6.5 (TARGET-B) and 6.6 (TARGET-D)

the corresponding EGF recording and their spectral ratio are determined at each station. In order to smooth instabilites in the spectra, the log frequency axis is divided into a certain number of frequency bins (I use 20 bins) within the frequency range of interest (0.5-20 Hz for TARGET-A and TARGET-D, 0.4-12 Hz for TARGET-B).
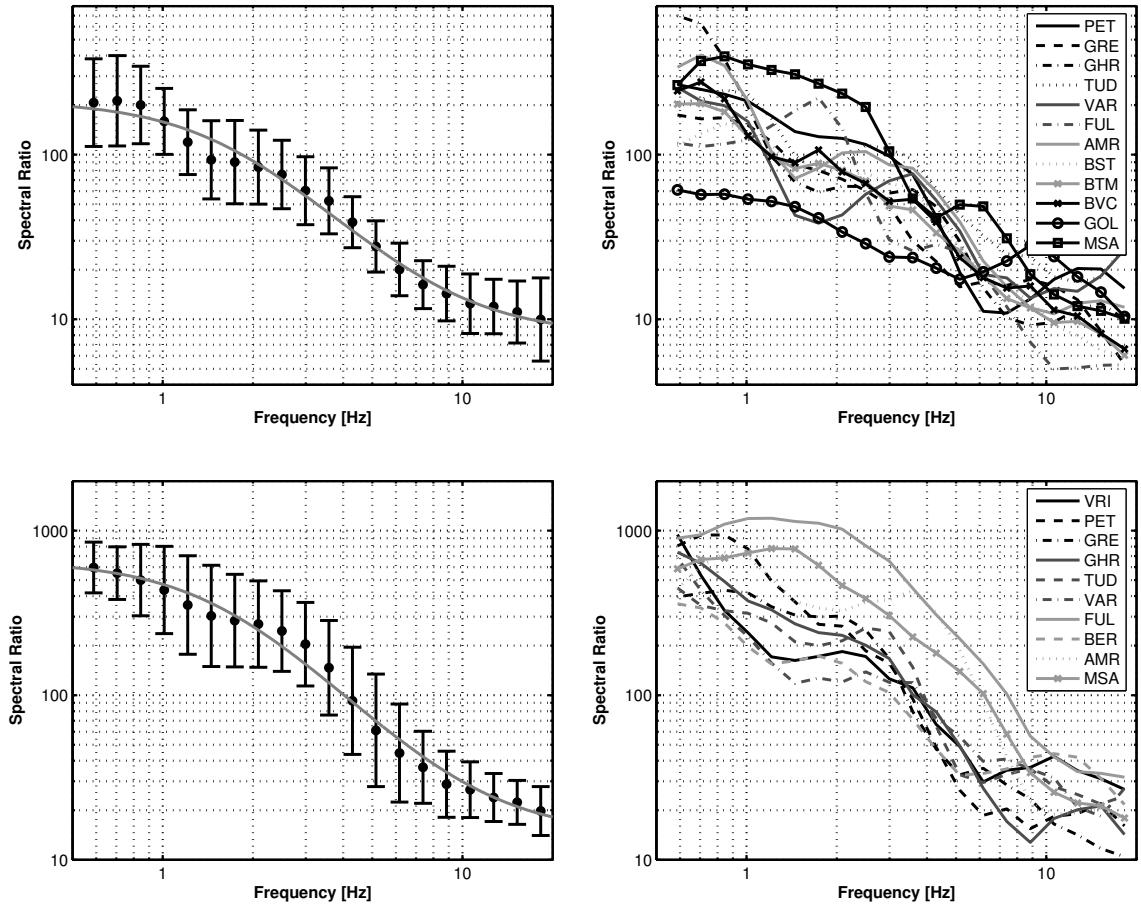
Figure 6.4: Spectral ratios between TARGET-A and EGF-A200209 (upper row) and EGF-A200211 (bottom row). Left column: Average values with standard deviations and best fitting theoretical function as given in Table 6.2. Right column: Spectral ratios for all considered sites.

For each bin, the logarithmic average of the frequency points within this bin is computed for each spectral ratio function and assigned to the bin's central frequency. Finally, the logarithmic average and standard deviations for all the spectral ratios within each frequency bin are obtained. A theoretical spectral ratio function is then fitted to the observation by searching the minimum of the weighted (each frequency bin is weighted according to its standard deviation) least squares. This way, the ratio of the seismic moments M_0/m_0 and the corner frequencies $f_{c,T}$ and $f_{c,E}$ are computed. N and C are then estimated from (4.24) and (4.25).

The results of this procedure are listed in Table 6.2 and graphically displayed in Figures 6.4 (TARGET-A), 6.5 (TARGET-B) and 6.6 (TARGET-D). The first striking feature which should be noted are the very high corner frequency values as well for TARGET-A (around 1.6 Hz, practically identically determined with both EGF earthquakes) as for its EGF events. Regarding TARGET-B, a few problematic aspects require further discussion. First of all, the database is rather sparse compared to the one of TARGET-A (this is also valid for TARGET-D). Yet, the more relevant problem resides in the fact that the corner frequency for TARGET-B is lower than the lowest frequency analyzed (which is 0.4 Hz, due to the SN-ratio constraints). This is a general problem of this methodology if very large earthquakes are considered. A a result, it is rather difficult, if not impossible, to firmly constrain the low-frequency plateau M_0/m_0 and corner frequency $f_{c,T}$ with this approach in the case of very large earthquakes.

Nevertheless, the obtained results for TARGET-B may be regarded to be plausible, as the corner frequency (around 0.3 Hz) is in good agreement with the value determined in an earlier study by Oncescu (1989) and the moment ratios between TARGET-B and its EGF earthquakes are close to the values that would be expected if the seismic moments were deduced from the moment magnitudes using the relation of Hanks and Kanamori (1979). Yet, these difficulties have to be kept in mind and are probably one of the reasons for the ambiguous inversion results presented in the following section.

Regarding TARGET-D, it is interesting to note that, even though its moment magnitude is smaller than the one of TARGET-A by approximately half a unit, its corner frequency is significantly lower. If one would try to anticipate at this point the results of the following inversions by looking at the spectral properties only, one would expect to find quite small SMGA's and short particle dislocation rise times (which is equivalent to high static and dynamic stress drops), as the corner frequencies are generally very high. Following their corner frequencies, TARGET-D is expected to show larger source dimensions than TARGET-A, even though it is a lower magnitude earthquake. Instead of performing the inversions below, it is of course possible to simply use a model such as the one of Brune (1970, 1971) or Madariaga (1976) and calculate the fault radius directly from the corner frequency. Yet, due to the ambiguities discussed in Chapter 3.2, it is not possible to seriously assess the quality of the source size determined this way.

As only one strong motion recording is available for TARGET-C, it is not possible to seriously evaluate the spectral ratio, as the latter can show a large variability from one station to another. This can be due for instance to directivity effects. As a result, C and N cannot be derived in the same way as for TARGET-A, -B and -D. In view of the results presented for these events, where C ranges between 0.7 and 2.1, setting the value of C to 1 is an acceptable assumption, which can even be verified after the inversion. As TARGET-A (respectively EGF-C200410) is used as EGF in the intensity inversion for TARGET-C, the subfault size resulting in the latter inversion should be in agreement with the SMGA size determined for TARGET-A. I will discuss this issue later in this chapter. If $C = 1$, N is simply the cube root of the moment ratio (the moments are computed from Hanks and Kanamori, 1979).
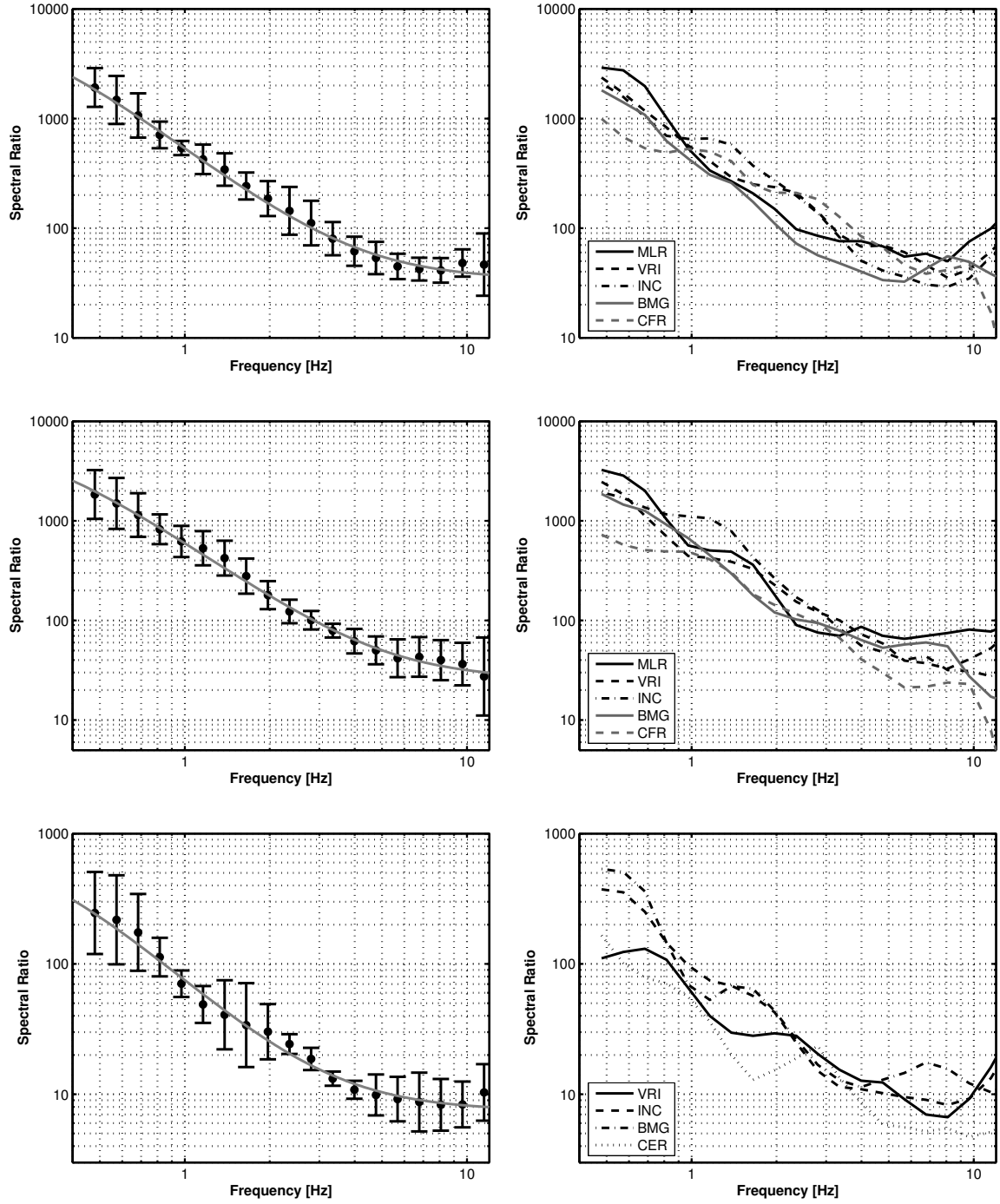
Figure 6.5: Spectral ratios between TARGET-B and EGF-B19991108 (upper row), EGF-B19991114 (middle row) and EGF-B200004 (bottom row). Left column: Average values with standard deviations and best fitting theoretical function as given in Table 6.2. Right column: Spectral ratios for all considered sites.
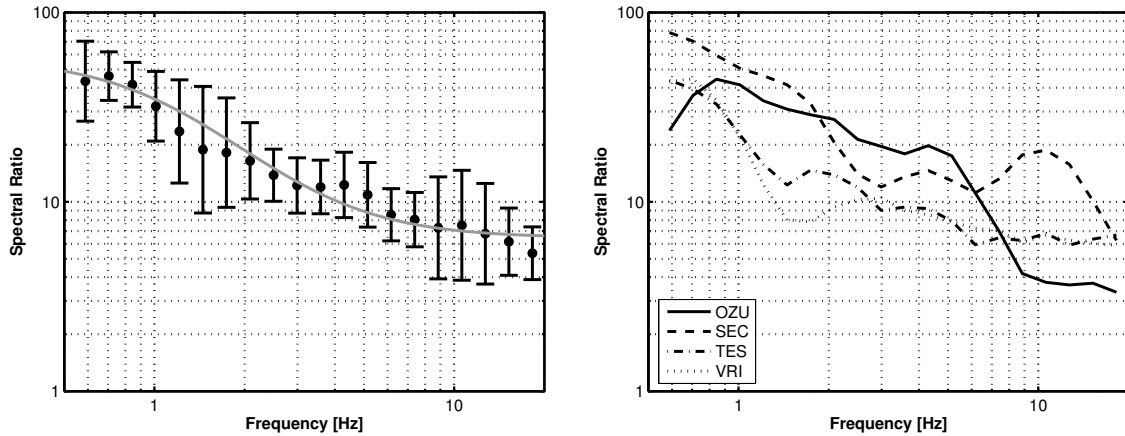
Figure 6.6: Spectral ratios between TARGET-D and EGF-D199907. Left column: Average values with standard deviations and best fitting theoretical function as given in Table 6.2. Right column: Spectral ratios for all considered sites.

6.4 Inversion Procedure and Results

The SMGA is characterized by seven parameters: Stress drop ratio C, scaling factor N, length L, width W, rise time T_r and rupture initiation point along strike and along dip. As C and N have already been determined, the number of free parameters is reduced to five (strictly speaking, the rupture and shear wave velocities would be additional parameters, which I regard as fixed, as otherwise the inversion results would be poorly constrained – different ratios of rupture to shear wave velocity are tested below). Thus, the problem which I wish to solve is a non-linear one depending on five controlling parameters. A good way to do so is to evaluate many different trial models regarding a certain criterion and to exploit for instance the evolutionary concept of the genetic algorithm (see Chapter 5) in order to find the minimum cost solutions for the SMGA source model of each TARGET earthquake.

First, I present the results from the inversion performed with TARGET-A, -B and -D, which are based on the recorded time histories. Using the fit between synthetic and observed time series is of course the usual and best criterion to invert for earthquake source properties. However, this cannot be done for TARGET-C, as there is no appropriate database of strong motion recordings from this TARGET. Therefore, I invert for the source parameters using macroseismic intensities (MSK scale). As I will show, this approach leads to highly satisfactory results and could be of high interest in order to derive fundamental source properties of large historical earthquakes.

6.4.1 Waveform Based Inversion

For the events TARGET-A, TARGET-B and TARGET-D, a waveform based inversion is performed. The initial population consists of 150 trial models, the 100 fittest of which are kept to run the algorithm over 200 generations. Further details of the algorithm are given in Chapter 5.3. The most important point when using such an algorithm is the definition of the cost function. Here, I use the L2 norm for acceleration envelopes and displacement waveforms (similarily defined e.g. by Suzuki et al., 2005;

Suzuki and Iwata, 2005b):

$$cost = \sum_{records} \left(\frac{\sum_t (u_{obs} - u_{syn})^2}{\sqrt{\sum_t u_{obs}^2 \sum_t u_{syn}^2}} + \frac{\sum_t (e_{obs} - e_{syn})^2}{\sqrt{\sum_t e_{obs}^2 \sum_t e_{syn}^2}} \right), \qquad (6.1)$$

where u_{obs} and e_{obs} denote the observed displacement waveform and acceleration envelope whereas u_{syn} and e_{syn} are the simulated ones and the acceleration envelope is computed from its Hilbert transform. This cost function is designed to evaluate both the fit at high frequencies (via the acceleration envelope) and low frequencies (via the displacement waveforms). Commonly, seismic sources are either modeled in view of high frequencies (generally with the stochastic technique for engineering applications or seismic hazard assessment) or low frequencies (if finite-fault rupture models are sought). This cost function enables to catch both the main high and low frequency characteristics. As mentioned in Section 6.2, the records are 15s long SH-wave traces starting 2 s before the S-wave onset. Therefore, it should be noted that with the above cost function, the *average* cost over the 15s window is minimized, thus optimizing the overall characteristics of the time histories rather than trying to reproduce each single wiggle. The latter idea is only reasonable for very long period waves (as used in global seismology e.g. to determine moment tensors of distant earthquakes) and would not lead to any success with the frequencies used in this study.

Acceleration, velocity and displacement waveforms are computed for each trial model using Irikura's summation scheme given by (4.15), (4.16) and (4.17). Velocity and displacement waveforms of EGF and TARGET earthquakes are obtained by integration and bandpass-filtering within the frequency range 0.5-12 Hz for TARGET-A and -D and 0.4-12 Hz for TARGET-B. The genetic algorithm is run for three different ratios of rupture to shear wave velocity, which are $v_R = 0.7v_S$, $v_R = 0.8v_S$ and $v_R = 0.9v_S$, and the shear wave speed in the source region is set to $v_S = 4.5$ km/s, which is a reasonable value as the earthquakes occur at intermediate depth. For each v_R/v_S-value, the algorithm is run five times with a different initial population in order to evaluate the acceptable solution space and convergence. This issue is discussed in more details for each TARGET earthquake further below.

The October 2004 Earthquake – TARGET-A

For this event, the search ranges for the parameters are set to 0.5-15 km for L and W and 0.01-2 s for T_r. Two EGF earthquakes are simultaneously inverted (see Table 6.1). As these EGF events have different scaling factors N, the distance along strike and dip (which is usually characterized by integer numbers within the interval $[1\ N]$) is normalized to the interval $[0\ 1]$ and for each trial model, the subfault wich corresponds most closely to the normalized position is chosen to compute the respective simulations.

The lowest cost models for TARGET-A's SMGA resulting from each run of the algorithm are summarized in Table 6.3. The value of the cost is given in the last column. A first observation is that, for a $M_W = 5.8$ earthquake, the SMGA dimensions as well as the rise times are extraordinary small. There are no large differences in the inverted parameters within the different runs for each v_R/v_S-value, and, furthermore, the ratio of rupture to shear wave velocity does not seem to play a key role regarding the inversion results. The only noticeable trend is that the rupture initiation point along dip is a bit different and the SMGA size gets a bit larger from $v_R = 0.7v_S$ to $v_R = 0.9v_S$.

In terms of waveforms, the comparison of simulations using the lowest cost model (run 2 or 3 with $v_R = 0.9v_S$) with the observations are depicted in Figures 6.7 and 6.8 for EGF-A200209 and Figures

Rupture velocity	Run	L [km]	W [km]	T_r [s]	Pos. along strike	Pos. along dip	Cost
	1	0.73	1.08	0.06	0.3	0.5	54.24
	2	0.73	1.08	0.06	0.3	0.4	54.24
$v_R = 0.7 \cdot v_S$	3	0.67	0.73	0.19	0.3	0.6	54.87
	4	0.62	1.08	0.07	0.3	0.4	54.33
	5	0.82	1.36	0.12	0.3	0.6	54.99
	1	0.81	1.23	0.15	0.3	0.6	54.14
	2	0.96	1.27	0.13	0.3	0.6	54.09
$v_R = 0.8 \cdot v_S$	3	0.95	1.29	0.13	0.3	0.6	54.09
	4	0.96	1.27	0.14	0.3	0.6	54.13
	5	0.95	1.35	0.14	0.3	0.7	54.20
	1	0.95	1.43	0.15	0.3	0.7	53.72
	2	1.16	1.78	0.11	0.3	0.7	53.62
$v_R = 0.9 \cdot v_S$	3	1.16	1.78	0.11	0.3	0.7	53.62
	4	1.04	1.39	0.13	0.3	0.6	53.75
	5	0.96	1.33	0.15	0.3	0.7	53.68

Table 6.3: Lowest cost models resulting from 5 runs of the genetic algorithm for the 2004 (TARGET-A) earthquake ($M_W = 5.8$). The inversion is simultaneously performed for both EGF-A-events. The position of the rupture initiation point is normalized to the interval [0 1].

6.9 and 6.12 for EGF-A200211. Here, the acceleration and displacement time histories of the SH-wave are shown. Generally, the fit ranges from fair to excellent, although at stations GOL (Figure 6.8) and VAR (Figure 6.12) there are, admittedly, not too many common features between observations and simulations. In some cases (e.g. station FUL) the amplitudes are slightly misestimated (with a maximum factor of about 2). An excellent agreement can for instance be found at station MSA (EGF-A200211), station AMR or station BTM (EGF-A200209).

Figure 6.10 shows the evolution of the minimum (left column) and mean (right column) cost with generation, averaged over the five runs performed for each ratio of rupture to shear wave velocity. After approximately 25 generations, the mean cost remains at a stable level and shows no systematic enhancement anymore. The minimum cost needs somewhat longer to reach its final value, and during some runs, it takes more than 100 generations to find it. This is due to the rather low crossover and mutation rates chosen as well as the very weak form of elitism, which are discussed in Chapter 5.3. As a result, the algorithm's convergence is not excessively fast and a good sampling of the parameter space is obtained.

In order to evaluate the distribution of the lowest cost models in the parameter space, histogram plots for each parameter, as shown in Figure 6.11 for $v_R = 0.9v_S$, are a powerful visualization. As can be clearly seen, all five SMGA parameters from the best 750 models found cluster in a very narrow area of the parameter space. The histogram plots for $v_R = 0.7v_S$ and $v_R = 0.8v_S$ show essentially the same features, even though the rupture initation point along dip is not that good resolved for $v_R = 0.7v_S$. Thus, in summary, the SMGA parameters derived for TARGET-A are very stable and the inversion results are reliable as far as convergence and uniqueness of the solution are concerned. TARGET-B will show some severe problems in this regard, as I will discuss in a few moments. As depicted in Figure 6.11, the initial sampling of the parameter space (white bars) is almost perfectly uniform, which means that the entire parameter space is effectively sampled.
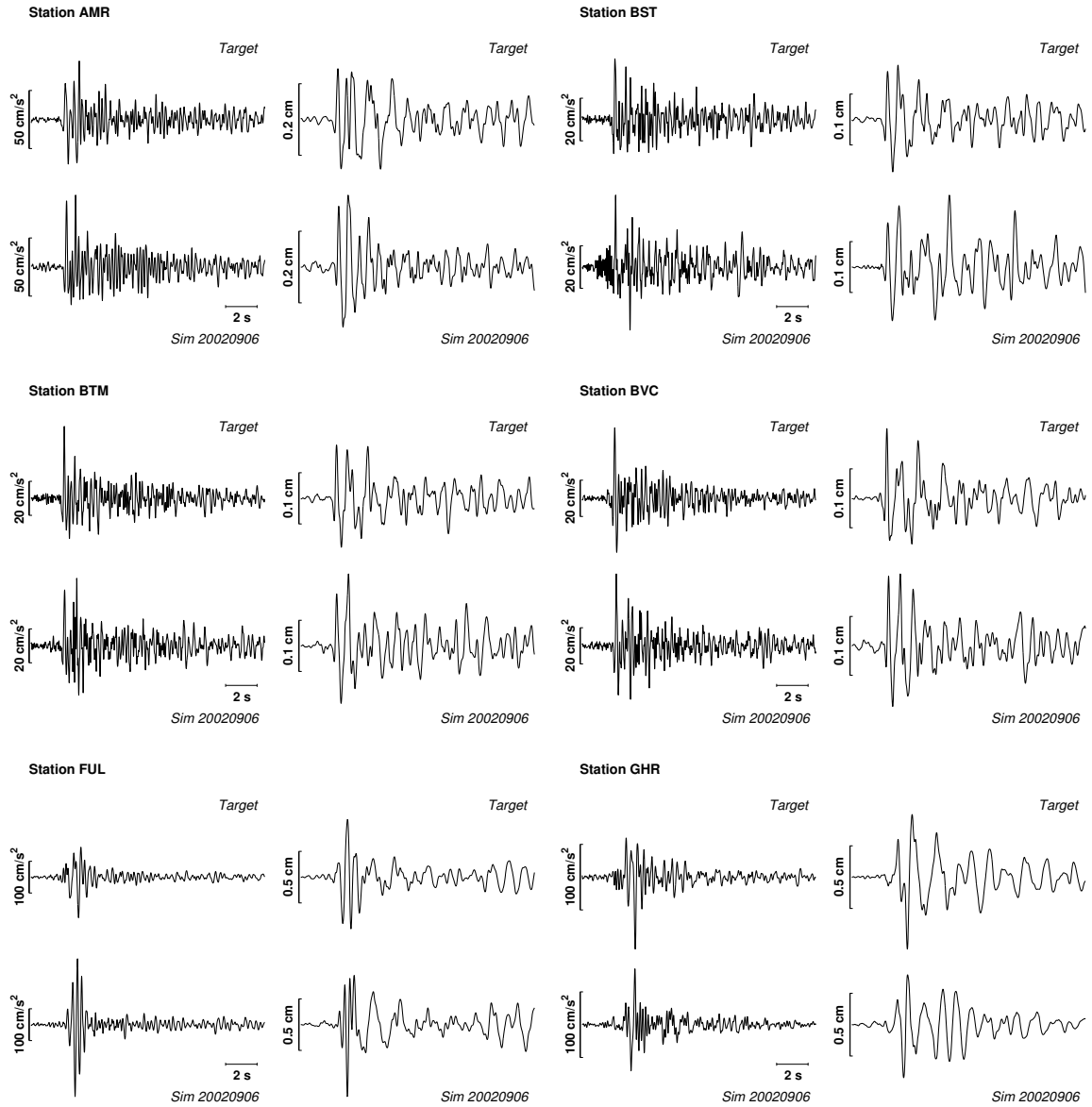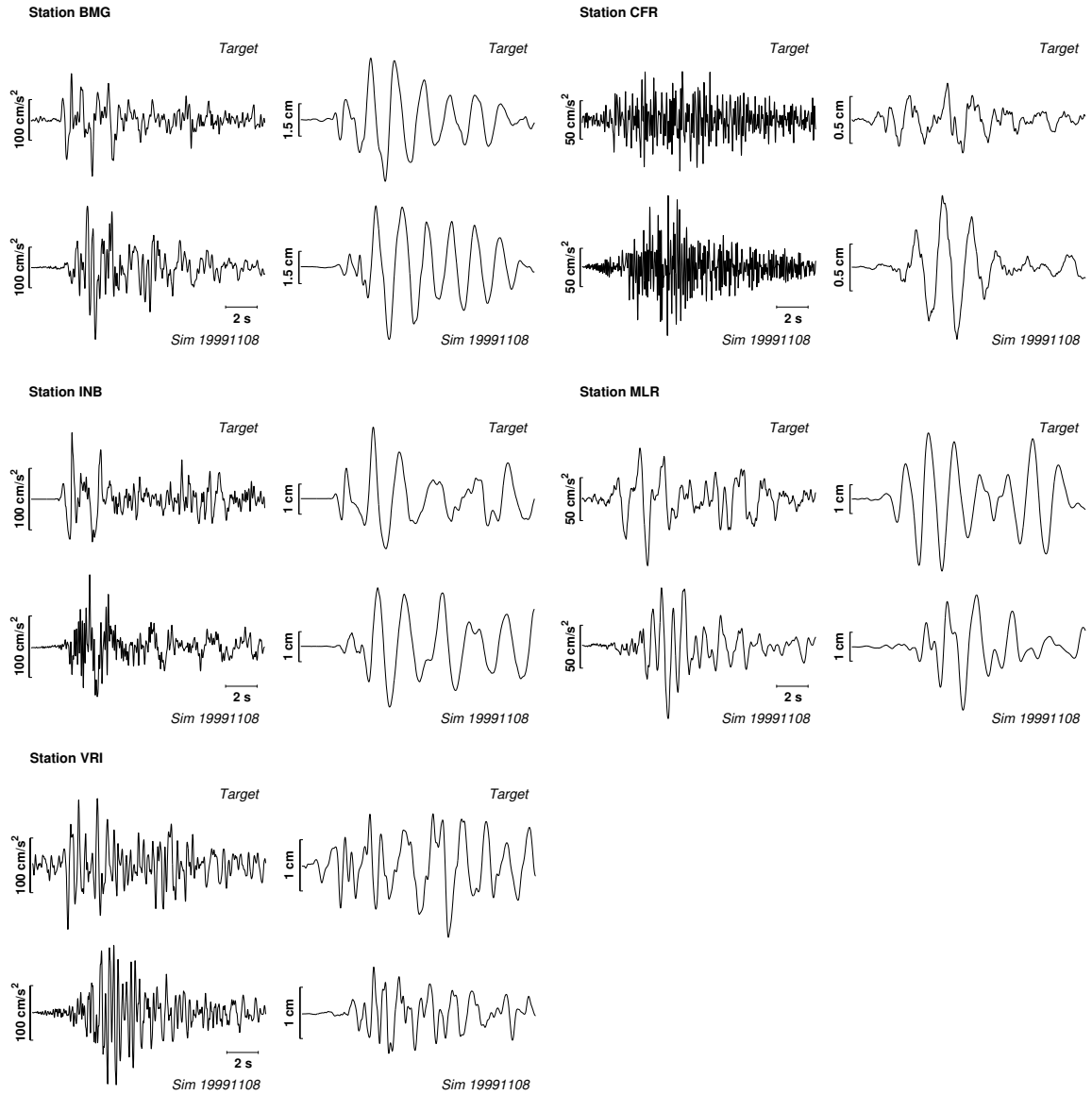
Figure 6.7: TARGET-A waveforms (synthezised from EGF-A200209) simulated with lowest cost SMGA model. For each station, the observed (top) and simulated (bottom) acceleration (left) and displacement (right) 15 s SH-waveforms are displayed. Each set of corresponding observed and simulated traces is scaled to the same maximum value.
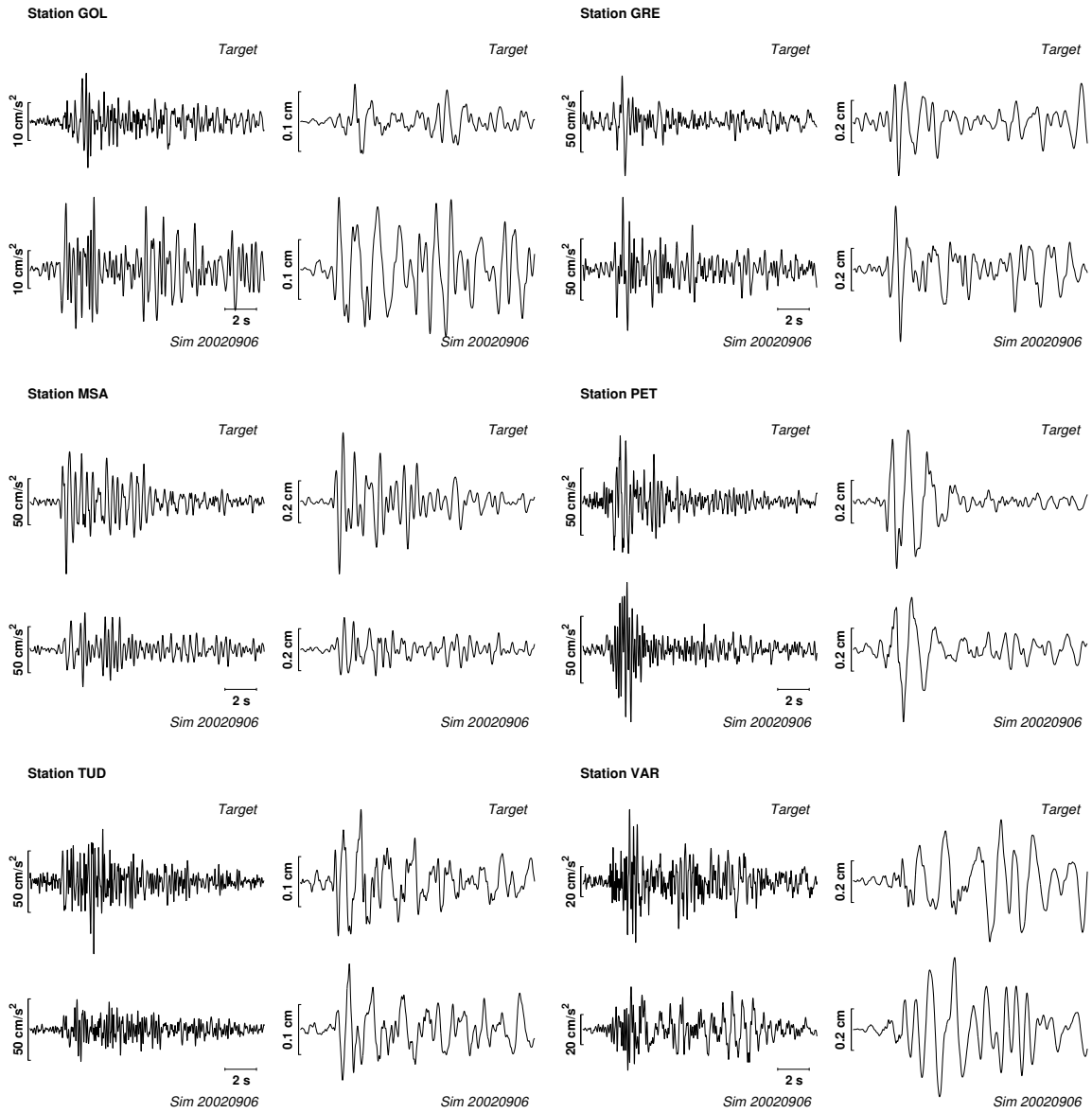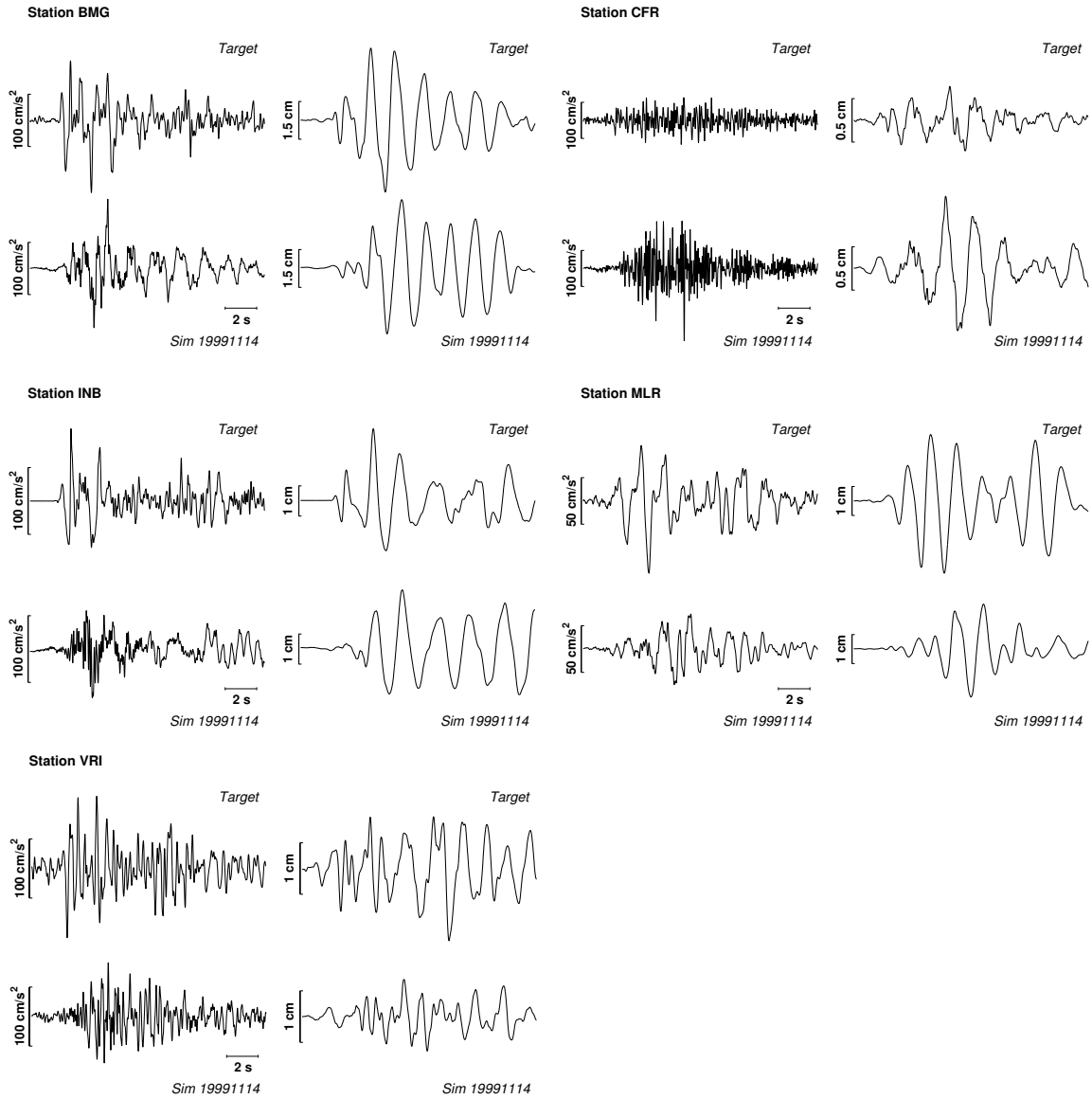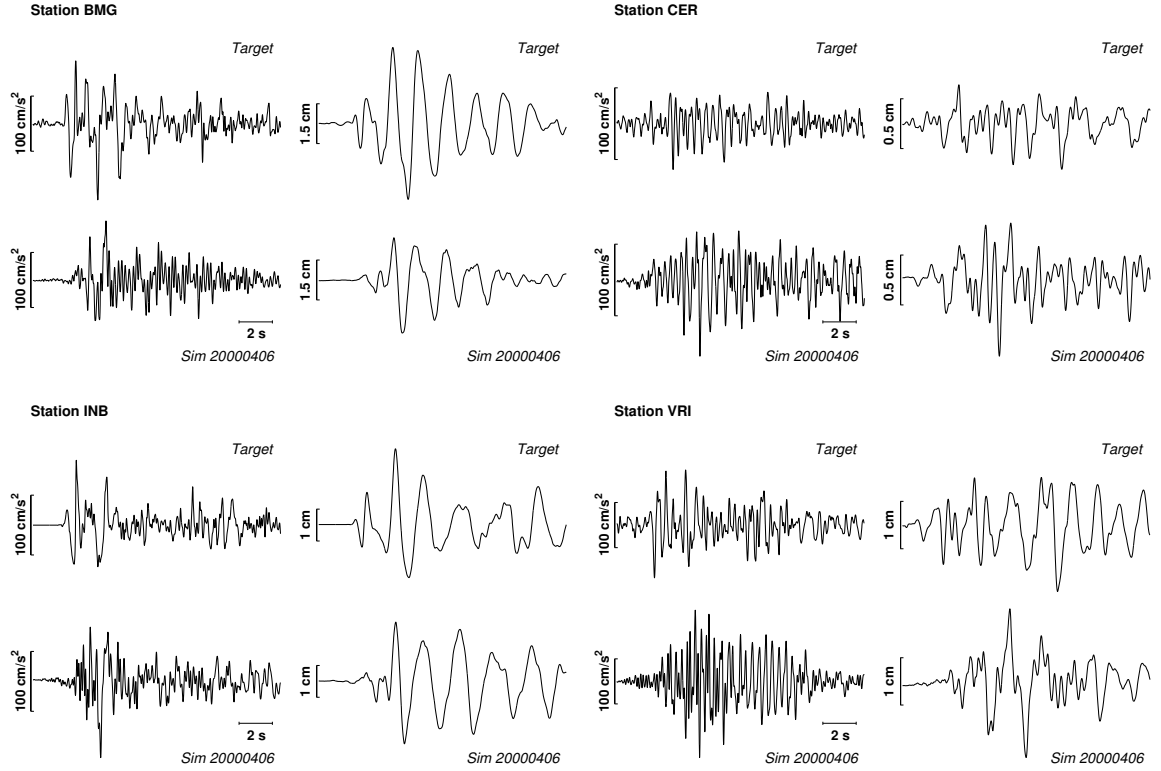
Figure 6.8: TARGET-A waveforms (synthezised from EGF-A200209) simulated with lowest cost SMGA model. For each station, the observed (top) and simulated (bottom) acceleration (left) and displacement (right) 15 s SH-waveforms are displayed. Each set of corresponding observed and simulated traces is scaled to the same maximum value. Continuation of Figure 6.7.
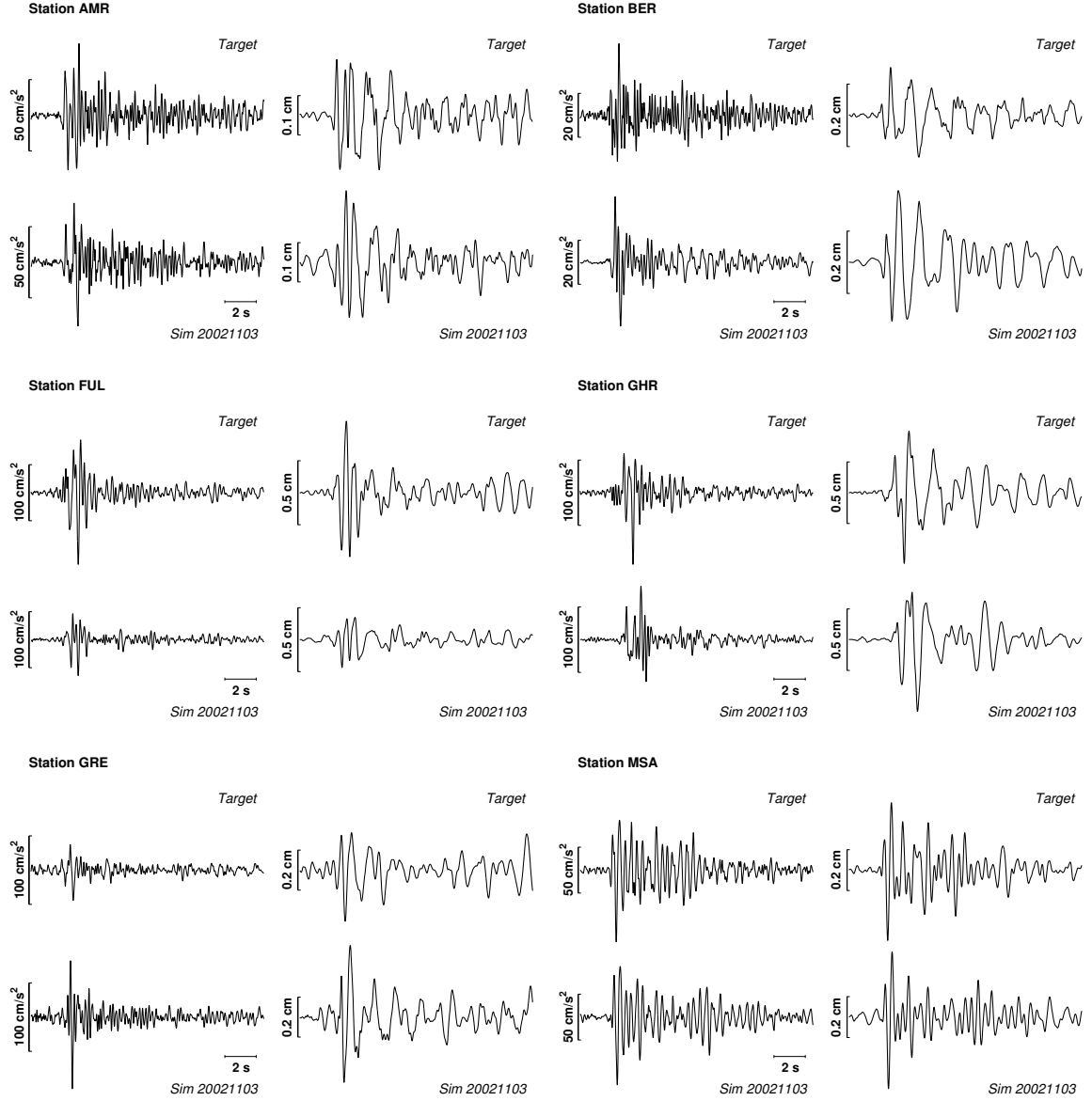
Figure 6.9: TARGET-A waveforms (synthezised from EGF-A200211) simulated with lowest cost SMGA model. For each station, the observed (top) and simulated (bottom) acceleration (left) and displacement (right) 15 s SH-waveforms are displayed. Each set of corresponding observed and simulated traces is scaled to the same maximum value.
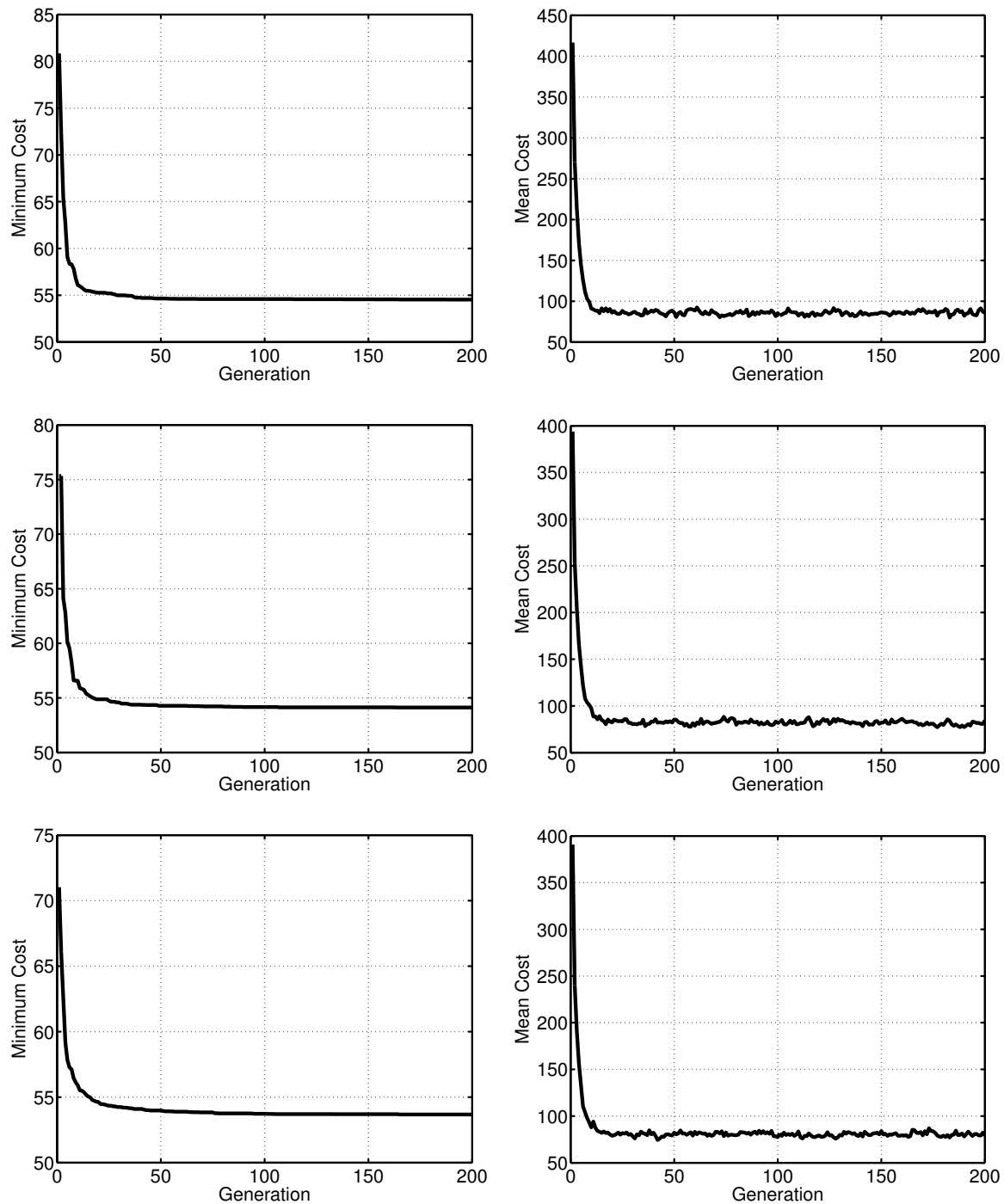
Figure 6.10: Convergence plots for the 2004 (TARGET-A) earthquake (upper row: $v_R/v_S = 0.7$, middle row: $v_R/v_S = 0.8$, bottom row: $v_R/v_S = 0.9$). Left: Evolution of the minimum cost (misfit) from generation to generation. Right: Evolution of mean cost. The curves shown here represent the evolution of the cost averaged over 5 runs of the algorithm. The mean cost does not show any systematic improvement anymore after approx. 25 generations. The minimum cost model is, during some runs, only reached after about 100 generations.
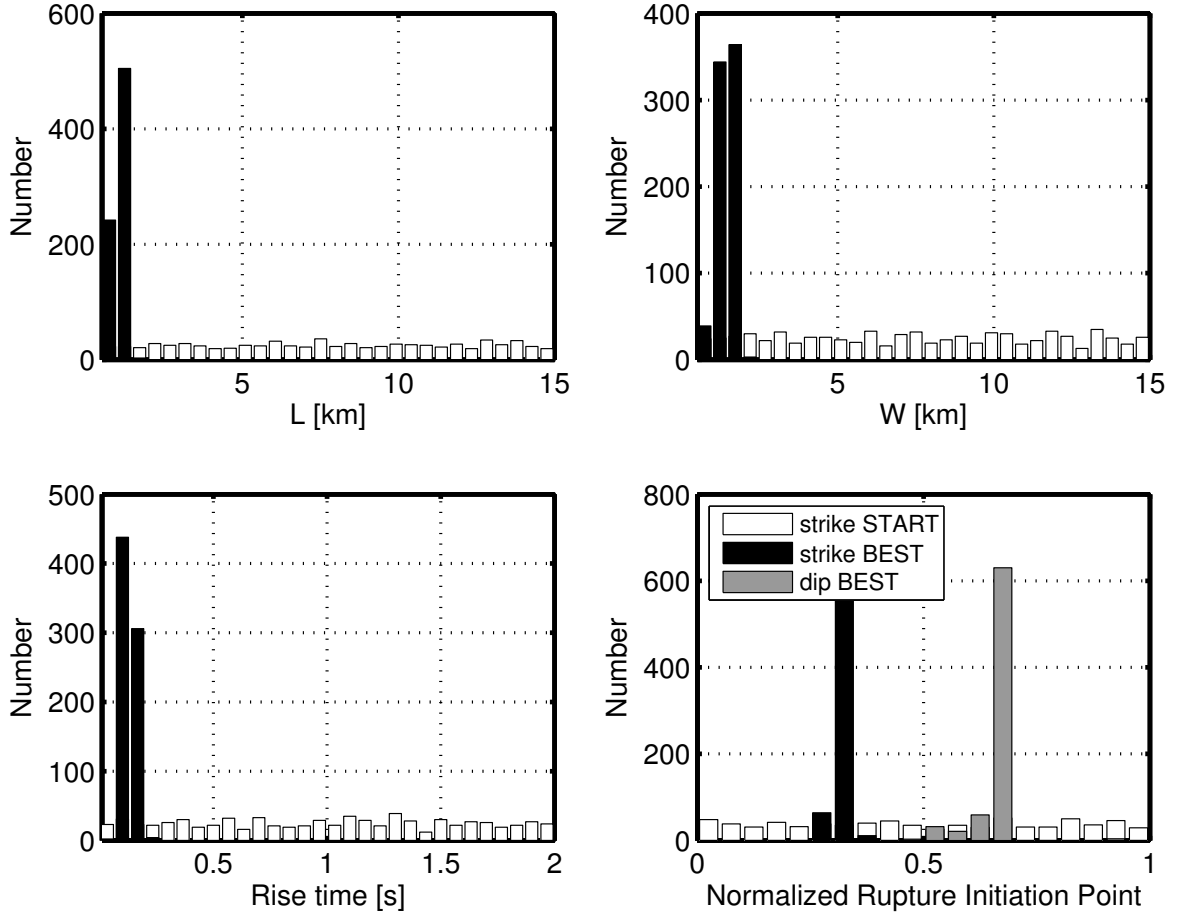
Figure 6.11: Histograms of 750 best solutions for the 2004 (TARGET-A) earthquake (150 best from each of 5 runs) for v_R/v_S = 0.9. Upper left: SMGA length L [km]. Upper right: SMGA width W [km]. Bottom left: Rise time T_r [s]. Bottom right: Normalized rupture initiation location along strike (black) and dip (grey). White bars: Initial sampling of the parameter space when starting the genetic algorithm (150 starting models from each run). As can be clearly seen, all the parameters resulting from the inversion are well constrained.
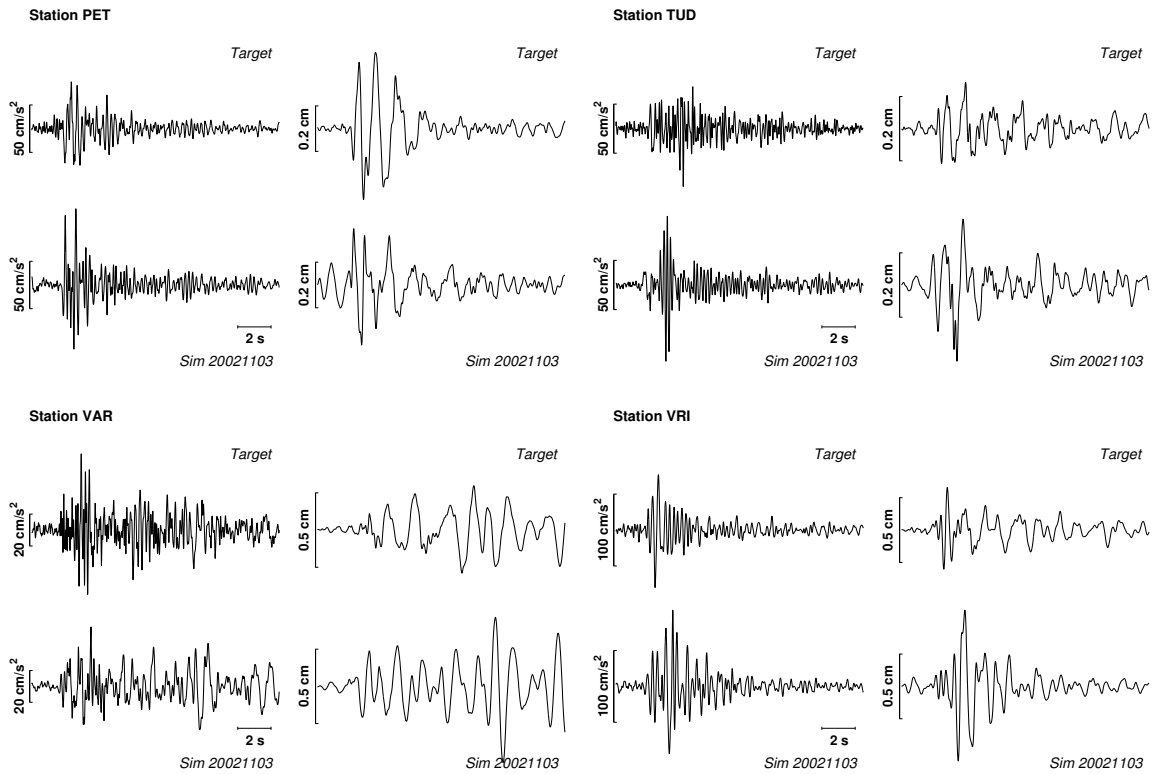
Figure 6.12: TARGET-A waveforms (synthezised from EGF-A200211) simulated with lowest cost SMGA model. For each station, the observed (top) and simulated (bottom) acceleration (left) and displacement (right) 15 s SH-waveforms are displayed. Each set of corresponding observed and simulated traces is scaled to the same maximum value. Continuation of Figure 6.9.

The August 1986 Earthquake – TARGET-B

For TARGET-B, the search ranges are set to 1-40 km for L and W and 0.05-5 s for T_r. The inversion is performed with three different EGF earthquakes simultaneously and therefore, once more, the rupture initiation point is normalized to the interval [0 1]. The resulting lowest cost SMGA models are summarized in Table 6.4. Here, the situation is rather different from the one presented above for TARGET-A with respect to solution uniqueness and convergence. This time, the lowest costs are found for $v_R/v_S = 0.7$. By only looking at the table, it is immediately clear that the inversion seems to be stable for $v_R = 0.7v_S$ and $v_R = 0.8v_S$, but there appear strongly different lowest cost solutions when $v_R = 0.9v_S$. This problem requires further investigation and I will come back to it after a short discussion on the waveform fits.

The fit between synthetic and recorded time histories (Figures 6.13, 6.14 and 6.15) is not as good as the one observed for TARGET-A, even though it can be regarded as acceptable. Whereas stations BMG, CER, CFR and INB show rather good agreement, both in acceleration and displacement, stations MLR and VRI are not satisfactorily matched. In that sense, it is interesting to note that it seems to depend on the station rather than on the considered EGF earthquake whether the fit is acceptable or not, as the unsatisfactory agreement is always observed for the same stations, regardless of the EGF event.

Figure 6.13: TARGET-B waveforms (synthezised from EGF-B19991108) simulated with lowest cost SMGA model. For each station, the observed (top) and simulated (bottom) acceleration (left) and displacement (right) 15 s SH-waveforms are displayed. Each set of corresponding observed and simulated traces is scaled to the same maximum value.

Figure 6.14: TARGET-B waveforms (synthezised from EGF-B19991114) simulated with lowest cost SMGA model. For each station, the observed (top) and simulated (bottom) acceleration (left) and displacement (right) 15 s SH-waveforms are displayed. Each set of corresponding observed and simulated traces is scaled to the same maximum value.

Figure 6.15: TARGET-B waveforms (synthezised from EGF-B200004) simulated with lowest cost SMGA model. For each station, the observed (top) and simulated (bottom) acceleration (left) and displacement (right) 15 s SH-waveforms are displayed. Each set of corresponding observed and simulated traces is scaled to the same maximum value.

Yet, a more fundamental problem is the one of the solution uniqueness. As can be seen from Table 6.4, the algorithm does not converge to similar best solutions for each of the five runs when a rupture to shear wave velocity ratio of 0.9 is assumed. It is evident that there are at least two 'best' solutions, i.e. with very similar cost. The algorithm's convergence is also much slower than for TARGET-A (Figure 6.16), especially if $v_R/v_S = 0.9$. Even though the mean cost, on average, reaches a stable value after approximately 25-30 generations, the minimum cost jumps into a lower minimum as late as in the 180th generation in some runs.

It is not necessarily surprising that such a non-linear inverse problem shows several distinct (and almost equivalent in terms of cost) solutions. If for instance two solutions with comparable cost exist, it strongly depends on the initial set of trial models, the configuration of the algorithm and on the 'luck' in the genetic operations whether the algorithm will finally make its way into one or the other minimum. The goal that shall be achieved, however, is to find them both.

An elucidating way to look at the problem are the histogram plots shown in Figures 6.17, 6.18 and 6.19. Whereas the best 750 solutions are acceptably well clustered in the parameter space for the cases $v_R/v_S = 0.7$ (Figure 6.17) and $v_R/v_S = 0.8$ (Figure 6.18), the parameters W, T_r and rupture initiation point along dip depict several peaks in the histograms when $v_R/v_S = 0.9$ (Figure 6.19). Together with the table of best models, one may thus rather speak about two to three different low cost solutions than strong overall variability. The inversion still enables us to clearly restrict the solution space of

Rupture velocity	Run	L [km]	W [km]	T_r [s]	Pos. along strike	Pos. along dip	Cost
	1	10.12	13.10	0.36	0.2	1.0	30.06
	2	12.98	12.62	0.26	0.4	1.0	28.75
$v_R = 0.7 \cdot v_S$	3	12.84	12.60	0.26	0.4	1.0	28.74
	4	10.54	13.13	0.26	0.2	1.0	29.07
	5	10.75	13.26	0.26	0.2	1.0	28.96
	1	14.31	18.14	0.36	0.3	1.0	29.16
	2	14.87	18.88	0.28	0.3	1.0	28.77
$v_R = 0.8 \cdot v_S$	3	14.69	20.96	0.31	0.3	1.0	29.14
	4	14.34	18.45	0.36	0.3	1.0	29.00
	5	15.02	18.86	0.28	0.3	1.0	28.92
	1	6.15	33.74	0.41	0.4	0.7	32.33
	2	5.86	3.98	0.27	0.4	0.2	30.42
$v_R = 0.9 \cdot v_S$	3	6.58	3.70	0.25	0.4	0.1	30.14
	4	5.87	27.43	0.43	0.4	0.9	32.20
	5	5.24	34.61	0.42	0.4	0.7	31.77

Table 6.4: Lowest cost models resulting from 5 runs of the genetic algorithm for the 1986 (TARGET-B) earthquake ($M_W = 7.1$). The inversion is simultaneously performed for all three EGF-B-events. The position of the rupture initiation point is normalized to the interval [0 1].

the problem to a few different minima in cost. The algorithm converges either to $W \approx 30$ km, $T_r \approx 0.4$ s and a rupture initiation location along dip of around 0.7 or to $W \approx 4$ km, $T_r \approx 0.25$ s and a rupture initiation location along dip of around 0.2. There is also a certain amount of models with a rise time higher than 1 s (see Figure 6.19, lower left). Interestingly, the length L and rupture initiation point along strike are well constrained, which actually means that the main difficulties seem to reside in the rupture characteristics along dip (i.e. in the parameters W and rupture initiation point along dip).

The costs of the best solutions for $v_R/v_S = 0.9$ are approximately 10-15% higher than the ones for $v_R/v_S = 0.7$ or $v_R/v_S = 0.8$. In that sense, one may also simply argue that the former ratio of rupture to shear wave velocity is less probable than the latter ones. Yet, the cost differences are not large enough to strictly rule them out.

This non-uniqueness is probably due to the combination of several factors. First of all, the database is much sparser than e.g. the one for TARGET-A. Especially the azimuthal coverage is not as one would like it to be, as from the six stations in the dataset, two are located in Bucharest (BMG and INB). This, however, cannot be the only explanation, as the ambiguity observed here does not show up for TARGET-D, as we will see, where only six stations are usable as well. A more fundamental issue is, however, the problem of the determination of the correct values for C and N required in Irikura's technique (Chapter 4.1). If these parameters are wrongly chosen, severe differences in the estimates for the other parameters, such as size and rise time, may result. Different combinations of C and N imply different ratios $f_{c,T}/f_{c,E}$, as equations (4.24) and (4.25) show. Event though the moment ratio may be identical, this leads to strong differences in assumed high frequency content (see also Figure 4.4 and the explanations in Chapter 4.1). Therefore, it is essential to derive sensible estimates for these two parameters. However, it is not possible to compute them from the spectral ratios for TARGET-B with as good confidence as in the cases of TARGET-A and -D due to the problems mentioned in Section 6.3. Finally, the higher the value of N is, the larger is the number of subfaults and, as a
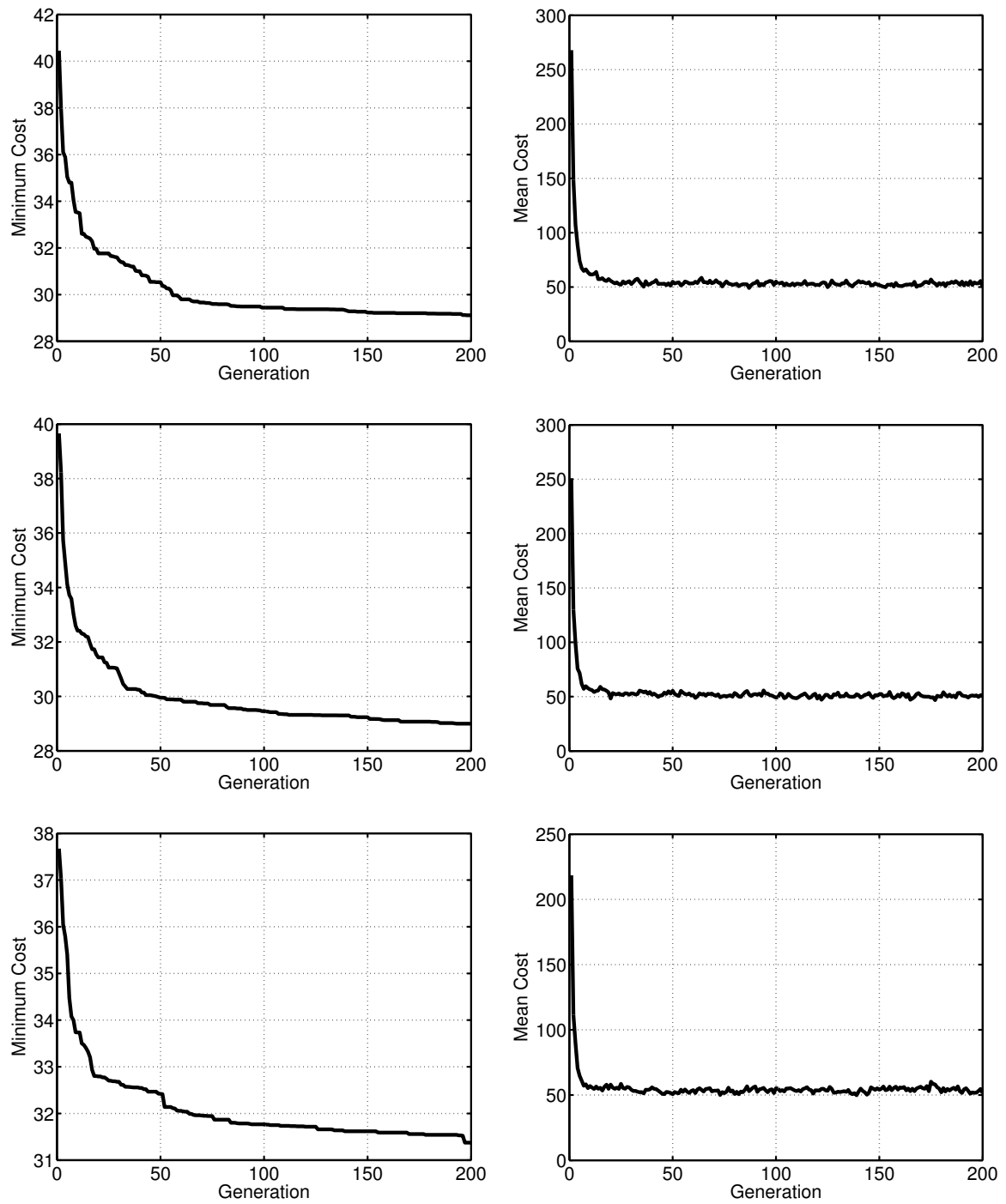
Figure 6.16: Convergence plots for the 1986 (TARGET-B) earthquake (upper row: $v_R/v_S = 0.7$, middle row: $v_R/v_S = 0.8$, bottom row: $v_R/v_S = 0.9$). Left: Evolution of the minimum cost (misfit) from generation to generation. Right: Evolution of mean cost. The curves shown here represent the evolution of the cost averaged over 5 runs of the algorithm. Note the very slow convergence towards the minimum cost model in the left column. This very slow convergence is due to the non-uniqueness problems discussed in the text.
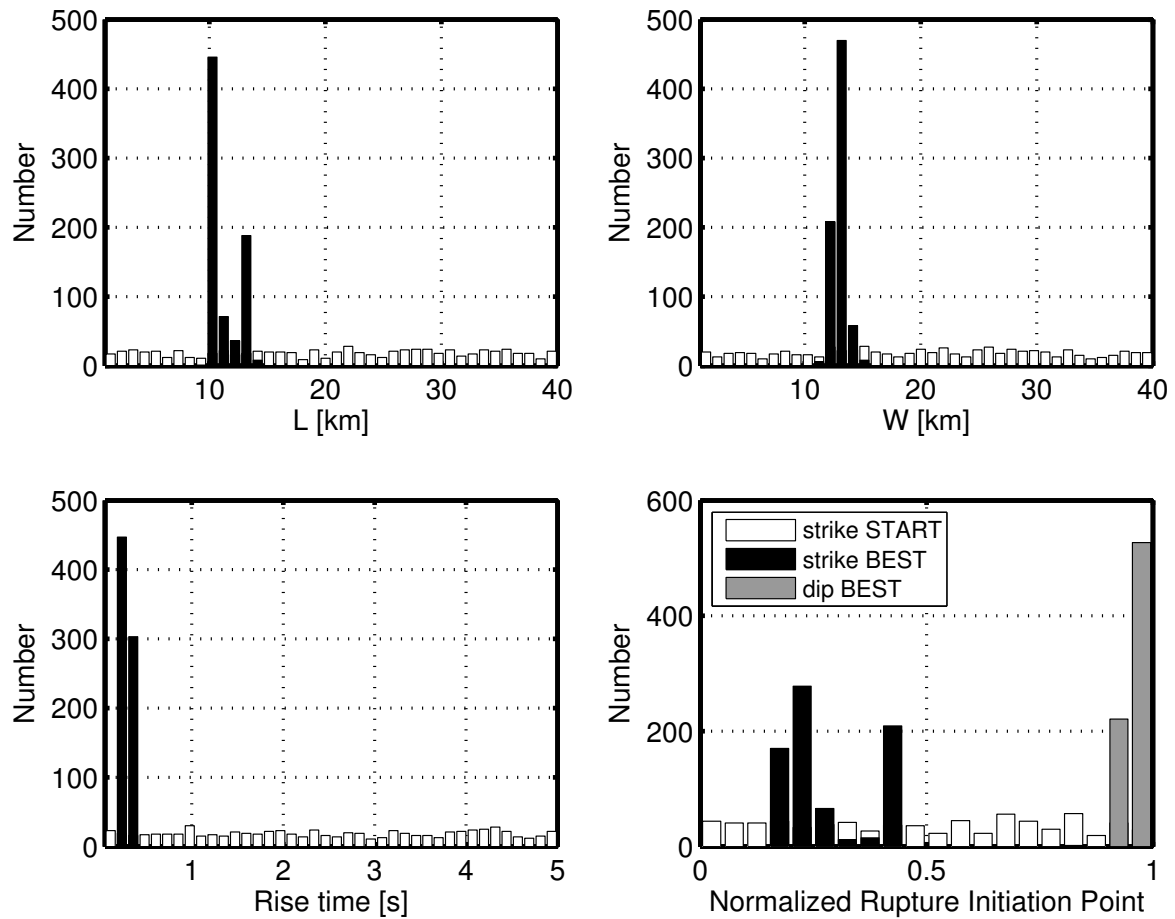
Figure 6.17: Histograms of 750 best solutions for the 1986 (TARGET-B) earthquake (150 best from each of 5 runs) for v_R/v_S = 0.7. Upper left: SMGA length L [km]. Upper right: SMGA width W [km]. Bottom left: Rise time T_r [s]. Bottom right: Normalized rupture initiation location along strike (black) and dip (grey). White bars: Initial sampling of the parameter space when starting the genetic algorithm (150 starting models from each run). All the parameters resulting from the inversion are well constrained (altough there is some scatter in the position of rupture initiation along strike).
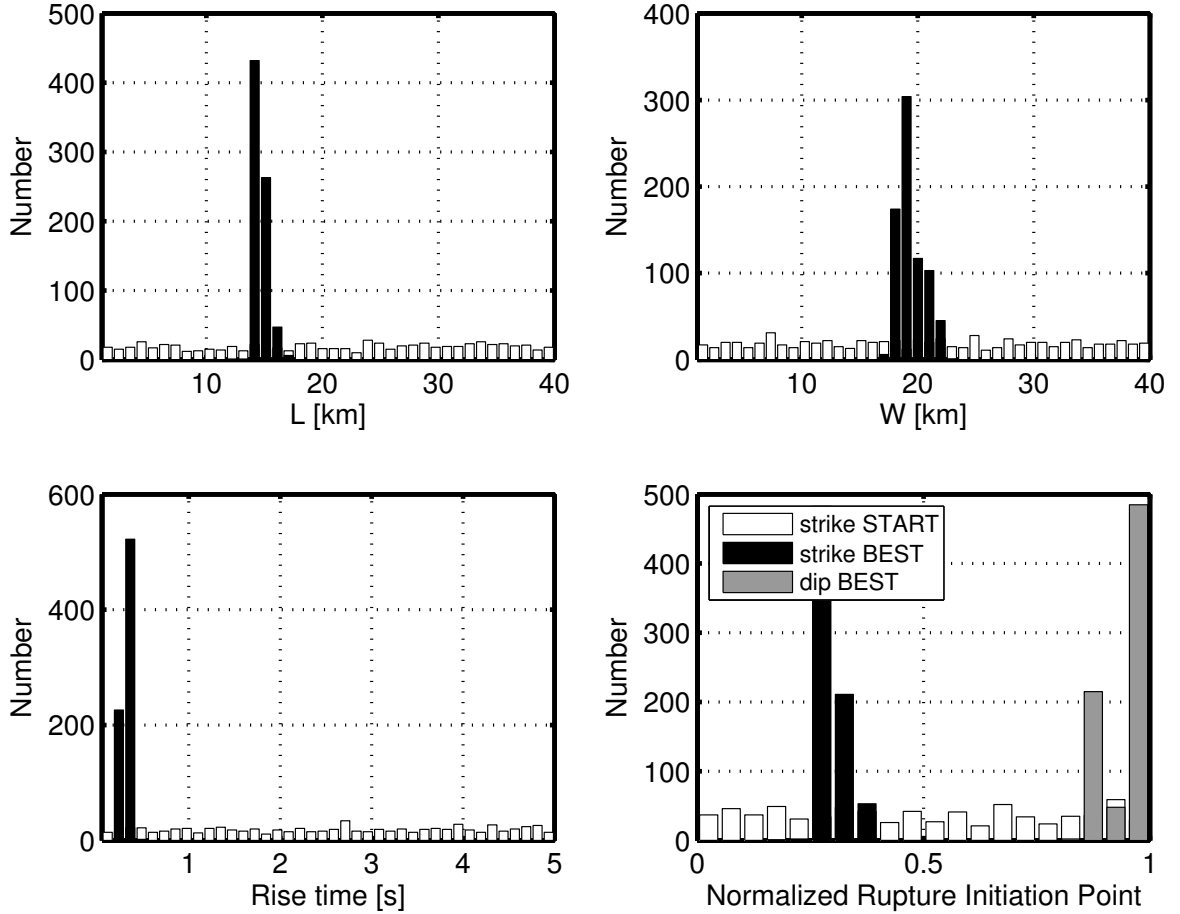
Figure 6.18: Histograms of 750 best solutions for the 1986 (TARGET-B) earthquake (150 best from each of 5 runs) for v_R/v_S = 0.8. Upper left: SMGA length L [km]. Upper right: SMGA width W [km]. Bottom left: Rise time T_r [s]. Bottom right: Normalized rupture initiation location along strike (black) and dip (grey). White bars: Initial sampling of the parameter space when starting the genetic algorithm (150 starting models from each run). All the parameters resulting from the inversion are well constrained.
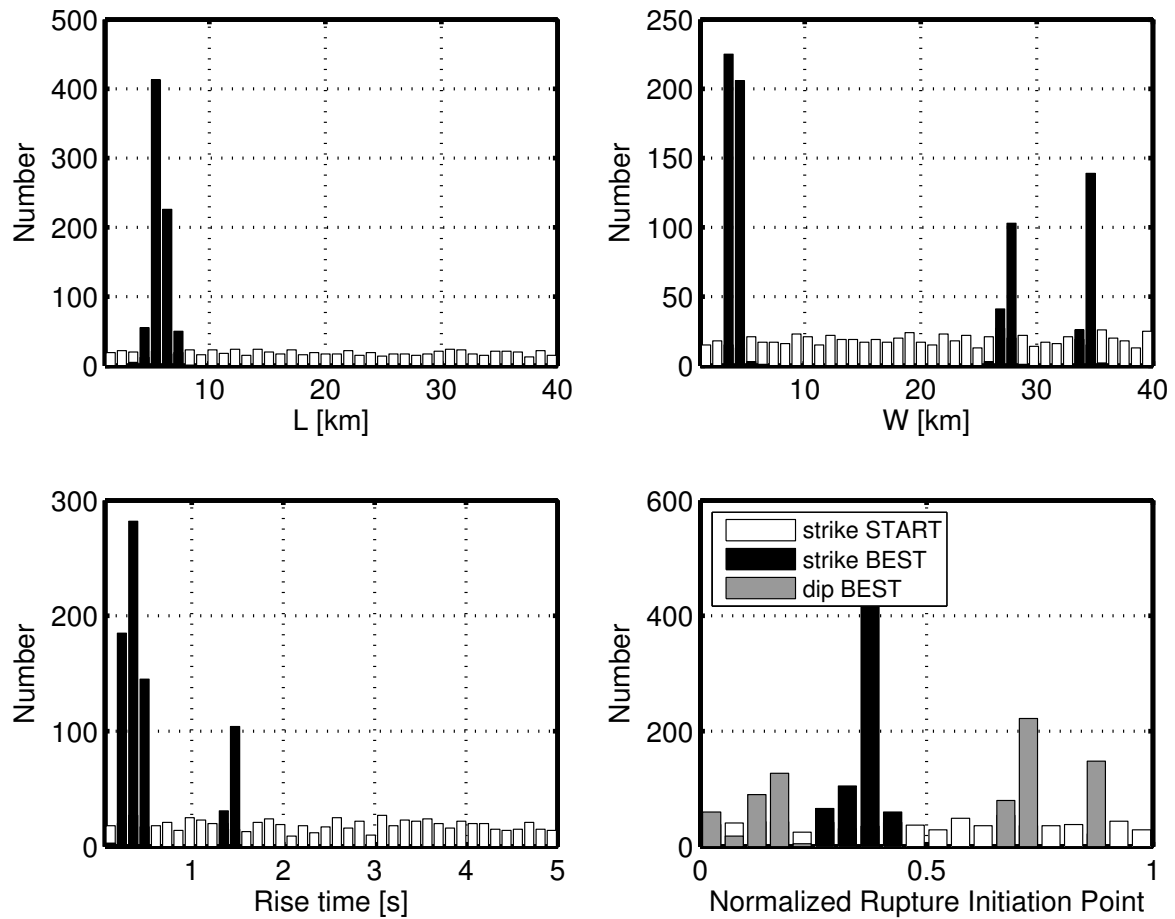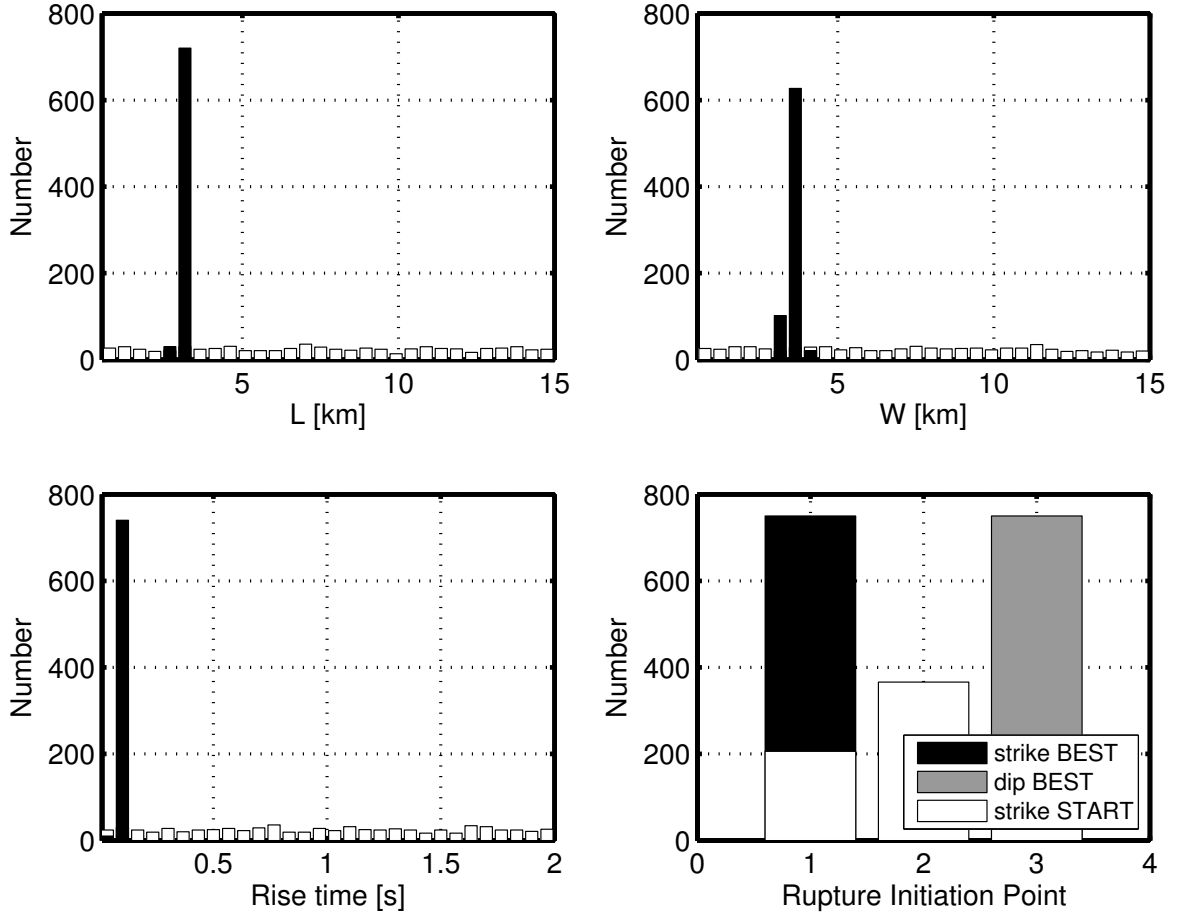
Figure 6.19: Histograms of 750 best solutions for the 1986 (TARGET-B) earthquake (150 best from each of 5 runs) for $v_R/v_S = 0.9$. Upper left: SMGA length L [km]. Upper right: SMGA width W [km]. Bottom left: Rise time T_r [s]. Bottom right: Normalized rupture initiation location along strike (black) and dip (grey). White bars: Initial sampling of the parameter space when starting the genetic algorithm (150 starting models from each run). The width, rise time and rupture initiation point along dip show several distinct peaks in the histograms. Further explanations are given in the text.
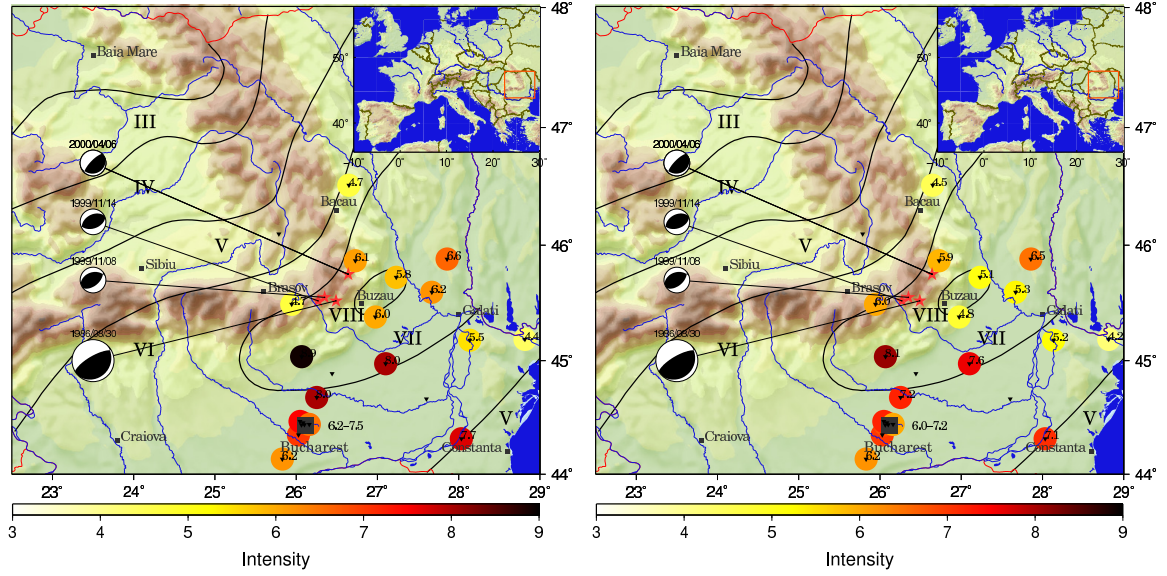
Figure 6.20: Comparison of simulated intensity using the lowest cost SMGA's for TARGET-B with $v_R/v_S = 0.7$ (run 3 in Table 6.4, left) and $v_R/v_S = 0.9$ (also run 3 in Table 6.4, right) with observed intensity pattern (black isolines, compare with Figure 6.24). The simulated intensity values have been obtained using all available records from EGF-B19991108, EGF-B19991114 and EGF-200004. Here I only show the result for EGF-19991108 as an example. Note the higher simulated intensities in and around the epicentral area (observed intensity patch VIII) on the left compared with the map on the right. Yet, the simulated values are about one unit too low with respect to that patch, whereas they are too high in the foredeep basin.

result, the number of possible rupture initiation points will be. This fact may also contribute to the non-uniqueness of the solution, as the simulations are strongly dependent on the position of rupture starting (see Figure 4.4). Thus, it would indeed be desirable to use EGF events one unit of magnitude larger than the ones used here to simulate the TARGET-B earthquake. However, the available database does not contain any better EGF earthquakes than the ones employed so far.

Figure 6.20 shows the comparison of simulated intensities using the lowest cost SMGA models for $v_R/v_S = 0.7$ (run 3) and $v_R/v_S = 0.9$ (run 3) with the observed intensity pattern. The SMGA models were used with all available records from the EGF-B earthquakes to simulate TARGET-B time histories from which instrumental intensity was deduced using the methodology of Sokolov (2002). More details on this procedure are given in Section 6.4.2. The scatter in intensity is rather large, and the simulated intensities using the lowest cost model with $v_R/v_S = 0.9$ show values in the epicentral area which are about one unit lower than the ones simulated using the lowest cost model with $v_R/v_S = 0.7$, which is also the lowest cost model in the absolute sense. This difference is probably due to the different rupture propagation updip of the different models. Whereas the lowest cost model with $v_R/v_S = 0.7$ shows rupture directivity updip, the lowest cost model with $v_R/v_S = 0.9$ shows rupture directivity purely downdip. In order to explain the observed intensity pattern in and around the epicentral area, the lowest cost model (run 3 with $v_R/v_S = 0.7$) seems to be better suited, and the cost of this model in terms of intensity as derived using equation (6.2) is about 10% lower. Therefore, I will limit the oncoming discussion to the latter SMGA model.

Rupture velocity	Run	L [km]	W [km]	T_r [s]	Pos. along strike	Pos. along dip	Cost
$v_R = 0.7 \cdot v_S$	1	2.04	2.17	0.14	1 (3)	3 (3)	12.17
	2	2.05	2.10	0.13	1 (3)	3 (3)	12.21
	3	2.04	2.16	0.12	1 (3)	3 (3)	12.20
	4	2.05	2.15	0.11	1 (3)	3 (3)	12.21
	5	2.03	2.16	0.12	1 (3)	3 (3)	12.20
$v_R = 0.8 \cdot v_S$	1	2.71	2.89	0.09	1 (3)	3 (3)	12.04
	2	2.73	2.83	0.09	1 (3)	3 (3)	12.05
	3	2.58	2.80	0.10	1 (3)	3 (3)	11.98
	4	2.59	2.75	0.09	1 (3)	3 (3)	12.07
	5	2.71	2.87	0.09	1 (3)	3 (3)	12.04
$v_R = 0.9 \cdot v_S$	1	3.01	3.53	0.08	1 (3)	3 (3)	11.79
	2	2.99	3.54	0.09	1 (3)	3 (3)	11.82
	3	3.04	3.67	0.08	1 (3)	3 (3)	11.80
	4	3.03	3.65	0.09	1 (3)	3 (3)	11.82
	5	2.99	3.54	0.08	1 (3)	3 (3)	11.78

Table 6.5: Lowest cost models resulting from 5 runs of the genetic algorithm for the 2005 (TARGET-D) earthquake ($M_W = 5.2$). The position of the rupture initiation point is not expressed as a normalized value in the interval [0 1], but absolutely (the number in parentheses is the scaling factor $N = 3$).

The May 2005 Earthquake – TARGET-D

The last earthquake for which a waveform based inversion is performed is TARGET-D, the most recent Vrancea earthquake with a moment magnitude larger than 5 ($M_W = 5.2$). Only one appropriate EGF earthquake was found in the database and six records can be used for the inversion purpose. Thus, the usable database is not larger than the one for TARGET-B, and yet, the results are not ambiguous. The possible reasons for the non-uniqueness arising for TARGET-B have been discussed above.

The results of the inversion for the three considered rupture velocities are summarized in Table 6.5 and the comparison between simulated and observed time histories is shown in Figure 6.21. The fit is fair for all stations except OZU. As expected from the computed corner frequency for TARGET-D, the SMGA of this earthquake depicts larger dimensions than the one of TARGET-A. The physical consequences and further discussion, however, is postponed to Section 6.5. As only one EGF event is used, the rupture initiation point is not searched as a normalized value between 0 and 1, but absolutely, i.e. as an integer value ranging in the interval [1 N], with $N = 3$ in this case.

The convergence plots (Figure 6.22) show a faster convergence than for TARGET-B, and only 100 generations are computed, as there is, in almost every run, no further improvement of the solution after roughly 50 generations. The stable value for the mean cost is reached after approximately 20 generations. From the histograms presented in Figure 6.23 (I only show the histograms for $v_R/v_S = 0.9$), it is evident to see that all inverted parameters are very well constrained.

In general, the estimated size of the SMGA increases with rupture velocity, while the estimated rise time decreases. The lowest cost values are obtained with a rupture velocity of $v_R = 0.9v_S$.
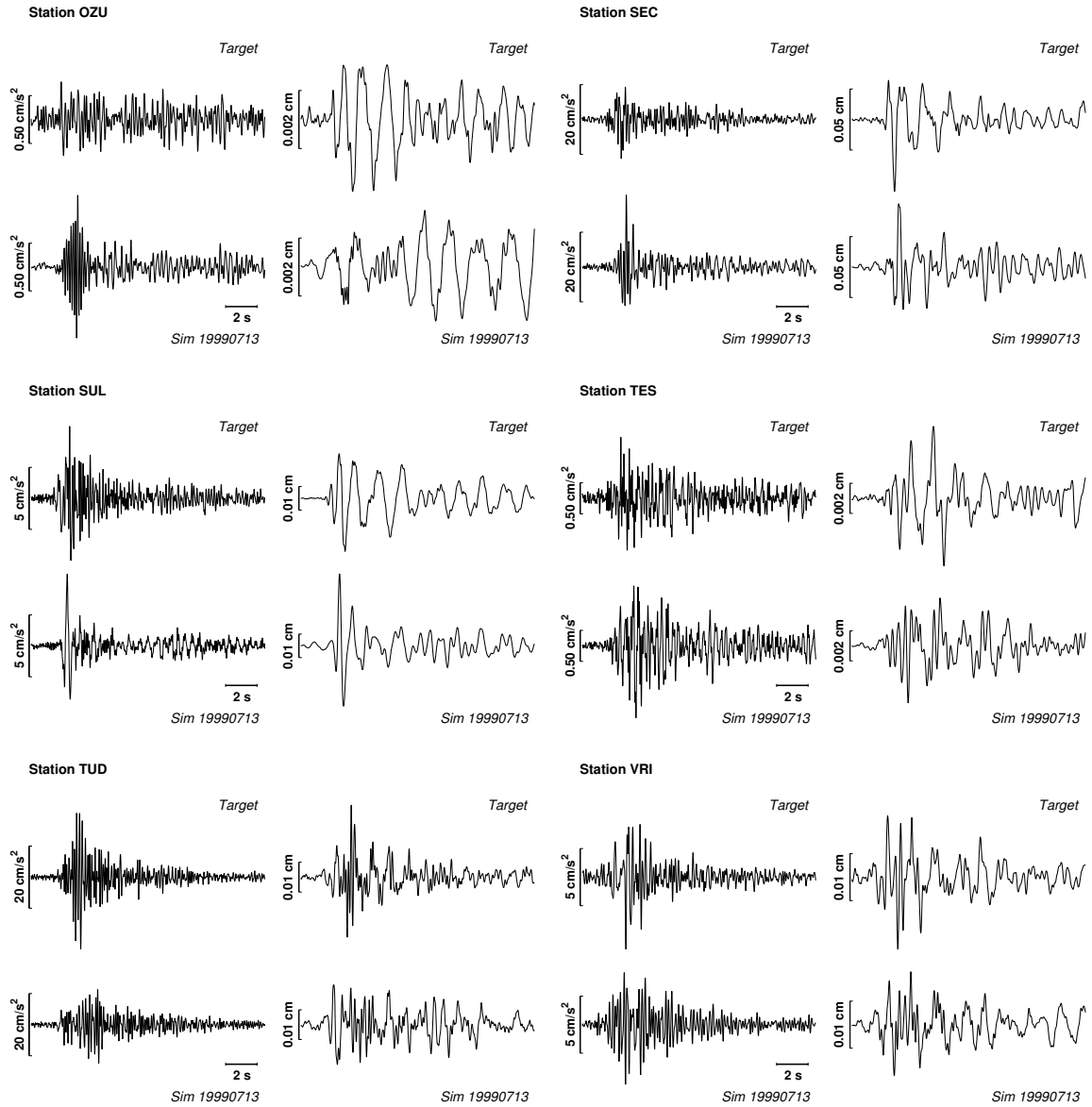
Figure 6.21: TARGET-D waveforms (synthezised from EGF-D199907) simulated with lowest cost SMGA model. For each station, the observed (top) and simulated (bottom) acceleration (left) and displacement (right) 15 s SH-waveforms are displayed. Each set of corresponding observed and simulated traces is scaled to the same maximum value.
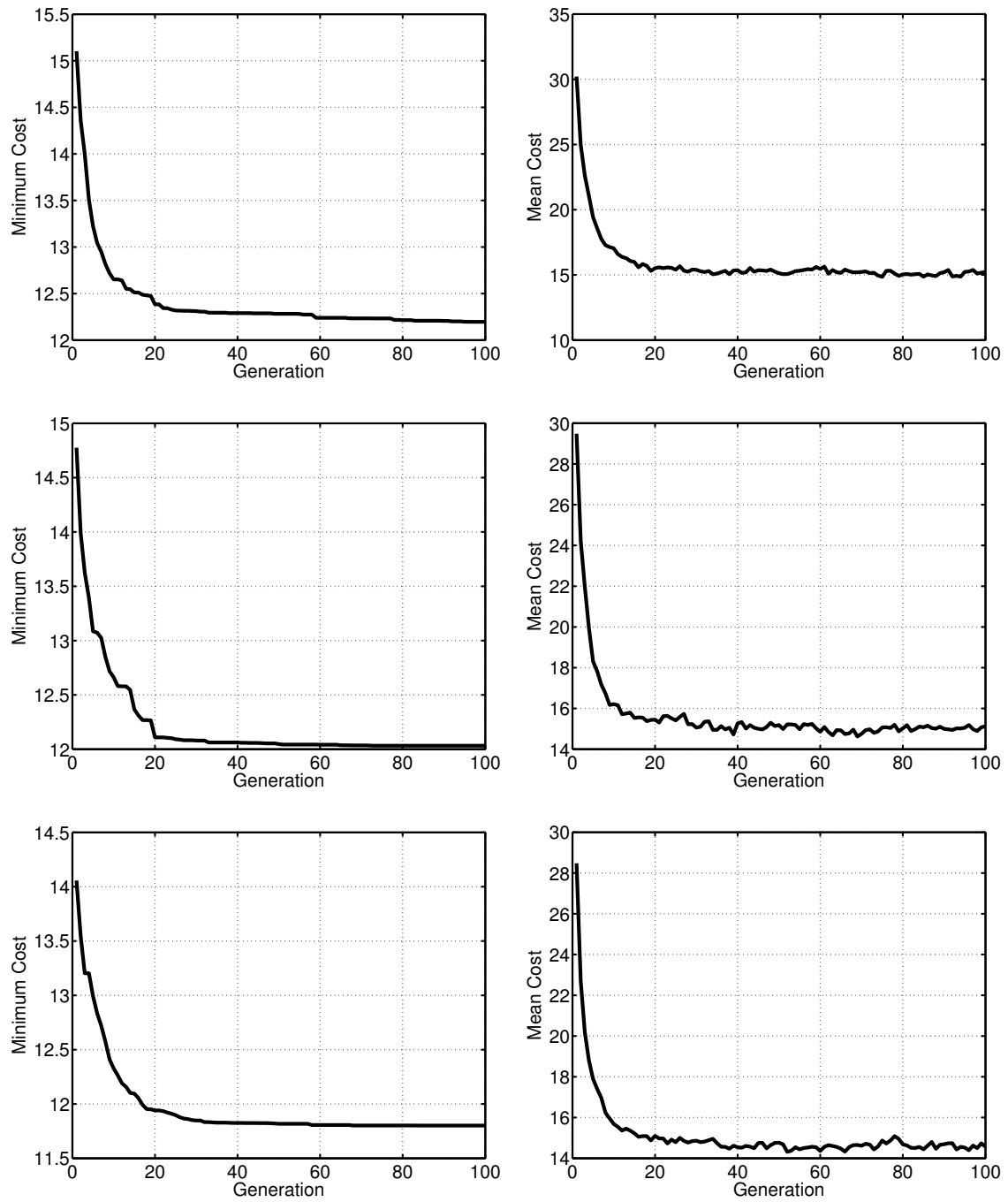
Figure 6.22: Convergence plots for the 2005 (TARGET-D) earthquake (upper row: $v_R/v_S = 0.7$, middle row: $v_R/v_S = 0.8$, bottom row: $v_R/v_S = 0.9$). Left: Evolution of the minimum cost (misfit) from generation to generation. Right: Evolution of mean cost. The curves shown here represent the evolution of the cost averaged over 5 runs of the algorithm.

Figure 6.23: Histograms of 750 best solutions for the 2005 (TARGET-D) earthquake (150 best from each of 5 runs) for v_R/v_S = 0.9. Upper left: SMGA length L [km]. Upper right: SMGA width W [km]. Bottom left: Rise time T_r [s]. Bottom right: Rupture initiation location along strike (black) and dip (grey). White bars: Initial sampling of the parameter space when starting the genetic algorithm (150 starting models from each run).

6.4.2 Intensity Based Inversion

Now that the inverted SMGA models for TARGET-A, -B and -D have been presented, I will focus my attention on TARGET-C, for which the different situation with respect to data availability requires a different approach. As mentioned earlier, only one strong motion recording exists, which has been obtained within the city of Bucharest at station Incerc (named INB). Thus, an inversion based on waveforms, which is of course the favored case, cannot be performed. With seven controlling parameters, one should expect that it is possible to fit this single recording with a large number of completely different combinations of these, whether these combinations may be physically reasonable or not.

However, two facts are worth noting: first, there is a large amount of accelerograms available for the October 2004 earthquake (EGF-C200410), which has already been treated as TARGET-A. Moreover, the latter earthquake represents an almost perfect EGF with respect to TARGET-C (Figure 6.2 or 6.25). The key question is only how this abundant dataset can be used to derive an SMGA source model for TARGET-C.

The Macroseismic Intensity Maps as an Inversion Criterion

The approach adopted in this work is rather simple. There is abundant macroseismic information available for the March 1977 earthquake. If it were possible to link the simulations with the trial SMGA parameters using EGF-C200410 (or TARGET-A) at a given site to the macroseismic intensity observation of TARGET-C (MSK scale), it would be feasible to use intensity as the criterion to be optimized. From the simulated accelerograms, MSK intensity is estimated using the method of Sokolov (2002), which I introduced in Chapter 2.5. Then, this instrumental intensity is compared to the observed MSK intensity derived from the intensity map (Figure 6.24, Radu et al., 1979).

The criterion of fit (respectively the cost function) is defined as the L1-norm between observed and simulated intensity:

$$cost = \sum_{records} |Intensity_{observed} - Intensity_{simulated}|, \tag{6.2}$$

Note that, in contrast to the cost function used for the waveform based inversion given by (6.1), no normalization is necessary, as a given absolute difference in intensity (e.g. half a unit) shall be weighted identically regardless whether both intensity values are for instance higher than VIII or lower than V. As, in the technique of Sokolov (2002), the computation of instrumental intensity is based on the entire FAS of ground motion, an inversion performed with the above cost function can actually be regarded as a sort of frequency domain inversion (although indirect, of course, and without any phase information). Due to the missing phase information, I decided to introduce a further constraint to stabilize the inversion problem: the aspect ratio (i.e. the ratio L/W) is fixed in the inversions presented below.

The MSK-intensity maps of the large Vrancea earthquake which occurred in 1977 (TARGET-C) (Radu et al., 1979) and 1986 (TARGET-B) (Radu et al., 1987) are presented in Figure 6.24. The isoseismals show an elongated shape, with the areas of large intensities stretching from SW to NE. In 1977, a large area was affected by intensities VII or VIII, including Bucharest, which was heavily damaged. In 1986, Bucharest was only affected by intensities about one unit smaller than in 1977. Some researchers attribute these differences to different directivity effects (Hartzell, 1979, discussed such differences between the 1977 and the large 1940 earthquakes). I will come back to this issue later. The intensity patterns from Vrancea earthquakes show a rather characteristic shape, deviating to a large
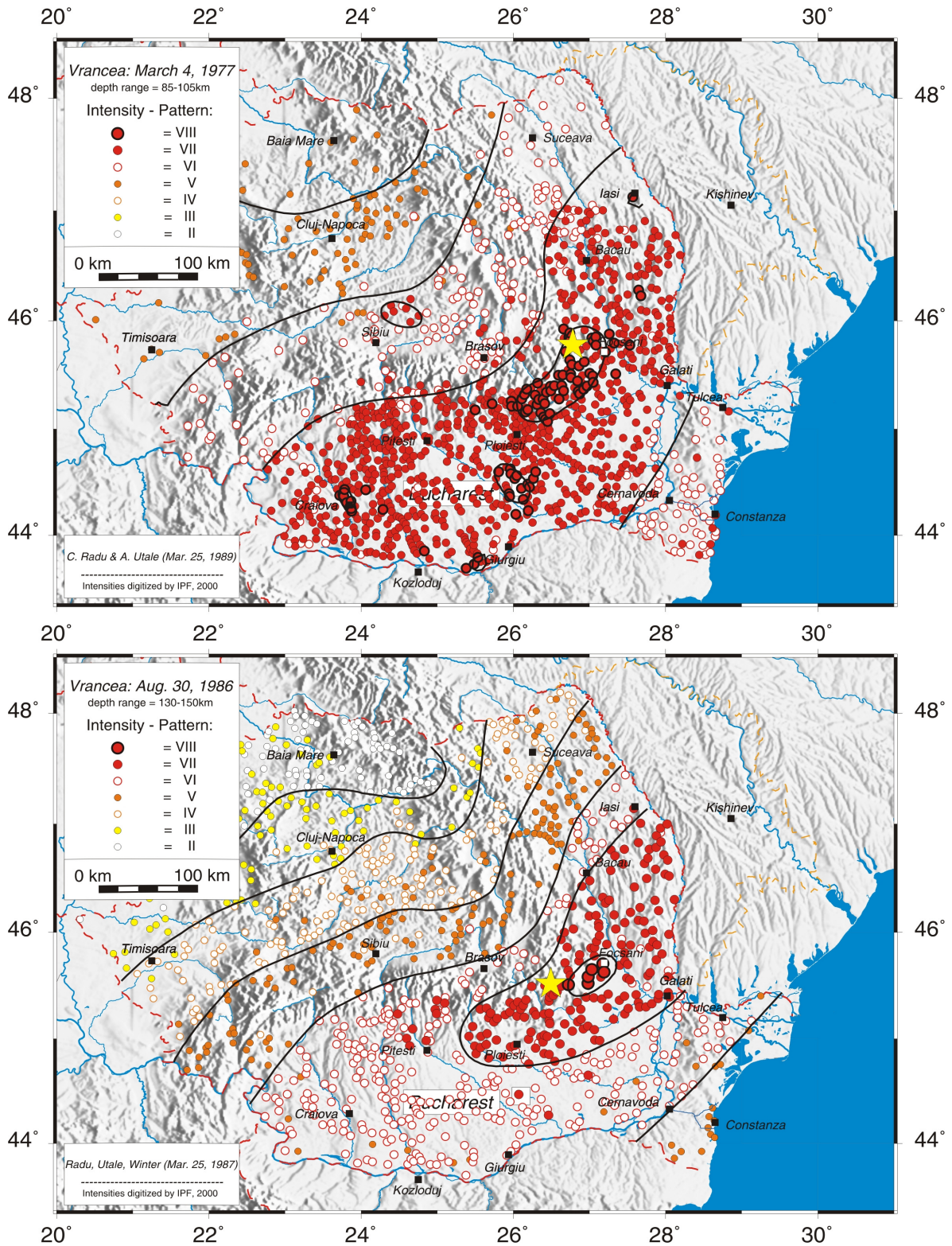
Figure 6.24: Observed macroseismic intensity maps (MSK scale) of the 1977 (TARGET-C) (top) and 1986 (TARGET-B) (bottom) earthquakes, compiled by Bonjer (personal communication, 2006). The stars indicate the epicenters of the respective earthquakes.

Square SMGA	Run	L [km]	W [km]	T_r [s]	Pos. along strike	Pos. along dip	Cost
	1	8.07	8.07	0.97	1 (6)	4 (6)	25.45
	2	8.10	8.10	0.97	1 (6)	4 (6)	25.45
$v_R = 0.9 \cdot v_S$	3	8.13	8.13	0.96	1 (6)	4 (6)	25.45
	4	8.12	8.12	0.96	1 (6)	4 (6)	25.45
	5	8.11	8.11	0.96	1 (6)	4 (6)	25.45
Aspect ratio 1:1.5	Run	L [km]	W [km]	T_r [s]	Pos. along strike	Pos. along dip	Cost
	1	7.88	12.05	0.74	1 (6)	3 (6)	26.35
	2	7.89	12.07	0.74	1 (6)	3 (6)	26.35
$v_R = 0.9 \cdot v_S$	3	7.79	11.91	0.73	1 (6)	3 (6)	26.40
	4	7.60	11.63	0.73	1 (6)	3 (6)	26.35
	5	7.60	11.63	0.73	1 (6)	3 (6)	26.35

Table 6.6: Lowest cost models resulting from 5 runs of the genetic algorithm for the 1977 (TARGET-C) earthquake ($M_W = 7.4$). The algorithm is run for a 90% ratio of rupture to shear wave velocity. The SMGA is once supposed to be square, once to have an aspect ratio of 1:1.5 (L:W). The position of the rupture initiation point is not expressed as a normalized value in the interval [0 1], but absolutely (the number in parentheses is the scaling factor $N = 6$).

degree from an isotropic decay with distance. It is not quite clear whether this shape is due to source effects (Miksat, 2006, reproduces these patterns by finite-difference simulations, where the source implementation is the dominant factor) or site respectively basin effects (Sokolov et al., 2004, on the other hand, manage to reproduce the intensity pattern by stochastic simulations assuming isotropic point sources).

The March 1977 Earthquake – TARGET-C

In principle, the inversion procedure is identical to the one described above for the waveform based inversions. The number of generations, after several test runs, is set to 150. In total, 15 s SH-wave records are simulated at 33 locations (from which instrumental intensities are estimated) using EGF-C200410 as empirical Green's function, and the frequency range considered is 0.2-12 Hz. This is approximately also the range of frequencies that are of importance in Sokolov (2002)'s method. As discussed in Section 6.3, the values of C and N cannot be evaluated from the spectral ratios in this case. Therefore, C is set to 1 (which is equivalent to pure self-similarity) and N is computed to be 6 from the seismic moment ratio.

I perform two different inversions. During the first one, the aspect ratio of the SMGA is supposed to be square (which is, in view of the results obtained for the other TARGET events, a reasonable approximation), while the second inversion is computed for an aspect ratio identical to the one of the lowest cost SMGA model of TARGET-A (which is approximately L:W=1:1.5). As the latter earthquake is used as EGF here, the subfault size resulting from this inversion should be approximately the same as the SMGA size derived for TARGET-A. Furthermore, the observed record at station INB can be used an independent additional information in order to check the result of the inversion. The simulation at station INB using the lowest cost SMGA model should of course not completely contradict the only observation.
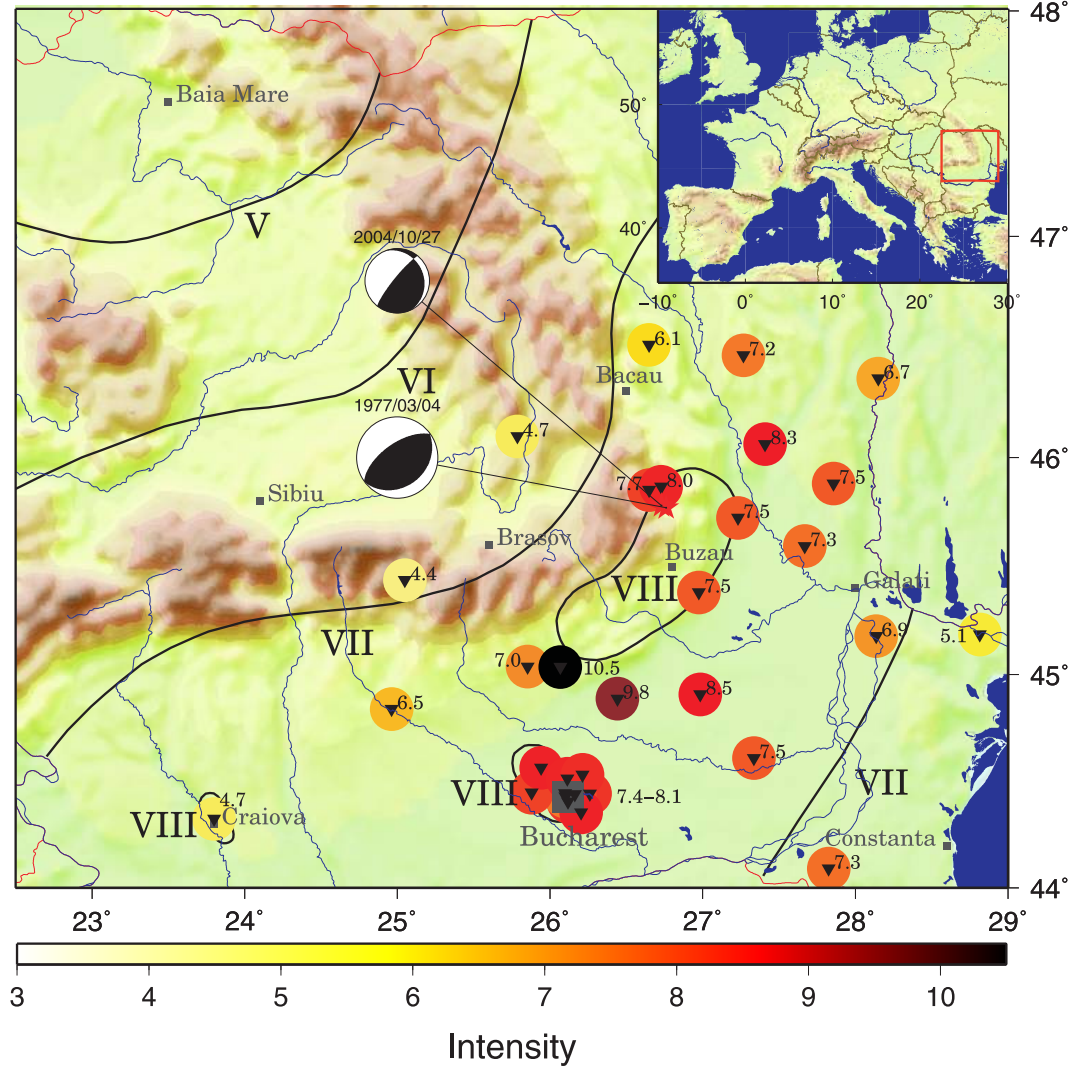
Figure 6.25: Comparison of simulated (with square SMGA) and observed intensities for the 1977 (TARGET-C) earthquake. The black lines indicate the observed isoseismals (cf. Figure 6.24), whereas the colored dots show the simulated intensity values using the methodology of Sokolov (2002) for the lowest cost SMGA model. The simulated intensities are additionally displayed close to each dot. The epicenters of TARGET-C and EGF-C200410 are included in the map.

As the lowest cost SMGA model for TARGET-A was obtained for a ratio of rupture to shear wave velocity of $v_R/v_S = 0.9$, the inversion here is performed for this value of v_R/v_S. The results are listed in Table 6.6 and the intensity values at the 33 stations which result from the best SMGA model (square SMGA) are plotted, together with the observed isoseismals, in Figure 6.25. Although the scatter is rather large, the main features of the intensity pattern can be explained acceptably well with the inverted solution (both with the square and aspect ratio 1:1.5 SMGA). If only the inverted intensity values were known, one would probably draw a continuous isoseismal line for intensity VIII around the epicentral area and Bucharest instead of separate patches, and this intensity VIII area would be a bit larger than the observed ones. The small patch of large intensity (VIII) around Craiova cannot be reproduced with this dataset. However, as only one observation in that area has been included in the
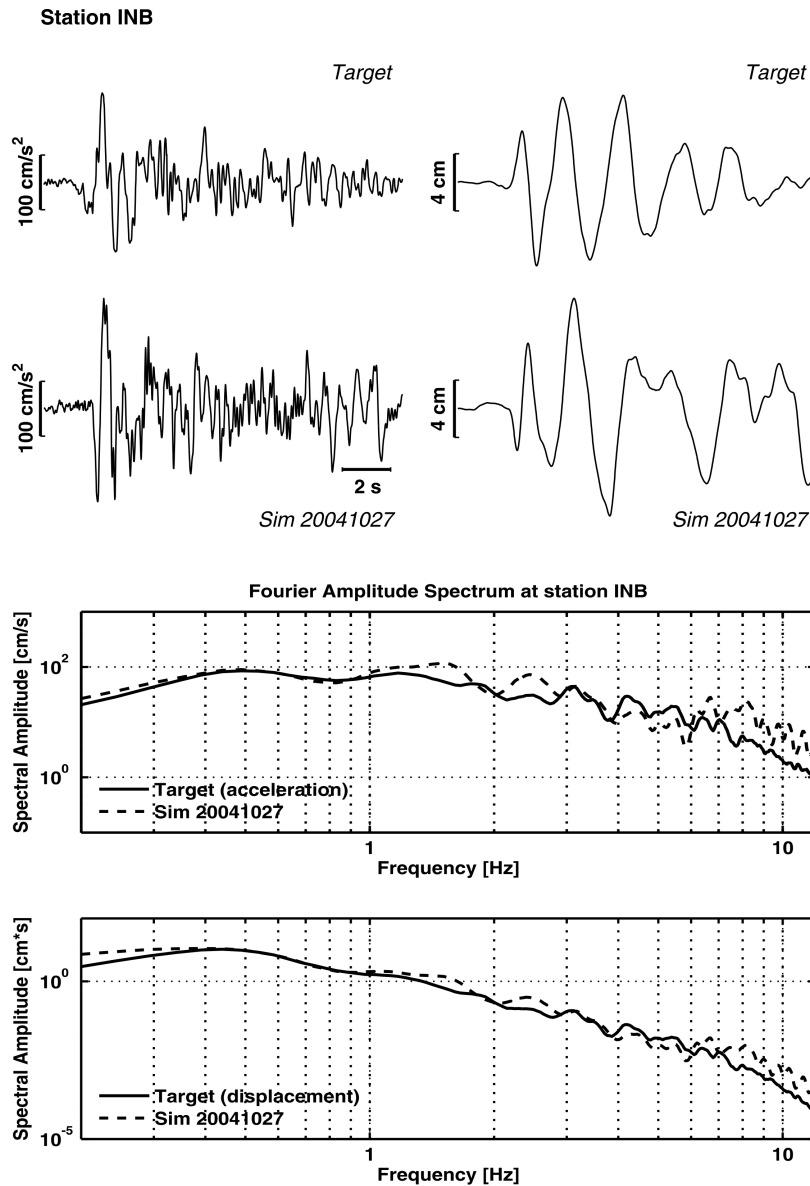
Figure 6.26: Top: Comparison of acceleration (left) and displacement (right) observed (top) and simulated (bottom) EW-component waveform at station Incerc (named INB in this study) of the 1977 (TARGET-C) earthquake. Bottom: Comparison of Fourier amplitude spectra.

inversion and intensity values reported at a given location strongly depend on local site conditions, it is not possible to draw any conclusion about this fact which would be representative. In summary, taking into consideration all the problems and uncertainties related with the compilation of such intensity maps and the unavoidable, quite large, standard deviation on the empirical relations between FAS and intensity, the overall inversion results are regarded to explain the observations sufficiently well.

Furthermore, it is encouraging to see that the only observed record is well fitted by the simulation using the intensity-derived SMGA model (Figure 6.26). Only the EW component is used as a means of evaluation as the NS component shows a peculiar dominance in terms of frequency content around

0.5 Hz. In addition, the subfault size and rise time are in very good agreement with the SMGA size and rise time for TARGET-A (see Tables 6.3 and 6.6), as required in order for the inversions for TARGET-A and -C to be consistent with each other.

The convergence of the algorithm is rather quick, as can be seen from Figure 6.27, and the histograms for the different model parameters depicted in Figures 6.28 (square SMGA) and 6.29 (aspect ratio 1:1.5 SMGA) prove that the lowest misfit models are well constrained.
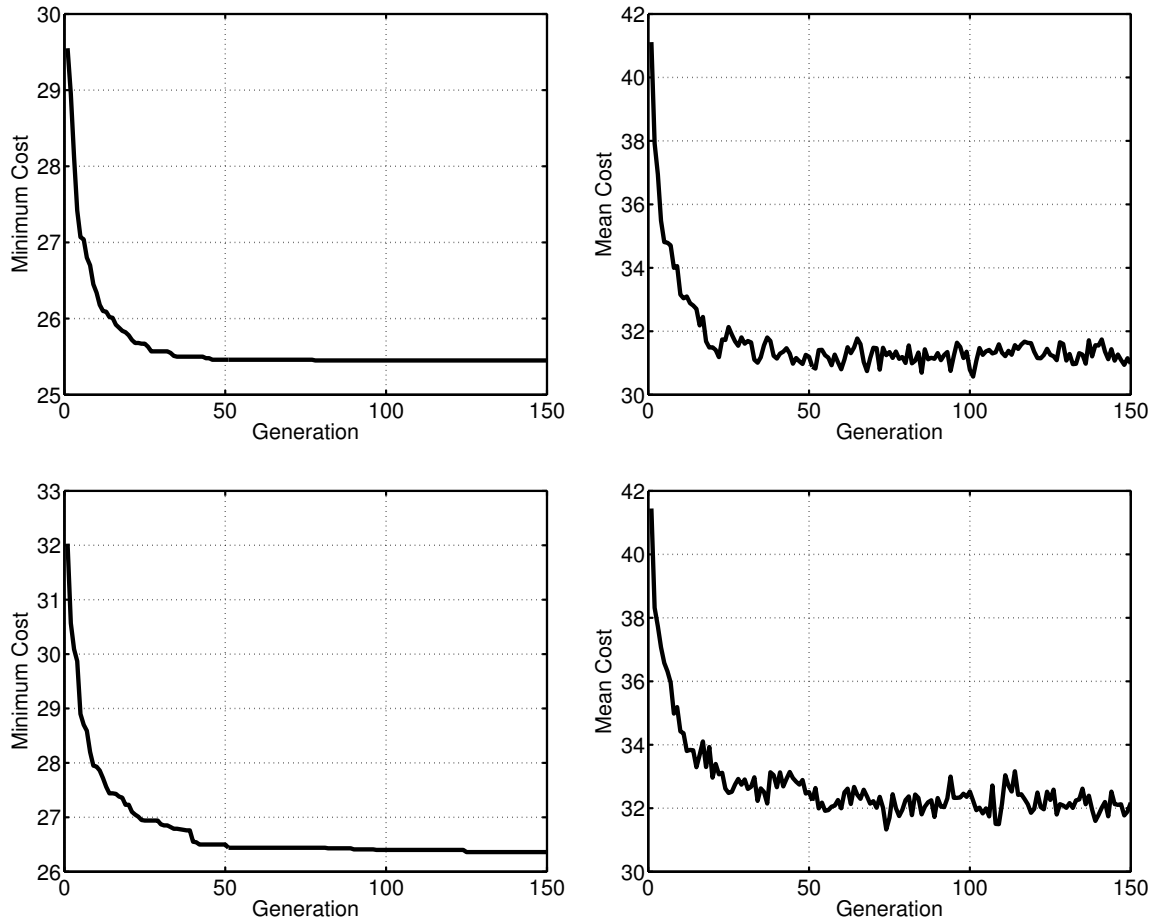
Figure 6.27: Convergence plots for the 1977 (TARGET-C) earthquake for $v_R/v_S = 0.9$. Top: Square SMGA. Bottom: SMGA with aspect ratio 1:1.5. Left: Evolution of the minimum cost (misfit) from generation to generation. Right: Evolution of mean cost. The curves shown here represent the evolution of the cost averaged over 5 runs of the algorithm.

6.5   Physical Interpretation and Discussion

The lowest cost SMGA models of the four analyzed earthquakes are schematically shown in Figure 6.30. The 'grid' composed of the subevents is only shown for TARGET-C and TARGET-D, as these SMGA's were inverted using one EGF only. For the other two events, the approximate rupture starting point has been determined from the normalized value. Further discussions on these sketches follow further below.
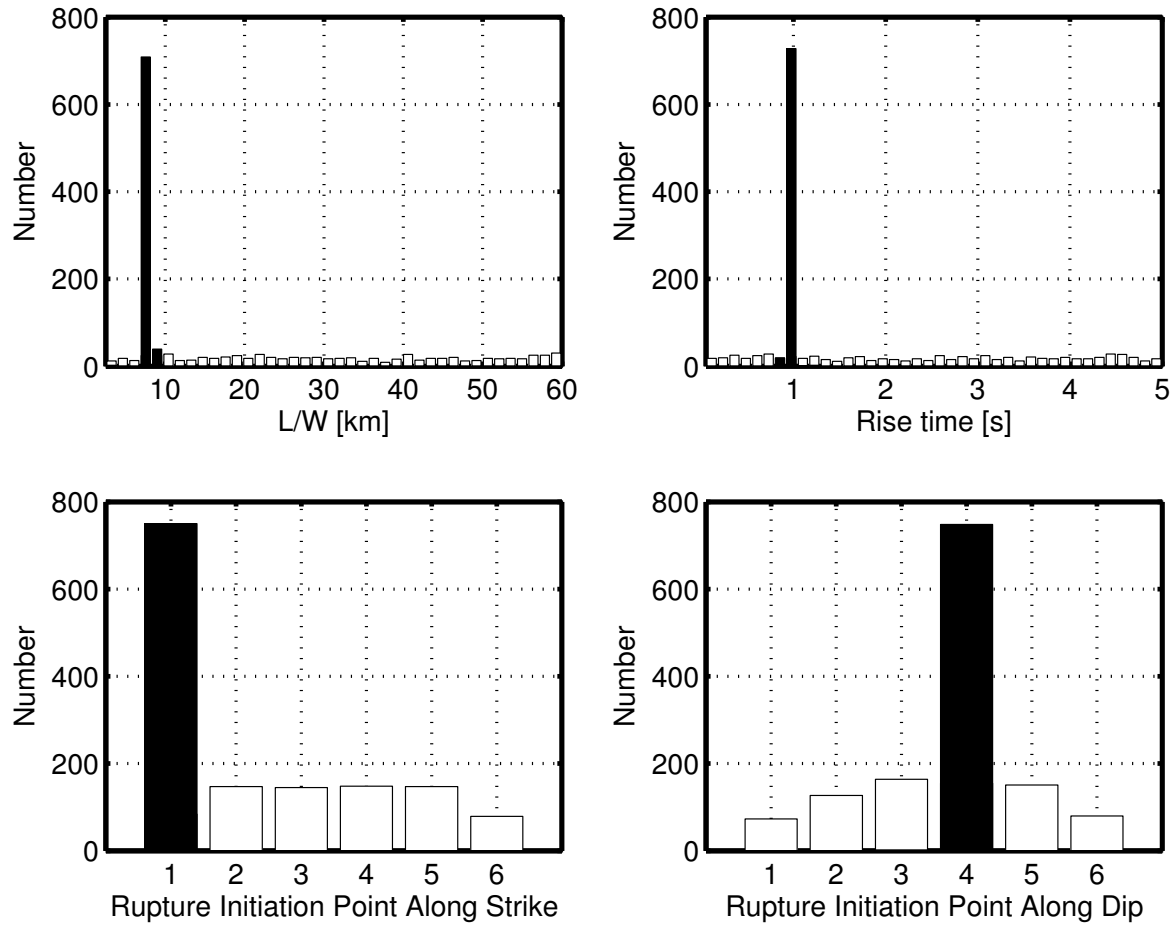
Figure 6.28: Histograms of 750 best solutions for the 1977 (TARGET-C) earthquake for $v_R/v_S = 0.9$ and a square SMGA (150 best from each of 5 runs). Upper left: SMGA length/width L/W [km]. Upper right: Rise time T_r [s]. Bottom left: Rupture initiation location along strike. Bottom right: Rupture initiation point along dip. White bars: Initial sampling of the parameter space when starting the genetic algorithm (150 starting models from each run).

Several studies concerning the source parameters of Vrancea earthquakes exist and especially the stress drop values of these are a matter of an ongoing debate. Different approaches have been used to determine stress drop values, and these techniques have been discussed in Chapter 3. The assumption that the rupture area is equal to the area where aftershocks occurr has been used by Räkers and Müller (1982) and Trifu and Oncescu (1987) to estimate the static stress drop of the 1977 and 1986 Vrancea earthquakes. These authors obtained stress drop values ranging around 50 bars. Another common approach is to compute the corner frequency and seismic moment from the source spectra and to estimate the (static and/or dynamic) stress drop using e.g. the model of Brune (1970, 1971) or Madariaga (1976). Gusev et al. (2002) found stress drops of the order of 100 to 200 bars for the two large 1977 and 1986 earthquakes, which have also been analyzed above, using long-range (several hundred to thousands km) and teleseismic data. Oncescu (1989) applied this methodology to analogue strong motion recordings (some of which being also used in this study) of the 1986 earthquake and computed a Brune stress drop (meaning using Brune's relation between corner frequency and source
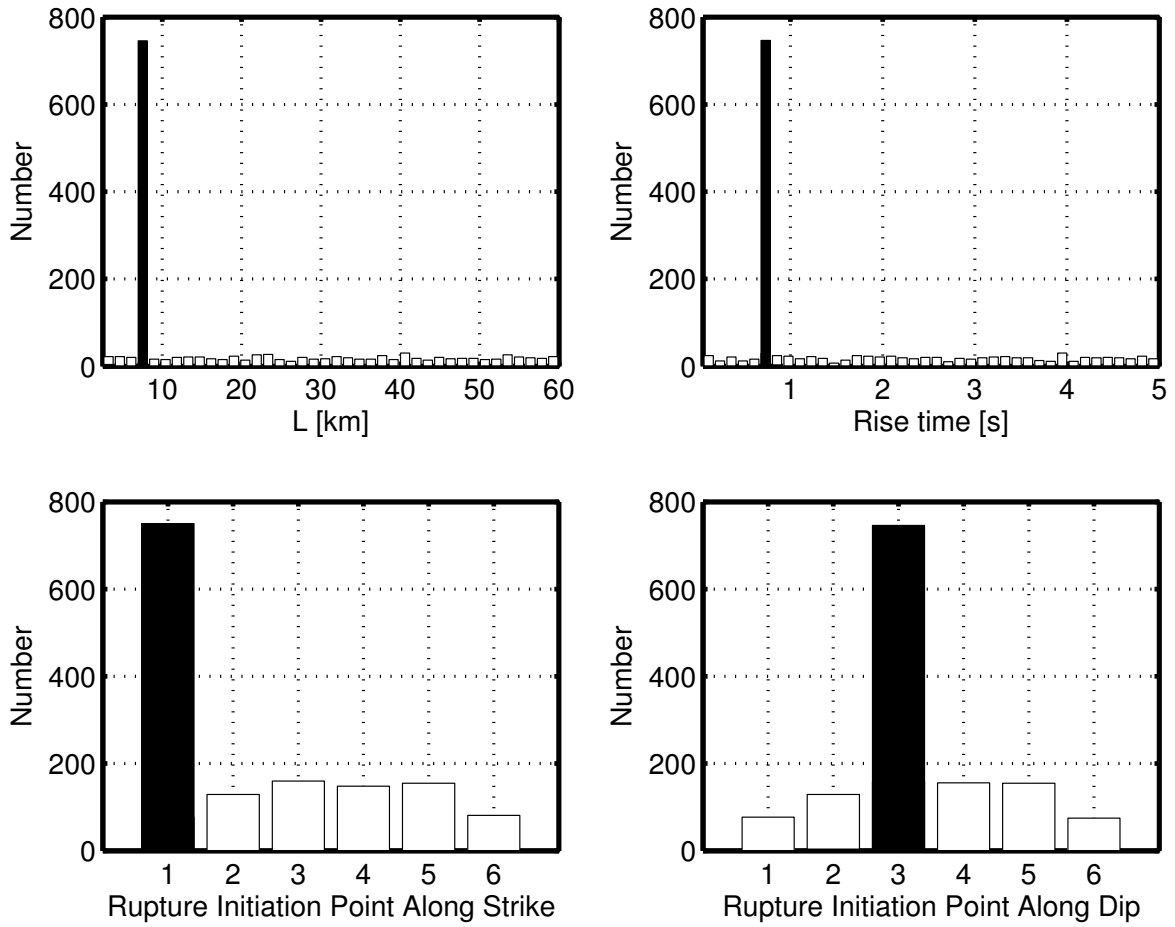
Figure 6.29: Histograms of 750 best solutions for the 1977 (TARGET-C) earthquake for $v_R/v_S = 0.9$ and an SMGA with $W = 1.5 \cdot L$ (150 best from each of 5 runs). Upper left: SMGA length L [km]. Upper right: Rise time T_r [s]. Bottom left: Rupture initiation location along strike. Bottom right: Rupture initiation point along dip. White bars: Initial sampling of the parameter space when starting the genetic algorithm (150 starting models from each run).

radius) of around 850 bars. Furthermore, Oncescu (1989) determined estimates of the dynamic stress drop using the methods described in Chapter 3.3, which range between 950 bars and 1.4 kbar.

As discussed in the latter chapter, if the aftershock area is being used as a criterion for fault size, static stress drop is estimated as an average value over the entire fault rather than asperity area. This applies to the corner frequency technique too in the case where long-range or even teleseismic data are utilized. High frequency components of ground motion are efficiently attenuated for this type of data due to the long propagation paths. For instance, a crustal earthquake of magnitude 5.5 is expected to show a corner frequency of around 0.5 Hz, assuming Brune (1970, 1971)'s model with a typically used stress parameter of 50 bars and a shear wave velocity of 3.5 km/s. With a Q-model of, for instance, $Q(f) = 100 f^{0.8}$ and an attenuation operator of the form (2.44), the spectral amplitude at 0.5 Hz is damped by a factor 5-10 at a distance of 250 km and by a factor of 20-50 at a distance of 500 km, depending on the chosen shear wave velocity. This effect even aggravates for higher corner frequencies, as they have been determined for Vrancea earthquakes in this study. Thus, attenuation
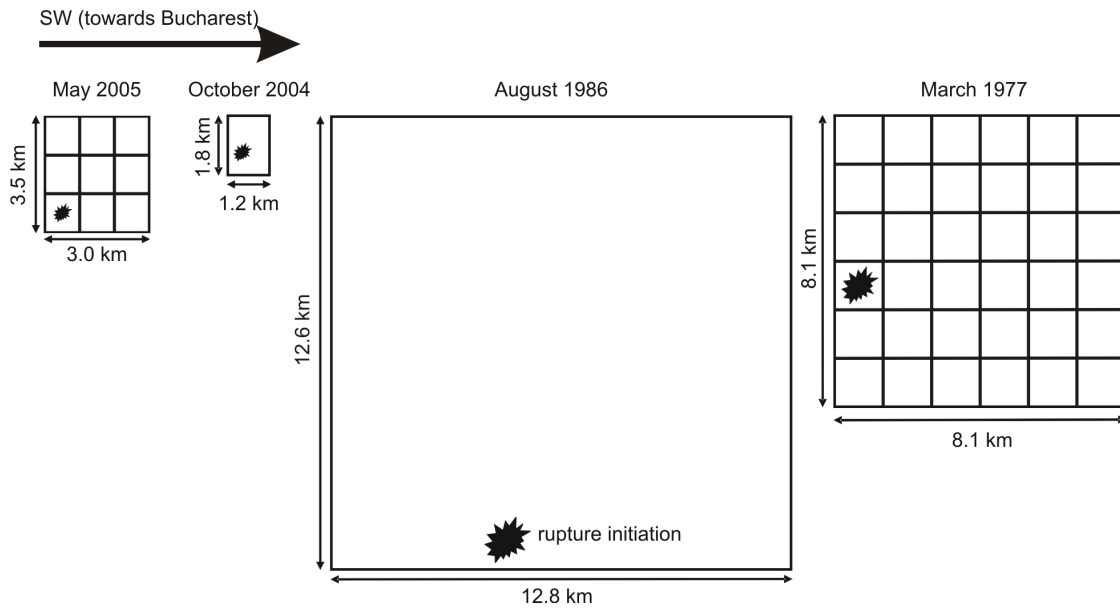
Figure 6.30: Sketches of the SMGA lowest cost models for the four analyzed moderate to large Vrancea earthquakes. The relative dimensions are scaled correctly. The (approximate) rupture initiation locations are depicted by stars. The 2005 (TARGET-D) and 1977 (TARGET-C) SMGA's are shown with the 'grid' composed of its subevents (as the inversion is performed using one EGF only). Note the very similar size of the SMGA of the 2004 (TARGET-A) earthquake and the subevent (EGF-C200410) of the 1977 (TARGET-C) event.

is expected to radically filter away high frequency ground motions around and larger than the corner frequency, which are absolutely essential in order to estimate the asperity stress release.

It is hence not surprising that these techniques and/or datasets lead to rather low stress drop estimates. In order to get insight into the asperity stress release, which is the most important with respect to strong ground motion prediction and seismic hazard assessment, it is indispensable to analyze local strong motion data, as done by Oncescu (1989) and in this work.

Interpreting the results of my inversions in terms of stress drop and other physical source parameters is not a trivial task either, since these estimates strongly depend on whether the SMGA is considered to be an asperity within a larger background rupture area that shows no significant stress drop, but, due to its slippage, contributes to the seismic moment of the event, or a simple crack releasing the complete seismic moment. This difference has already been discussed in Chapter 4.1 in the framework of Irikura's source model. As noted there, one should expect to see a systematic difference at low frequencies (i.e., if it can be seen, then in displacement) between synthetic and observed time histories if the SMGA is equivalent to an asperity in the stress-free field, which should be an underestimation of the low frequency ground motion by the simulations. By looking at the comparisons between best fitting synthetics and observations, even if all high frequency components are filtered away, no such systematic underestimation could be detected. This may however also be due to the fact that very low frequencies cannot be modeled due to the SN-ratio constraints. Therefore, from this point of view, I cannot prefer one model to the other.

Yet, a simple crack model would lead to exorbitantly high stress drop estimates (up to 5-10 kbar). As the aftershock distribution can be seen as an estimate for the total fault area (and, if the earthquake is

crack-like, the size of the crack is equal to the entire fault plane), such an interpretation would also be inconsistent with earlier studies on aftershock distributions (e.g. Trifu and Oncescu, 1987).

Therefore, I follow the interpretation of Miyake et al. (2003) and consider the SMGA to be equivalent to an asperity in the stress-free field. They came to this conclusion by comparing the size and position of the SMGA with the results derived from low frequency slip inversions for several japanese crustal earthquakes. Such slip inversions do unfortunately not exist for intermediate-depth Vrancea earthquakes. There-

Event ID	$\Delta\sigma_{SMGA}$ [bar]	$\langle\dot{U}\rangle$ [m/s]	$\bar{D}$ [m]
TARGET-A (2004)	900-1200	3.5-4.5	0.8-1.0
TARGET-B (1986)	300	4.0	2.2
TARGET-C (1977)	900-1200	3.0-3.5	5.0-5.5

Table 6.7: Approximate static stress drop, particle velocity and slip estimates for the lowest cost SMGA models for the different TARGET earthquakes. The range of values given for TARGET-C is due to the fact that two separate inversions were computed, and the one for TARGET-A is due to the same origin, as the stress drop ratio between these earthquakes has been assumed to be $C = 1$.

fore, in order to estimate the spatial extent of the entire rupture plane, the only source of information that can be relied on are the aftershock distributions. If the approximate radius of the total rupture plane is known, the static stress drop within the asperity can be computed using equation (4.26):

$$\Delta\sigma_{asperity} = \frac{7}{16} \cdot \frac{M_0}{Rr^2}, \tag{6.3}$$

where r is the radius of the equivalent circular asperity and R is the radius of the equivalent circular fault plane.

For TARGET-B (1986), Oncescu (1989) proposed an asperity of approximately 160 km^2 within a total rupture area of about 700 km^2. The size of the lowest misfit SMGA (Table 6.4) is surprisingly close to this asperity size estimate. For TARGET-A (2004), the situation is complicated by the fact that almost no aftershocks occurred (Bonjer, personal communication, 2006), which makes it impossible to estimate the extent of the rupture using this information. The same problem applies to TARGET-D (2005), where no information on the entire fault plane extent is available. For TARGET-C (1977), Hartzell (1979) and Räkers and Müller (1982) proposed fault dimensions ranging around 2000 km^2 (Hartzell proposed a circular fault with 25 km radius, whereas Räkers and Müller favored a spatial extent of 60×40 km).

As already mentioned in Chapter 4.1, relation (6.3) means in fact nothing else than computing the stress drop for a circular crack with the same size as the desired asperity with a seismic moment reduced by the factor r/R to account for the slip existence outside the asperity. With this reduced seismic moment, estimates for further parameters, such as slip $\bar{D}$ and particle velocity $\langle\dot{U}\rangle$ (in combination with the rise time T_r) on the asperity can be derived. The approximate values computed for TARGET-A, -B and -C are listed in Table 6.7 (assuming $\mu = 7 \cdot 10^{10} N/m^2$). TARGET-D is not listed as there is no possibility to obtain any information on the size of the entire rupture plane. This problem is circumvent for TARGET-A, as it was assumed in the inversions for TARGET-C that these two earthquakes depict the same stress drop. From this stress drop estimate obtained for TARGET-A, a total fault plane size of roughly 30-40 km^2 can be deduced. It must however be noted that these source parameter estimates are all only approximate, as they are based on the simple model of an asperity in the stress-free field as considered by Madariaga (1979), Das and Kostrov (1986) or Boatwright (1988) and represent an average over the asperity, as no heterogeneities of faulting are included in the SMGA source model.

Event ID	f_c [Hz]	SMGA size [km²]	Brune [km²]	Madariaga [km²]
TARGET-A (2005)	1.60	2.1	3.4	1.1
TARGET-B (1986)	0.30	161.8	98.0	31.2
TARGET-C (1977)	0.26	65.1	130.5	41.5
TARGET-D (2005)	1.10	10.6	7.3	2.3

Table 6.8: Comparison of the lowest cost SMGA dimensions with predictions of Brune's (1970,1971) and Madariaga's (1976) model. The corner frequency for TARGET-C is estimated from the one of TARGET-A by division through the scaling factor $N = 6$.

Two major conclusions arise from the results of this study. First, the 1977 as well as the 2004 earthquakes seem to show 2-3 times larger (static) stress drops than the 1986 earthquake. The second striking feature is the fact that the three events included in Table 6.7 are very similar from the dynamic point of view, as they display very similar particle velocities and thus, dynamic stress drops ranging around 1 kbar. TARGET-D, even though its absolute value of slip velocity cannot be computed, also shows a short rise time, which is an indication for a high particle velocity too. These large values of the particle velocity respectively dynamic stress drop are responsible for the strong high frequency radiation.

Regarding the discussion on the relation between corner frequency and source radius in Chapter 3.2, one may of course compare the results obtained for the source area of the SMGA with the predictions of different models, such as Brune's (1970,1971) or Madariaga's (1976) model, as done in Table 6.8. Madariaga (1976)'s model systematically underestimates the SMGA size by a factor 1.5-5, whereas Brune's (1970,1971) model once predicts a larger source size, once a smaller one, with a maximum difference of a factor of 2. The formulas between corner frequency f_c and source radius r are for both models:

$$f_c = C \cdot \frac{v_S}{r} , \tag{6.4}$$

with $C = 2.34/2\pi$ in Brune's case and $C = 1.32/2\pi$ for Madariaga's model. It is interesting to note that, apparently, the deeper two events (TARGET-B and -D) are better explained by Brune's relation, whereas the two shallower ones (TARGET-A and -C) are closer to the expectations resulting from Madariaga's relation. Note however that I do not intend to provide a relation between f_c and r, due to the fundamental problems pointed out in Chapter 3.2. This comparison is only for the sake of completeness, as such models are often used in seismological practice. Additionally, especially the Madariaga (1976) model is a crack type model, which would be in contradiction with the asperity interpretation and the short rise times determined above. For instance, with equation (4.27), a static stress drop of 10 kbar would be deduced using Madariaga's relation.

The differences in SMGA size and stress drop between the 1977/2004 and 1986/2005 earthquakes (and, which should not be forgotten at this point, their EGF events), also lead to the possible conclusion that the events occurring in the depth range 90-110 km show somewhat different source properties than the deeper ones (130-150 km). Yet, the database is definitely not large enough to firmly constrain such a hypothesis and it is, at present, a matter of speculation founded on few data.

The sketches depicted in Figure 6.30 are also interesting regarding directivity effects. During the 1977 earthquake, strong damage and many fatalities occurred in Bucharest, whereas the city was not that heavily harmed during the 1986 event. Hartzell (1979) already discussed directivity differences between the 1977 and 1940 earthquakes. All SMGA models shown in Figure 6.30 depict a clear

directivity effect towards Bucharest. For TARGET-B (1986), however, the directivity is much stronger updip than along strike, which could be an explanation for the high intensity spot close to the epicenter, whereas the areal distribution of high intensities is much smaller than for TARGET-C (1977), as Figure 6.24 clearly indiciates. In 1977, the main directivity effect on the SMGA seems to have taken place along strike, towards Bucharest, and only a weaker directivity updip is observed. This may be one of the factors explaining the intensity VIII spot in Bucharest and the very large extent of the intensity VII area. Other contributing factors to the strong differences in the intensity maps of these two earthquakes may also include differences in the stress release, as the results presented above indicate, and of course the shallower depth of the 1977 earthquake (which took place about 40 km closer to the Earth's surface than the 1986 event). This discussion can however not be conclusive on this matter, as the inversion results for TARGET-B are not unambiguous.

The scaling behavior of the SMGA size and rise time with seismic moment is graphically displayed in Figure 6.31. The black line in these Figures represents the scaling relations empirically determined by Somerville et al. (1999) for crustal earthquakes from low frequency finite-fault rupture models. As can be seen, the SMGA dimensions are smaller by a factor up to 10 for the four Vrancea earthquakes treated in this study. Only the 2005 earthquake (TARGET-D) shows an SMGA size a bit larger than expected for a crustal SMGA (Miyake et al., 2003, show that the SMGA of crustal earthquakes closely follows the scaling of Somerville et al., 1999). The rise time is systematically smaller than the one expected for crustal earthquakes by a factor of 2-8, which indicates that the particle velocity will also be larger. Miyake et al. (2003) conclude that the crustal SMGA, which obeys Somerville et al.'s (1999) scaling relations, corresponds to a 100 bar (static) stress drop asperity. Thus, if, on average, the SMGA size of Vrancea earthquakes is smaller by a factor of about 5, the static stress drop will be, on average, larger by roughly an order of magnitude. Consequently, even though four earthquakes are of course not a very large dataset (nevertheless, it is the largest dataset of moderate to strong Vrancea earthquakes in terms of high-quality recordings ever analyzed), the results presented here lead to the conclusion that the intermediate-depth Vrancea earthquakes are inherently different from crustal ones.

Do intermediate-depth earthquakes in other areas of the world show similar source characteristics? Suzuki and Iwata (2005a) present SMGA parameters from a very similar study than the one performed in this work for ten japanese interplate earthquakes (with depths ranging between 30 and 50 km, which is somewhat shallower than the Vrancea events, but yet larger than for typical crustal earthquakes), which are included as a means of comparison in Figure 6.31. These earthquakes seem to show a very similar scaling behavior of the SMGA, although the scatter (especially in the rise time estimates) is also rather large. Within the uncertainity ranges, the results obtained for the four Vrancea earthquakes can be regarded to be compatible with the ones of Suzuki and Iwata (2005a). Thus, there is a line of evidence which leads to the conclusion that the scaling behavior of the SMGA's (respectively asperities) for intermediate-depth earthquakes is rather different of the one for crustal earthquakes. The former ones show a much larger particle velocity and static stress drop, and these facts have to be taken into account when performing strong motion simulations and when assessing seismic hazard from this type of earthquakes.
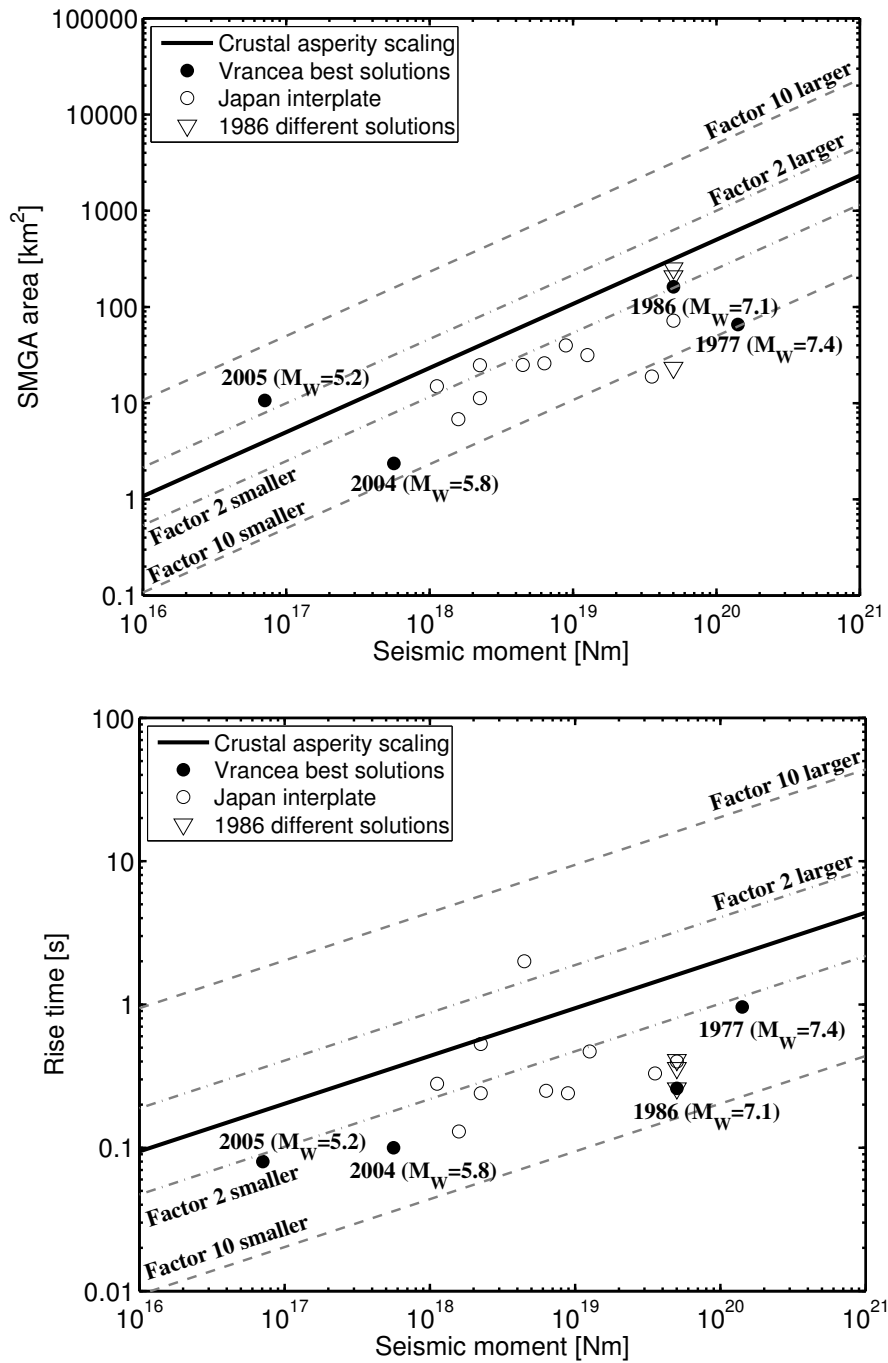
Figure 6.31: Top: Scaling of the SMGA size with seismic moment. Bottom: Scaling of the rise time with seismic moment. The black line represents the scaling for crustal asperities as given by Somerville et al. (1999) (the grey dotted lines indicate sizes a factor of 2 and 10 smaller/larger than Somerville et al.'s scaling). The black dots depict the best solutions for the four Vrancea earthquakes treated in this work. As the results for the 1986 (TARGET-B) earthquake are ambiguous, the different 'best' solutions with similar cost are plotted with open triangles. As a means of comparison, the results for Japanese interplate earthquakes (Suzuki and Iwata, 2005a) are shown by open circles.

Chapter 7

Spectral Ground Motion Models of Vrancea Earthquakes

After the investigation of the source processes of Vrancea earthquakes with empirical Green's functions simulations presented in the previous chapter, the purpose of this chapter is to determine spectral ground motion models which describe the source, propagation (i.e. attenuation along the path) and site effects. The aim of this effort is two-folded: first, by separating the three above-mentioned contributions from each other, important physical insights can be gained on the source process of these earthquakes (in addition to the information gained in Chapter 6), the attenuation characteristics of seismic waves in the region of interest and the site amplification at the station locations. A detailed knowledge on the expected site amplification is of central importance for the design of earthquake resistent structures. Second, the derived spectral ground motion models can in principle be used to stochastically simulate (e.g. Boore, 2003, see also Chapter 4.2) acceleration time histories of hypothetical large earthquakes at any site of interest (after an appropriate classification of the site) on Romanian territory. This approach has already been applied by Sokolov et al. (2004) with a different spectral model than the one derived in this work, and the differences will be discussed at the end of the chapter. A further attempt of stochastically simulating Vrancea earthquakes is given by Benetatos and Kiratzi (2004), who used the FINSIM methodology (Beresnev and Atkinson, 1997, 1998) to simulate the large Vrancea earthquake which occurred on May 30, 1990 ($M_W = 6.9$).

Using the *generalized inversion technique (GIT)* (e.g. Castro et al., 1990; Parolai et al., 2000, 2004a; Bindi et al., 2006a), the S-wave acceleration Fourier amplitude spectra (FAS) of 55 intermediate-depth Vrancea earthquakes at 43 K2 stations spread over Romania are analyzed. This methodology is commonly applied for crustal earthquakes, where the azimuthal coverage of the sources around the stations is usally good and inhomogeneities in attenuation average out (and can consequently be described by one average function). As I will show below, this is not true in the case of the intermediate-depth Vrancea earthquakes, as the geometry of the dataset is very special. To my knowledge, the GIT has not been applied to such a dataset before. Therefore, it should be emphasized that this is not a routine application of this well-studied technique and several complicating aspects unkown in GIT applications before have to be taken into account. Especially with respect to attenuation, the GIT method is adapted to this new situation and hence, this study also provides new insights from the methodological point of view.

In Section 7.1, a short introduction into the GIT method is given, followed by a description of the database and the processing of the data in Section 7.2. Section 7.3 deals with the attenuation in

the area, which must be described with two separate functions for different regions, indicating strong changes in attenuation depending on the path traveled by the seismic waves. Following a discussion of the obtained attenuation functions, both in terms of their physical meaning as well as the implications for seismic hazard assessment, the attenuation-corrected data are inverted to isolate the source and site contributions to the spectra in Section 7.4, and the resulting source spectra are further interpreted in the context of the ω^{-2}-model (Brune, 1970, 1971). The site amplification functions are then compared to the H/V ratios (Section 7.5). Finally, the implications for ground motion simulations and a comparison with existing ground motion models (Sokolov et al., 2004, 2005) are discussed in Section 7.6. A final summary concludes the chapter in Section 7.7.

7.1 The Generalized Inversion Technique (GIT)

The generalized inversion technique is based on the convolutional model of ground motion (corresponding to a multiplication in frequency domain) given by equation (2.39):

$$U_{ij}(f, R) = S_i(f) \cdot P(f, R) \cdot I_j(f), \qquad (7.1)$$

where $U_{ij}(f, R)$ denotes the observed (in this case acceleration, either horizontal or vertical component of ground motion) FAS from source i and site j (located at hypocentral distance R), $S_i(f)$ is the source contribution, $P(f, R)$ the attenuation along the travel path and $I_j(f)$ represents the local site amplification. By taking the logarithm (I use $\log_{10}$) of the above equation, the problem can be linearized (instabilities where the spectral amplitude is close to zero are smoothed away, see Section 7.2):

$$\log U_{ij}(f, R) = \log S_i(f) + \log P(f, R) + \log I_j(f). \qquad (7.2)$$

For N_{rec} available recordings, (7.2) represents a linear system of equations (with N_{rec} equations) of the form:

$$\mathbf{Ax} = \mathbf{b}, \qquad (7.3)$$

with system matrix $\mathbf{A}$, model vector $\mathbf{x}$ and data vector $\mathbf{b}$. In contrast to e.g. seismic tomography problems, which are usually mixed-determined, the inverse problem given by (7.2) and (7.3) is generally overdetermined, as of course at least one record for each station and one record for each source are included in the dataset. Usually only stations and, respectively, sources with a certain minimum number of recordings (I use a minimum number of three records per station and event) are used in order to ensure well-constrained solutions for each of the variables. Thus, for each frequency, the least squares solution $\mathbf{x} = (\mathbf{A}^T\mathbf{A})^{-1}\mathbf{A}^T\mathbf{b}$ (if the system is numerically stable and a constraint fixing the undetermined degree of freedom discussed below has been introduced) can be computed by means of an appropriate inversion scheme (e.g. singular value decomposition, Menke, 1989).

This approach was first proposed by Andrews (1986), who worked on data recorded at small hypocentral distances (and corrected for geometrical spreading) and left out the second term on the right-hand side of equation (7.2):

$$\log U_{corr,ij}(f) = \log S_i(f) + \log I_j(f). \qquad (7.4)$$

If an appropriate attenuation model is known from other studies (geometrical spreading and Q-model if the distances are larger) and considering N_E sources and N_S sites, the number of unknowns is given by $N_E + N_S$ and the system matrix is composed solely of zeros and ones. Other examples for the inversion of attenuation-corrected data can be found in Hartzell (1992), Hartzell et al. (1996) or

Parolai et al. (2001). Equation (7.4) corresponds to the second step in the non-parametric two-step inversion scheme (Castro et al., 1990), which I introduce further below.

As Andrews (1986) and subsequent researchers discuss, there is one unresolved degree of freedom in (7.2) and (7.4), because multiplying all the solutions for the sources with a given function of frequency and dividing all the solutions for the sites by the same function would not alter the fit to the data. This can also easily be seen from the singular value decomposition of matrix **A**, where one singular value is zero. To remove this indetermination, one can for instance either fix (at least) one source or one site function to a given a priori value. A common constraint is to set the site response I of one rock station in the dataset to one (resp. zero in logarithm), irrespective of frequency (e.g. Hartzell, 1992; Hartzell et al., 1996), or to set the average of $\log I$ of several stations or the entire network in (7.2) to zero. Moya and Irikura (2003) present an inversion scheme using a reference event which is based on spectral ratios between different sites.

In order to invert simultaneously for source, attenuation and site effects, there are two approaches which are usually followed: the first one is to express the attenuation with a given model, thus assuming a certain distance dependence (the *parametric* approach, e.g. Castro et al., 1990; Salazar et al., 2007), while in the second one, attenuation is only constrained to be a smooth function of distance, without any predefined parametric shape (the *non-parametric* approach, e.g. Castro et al., 1990, 1996, 2003; Parolai et al., 2004a, 2007; Bindi et al., 2006a). I will now briefly describe both inversion schemes, but only results obtained using the non-parametric approach will be shown in this work.

7.1.1 Inversion with a Parametric Attenuation Model

The attenuation along the propagation path is commonly parameterized by equation (4.33):

$$P(f, R) = G(R)E(R, f) = G(R) \exp\left[-\frac{\pi f R}{Q(f)v_S}\right].$$ (7.5)

Thus, if the spectra are corrected for a given geometrical spreading function $G(R)$, for instance given by (4.34), the system of equations (7.2) becomes (with $\log e \approx 1/2.3$):

$$\log U_{ij}(f, R) - \log G(R) = \log S_i(f) - \underbrace{\frac{\pi f}{2.3 Q(f)v_S}}_{d(f)} R + \log I_j(f).$$ (7.6)

The system matrix is composed of ones and zeros for the source and site terms, whereas the last column has to be filled with the hypocentral distance R_{ij} for the couple S_i and I_j. Hence, for a given frequency, (7.6) can be written in matrix formulation:

$$
\begin{pmatrix}
1 & 0 & 0 & \cdot & \cdots & 1 & 0 & 0 & \cdot & \cdots & R_{11} \\
0 & 1 & 0 & \cdot & \cdots & 1 & 0 & 0 & \cdot & \cdots & R_{21} \\
\cdot & \cdot & \cdot & \cdot & \cdots & \cdot & \cdot & \cdot & \cdot & \cdots & \cdot \\
0 & 0 & 1 & \cdot & \cdots & 0 & 1 & 0 & \cdot & \cdots & R_{32} \\
\cdot & \cdot & \cdot & \cdot & \cdots & \cdot & \cdot & \cdot & \cdot & \cdots & \cdot \\
\cdot & \cdot & \cdot & \cdot & \cdots & \cdot & \cdot & \cdot & \cdot & \cdots & \cdot \\
\cdot & \cdot & \cdot & \cdot & \cdots & \cdot & \cdot & \cdot & \cdot & \cdots & \cdot \\
\vdots & \vdots & \vdots & \vdots & \vdots & \vdots & \vdots & \vdots & \vdots & \vdots & \vdots \\
0 & 0 & 0 & \cdot & \cdots & 1 & 0 & 0 & \cdot & \cdots & 0
\end{pmatrix}
\cdot
\begin{pmatrix}
\log S_1 \\
\cdot \\
\cdot \\
\log S_{N_E} \\
\log I_1 \\
\cdot \\
\cdot \\
\log I_{N_S} \\
d
\end{pmatrix}
=
\begin{pmatrix}
\log U_{11} - \log G(R_{11}) \\
\cdot \\
\cdot \\
\log U_{32} - \log G(R_{32}) \\
\cdot \\
\cdot \\
\cdot \\
\vdots \\
0
\end{pmatrix}.
$$ (7.7)

In (7.7), the site function $\log I_1(f)$ is constrained to equal zero (last row). From the obtained value for $d(f)$, an estimate for the quality factor $Q(f)$ can be derived. The inversion can be run for different geometrical spreading functions to assess the resulting variability in $Q(f)$, source and site functions. The parameterization of the attenuation model represents a rather strong constraint and possible differences between the true attenuation and the imposed model will inevitably appear in the source or site spectra.

A common problem is that negative estimates for $Q(f)$ are obtained (see e.g. Castro et al., 1990; Salazar et al., 2007). This would mean that the seismic waves are amplified with increasing distance traveled, which is unphysical, unless in the case where focusing effects play a role. Such results can for instance be due to the assumptions regarding the geometrical spreading, as discussed by Castro et al. (1990), or to the simple fact that the attenuation in the given region cannot be appropriately described with such a simple parameterization.

To compensate for the negative $Q(f)$, throughs appear either in the source or the site functions (depending on the chosen constraint). Thus, at least at the frequencies where the negative $Q(f)$ values appear, an interpretation of the inversion results is rather dangerous. Extensive trials using the parametric approach with the Vrancea data always led to negative $Q(f)$ values, mostly in the frequency range 2-5 Hz and even after consideration of the inhomogeneities in attenuation discussed in Section 7.3 and a respective modification of the scheme. Therefore, these results are not further discussed.

7.1.2 Two-Step Inversion with a Non-Parametric Attenuation Function

Castro et al. (1990) proposed a two-step inversion scheme which does not include any parameterization of the attenuation characteristics. In principle, the inversion could also be performed in one step, but splitting the problem into subinversions has the clear advantage that, for each of these, the number of unknowns involved is significantly smaller, which makes the inversion problem more practicable (Castro et al., 1995).

In a *first step*, the observed spectral amplitudes $U_{ij}(f)$ are expressed by the following model:

$$U_{ij}(f, R_{ij}) = M_i(f) \cdot A(f, R_{ij}), \qquad (7.8)$$

which, logarithmically, leads to:

$$\log U_{ij}(f, R_{ij}) = \log M_i(f) + \log A(f, R_{ij}). \qquad (7.9)$$

Herein, $M_i(f)$ is a scaling factor for the source i and $A(f, R_{ij})$ is the attenuation function describing the decay of the spectral amplitudes with distance. The site effects are absorbed in both $M_i(f)$ and $A(f, R_{ij})$, as discussed below. This function is not supposed to have any specific shape and implicitely contains all attenuation effects (geometrical spreading, anelasticity, scattering, . . .). Based on the idea that these properties vary slowly within the Earth, $A(f, R_{ij})$ is constrained to be a smooth function of distance and to take the value $A(f, R_0) = 1$ at the reference distance R_0. In matrix formulation, the

system of equations given by (7.9) takes the following form (see also Castro et al., 1990):

$$
\begin{pmatrix}
1 & 0 & 0 & \cdot & \cdots & 1 & 0 & 0 & \cdot & \cdots \\
0 & 1 & 0 & \cdot & \cdots & 1 & 0 & 0 & \cdot & \cdots \\
\cdot & \cdot & \cdot & \cdot & \cdots & \cdot & \cdot & \cdot & \cdot & \cdots \\
1 & 0 & 0 & \cdot & \cdots & 0 & 1 & 0 & \cdot & \cdots \\
\vdots & \vdots & \vdots & \vdots & \vdots & \vdots & \vdots & \vdots & \vdots & \vdots \\
w_1 & 0 & 0 & \cdot & \cdots & \cdot & \cdot & \cdot & \cdot & \cdots \\
-w_2/2 & w_2 & -w_2/2 & 0 & \cdots & \cdot & \cdot & \cdot & \cdot & \cdots \\
0 & -w_2/2 & w_2 & -w_2/2 & \cdots & \cdot & \cdot & \cdot & \cdot & \cdots \\
\cdot & \cdot & \cdot & \cdot & \cdots & \cdot & \cdot & \cdot & \cdot & \cdots
\end{pmatrix}
\cdot
\begin{pmatrix}
\log A_1 \\
\cdot \\
\cdot \\
\cdot \\
\log A_{N_D} \\
\log M_1 \\
\cdot \\
\cdot \\
\log M_{N_E}
\end{pmatrix}
=
\begin{pmatrix}
\log U_{11} \\
\cdot \\
\cdot \\
\log U_{ij} \\
\vdots \\
0 \\
0 \\
0 \\
\cdot
\end{pmatrix} . \quad (7.10)
$$

The attenuation function is computed for N_D distance bins, into which the distance range of the data is discretized. w_1 is a weighting factor to constrain $\log A(f, R_0) = 0$ and the value w_2 determines the degree of smoothness of the solution by imposing a small second derivative with respect to distance (i.e. imposing a piecewise linear function). It is important to note that the scaling factors $\log M_i(f)$ include the (logarithmic) average site effect of the stations which recorded this event. For each source, the deviation of the observed spectral amplitude for each datum from the function given by (7.8) respectively (7.9) is related to the difference of the site effect of this datum from the average value in $\log M_i(f)$. In other words: the site effects are supposed to average out in the determination of $A(f, R_{ij})$. Therefore, a reasonable choice for the weighting factor w_2 is important. If w_2 is too small, the undulations of the data related to site effects are not effectively suppressed. On the other hand, if w_2 is too large, the attenuation functions will results in straight lines, which would finally lead to the suppression of variations of attenuation characteristics with distance, which is just the effect that one is interested in.

Commonly, $R_0 = 0$ is chosen if the gap at low hypocentral distances in the database is not too large. As will be discussed later in this chapter, this is not possible in the case of the intermediate-depth Vrancea earthquakes, as the hypocentral distance is in this case mainly controlled by the large depth of the events. In this case, by setting $A(f, R_0) = 1$, one assumes that there is no attenuation up to reference distance (or, rather, one admits that one is not able to resolve what if happening over the scale of R_0). If R_0 is quite large, as it is the case for Vrancea earthquakes ($R_0 = 90$ km will be used below), the spectra are of course affected by attenuation over this distance. Therefore, this 'residual' attenuation appears in the second step of the inversion, either in the source spectra (if a site constraint is used, as is done in this work), or in the site amplification functions (if one of the sources is contraint to its absolute value at the hypocenter).

A clear advantage with respect to the parametric approach above is that the obtained attenuation functions can be evaluated with any kind of parametric model without the necessity to recompute the inversion. Comparison with equation (7.5) leads for instance to:

$$
\log A(f, R) = \log G(R) - \frac{\pi f}{2.3 Q(f) v_S} R . \quad (7.11)
$$

Thus, by fitting a straight line to the logarithm of the attenuation functions corrected by geometrical spreading and plotted versus distance, $Q(f)$ can be evaluated from the slope. One may also simultaneously fit $Q(f)$ and the geometrical spreading exponent to the data instead of correcting for a predefined geometrical spreading function, as done for instance by Bindi et al. (2006a).

The *second step* of the inversion deals with the separation of source $S_i(f)$ and site $I_j(f)$ functions. As explained by Castro et al. (1990), the attenuation functions obtained in the first step can be used to normalize the spectral amplitudes to the reference distance R_0 by computing:

$$R_{ij}(f) = \frac{U_{ij}(f, R_{ij})}{A(f, R_{ij})} = S_i(f) \cdot I_j(f). \tag{7.12}$$

As mentioned in the discussion on the first step, it is assumed that the site effects average out in the determination of $A(f, R_{ij})$. Taking the logarithm of this equation leads back to equation (7.4):

$$\log R_{ij}(f) = \log S_i(f) + \log I_j(f). \tag{7.13}$$

The system matrix is composed of zeros and ones. Here, the most important advantage of the non-parametric attenuation functions comes into play. No specific model assumption regarding attenuation is necessary to correct the data, which is especially advantageous if the non-parametric attenuation functions show variations with distance which cannot be easily explained by a simple model. Especially in the case of Vrancea earthquakes, as we will see below, the complexity of the attenuation characteristics is one of the key factors for understanding the observed ground motion spectra. The unresolved degree of freedom, as mentioned earlier, can be removed by either imposing one or several site or source constraints.

Two final important remarks on the GIT should be made at this point. First, the earthquake sources are supposed to be isotropic point sources. Thus, no directivity or other rupture propagation effects are taken into account. In the case study presented here, this approximation is acceptable, as most of the earthquakes are rather small magnitude events ($4 \leq M_W \leq 5$) and the hypocentral distances are always greater than approximately 90 km. Thus, the condition to be located in the far-field is certainly fulfilled. Regarding the isotropy of the source, radiation pattern effects are considered to be negligible in the frequency range used here (e.g. Takenaka et al., 2003; Castro et al., 2006). Second, the site amplification a each station is supposed to be the same for all earthquakes in the dataset, i.e. linear soil behavior is assumed. As already mentioned in Chapter 4.1, in view of the observed PGA values for large Vrancea earthquakes, this assumption is regarded to be acceptable. Moreover, the dataset analyzed here only includes very few records from stronger events.

7.1.3   A Note on Error Analysis

For all inversions performed in this work, the stability and standard error of the inverted model parameters are assessed by the computation of *bootstrap samples* (e.g. Efron and Tibshirani, 1994), with the same procedure as explained in Parolai et al. (2001, 2004a) and Bindi et al. (2006b). Given an original dataset with N_{rec} datapoints (in this case, N_{rec} spectral amplitudes at a given frequency), this technique works by repeated inversions of datasets obtained by randomly resampling the original one. From the original system matrix given for instance by (7.10), a new one of the same size is derived by randomly selecting N_{rec} rows. A given row can either be selected several times or never. Of course, the rows containing the constraints are included in each bootstrap sample. I compute, for each frequency, 200 bootstrap replications. Finally, the mean and standard deviation of these 200 samples are calculated for each model parameter. In all cases, the mean of the bootstrap samples and the model parameters obtained by inversion of the original dataset are in very good agreement. All the plots showing the inversion results in the following sections display the mean of the 200 bootstrap replications and, grayshaded, the mean ± one standard deviation.
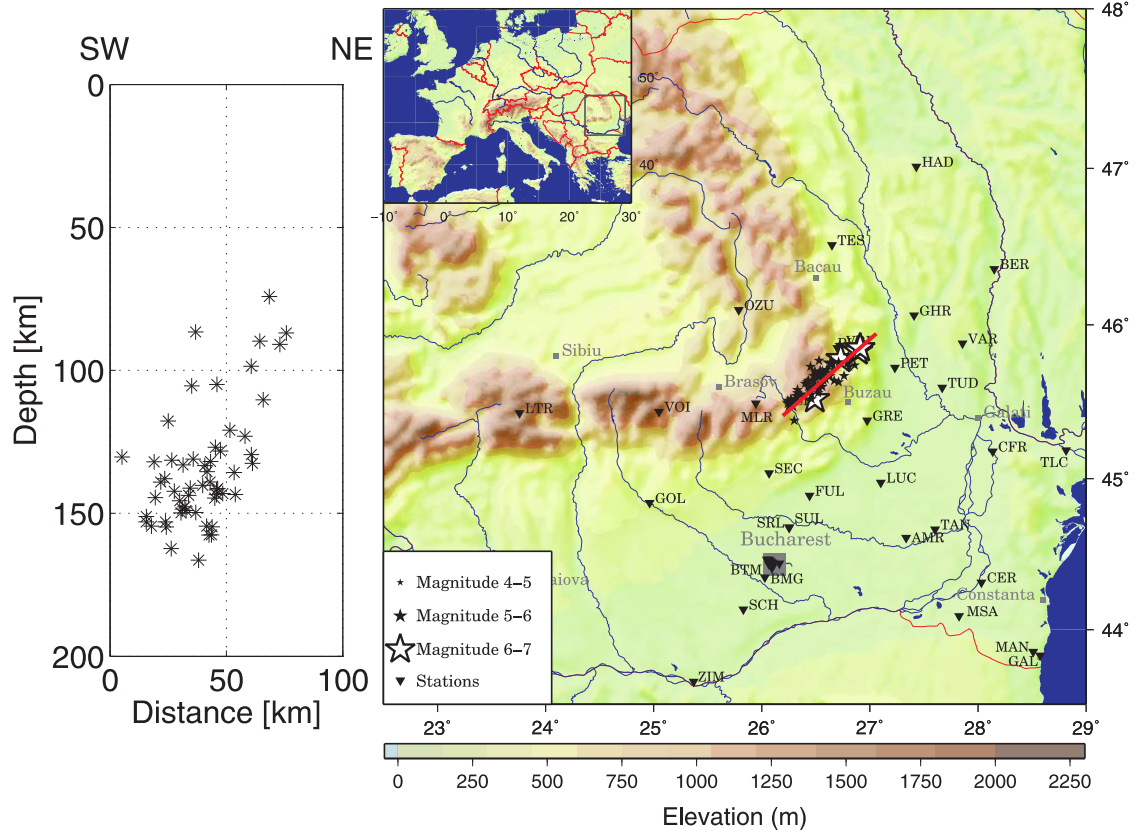
Figure 7.1: Topographic map of the Carpathian area. The epicenters of the earthquakes utilized are depicted by stars. In total, 55 earthquakes and 43 stations (inverse triangles) are used. On the left, a SW-NE vertical cross section through the epicentral area is shown (red line on the map).

7.2 Database and Processing

The acceleration data used have been recorded by the K2 network spread over Romania, which has already been described in Chapter 6.2. This dataset has been complemented with several analogue SMA-1 recordings of the large Vrancea earthquakes which occurred in 1986 (M_W = 7.1, eight records), and 1990 (M_W = 6.9, eight records and M_W = 6.4, three records). Figure 7.1 shows the epicenters of the 55 utilized earthquakes (Tables 7.1 and 7.2) and the 43 considered stations (Table 7.3). Because there are more than 10 stations located in Bucharest, they are not all labeled on the map. As can be seen from Figure 7.1 and has been explained in Chapter 6.1, the earthquake sources in the dataset are strongly clustered together in a small epicentral area and the hypocenters range in an almost vertical stripe extending from around 70 to 170 km in depth (Tables 7.1 and 7.2). The locations and moment magnitudes compiled in these Tables were extracted from the ROMPLUS catalogue (Oncescu et al., 1999b). The K2 data were sampled at 200 samples/s, whereas the SMA-1 data were digitized with a sampling rate of 100 samples/s (Chapter 6.2).

More than 850 three-component acceleration recordings are included in the final dataset useable for the inversion. Baseline correction was performed by substracting the mean value and the P- and S-wave onsets were picked. Only the S-wave portions of the time histories are analyzed here. For this purpose, time windows starting 1 s before the S-wave arrival and ending when 80% of the total energy

Date	Latitude [°]	Longitude [°]	Depth	M_W
1986/08/30	45.52	26.49	132	7.1
1990/05/30	45.83	26.89	91	6.9
1990/05/31	45.85	26.91	87	6.4
1997/10/11	45.80	26.80	110	4.5
1997/11/18	45.76	26.71	123	4.7
1997/12/30	45.54	26.32	139	4.6
1998/01/14	45.71	26.60	143	4.0
1998/01/19	45.64	26.67	105	4.0
1998/03/13	45.56	26.33	155	4.7
1998/05/04	45.73	26.45	145	4.0
1998/07/03	45.67	26.76	136	4.2
1998/07/27	45.67	26.53	135	4.4
1999/01/23	45.67	26.48	140	4.1
1999/03/17	45.70	26.56	142	4.1
1999/03/22	45.52	26.31	145	4.4
1999/03/23	45.68	26.50	155	4.0
1999/04/28	45.49	26.27	151	5.3
1999/04/29	45.62	26.40	148	4.0
1999/06/29	45.61	26.52	131	4.2
1999/07/13	45.70	26.49	132	4.0
1999/11/08	45.55	26.35	138	4.6
1999/11/14	45.52	26.27	132	4.6
2000/03/08	45.87	26.72	74	4.4
2000/04/06	45.75	26.64	143	5.0
2000/05/10	45.56	26.52	133	4.1
2000/11/30	45.59	26.53	141	4.1
2001/03/04	45.51	26.24	155	4.8
2001/03/18	45.49	26.24	153	4.1
2001/03/28	45.77	26.53	121	4.3

Table 7.1: Date, hypocentral coordinates and moment magnitudes of utilized events. The moment magnitudes given in this table are from the ROMPLUS catalogue (Oncescu et al., 1999b).

of the record are reached were extracted in order to compute the FAS. The typical window lengths range between 5 and 15 s. In the few cases where the determined window length were longer than 20 s, they were fixed to have a maximum length of 20 s in order to avoid having too much coda energy in the analyzed time windows. Each window is cosine-tapered (5%) and Fourier transformed. Finally, the spectral amplitudes are smoothed around 30 frequency points (equidistant in logarithmic scale) between 0.5 and 20 Hz (below 0.5 Hz, the SN-ratio is in general not satisfactory for the smaller events) using the windowing function proposed by Konno and Ohmachi (1998):

$$W_B(f, f_c) = \left[\frac{\sin\left(\log\left(\frac{f}{f_c}\right)^b\right)}{\log\left(\frac{f}{f_c}\right)^b} \right]^4 , \qquad (7.14)$$

where f_c denotes the center frequency around which the smoothing is performed and $b = 20$. This window has constant width on the logarithmic frequency axis. Noise spectra were calculated from

Date	Latitude [°]	Longitude [°]	Depth	M_W
2001/05/20	45.59	26.44	150	4.2
2001/05/24	45.63	26.42	144	4.9
2001/07/20	45.75	26.79	133	4.8
2001/08/01	45.69	26.57	127	4.1
2001/10/17	45.60	26.56	87	4.2
2002/01/25	45.63	26.71	128	4.0
2002/03/16	45.55	26.46	142	4.3
2002/05/03	45.58	26.33	162	4.6
2002/05/15	45.55	26.36	153	4.0
2002/06/14	45.64	26.57	133	4.0
2002/08/03	45.67	26.63	141	4.4
2002/08/27	45.60	26.43	149	4.0
2002/09/06	45.64	26.43	105	4.1
2002/09/10	45.73	26.81	130	4.0
2002/11/03	45.74	26.86	90	4.0
2002/11/30	45.62	26.55	166	4.7
2002/12/30	45.68	26.56	155	4.1
2003/04/13	45.38	26.30	130	4.0
2003/08/02	45.60	26.47	149	4.1
2003/10/05	45.58	26.45	146	4.6
2004/01/21	45.52	26.46	118	4.1
2004/02/07	45.67	26.62	144	4.4
2004/03/17	45.69	26.53	158	4.1
2004/04/04	45.64	26.48	150	4.3
2004/10/27	45.78	26.73	99	5.8
2005/05/14	45.68	26.54	140	5.2

Table 7.2: Continuation of Table 7.1.

pre-event noise windows of equal length as the considered signal windows. For each of the 30 frequencies, only data points with a signal-to-noise (SN) ratio higher than three are included in the final dataset. Thus, the database is a bit sparser at lower frequencies than at the higher ones due to SN-ratio constraints. For the inversions below, the root-mean-square (rms) average of the spectra of the two horizontal components is used and denoted by the letter H in the following. Several data examples are depicted in Figure 7.2. The left panel shows several time histories and the selected S-wave windows, whereas on the right-hand side, the computed spectra for the selected windows are shown.

There are some rather obvious problems related to the dataset. First, due to the depth range of the earthquakes, the smallest hypocentral distance is approximately 85 km. Thus, with distance bins which are 10 km wide, the reference distance R_0 mentioned in Section 7.1.2 is 90 km. Therefore, the source spectra derived in Section 7.4 are scaled to that distance. Histogram plots showing the distribution of the data with respect to hypocentral distance are depicted in Figure 7.3. The largest amount of data points are given for hypocentral distances between 130 and 250 km. Second, because the sources are clustered in the same region, there are very few crossing ray paths from the sources to the stations. Because of this configuration, one cannot expect that inhomogeneities in the anelastic properties of the medium would be averaged out, as all the rays from any source to a given station will always travel similar paths.

Station	Latitude [°]	Longitude [°]	site conditions
AMR	44.61	27.34	sediments
BCU	44.41	26.09	sediments
BDL	44.46	26.07	sediments
BER	46.36	28.15	sediments
BFG	44.44	26.10	sediments
BGM	44.45	26.09	sediments
BHM	44.43	26.10	sediments
BMG	44.35	26.03	sediments
BOT	44.44	26.07	sediments
BPF	44.46	26.05	sediments
BST	44.45	26.10	sediments
BTM	44.44	26.11	sediments
BVC	44.43	26.10	sediments
CER	44.31	28.03	consolidated sediments
CFR	45.18	28.14	metamorphic rock
FUL	44.88	26.44	sediments
GAL	43.83	28.58	sediments
GHR	46.06	27.41	consolidated sediments
GOL	44.84	24.96	sediments
GRE	45.38	26.97	consolidated sediments
HAD	47.02	27.43	consolidated sediments
INB	44.44	26.16	sediments
LTR	45.43	23.76	crystalline rock
LUC	44.97	27.10	sediments
MAN	43.85	28.51	sediments
MLR	45.49	25.95	rock
MSA	44.09	27.83	sediments
OZU	46.10	25.79	volcanic rock
PET	45.72	27.23	sediments
PLO	45.85	26.65	rock
SCH	44.13	25.83	sediments
SEC	45.03	26.07	sedimentary rock
SIR	45.48	26.26	sedimentary rock
SRL	44.68	26.26	sediments
SUL	44.68	26.25	sediments
TAN	44.67	27.60	sediments
TES	46.51	26.64	consolidated sediments
TLC	45.19	28.82	metamorphic rock
TUD	45.59	27.67	sediments
VAR	45.88	27.86	consolidated sediments
VOI	45.43	25.05	crystalline rock
VRI	45.86	26.72	sedimentary rock
ZIM	43.65	25.37	sediments

Table 7.3: Stations included in the database.
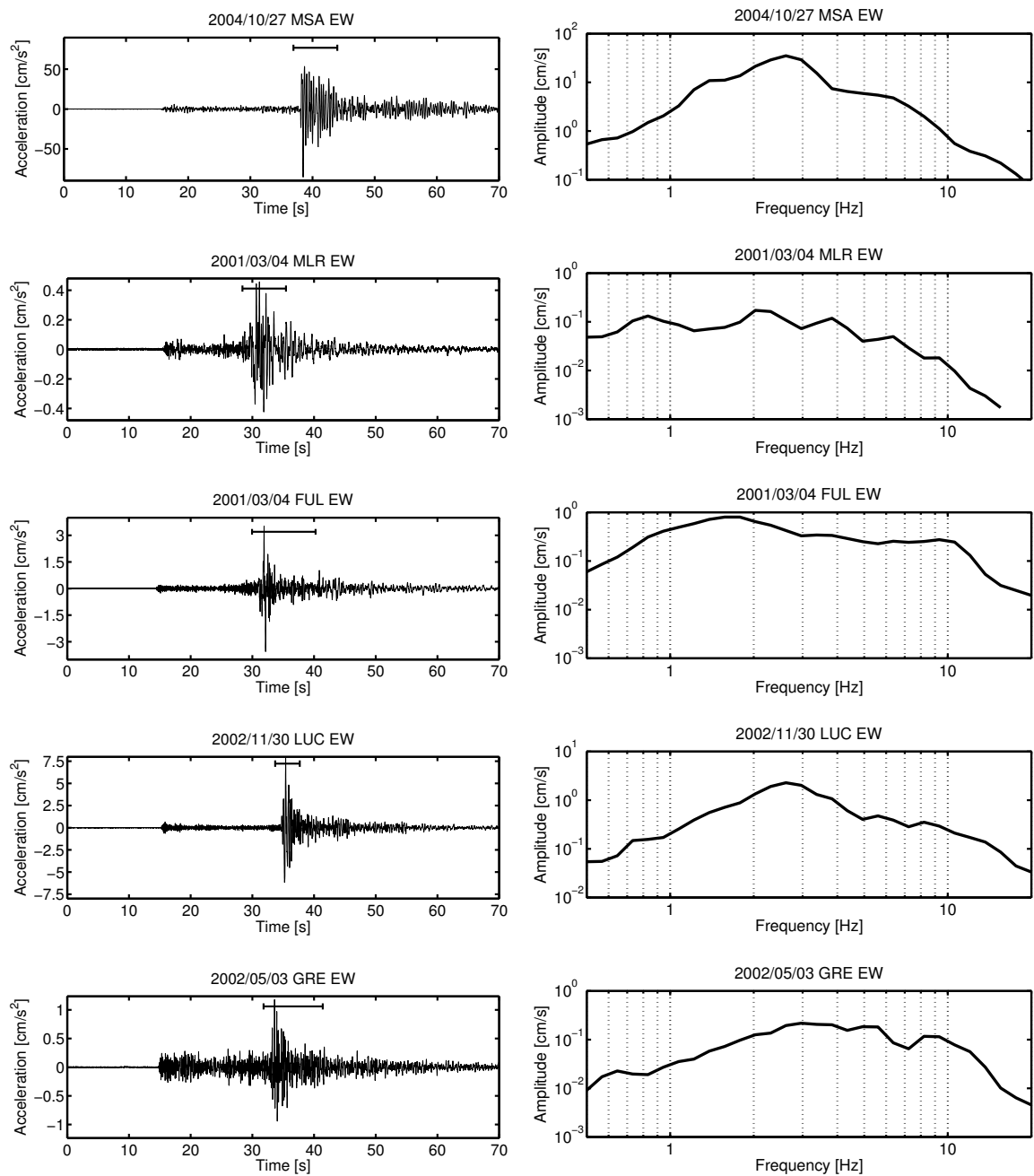
Figure 7.2: Left panel: Example records (EW components) and S-wave time windows (marked by the bar above the time history) used for the computation of Fourier amplitude spectra. The coordinates and magnitudes of the respective events can be found in Tables 7.1 and 7.2. The origin of the time axis does not correspond to the origin time of the respective earthquake but was adjusted for displaying purposes. Right panel: smoothed Fourier amplitude spectra of the selected S-wave windows. Note the two records of the 2001/03/04 event at stations MLR and FUL and the difference in frequency content.
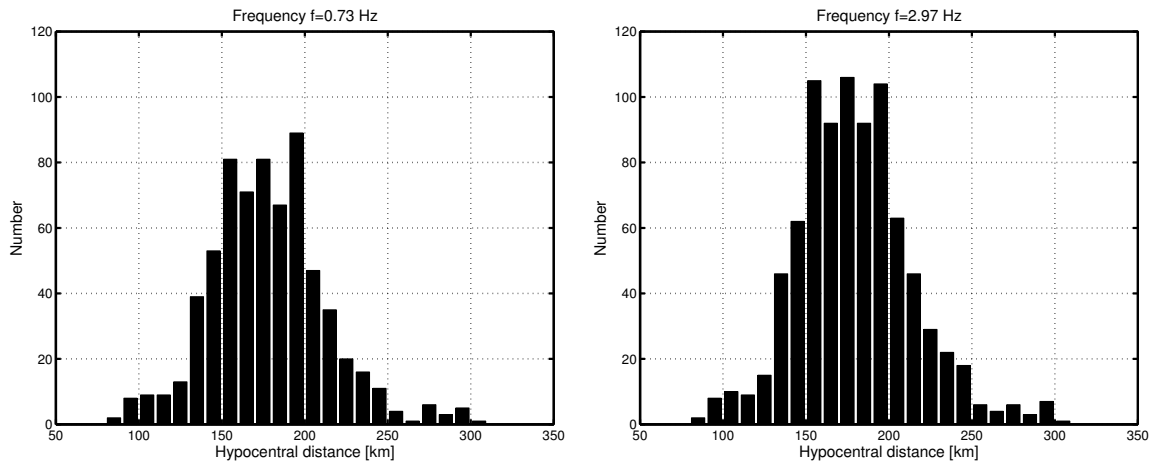
Figure 7.3: Distribution of hypocentral distances in the dataset at two selected frequencies. The largest amount of data is given for hypocentral distances between 130 and 250 km.

A final important point is the near vertical incidence. Therefore, one should expect very strong P-wave arrivals and very little S-wave energy on the vertical component (Z). Giving a look at the three-component recordings (two examples are depicted in Figure 7.4), these expected features can indeed be seen in many cases. Sometimes (for instance the recording at station PET in Figure 7.4), the P-wave on the Z component shows larger amplitudes than the S-waves on the H components. Of course, the frequency content is also totally different, with much higher frequencies in the P-wave on the Z component. Moreover, for stations located in the Focsani (forearc) basin, phases with strong amplitudes appear on the Z component of several recordings roughly between 5 and 8 s before the S-wave arrival (see GRE in Figure 7.4). These may be related to S-P conversions at the base of the deep Focsani basin (with depths up to 22 km, Hauser et al., 2007). These time differences are a bit larger than what would be expected by deriving a weighted average of the P-wave velocity in the basin from the results of Hauser et al. (2007) (approximately 4 km/s) and using the typical $\sqrt{3}$ ratio between v_P and v_S. This leads to an estimated time difference between the S-P conversion and the S-wave around 4-4.5 s for a depth of 20 km. However, this rough estimate does not account for possible very slow near-surface seismic velocities, which are not included in this velocity model (lowest P-wave velocity 2 km/s). Therefore, to first order, the observed time difference is consistent with the velocity model from refraction seismics.

Generally, the Z component is composed of different phases (scattered, converted, reflected, refracted, etc.) rich in high-frequency energy with, in many cases, no clear S-wave train, as expected from the near vertical incidence. Therefore, the Z component does not provide information on the properties of S-waves. The results obtained for the attenuation of the Z component in the section below (which demonstrate that indeed this component does not reflect the attenuation characteristics of S-waves) are thus not surprising. Nevertheless, the Z component is also shown, mainly in view of the H/V ratios and the discussion on their applicability in Romania in Section 7.5, where the amplification of the Z component derived from the GIT inversion is needed.

Due to the described pecularities of the dataset (clustered sources, very large reference distance, behavior of the Z component, etc.) the application of the GIT technique requires some modifications with respect to standard applications, especially regarding the first step inversion for the attenuation properties. Datasets from crustal earthquakes are usually much easier to deal with (relating to the
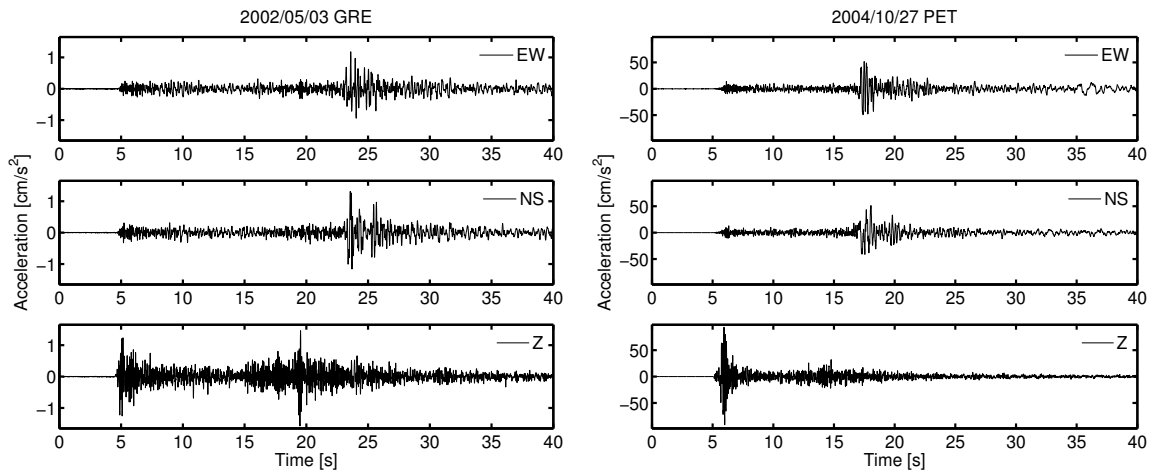
Figure 7.4: Examples for the three component accelerometric recordings at stations GRE (left) and PET (right). More explanations are given in the text.

GIT). Several assumptions which are justified in the crustal case and facilitate the inversion (e.g. inhomogeneities in attenuation average out over the entire dataset, the reference distance can be set to zero) cannot be made here and have to be approached differently. These difficulties have not been met before during such an inversion and make this study a valuable contribution also in terms of methodology.

7.3 Attenuation Characteristics Beneath Vrancea

In order to investigate the attenuation characteristics beneath Vrancea, the first step of the two-step inversion scheme presented in Section 7.1.2 is applied to the spectral amplitudes at each of the 30 selected frequencies. However, the obtained attenuation functions $A(f,R)$ show a peculiar feature at frequencies higher than about 4 Hz, namely a strong bump (i.e. amplification with distance instead of attenuation), which takes its maximum value at a hypocentral distance of roughly 180 km.

In this section, I will now first show the obtained results and provide a possible explanation for this peculiarity by performing several tests with synthetic data. Following these considerations, a slight modification is introduced in the inversion scheme in order to account for variations in attenuation along the paths for two different sets of stations. The first set consists of stations located mostly in the South (including Bucharest and environs), East and Northeast of the epicentral area, whereas the second one comprises those sites which are situated directly within (or behind) the bending part of the mountain arc, most of them directly in the epicentral area (Figure 7.6).

The results of this modified inversion using two separate attenuation functions clearly reveal that the travel paths to the sites located directly above the hypocenters (thus for propagation almost vertically upwards) are affected by an attenuation almost one order of magnitude stronger at high frequencies than those in the forearc region. The physical meaning and the implications in terms of seismic hazard are finally discussed at the end of this section, before moving on to the source and site functions.
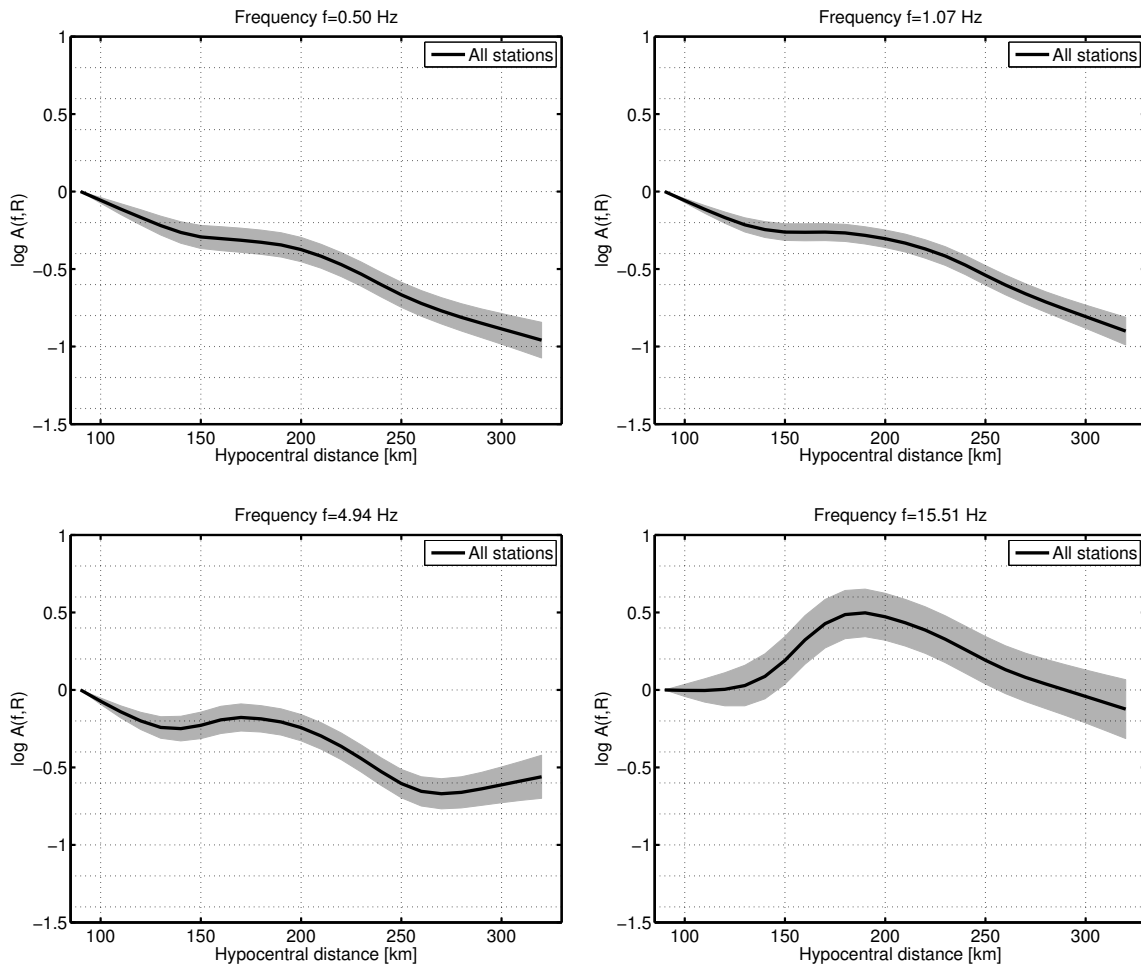
Figure 7.5: Attenuation functions ($\log A(f, R)$ versus R) at four selected frequencies (one non-parametric function). Black line: mean of 200 bootstrap samples. Grayshaded area: mean ± one standard deviation.

7.3.1 Inversion with One Attenuation Function

Initially, exactly the first inversion step as presented in Section 7.1.2 is performed. All the data at a given frequency are fitted with a source scaling factor and the attenuation function given by (7.9) and the system matrix has the form given by (7.10). As already mentioned earlier, the lowest hypocentral distance in the dataset amounts to approximately 85 km. The distance range of the data is subdivided into distance bins 10 km wide, and the reference distance (the center of the first bin) is chosen as $R_0 = 90$ km.

Results & Synthetic Data Test

Figure 7.5 shows the obtained attenuation functions at four selected frequencies. At $f = 0.50$ Hz and $f = 1.07$ Hz, they are monotonically decreasing with distance, while the bump starts to develop at around $4 - 5$ Hz (see $f = 4.94$ Hz). At high frequencies (e.g. $f = 15.51$ Hz), the effect is very strong. By plotting the spectral amplitudes (as they enter into the inversion) versus hypocentral distance, one can see a clear trend for stations MLR, SIR, VRI, PLO, GRE and OZU to show systematically much
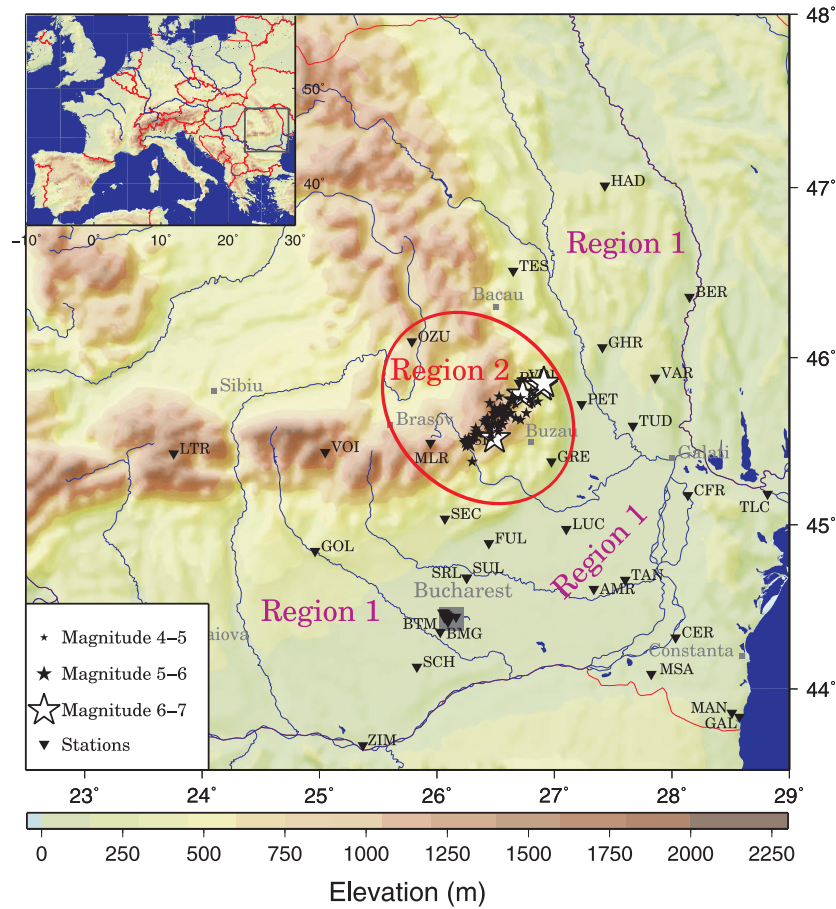
Figure 7.6: Map depicting the classification of the stations into region 1 and 2. The choice to subdivide the area into these two regions is based on the fact that the stations in region 2 show comparably very low spectral amplitudes at high frequencies.

lower amplitudes (up to one order of magnitude) at higher frequencies than the other stations in the network. In Figure 7.6, these six stations are grouped together in region 2, while region 1 will denote the rest of the network for the remainder of this chapter. VOI might also be a candidate for region 2, but from the few datapoints available at high frequencies the effect is not that clear as for the other stations mentioned above. Figure 7.7 depicts the spectral amplitudes at four different frequencies for a narrow magnitude range ($4 \leq M_W \leq 4.3$). At low frequencies, there is no severe difference between region 1 and 2, while at high frequencies ($\geq 4 - 5$ Hz), the spectral amplitudes in region 2 are consistently lower than those in region 1 at similar distance.

This remarkable difference in spectral amplitudes could in principle be explained either by a source, site or attenuation effect. Regarding the source, directivity is an improbable cause, as the effect also appears for small earthquakes, for which this source effect is probably unimportant due to the very small source size of the smaller Vrancea earthquakes (Chapter 6). As the effect appears at high frequencies, the radiation pattern cannot lead to these systematic differences. If the radiation pattern were the cause, one should rather expect to see systematic differences at low frequencies, as the influence of the radiation pattern is generally thought to decrease with increasing frequency (e.g. Takenaka et al., 2003; Castro et al., 2006).
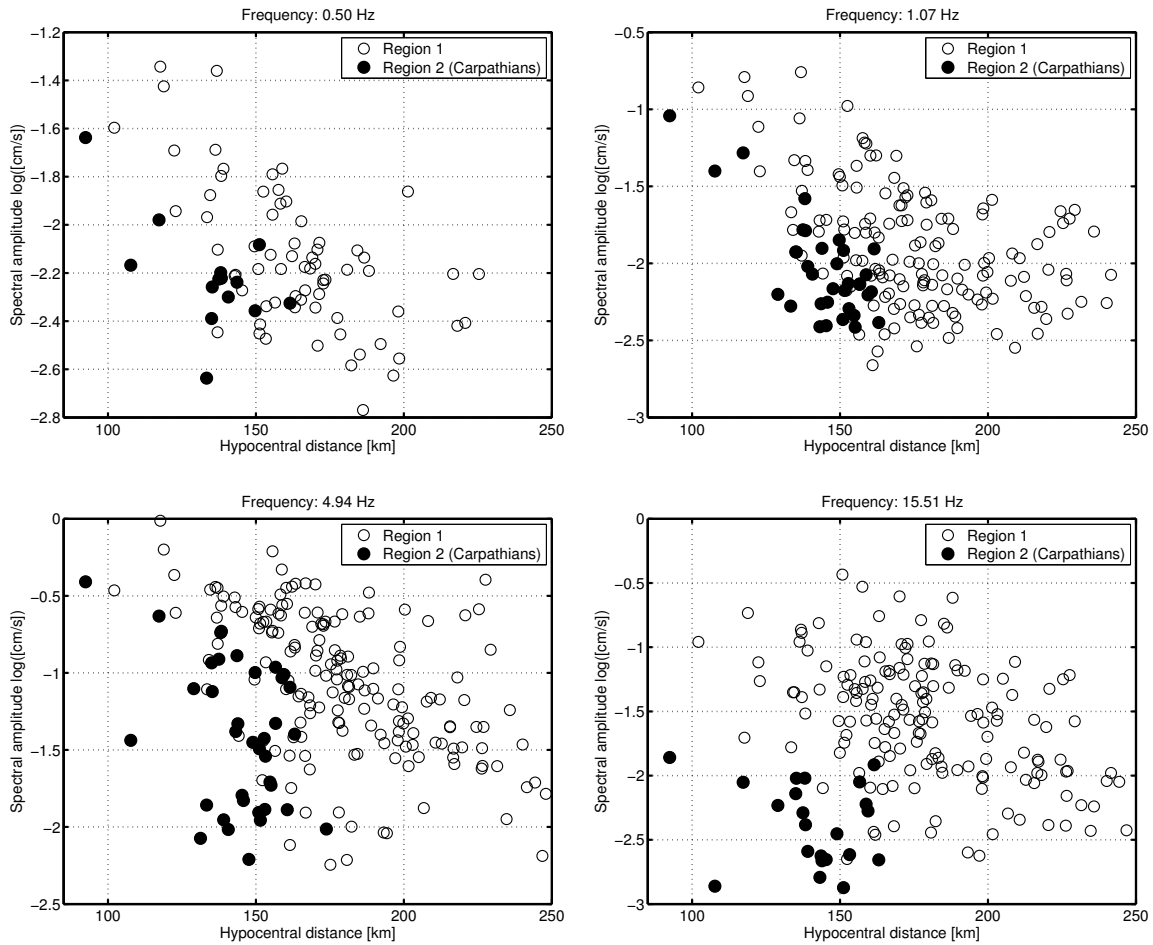
Figure 7.7: Spectral amplitudes (H component) observed at four selected frequencies (magnitude range 4-4.3). At low frequencies, the amplitudes in region 2 (black dots) show similar values than the ones in region 1 (open circles) at a given distance. However, with increasing frequency, the amplitudes in region 2 are systematically lower than the ones in region 1 by about one order of magnitude.

The possibility that these large differences in amplitude result from different site and basin effects is also unlikely, because except GRE, all the sites in region 2 are classified as rock stations (Table 7.3, which is however a qualitative classification and does therefore not automatically mean that they do not show any amplification at all). If they were the cause, one would expect that a station such as SEC or FUL, located in the deep Focsani basin (Hauser et al., 2007), should show large amplification at some low resonance frequency (as the basin is very deep, see e.g. Bard, 1999) and large attenuation at high frequencies due to the strong damping in the sediments. However, the opposite of this expected effect is observed.

Hence, a strong difference of attenuation along the travel path is the preferred explanation for these results. In order to verify this hypothesis, I will now summarize the results of two synthetic data tests. The *first test* is intended to verify whether the bump is a simple problem related to the geometry of the dataset. Therefore, no inhomogeneities in attenuation are considered, using a homogeneous halfspace Q-model (*model A*).

A dataset of synthetic spectra with exactly identical number of sources and stations as well as identical source-to-station geometry as the real data is generated. The spectra are computed following the spectral model given by (4.30) (Boore, 2003):

- In all cases, the source spectra are modeled following the ω^{-2}-model (Brune, 1970, 1971). The utilized corner frequencies f_c are randomly chosen, yet decreasing with increasing magnitude (for different magnitude bins, the bounds inbetween which f_c is chosen are different – for instance, f_c is given in the interval [5 10] Hz for $4 \leq M_W < 4.5$ and [2 6] Hz for $4.5 \leq M_W < 5$). The ranges are deliberately chosen this high, as high f_c are expected for Vrancea earthquakes (Chapter 6 and e.g. Oncescu, 1989).

- The average radiation pattern was chosen as $\langle \mathfrak{R}^{\theta\phi} \rangle = 0.6$, the shear wave velocity $v_S = 4.5$ km/s and the density $\rho = 3.2$ g/cm^3.

- The Q-model (model A) consists in a homogeneous halfspace with a frequency dependent value given by $Q_A(f) = 100f^{0.8}$. Attenuation is then computed using body wave geometrical spreading $1/R$ and the usual formula (4.33). These Q values are arbitrarily chosen, but close to estimates used by other authors (e.g. Sokolov et al., 2005). In any case, as I only wish to stress a relative effect further below, the absolute values of Q are not decisive.

- Site effects are, in a first approximation, modeled from the H/V ratio at each station, even if, in Section 7.5, it will turn out that the H/V ratio is not a good estimator of site amplification in the case of Vrancea earthquakes. One dataset with and without the so-modeled site amplification are generated. Here, I only show results obtained including the modeled site effects (H/V). However, the effect that I wish to emphasize at this point (the bump in the attenuation curves) proved not to depend on whether the synthetics include an estimate of site effect or not.

- Finally, normally distributed random noise with a standard deviation of 10% of the respective data values is added to the synthetic spectra.

Figure 7.8 shows the attenuation functions obtained from the inversion of the spectra calculated with model A at the same frequencies than the ones from the real data (Figure 7.5). No bump is observed in any of the attenuation functions, neither for the dataset with a site amplification estimate nor for the one without. Therefore, the problem is not due to the geometry of the dataset.

With the *second test*, I investigate whether the bump observed before can be reproduced under the assumption of a variation of Q between region 1 and 2. The generation of the dataset is the same as described above, but with a Q-model which incorporates higher attenuation (i.e. lower Q) for region 2 than for region 1 (*model B*). The utilized Q values for both regions are in this case: $Q_{B,1}(f) = 150f^{0.8}$ and $Q_{B,2}(f) = 100f^{0.5}$. This is the only difference between the datasets of model A and B.

Figures 7.9 shows the resulting attenuation functions. The results for model B show a striking similarity with the observed bump from the real data. This outcome strongly suggests that the variation in spectral amplitudes between region 1 and 2 is the result of inhomogeneities in whole path attenuation. The stations in region 2 are strongly influencing the dataset at small hypocentral distances, and with increasing distance, their contribution is constantly reduced until they disappear for distances higher than about 180 km (Figure 7.10). As a result, the attenuation function at high frequencies first increases with distance and starts decaying again for distances higher than about 180 km. Thus, in order to account for such variations in attenuation, I perform the inversion for the real data with a slightly modified inversion scheme using two different attenuation functions for region 1 and 2.
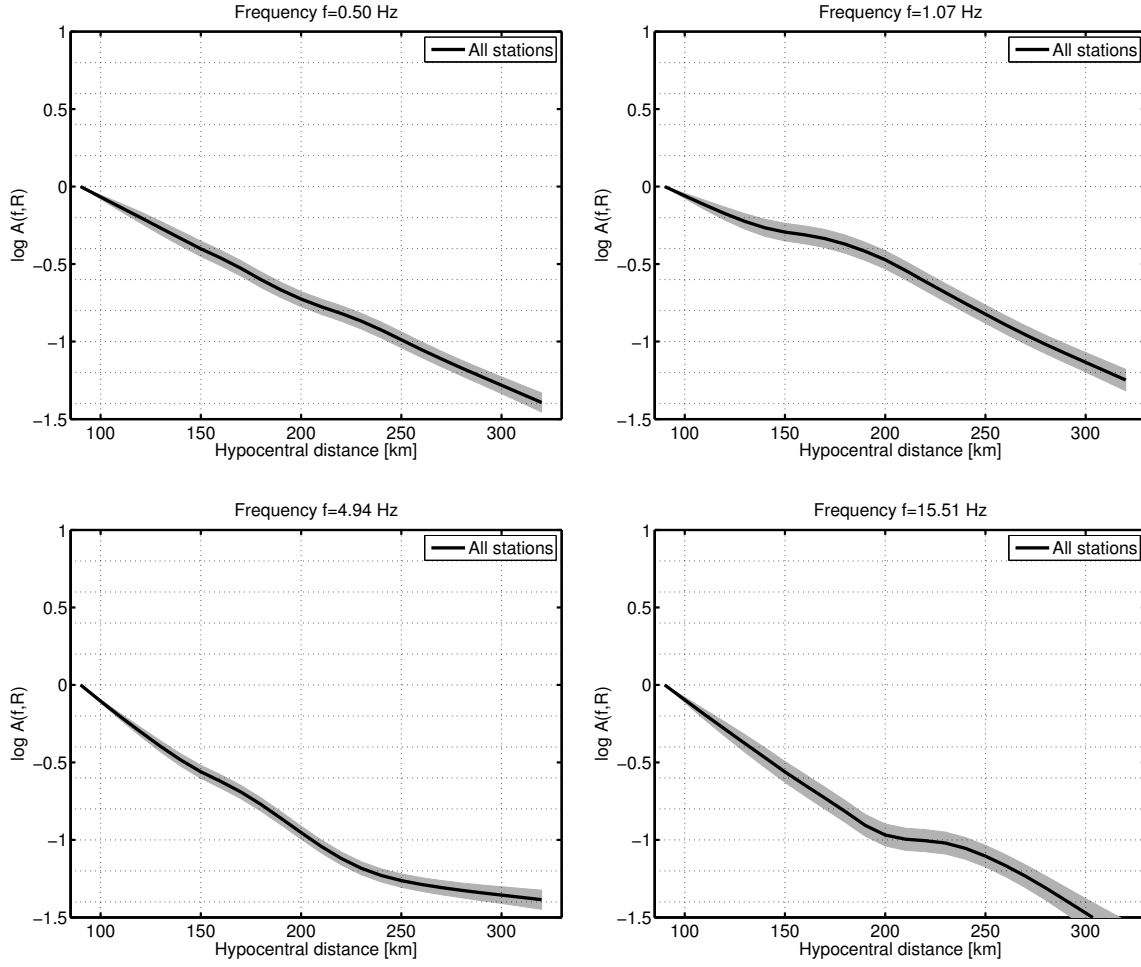
Figure 7.8: Attenuation functions ($\log A(f, R)$ versus R) at four selected frequencies derived from synthetic data using a homogeneous halfspace Q-model (model A). Black line: mean of 200 bootstrap samples. Grayshaded area: mean ± one standard deviation.

Note that the synthetic data are only used to investigate whether or not a change in whole path attenuation between region 1 and 2 can qualitatively explain the observed shape of the attenuation functions obtained from the real data. It is not my intention to derive any quantitative conclusions from these synthetic data. The effect is quantitatively examined by applying the modified inversion scheme below to the real data, without any further reference to the synthetics above.

7.3.2 Inversion with Two Attenuation Functions – The Modified Inversion Scheme

The first step inversion scheme given in Section 7.1.2 is modified in a way to invert simultaneously for two separate attenuation functions. Thus, the scheme can be written as:

$$\log U_{ij}(f) = \log M_i(f) + p_1 \log A_1(f, R_{ij}) + p_2 \log A_2(f, R_{ij}), \tag{7.15}$$

where p_1 equals one if the considered station is located in region 1 and otherwise zero and p_2 is defined the opposite way. $A_1(f, R)$ is discretized into N_{D1} while $A_2(f, R)$ is discretized into N_{D2} equally sized
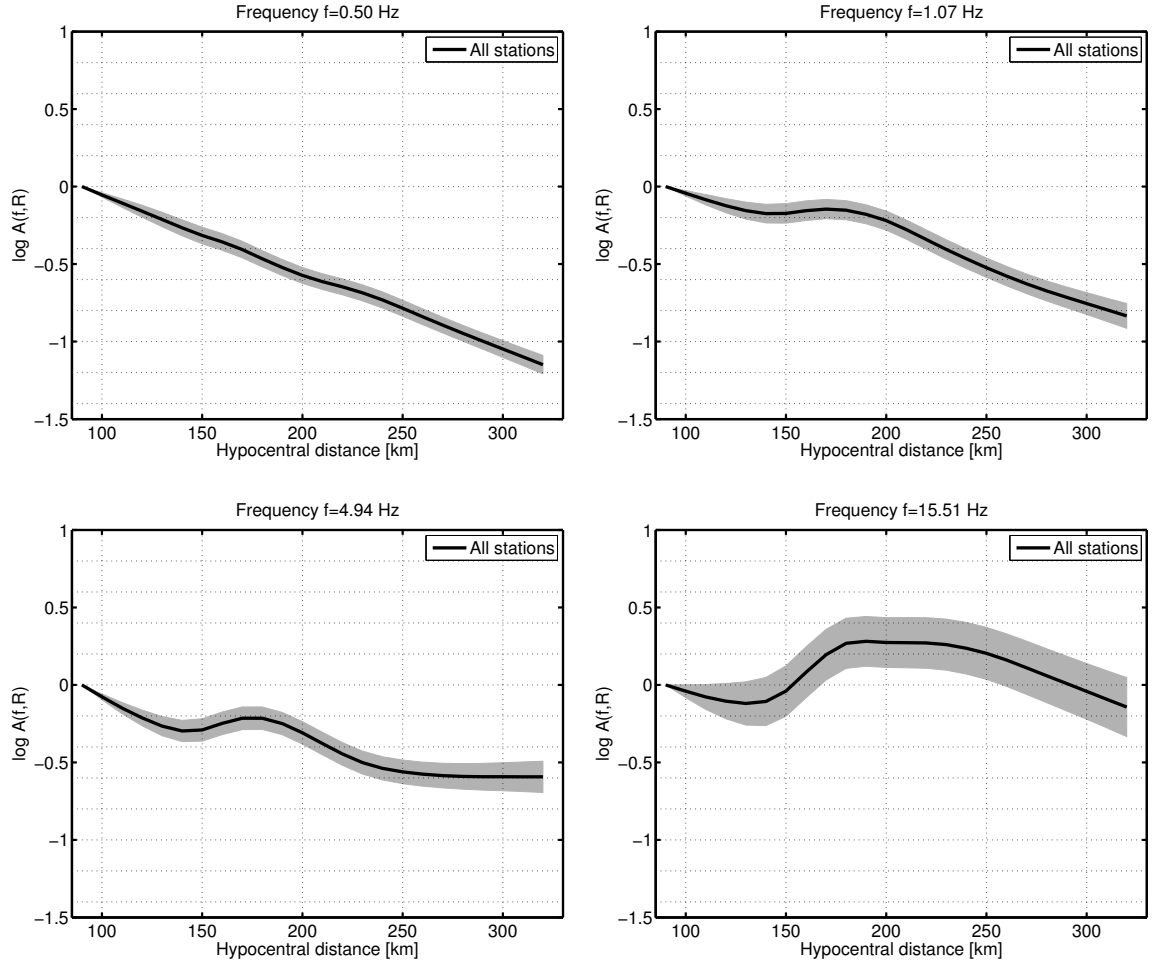
Figure 7.9: Attenuation functions ($\log A(f,R)$ versus R) at four selected frequencies derived from synthetic data using different Q-models for travel paths ending in region 1 and 2 (model B). Black line: mean of 200 bootstrap samples. Grayshaded area: mean ± one standard deviation.

bins (10 km), with $N_{D2} < N_{D1}$ in the case analyzed here (as the maximum hypocentral distance for region 2 is approximately 180 km). For both attenuation functions, the reference distance is set to $R_0 = 90$ km. Regarding the constraints, I impose $A_1(f,R_0) = 1$ whereas the origin (i.e. the value of $A_2(f,R_0)$) of $A_2(f,R)$ is free. These constraints allow to account for the fact that not only the decay with distance, but also the general level of the spectral amplitudes may be different, which, as shown above, is clearly the case for Vrancea earthquakes. In other words: the shift of the origin between the two attenuation functions reflects the (cumulative) difference in attenuation over the distance R_0 for both sets of travel paths defined by regions 1 and 2. Both attenuation functions are of course also constrained to be smooth functions of distance.

As for the traditional scheme, the source scaling factors $\log M_i(f)$ include in this case the (logarithmic) average of the site amplification of the stations in region 1 which recorded the event, as the origin of $A_1(f,R)$ is fixed. Suppose that all earthquakes are recorded by all stations in region 1 and all stations in region 2 (which is of course not the case in reality). If now the average site amplification of the stations in region 1 differs from the one in region 2, this difference is also mapped into the offset of the
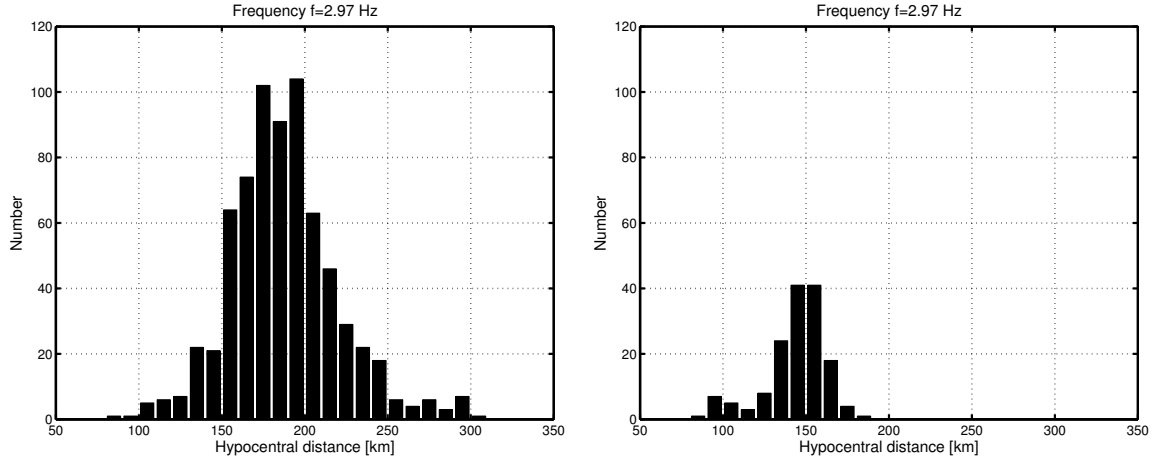
Figure 7.10: Distribution of hypocentral distances in the dataset for region 1 (left) and 2 (right) at a given frequency. The distance range in region 2 is restricted to distances lower than 180 km.

two attenuation functions. However, as each event is recorded by a different combination of stations in region 1 and in region 2, the relation of the average site amplifications between the two regions is different for each earthquake, and thus, the effect will most likely average out. Therefore, it is a reasonable assumption to suppose that the shift of the origin of $A_2(f,R)$ relative to $A_1(f,R)$ is really entirely determined by the difference in attenuation along the paths.

The system matrix takes the following form:

$$
\left(
\begin{array}{ccccc|ccccc|cccc}
1 & 0 & 0 & \cdot & \cdots & 0 & 0 & 0 & \cdot & \cdots & 1 & 0 & 0 & \cdots \\
0 & 0 & 0 & \cdot & \cdots & 1 & 0 & 0 & \cdot & \cdots & 1 & 0 & 0 & \cdots \\
\cdot & \cdot & \cdot & \cdot & \cdots & \cdot & \cdot & \cdot & \cdot & \cdots & \cdot & \cdot & \cdot & \cdots \\
0 & 1 & 0 & \cdot & \cdots & 0 & 0 & 0 & \cdot & \cdots & 0 & 1 & 0 & \cdots \\
\vdots & \vdots & \vdots & \vdots & \vdots & \vdots & \vdots & \vdots & \vdots & \vdots & \vdots & \vdots & \vdots & \vdots \\
w_1 & 0 & 0 & \cdot & \cdots & 0 & 0 & 0 & \cdot & \cdots & \cdot & \cdot & \cdot & \cdots \\
-w_2/2 & w_2 & -w_2/2 & 0 & \cdots & 0 & 0 & 0 & \cdot & \cdots & \cdot & \cdot & \cdot & \cdots \\
0 & -w_2/2 & w_2 & -w_2/2 & \cdots & 0 & 0 & 0 & \cdot & \cdots & \cdot & \cdot & \cdot & \cdots \\
\cdot & \cdot & \cdot & \cdot & \cdots & \cdot & \cdot & \cdot & \cdot & \cdots & \cdot & \cdot & \cdot & \cdots \\
0 & 0 & 0 & 0 & \cdots & -w_2/2 & w_2 & -w_2/2 & 0 & \cdots & \cdot & \cdot & \cdot & \cdots \\
0 & 0 & 0 & 0 & \cdots & 0 & -w_2/2 & w_2 & -w_2/2 & \cdots & \cdot & \cdot & \cdot & \cdots \\
\cdot & \cdot & \cdot & \cdot & \cdots & \cdot & \cdot & \cdot & \cdot & \cdots & \cdot & \cdot & \cdot & \cdots
\end{array}
\right),
\tag{7.16}
$$

and the solution vector now contains model parameters for both attenuation functions:

$$
\mathbf{x}^T = \left(\begin{array}{ccc} \log A_{1,1} & \cdot & \cdot & \log A_{1,N_{D1}} \end{array} \middle| \begin{array}{ccc} \log A_{2,1} & \cdot & \cdot & \log A_{2,N_{D2}} \end{array} \middle| \begin{array}{ccc} \log M_1 & \cdot & \cdot & \log M_{N_E} \end{array} \right). \tag{7.17}
$$

7.3.3 Results

The above inversion scheme is applied both to the H and Z component spectra. The resulting attenuation functions are depicted in Figures 7.11 (H component) and 7.12 (Z component). As expected from a closer look to the spectral amplitudes (Figure 7.7), the origin of the attenuation function for
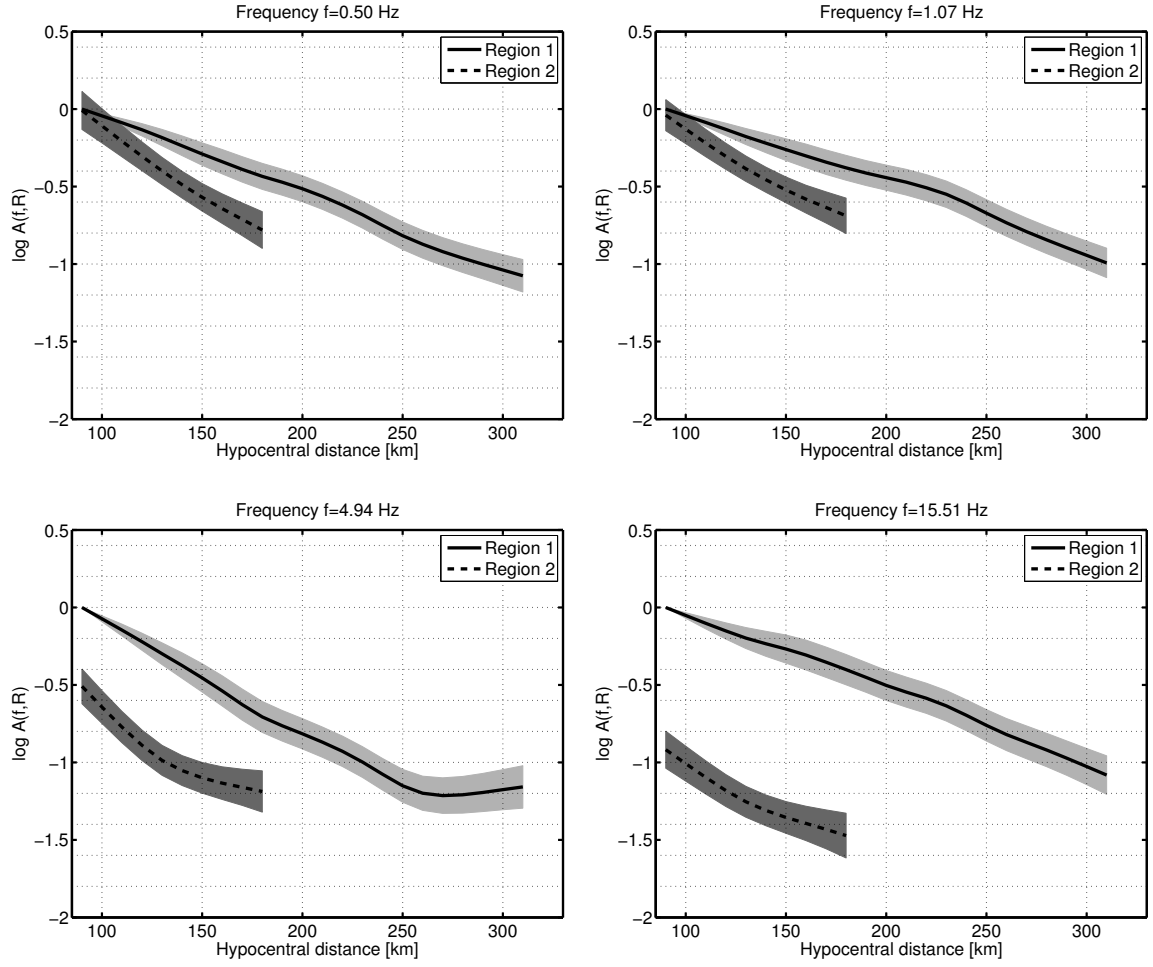
Figure 7.11: Attenuation functions ($\log A(f,R)$ versus R) for H component at four selected frequencies for region 1 (continuous line) and 2 (dashed line). Grayshaded area: mean of 200 bootstrap samples $\pm$ one standard deviation.

region 2 (i.e. the value at $R = R_0$) is very similar to the one for region 1 for low frequencies. For the Z component, it is even slightly higher. With increasing frequency, however, $A_2(f,R_0)$ is shifted further and further downwards, and for frequencies higher than about 10 Hz, the difference between $A_1(f,R_0)$ and $A_2(f,R_0)$ is almost one order of magnitude. This is the case both for the H and Z components. Note that there is no bump appearing in either one of the attenuation functions.

For each of these two attenuation functions, $Q(f)$ can in principle be evaluated with relation (7.11), even though (especially for the Z component) the shape of the attenuation function is often more complex than can be accounted for with such a simple model. However, it is not possible to consider the offset between the attenuation functions, corresponding to the difference in attenuation over R_0. Therefore, I normalize $A_2(f,R)$ to 1 at $R = R_0$ ($A_1(f,R)$ was already set to be 1 at $R = R_0$ during the inversion) for the determination of $Q(f)$. Only the slope of the attenuation function is thus evaluated in the following.

Due to the large depth of the Vrancea earthquakes, surface waves are probably only playing a minor
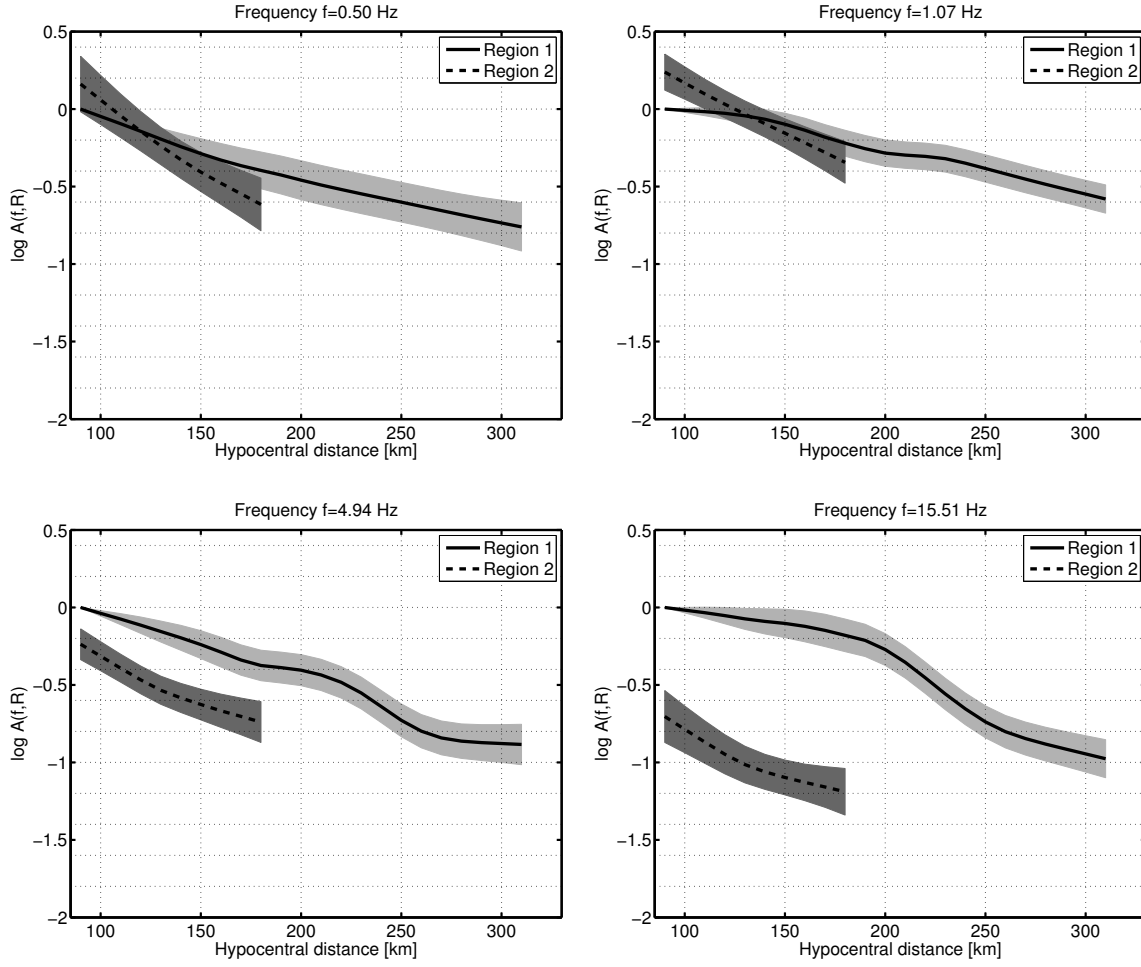
Figure 7.12: Attenuation functions ($\log A(f, R)$ versus R) for Z component at four selected frequencies for region 1 (continuous line) and 2 (dashed line). Grayshaded area: mean of 200 bootstrap samples $\pm$ one standard deviation.

role in the geometrical spreading term. Therefore, the geometrical spreading function is chosen as:

$$G(R) = \frac{R_0}{R}, \tag{7.18}$$

where R denotes the hypocentral distance and R_0 the reference distance. This correponds to geometrical spreading expected for body waves. Then, the (normalized) attenuation functions can be corrected to remove the geometrical spreading effect, and from (7.11), we get:

$$\log A_{normalized}(f, R) - \log G(R) = -\frac{\pi f}{2.3 Q(f) v_S} R. \tag{7.19}$$

To each attenuation function ($\log A_{normalized} - \log G(R)$ plotted versus hypocentral distance R), a straight line is fitted and from its slope, $Q(f)$ is calculated (with an average shear wave velocity estimate $v_S = 4.5$ km/s derived from the tomography model of Martin et al., 2006). This procedure is illustrated in Figures 7.13 for the H and 7.14 for the Z component. The obtained $Q(f)$ models for region 1 and 2 are displayed in Figure 7.15 for both components.
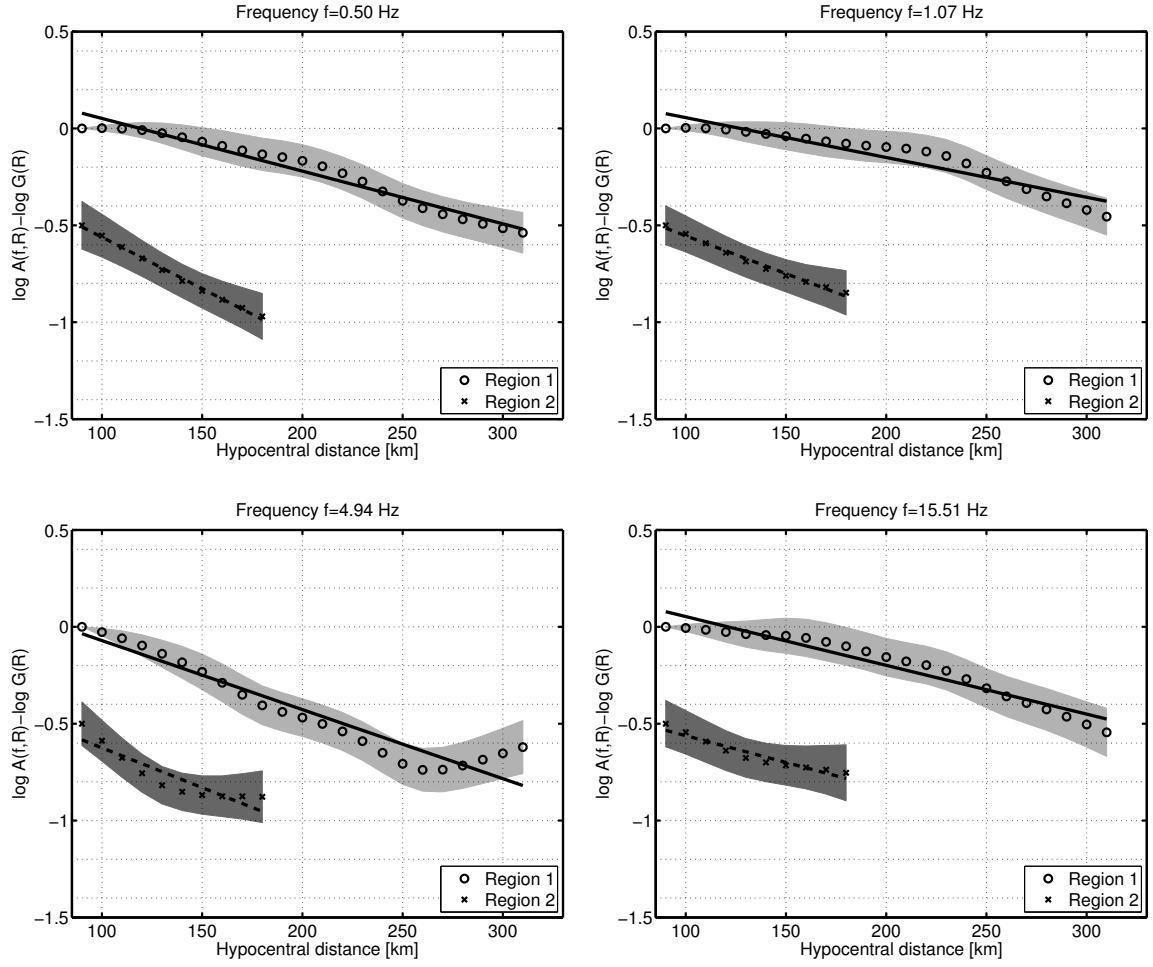
Figure 7.13: Attenuation functions corrected for geometrical spreading ($\log A(f, R) - \log G(R)$ versus R) and fitted straight line for H component at four selected frequencies for region 1 (continuous line) and 2 (dashed line). Both functions are normalized to 0 (in logarithm) at the reference distance R_0 (i.e. same origin), but offset with 0.5 in logarithm in these plots for viewing purposes.

For the H component, by fitting a model of the form $Q(f) = Q_0 f^N$ to the determined $Q(f)$ values, I obtain:

$$
\begin{aligned}
Q(f) &= 114 f^{0.96} \quad \text{for region 1 and} \\
Q(f) &= 72 f^{1.12} \quad \text{for region 2}.
\end{aligned}
\tag{7.20}
$$

These two models are, within the error bounds, approximately identical, which is surprising at first glance, as from the spectral amplitudes, a much stronger attenuation (and hence lower $Q(f)$ values) is expected for region 2. This issue is discussed in more detail below. The dependence on frequency in both $Q(f)$ models is almost linear (i.e. $N \approx 1$). Regarding the Z component, it is interesting to note that for region 2, the $Q(f)$ values follow roughly the same model which is obtained for the H component, whereas for region 1, the estimated $Q(f)$ values are not well constrained and seem to depict a much weaker dependence on frequency, with an exponent $N \approx 0.4$. Yet, the uncertainties are too large to reasonably assess the obtained values.
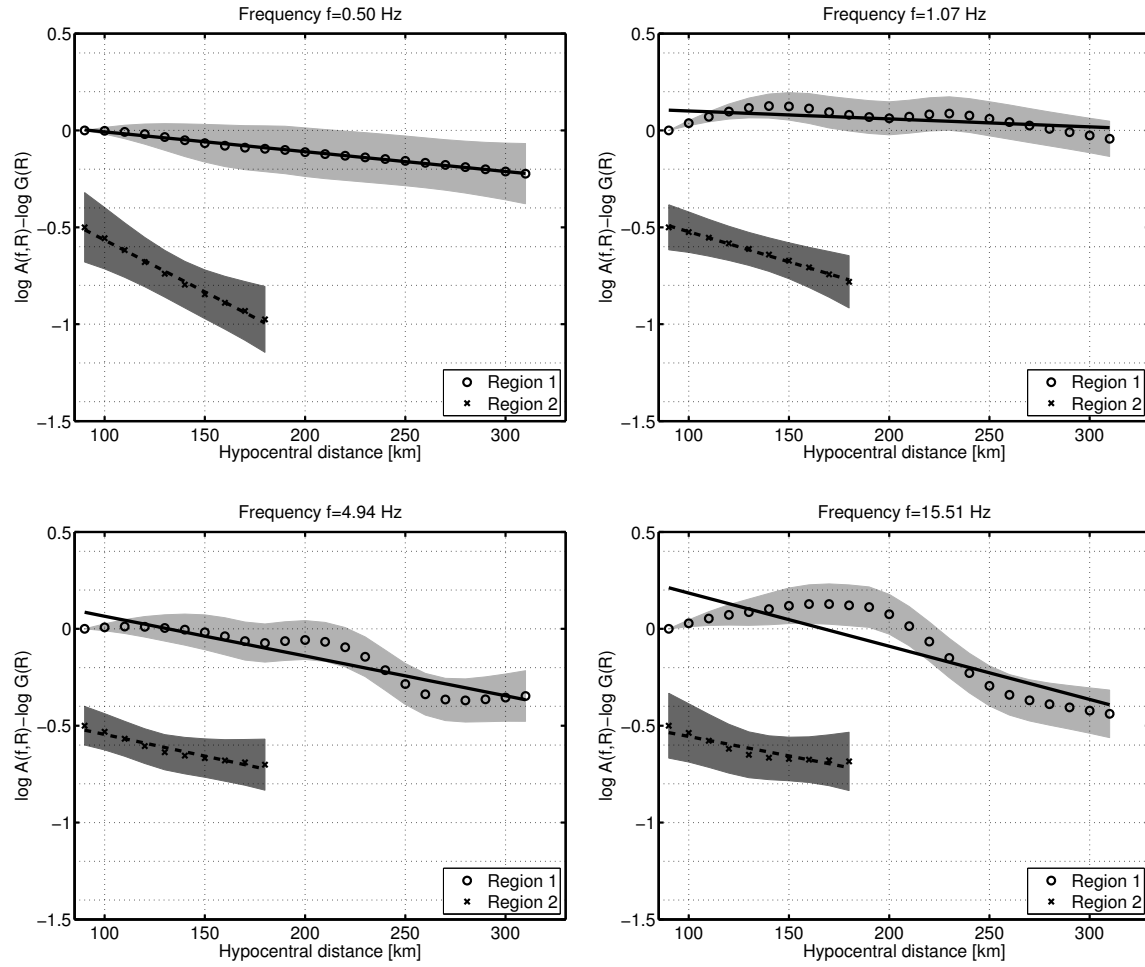
Figure 7.14: Attenuation functions corrected for geometrical spreading ($\log A(f, R) - \log G(R)$ versus R) and fitted straight line for Z component at four selected frequencies for region 1 (continuous line) and 2 (dashed line). Both functions are normalized to 0 (in logarithm) at the reference distance R_0 (i.e. same origin), but offset with 0.5 in logarithm in these plots for viewing purposes.

7.3.4   Discussion

As can be seen from Figure 7.14, after the correction of geometrical spreading, the spectral amplitudes on the Z component are practically not decaying anymore with distance for certain frequencies in region 1. This may lead to negative $Q(f)$ estimates if a line with positive slope is fitted to the data (negative $Q(f)$ values are not shown for the Z component of region 1 in Figure 7.15). The much smaller decay with distance is already visible on the Z component without correcting for geometrical spreading. This is not unexpected, due to the lack of S-wave energy on the vertical components already mentioned in the database section. Therefore, we cannot expect to observe the same decay with distance as on the H component (for instance, if the Z component would only contain noise, we would expect no decay with distance at all – however, a minimal signal-to-noise ratio of three was enforced in the data selection). From the results obtained for $Q(f)$, it is clear that this problem is mainly related to region 1, with many stations on sedimentary underground and some of them located
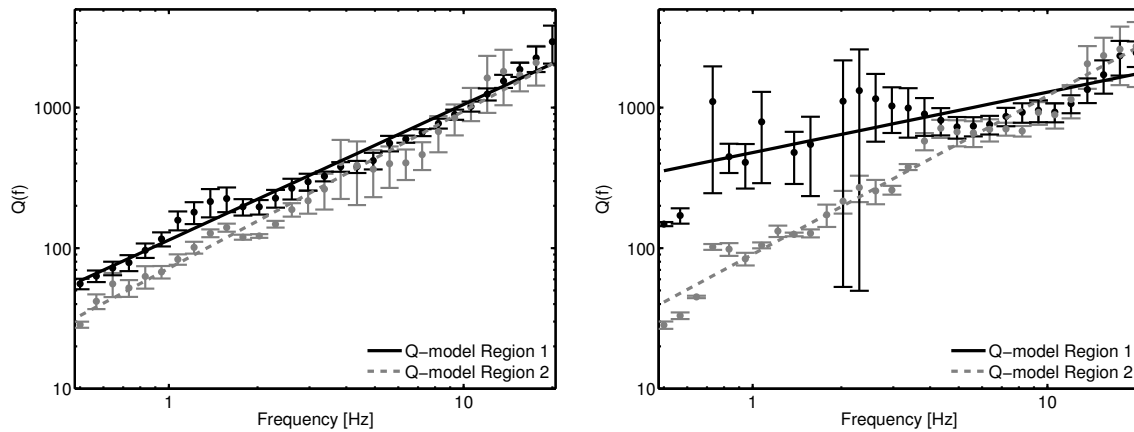
Figure 7.15: Derived $Q(f)$ models for region 1 and 2. Left panel: H component. Right panel: Z component. Note the differences in estimated $Q(f)$ models for H and Z components, especially in region 1.

in the very deep Focsani basin (Hauser et al., 2007). The differences in the obtained attenuation functions for H and Z components in region 1 reflect that at least a large part of the energy on the Z component in region 1 consists of scattered, converted and other phases. Russo et al. (2005) also note that S-wave energy is entirely absent on the Z component for a subset of the records from Vrancea events that they use.

Several other researchers focus their attention on the seismic attenuation in the Carpathians and surroundings. Popa et al. (2005), from a rather qualitative analysis of eight small magnitude Vrancea earthquakes which were recorded during the CALIXTO experiment in 1999 (e.g. Martin et al., 2006), come to the conclusion that in the Transylvanian basin (behind the mountain arc), the epicentral area and the Eastern Carpathians, the spectral amplitudes are lower by up to a factor of 100 compared to those in the foreland platform (region 1 in this work). They also find that the difference in attenuation is much stronger at higher frequencies than at lower ones and that it is most likely not attributable to source or site effects.

Russo et al. (2005) work with data from the same network (the accelerometric K2-network) as I use in this work. They use data from 65 small magnitude (mostly ≤ 4) earthquakes recorded in 1999. With several restrictive assumptions (the first one is that the site effect is equal for the S-wave window on the H component and P-wave window on the Z component, and the second one is that the source spectra for P- and S-waves are identical), they use the spectral ratio between the S-wave on the H components and the P-wave on the Z component to derive differential δt^* measurements. If a certain relation is assumed between Q_P and Q_S, an estimate of Q_S can be derived. Even though there may be some stations with a systematic error due to strong site effects, the problematic aspects mentioned above might average out if one looks at the entire dataset rather than a single station or single Q_S estimates. In summary, they find high attenuation (low Q_S) at stations VRI, SIR, OZU and MLR (which are all situated in region 2 defined here) and low attenuation in the foreland (region 1).

The results of these two studies are in good agreement with those presented here. The strong difference in attenuation characteristics between region 1 and 2 is quantified by the offset of the origins of the two attenuation functions. In Figure 7.16, I provide a possible explanation for the fact that, apparently, the slopes of the attenuation functions are similar (as in both cases, for the H components, almost identical
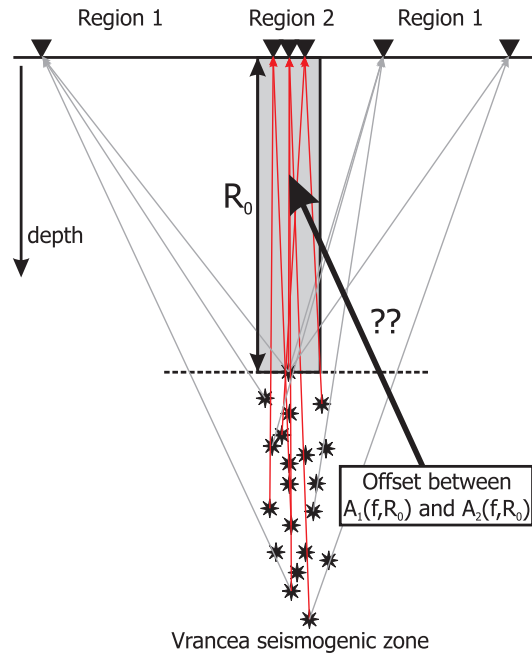
Figure 7.16: Sketch depicting the ray paths from sources to stations (orientation roughly SW-NE). For the stations in region 2, the rays from different earthquakes all travel the same path through the grayshaded region, which is defined by the depth of the shallowest event in the dataset. Increasing the distance R in the attenuation function $A_2(f, R)$ means to look mainly at data from deeper earthquakes and therefore, $A_2(f, R)$ only 'samples' the hypocentral zone. The offset between the origins of the two attenuation functions, $A_1(f, R_0)$ and $A_2(f, R_0)$, is most likely related to a process occurring somewhere in the grayshaded zone.

$Q(f)$ models were derived above). All the earthquake hypocenters are approximately located almost directly vertically below the stations in region 2. Thus, in order to increase the distance in $A_2(f, R)$, the source depth has to be increased. The difference in travel path for two datapoints at different distances in region 2 are hence related to the path traveled from the deeper event's hypocenter up to the one of the shallower one. As schematically indicated in Figure 7.16, within the grayshaded area, all the rays travel more or less the same path. In conclusion, $A_2(f, R)$ only 'samples' the lower part of the travel path, whereas the large offset observed between $A_1(f, R_0)$ and $A_2(f, R_0)$ is related to some strongly attenuating region somewhere in the grayshaded area, approximately between the shallowest event's hypocenter and the surface.

The seismic tomography results presented by Martin et al. (2006) and the outcome of the seismic refraction studies (Hauser et al., 2001, 2007) provide indications on the reasons for these strong lateral variations in seismic attenuation. The seismic refraction data (Hauser et al., 2001) suggest the presence of a low-velocity zone at a depth of 47 to 55 km beneath the Vrancea region, which, as Sperner and the CRC 461 Team (2005) note, coincides quite well with the observed seismic gap between 40 and 70 km depth already discussed by Fuchs et al. (1979). Here, the slab seems to be mechanically decoupled (or only weakly coupled) from the crust through a weak zone. This zone is commonly interpreted as the place where slab detachment currently takes place.

This area of weak coupling could be an explanation for the lower spectral amplitudes in the vicinity of the epicentral area (region 2) and the offset between the attenuation functions for the two regions.

Russo et al. (2005) invoke the existence of thermal anomalies influencing the travel paths to the stations SIR and MLR in view of recent volcanism at several sites near these stations. Ismail-Zadeh et al. (2005), following the work of Demetrescu and Andreescu (1994), show that indeed very high temperatures might persist in the subcrustal mantle (at a depth of around 50 km) beneath the mountain arc.

Beneath the Transylvanian basin, the tomography (Martin et al., 2006) clearly reveals a very strong low-velocity anomaly in the depth range 35-110 km, which is interpreted as the result of slab rollback and the delamination of continental lithosphere. Additionally, Martin et al. (2006) invoke the possible presence of partial melts at depth $\sim$ 100 km. The strong contrast between the high-velocity body (i.e. the slab with low attenutation), which influences the waves traveling to stations in the foreland (see tomography results, Martin et al., 2006), and the very strong low-velocity anomaly behind the mountain range is proposed by Popa et al. (2005) to explain the observed variations in attenuation, especially in the Transylvanian basin. I can neither confirm nor reject this interpretation regarding sites behind the mountain arc with this strong motion data set, as no such location is included in the database studied (station OZU is the only site which is close to the Transylvanian basin, although still in the mountain arc).

Yet, an interesting observation in that direction is the fact that not one single recording from stations DRG ($\sim$ 46.79° N, 22.71° E) and MED ($\sim$ 46.14° N, 24.37° E), located farthest to the NW from the Vrancea region (thus far behind the mountain arc), was usable in this analysis. This might also be explained with noisy locations or, for the smaller earthquakes, with the large distances, but also for the stronger events, no clear S-wave signal could be detected at these stations. For instance, the recordings at DRG and MED of the 2004/10/27 (M_W = 5.8) event show a clear P-onset, but no S-wave is detectable, neither on the horizontal nor on the vertical components, and the maximum amplitude is approximately 0.2 cm/s^2 (hypocentral distance $\sim$ 340 km) for DRG and 2.5 cm/s^2 for MED (hypocentral distance $\sim$ 215 km). At station ZML (not used in the inversion, but close to station ZIM, at hypocentral distance $\sim$ 280 km), the S-wave is very clear, with a maximum amplitude of around 30 cm/s^2, which is more than one order of magnitude larger than at MED, which is even at closer distance to the source, and more than two larger than at DRG. A very strong attenuation for travel paths behind the mountain arc might explain this pecularity. Thus, the observed inhomogeneity in attenuation is most likely explained by strong upper-mantle heterogeneity rather than crustal features.

These variations in seismic attenuation between the foreland (region 1) on one hand and the mountain range (region 2) and backarc area on the other also have important implications for the seismic hazard of Romania. As Popa et al. (2005) also note, the difference in attenuation is most relevant at high frequencies. This view is clearly confirmed by this study, and the main advantage of the results presented here is that the variation in attenuation has been quantitatively analyzed by means of an inversion scheme. At low frequencies, the spectral amplitudes of ground motion have similar values in region 1 and 2 (the slope of the attenuation function is slightly larger in region 2). Thus, for structures sensitive to low frequencies, such as high-rise buildings or long-span bridges, the risk is similar in the mountain range (and behind) and in the foreland (Popa et al., 2005), depending of course on the distance from the source region. At high frequencies, this situation changes drastically. Within and behind the mountain arc, the risk for e.g. buildings with less than three floors seems to be much smaller as compared with the foreland, as the high-frequency energy is efficiently attenuated for the latter region.

In view of the intensity maps from strong Vrancea earthquakes (the intensity maps of the large 1977 and 1986 events are depicted in Figure 6.24), the observed variations in attenuation might be the key

to understand the overall shape of the isoseismals. Apart from the small-scale structure within the high intensity (VII and VIII) areas (Figure 6.24, which I discussed in relation to the source properties of Vrancea earthquakes in Chapter 6.5), it is striking that the isoseismals separating the high and low intensities almost exactly follow the shape of the mountain arc.

Within the Carpathians as well as behind them, there is little infrastructure sensitive to low frequencies (as Popa et al., 2005, note, the largest amount of tall buildings is found in Bucharest) and the structures sensitive to higher frequencies are less affected due to the strong attenuation of high-frequency seismic waves. Thus, the overall shape of the macroseismic intensity pattern can be explained by the combination of less endangered infrastructure (with respect to low frequencies) and strong attenuation of high-frequency energy within and behind the mountain arc as compared with the foreland.

7.4   Site Amplification and Source Spectra

Using the non-parametric attenuation functions obtained in the preceding section, the spectral amplitudes are corrected for the effect of attenuation:

$$\log R_{ij}(f) = \log U_{ij}(f, R) - \log A_k(f, R) \,, \tag{7.21}$$

where $k = 1, 2$ depending on which region the station is located in. It is important to note that the corrected spectra still include an attenuation effect related to the propagation over the reference distance $R_0 = 90$ km. Furthermore, the cumulative effect represented by the offset between the origins of the two attenuation functions is also removed by the correction.

The attenuation-corrected spectral amplitudes $\log R_{ij}$ can be modeled by equation (7.13), and the second step of the non-parametric inversion presented in Section 7.1.2 is now performed in order to separate source and site contributions $S_i(f)$ and $I_j(f)$. A key issue in this inversion is the adopted constraint to remove the linear dependence between $S_i(f)$ and $I_j(f)$. As already discussed earlier, one can either fix one or several source and/or site functions or set the average site response over a given set of stations to unity. Using a source constraint is probematic with this dataset, even though there is strong evidence that for instance, the source spectrum of the 2004/10/27 ($M_W = 5.8$) event follows the ω^{-2}-model with a corner frequency of 1.6 Hz (Chapter 6.3). The difficulty resides in the unknown attenuation effect still included in the data, which would then be projected into the site amplification functions.

Therefore, I prefer to use a site constraint. As the H/V ratios are approximately flat for the rock stations MLR and SIR (see e.g. MLR in Figure 7.26 later in this work), I set the logarithmic average of these two stations to be equal to zero. As I will show later, the H/V ratio is generally not a good estimate of site amplification on the H component for most of the stations considered in this work. Yet, this site constraint is reasonable, as a flat H/V ratio (with approximate value 1) indicates that at least the site response for both the H and Z component is roughly identical. The combination of this observation and the fact that both stations are rock sites justifies the assumption of unit site response. Nevertheless, it must be kept in mind that all site amplification and source spectra are relative to the assumed average at these two sites.

The obtained site amplifications are shown for several stations in region 1 in Figures 7.17 for the H and 7.19 for the Z components and for all stations in region 2 in Figures 7.18 for the H respectively 7.20 for the Z component. The bootstrap analysis indicates that the results are very stable, except for the

highest frequency on the H component where the standard deviation is somewhat larger. As expected, the amplification for MLR and SIR ranges around their average value 1, as imposed by the constraint. A typical observation, both the for the H and even much stronger for the Z component, is the high level of amplification at high frequencies. For the H component, the amplification increases generally with frequency (e.g. VRI, SEC, LUC or CER) and stays on a high level, also at frequencies larger than 10 Hz. On the Z component, it is often observed that especially at these very high frequencies, the amplification rises strongly. The maximum amplification on the Z component is generally shifted to higher frequencies than on the H component. For several stations, the amplification of the H component from the GIT is more or less continuous over a large frequency band (e.g. SEC, BMG).

This strong amplification at high frequencies could be partially due to the fact that no κ-operator (e.g. Anderson and Hough, 1984; Boore and Joyner, 1997) has been taken into account when setting the site constraint for the two rock sites. For instance, Hartzell et al. (1996) constrained a hard rock site to show an amplification equal to one and a κ-related high frequency diminution, with $\kappa = 0.02$. The differential κ due to a different near surface atttenuation at different sites should however be reflected by the presented site amplification functions. Introducing κ for rock stations into the site constraint would lead to a fall-off of all site functions at high-frequencies (with the *same* κ-effect for all stations) and increase the high-frequency level in the source spectra, but relative to each other, nothing would change in the site functions.

κ is strongly dependent on the site conditions, reflecting attenuation in the near-surface weathered layers (Anderson and Hough, 1984), but also source (Papageorgiou and Aki, 1983) and propagation effects (Hanks, 1982) can lead to a high-frequency decay in the acceleration spectra, deviating from the ω^{-2}-model. Purvance and Anderson (2003) show that κ can be parameterized as a combination of a distance-, a site- and a source-dependent term. These terms can in principle be separated from each other with a similar inversion scheme as used in this work. However, the measured values of κ should be unaffected by site amplification effects (as Parolai and Bindi, 2004, show, the fundamental resonance frequencies of the site must be well below the frequency band used for the determination of κ) and must be measured well-above the corner frequency of the respective event. Even at high frequencies (above 10 Hz), considerable site effects are observable in Figures 7.17, 7.18, 7.19 and 7.20. Moreover, from the results obtained in Chapter 6, the corner frequencies of the smaller events tend to be very high too. Therefore, I refrain from further discussing κ measured from the high-frequency fall-off of the specta.

Oncescu et al. (1999a) used a similar approach as presented here to separate source and site contributions from a (much smaller) dataset of strong (the four large Vrancea events in 1977, 1986 and 1990) and weak motion (recorded from 1985-1990) spectra from Vrancea earthquakes. They determined a $Q(f)$-model for S-waves ($Q(f) = 109f^{0.81}$) by using the coda waves from two Vrancea earthquakes at station Incerc in Bucharest (which might be questionable due to the small amount of data used to derive it) and corrected the spectra for attenuation and geometrical spreading before performing the inversion. As a site constraint, they used the transfer function calculated from geotechnical data at station Incerc. The different correction of attenuation and the different site constraint make a direct comparison of the results difficult. However, they observe for instance a very strong deamplification at station MLR at high frequencies (also deamplification at VRI), which is most likely due to the fact that their attenuation model is inappropriate for these sites. They did not find strong evidence for non-linearity by comparing the site functions derived from weak and strong motion data. It is also worth noting that the transfer function which they computed at station Incerc shows a level of amplification quite similar to the amplification function obtained in this work at station INB, which resembles to the one shown in Figure 7.17 for station BMG.
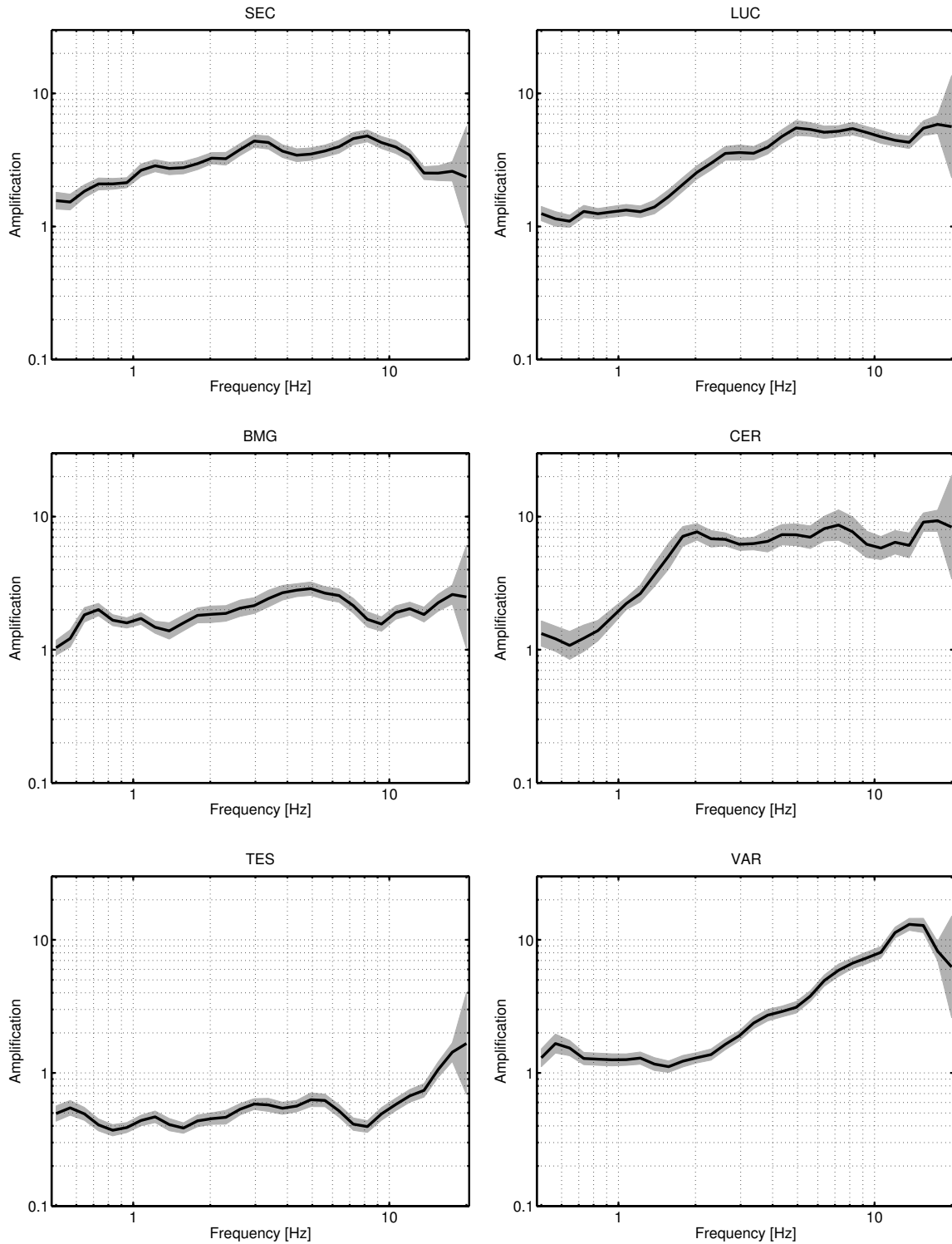
Figure 7.17: Examples of the obtained site amplification functions for the H component in region 1. Black line: mean of 200 bootstrap samples. Grayshaded area: mean ± one standard deviation.
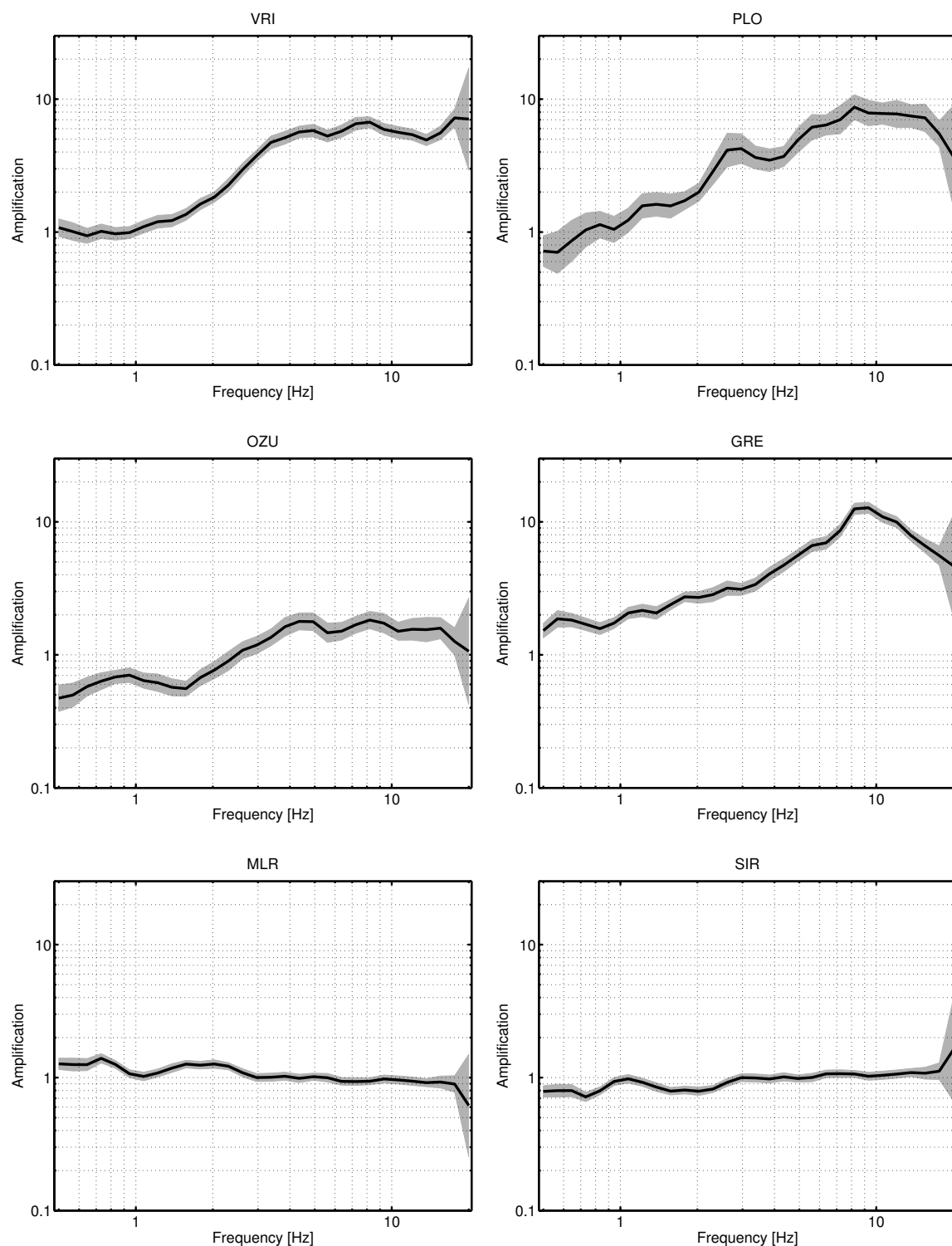
Figure 7.18: Obtained site amplification functions for the H component in region 2. Black line: mean of 200 bootstrap samples. Grayshaded area: mean ± one standard deviation.
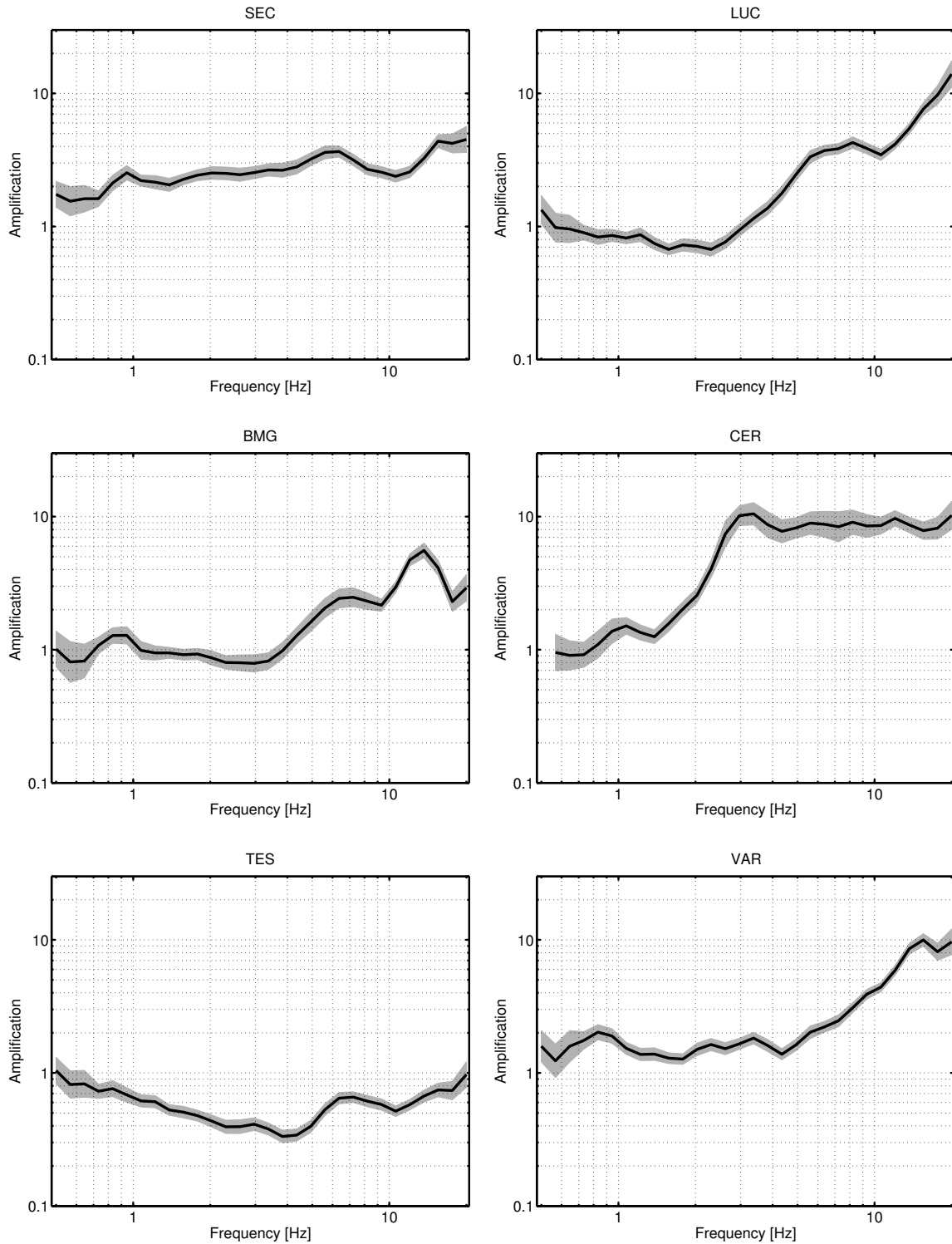
Figure 7.19: Examples of the obtained site amplification functions for the Z component in region 1. Black line: mean of 200 bootstrap samples. Grayshaded area: mean ± one standard deviation.
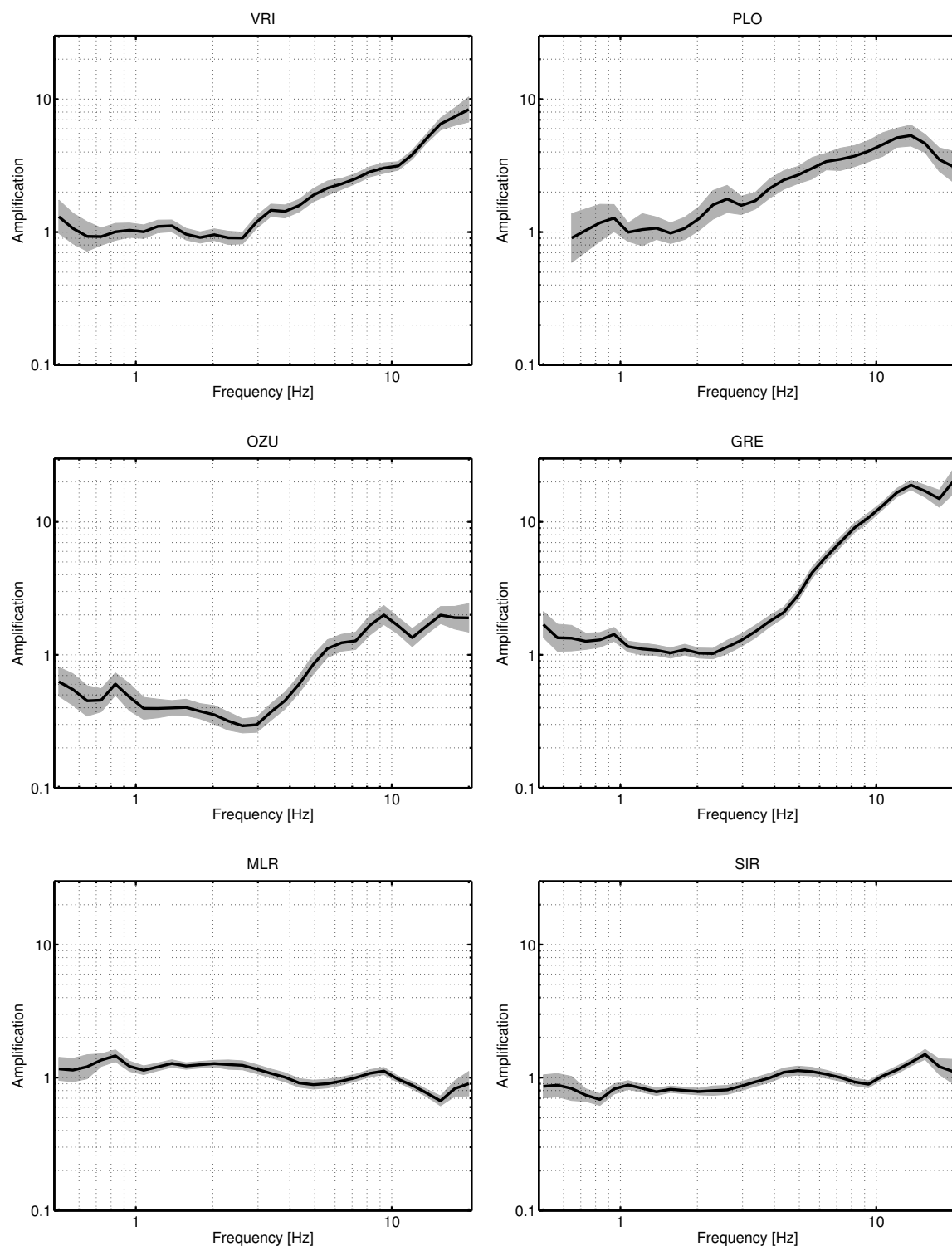
Figure 7.20: Obtained site amplification functions for the Z component in region 2. Black line: mean of 200 bootstrap samples. Grayshaded area: mean ± one standard deviation.
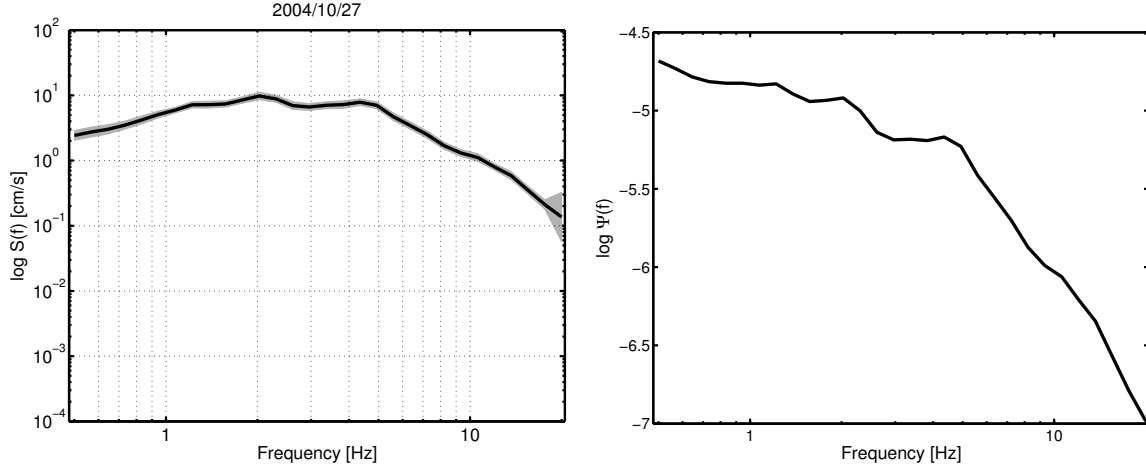
Figure 7.21: Inverted source function for 2004/10/27 event (left) scaled to a distance of $R_0 = 90$ km and correction function $\log \Psi(f)$ (right) derived by considering the results of the spectral ratio study in Chapter 6.3. The source spectrum of the 2004/10/27 earthquake is supposed to obey the ω^{-2}-model (Brune, 1970, 1971) with a corner frequency $f_c = 1.6$ Hz. The correction function only contains the difference between theoretical source spectrum and inverted source spectrum due to the attenuation over $R_0 = 90$ km (see text for more details).

Sokolov et al. (2004) derived site amplification functions for the same stations considered here by computing theoretical 'very hard rock' (VHR) spectra and comparing the observed spectra to the VHR ones. The residuals between these are interpreted as site effects. I discuss the relation between their results and the site functions computed from the above inversion in Section 7.7.

Regarding the source spectra, the obtained results are shown in Figure 7.21 (left panel) for the 2004/10/27 earthquake and in Figure 7.22 (left panel) for three other events in the database. As already mentioned at the beginning of this section, the attenuation-corrected spectra still include a cumulative attenuation effect over the reference distance $R_0 = 90$ km. As the constraint used in the inversion is related to the site functions and does not include this attenuation effect, the latter one is moved into the source spectra. Considering this fact, the source spectra can be written as:

$$\underbrace{(2\pi f)^2 \frac{\langle \mathcal{R}^{\theta\phi} \rangle VF}{4\pi\rho v_S^3} \cdot M_0 \left[1 + \left(\frac{f}{f_c}\right)^2\right]^{-1}}_{\text{compare with (4.30)-(4.32)}} \cdot \Psi(f). \qquad (7.22)$$

Herein, the function $\Psi(f)$ represents the remaining attenuation over the distance $R_0 = 90$ km (including geometrical spreading, anelastic attenuation, ...). The other parameters are free surface amplification $F = 2$, separation of S-wave energy on two horizontal components $V = 1/\sqrt{2}$, average radiation pattern $\langle \mathcal{R}^{\theta\phi} \rangle = 0.6$, density $\rho = 3.2$ g/cm^3 and shear wave velocity in the source region $v_S = 4.5$ km/s.

Writing the inverted source spectra in the form (7.22) implies that the source spectra unaffected by attenuation obey the ω^{-2}-model (Brune, 1970, 1971). For the 2004/10/27 event ($M_W = 5.8$), good indications are presented in Chapter 6.3 that this might indeed be the case. Therefore, with a corner frequency of 1.6 Hz for the latter event, $\Psi(f)$ can be computed from the inverted source spectrum
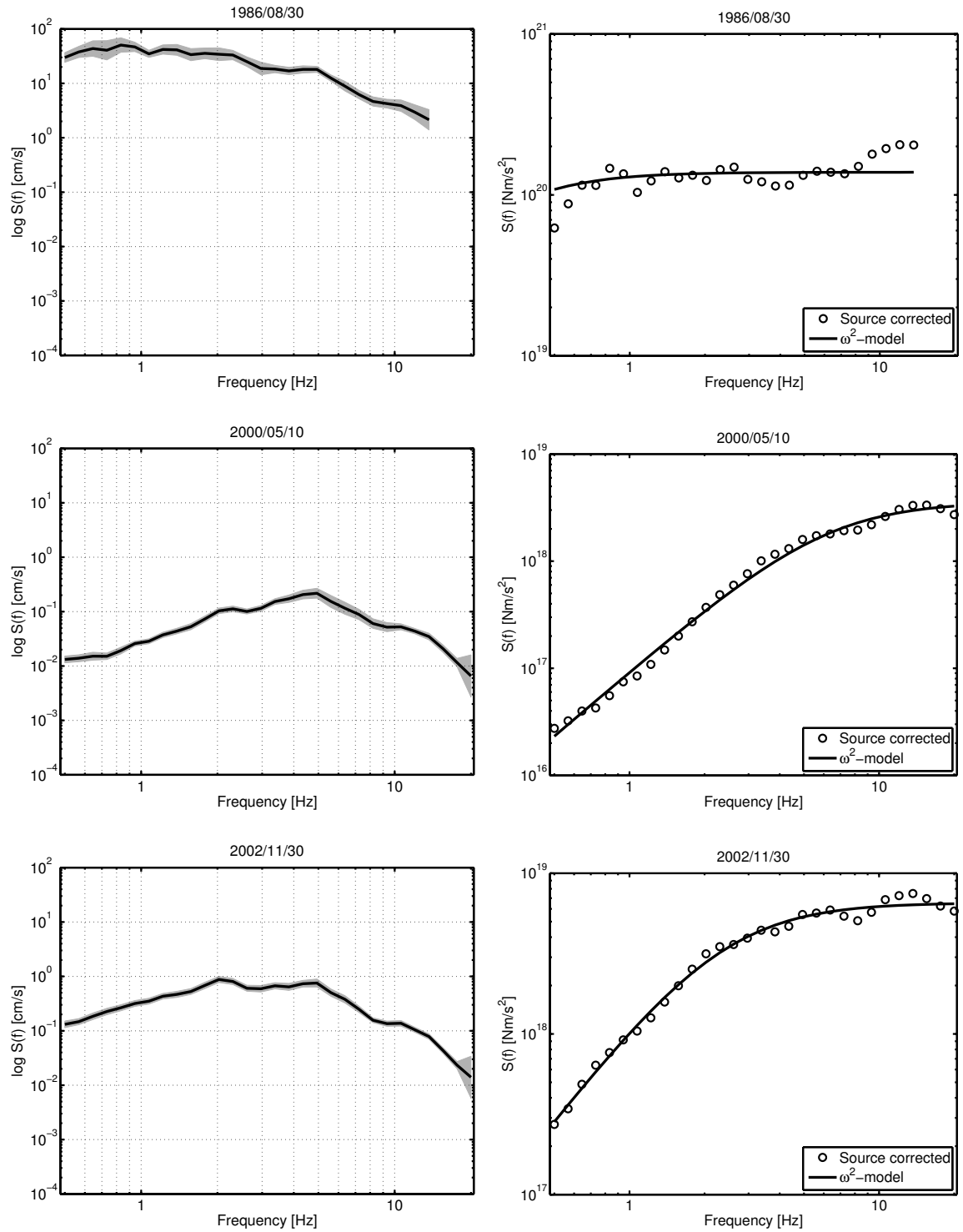
Figure 7.22: Inverted source functions (left) and source functions corrected for attenuation over $R_0 =$ 90 km (right) with the correction function derived using the 2004/10/27 earthquake (Figure 7.21). The obtained corrected source functions follow the ω^{-2}-model (Brune, 1970, 1971).

(Figure 7.21). Then, by correcting the other inverted source spectra by $\Psi(f)$, it is possible to check whether or not the corrected source spectra also follow the ω^{-2}-model.

This interpretation is based on the validity of the assumption made for the event 2004/10/27. This assumption is however reasonable, as this event has been investigated with a large database (Chapter 6, the results are well-constrained) and is in agreement with the large asperity stress release derived by other authors (e.g. Oncescu, 1989) for Vrancea earthquakes. In Figure 7.22 (right panel), the corrected source spectra are shown in three case, with an ω^{-2}-model fitted to the data with non-linear least squares (in the case of the large earthquakes in 1986 and 1990, M_0 was constrained, as the expected corner frequency is lower than the lowest frequency analyzed – if M_0 would

Figure 7.23: Corner frequencies of corrected source spectra versus seismic moment. The fitted straight line has a slope of -0.3, which is close to the expected value $-1/3$ in case of self-similarity (2.36). Note however that this trend is only suggestive, because only very few datapoints are available for large magnitude events.

not be constrained, the spectrum could be explained with any combination of M_0 and f_c in such a case). The corrected source spectra generally follow the ω^{-2}-model with, as expected from the results in Chapter 6.3, rather high f_c. As discussed earlier, a certain effect of near surface attenuation due to κ might also be projected into the source spectra. Therefore, by assuming an ω^{-2}-source, this contribution is included in the correction function $\Psi(f)$.

The corner frequencies obtained by fitting ω^{-2}-models to the corrected spectra are plotted versus seismic moment in Figure 7.23 (the error bars are indicative for the regressional error of the fit). M_0 was also derived from the spectra and may thus differ slightly from the ones expected using the moment magnitudes taken from the ROMPLUS catalogue (Oncescu et al., 1999b) given in Tables 7.1 and 7.2 (Figure 7.24, where M_W derived with (2.37) are plotted). First, the corner frequencies are generally very high, indicating large values of stress drop. This is in good agreement with the results presented in the previous chapter from the simulations using empirical Green's functions. Second, by fitting a straight line (least squares) to $\log f_c$ plotted against $\log M_0$, the slope is approximately equal to the one expected in the case of self-similarity, i.e. roughly $-1/3$. Note however that this trend is only suggestive, as only few stronger earthquakes are in the dataset. The spectral scaling analysis in Chapter 6.3 also indicates roughly self-similarity among Vrancea earthquakes, as the scaling factors C (denoting the stress drop ratio between large and small event) only vary from 0.7-2.

The source properties discussed above have been derived from the H component. Regarding the Z component, the source functions obtained from the inversion are somewhat different from those derived with the H component. Yet, this is again not unexpected, as there is only litte S-wave energy on many records on the Z component. Thus, the source functions obtained do not represent S-wave source spectra. Therefore, the source properties are only discussed using the results obtained from the H component.
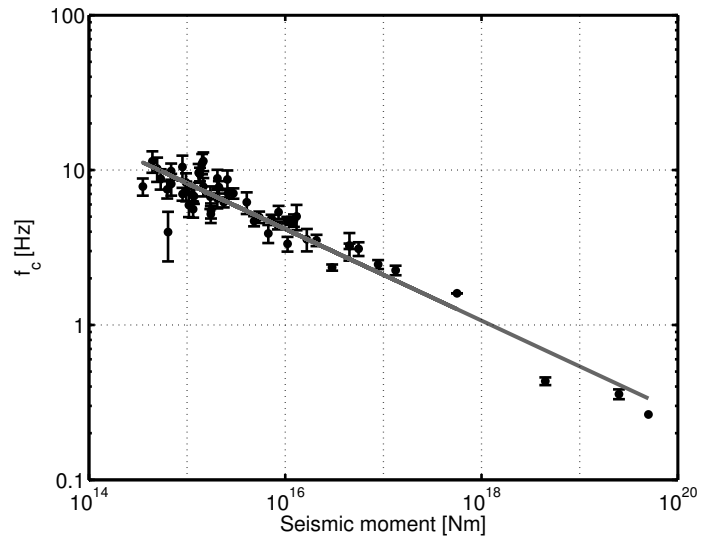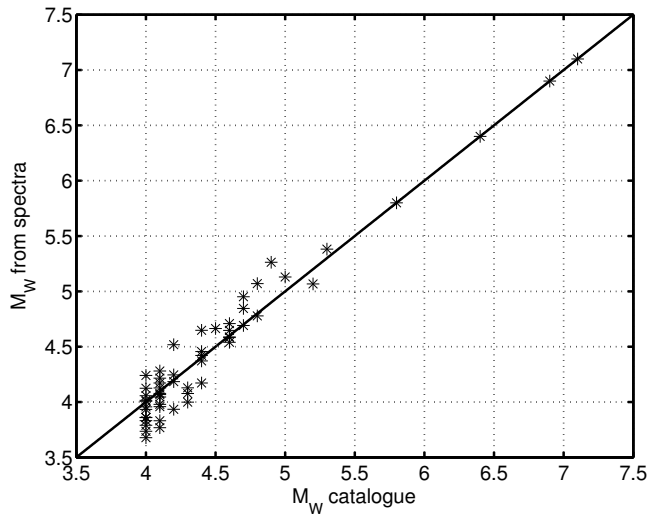
Figure 7.24: Moment magnitude from ROMPLUS catalogue (Oncescu et al., 1999b) versus moment magnitude from the spectra. The trend follows the straight line where they are identical. Note that the moments of the four largest events have been constrained when fitting the spectra – therefore, they are exactly identical with the ones from the catalogue.

Finally, I show several examples for the fit between observed spectra and the inverted spectral model (multiplying the terms for source, attenuation and site derived above with each other) in Figure 7.25. Generally, the agreement is fair to excellent, although in few cases the spectral amplitude in parts of the spectrum is misestimated up to a factor of around 2 to 3. Very few outliers show a stronger misestimation (only 5% of the spectra show a misestimation in amplitude higher than a factor 3.5 at some given frequency – it is not the entire spectrum which is misestimated). Such outliers which cannot be fitted by the inverted models are a natural phenomenon appearing in any inverse problem.

7.5 The GIT Site Functions and H/V Ratios

In recent years, the H/V spectral ratio technique, because of its simplicity and low costs, has been extensively applied in order to assess local site amplification effects. The technique has been made popular for ambient noise measurements by Nakamura (1989) and has been extensively studied (e.g. Parolai et al., 2004a,b) since then.

Lermo and Chavez-Garcia (1993) applied the approach to the S-wave part of earthquake recordings in Mexico and obtained a good agreement between the resulting H/V ratios and the site amplification estimated using spectral ratios with respect to a reference station (e.g. Borcherdt, 1970). Briefly, the method consists in dividing the horizontal component shear wave spectra at the site of interest by the vertical component ones, the latter ones being presumed to be much less affected by local site conditions. Since then, the H/V technique has been applied to earthquake recordings worldwide (e.g. Theodulidis and Bard, 1995; Chen and Atkinson, 2002; Siddiqqi and Atkinson, 2002; Sokolov et al., 2005). Comparsions between the H/V technique and other methods of site response estimation are for instance described by Field and Jacob (1995), Bonilla et al. (1997) and Parolai et al. (2000, 2004a). These studies indicate that, generally, the H/V method is capable of revealing the fundamental resonance frequency of a site, but often fails in amplitude estimation as compared with for instance the GIT technique used in this work.

Yet, if strong amplification effects occur on the vertical component, severe differences may be the consequence between the H/V spectral ratio and the site amplification estimated e.g. by the GIT inversion technique. As Parolai et al. (2004a) note, reliable estimates of the site amplification can only be derived from the H/V ratio if the sources are distributed all around the station at different distances and the H/V ratio depends on the incidence angle (Lermo and Chavez-Garcia, 1993).
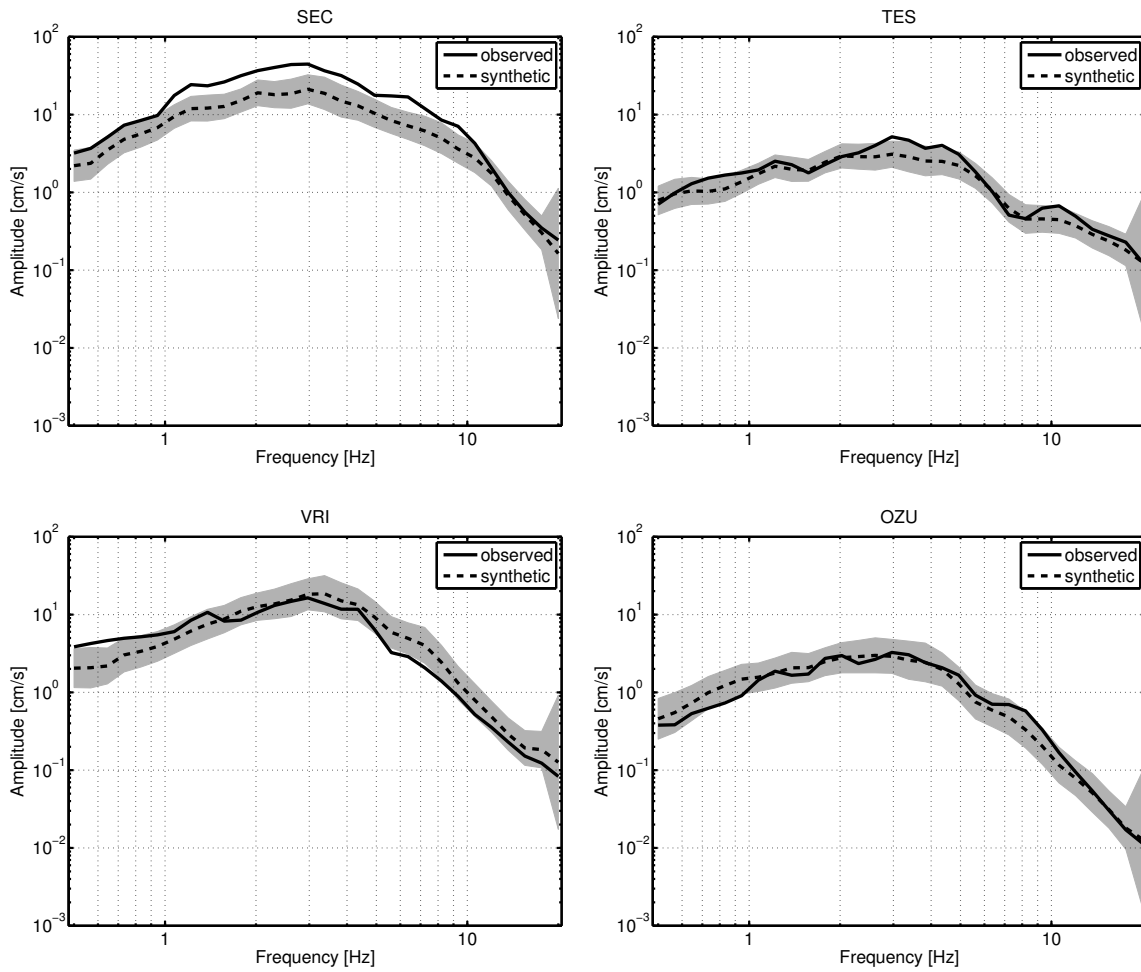
Figure 7.25: Example for the fit between observed spectra and those generated with the inverted spectral model for the 2004/10/27 earthquake at four sites (H component). Continuous line: observed spectrum. Dotted line: modeled spectrum. The grayshaded area indicates the modeled spectrum if for source, attenuation and site function ± one standard deviation is taken into account.

In the case of Vrancea earthquakes, the site amplification functions for the Z component derived using the GIT technique do show severe amplification effects, especially at high frequencies. Moreover, the source-to-station geometry is very special: the incidence angles do not vary a lot (always near-vertical incidence) as compared with the crustal earthquake case and, due to the strong clustering of the hypocenters, the sources are not at all distributed around a given station. Rather, all the source-to-station rays travel very similar paths for a given site. As discussed before, the Z component also seems to be mostly composed of different phases instead of carrying mainly S-wave energy, which is also a quite special case as compared with usual crustal earthquake recordings. For these reasons, it may be questionable whether the H/V ratio technique, applied to Vrancea earthquakes, provides reliable estimates of site amplification.

Indeed, if one compares the H/V ratios (Figure 7.26, the dashed curve represents the mean and the grayshaded area indicates the standard deviation) directly with the amplification functions obtained for the H component (Figures 7.17 and 7.18), strong differences can immediately be recognized,
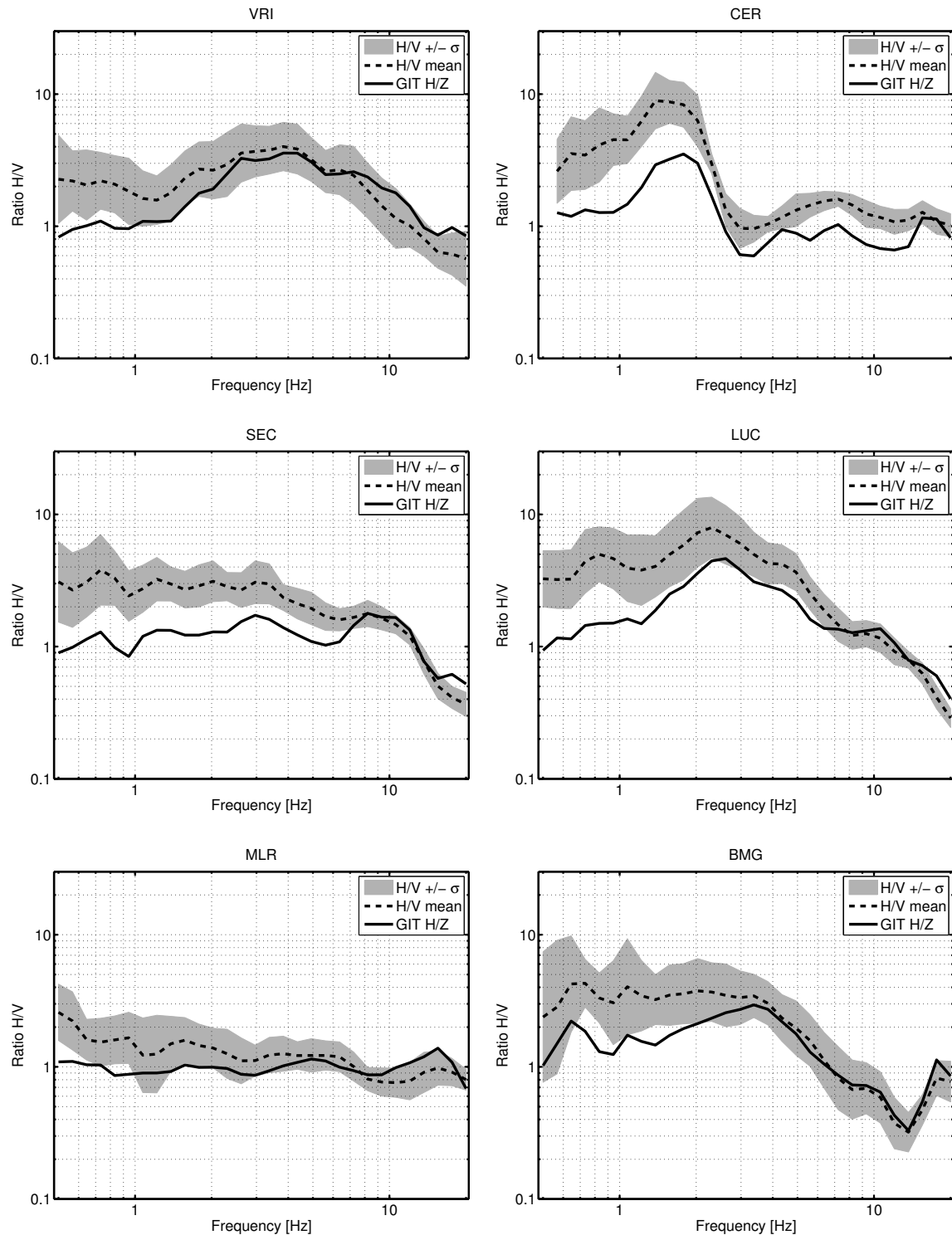
Figure 7.26: Comparison between H/V spectral ratios and the ratio of amplification functions H/Z obtained from GIT at six stations. The peaks observed in the H/V spectral ratio and its general shape can be well reproduced from the the GIT H/Z results. The differences, especially at low frequencies, are mostly due to the site constraint (logarithmic average of MLR and SIR equal to zero) and partly to the correction with different attenuation functions for H and Z component data in the GIT.
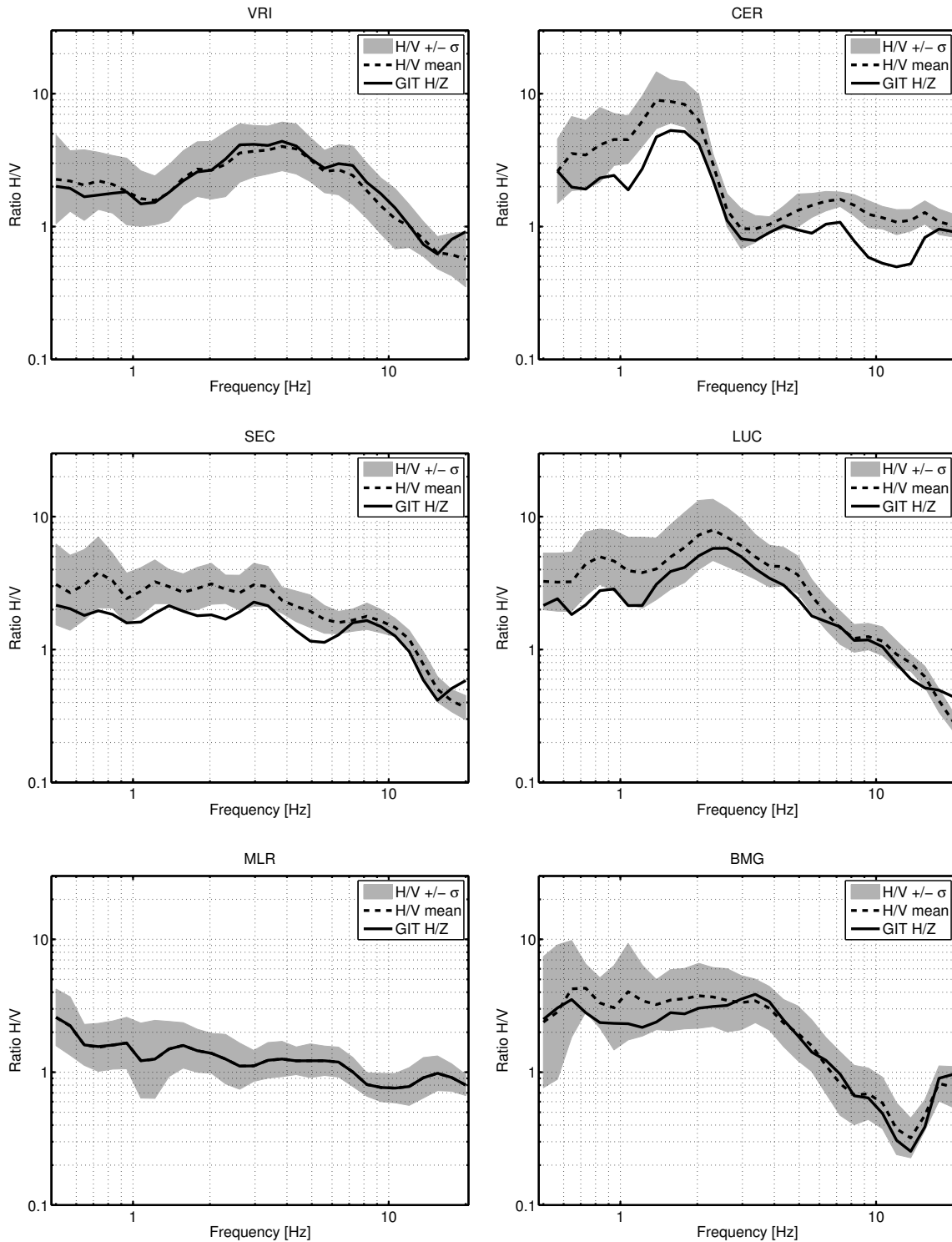
Figure 7.27: Comparison between H/V spectral ratios and the ratio of amplification functions H/Z obtained from GIT at six stations using the H/V ratio of MLR as site constraint for the H component (and the Z site function constrained to one) in the GIT.

especially at higher frequencies. For instance, at station CER, the site function from the GIT increases in the frequency range 1-2 Hz and remains at a level of approximately 7-8 for higher frequencies. The H/V ratio, on the other hand, indicates an isolated peak in the frequency range 1.5-2 Hz and almost no amplification at all at higher frequencies. In general, the H/V ratio misestimates the site amplification of the H component obtained from the GIT both in shape and in amplitude (especially at high frequencies).

If the site amplification on the Z component is not approximately one, then the H/V ratio should simply represent the amplification of the H component divided by the one of the Z component (as the source and attenuation contributions are in principle included in both components). Figure 7.26 shows the comparison of the H/V ratios with the ratio of the site amplification functions for the H and the Z component derived by the inversion (denoted as GIT H/Z in the following) at several stations. Interestingly, the general shape of the H/V ratios can be quite well explained with the GIT H/Z ratio. For instance, the prominent peak in the H/V ratio at station CER or the peak at station LUC between 2 and 3 Hz are astonishingly similar. There is, however, a discrepancy in amplitude at low frequencies.

This difference between the GIT H/Z and the H/V ratios at low frequencies is easy to explain. The H/V ratios at stations MLR and SIR are not entirely flat at low frequencies, but show an amplification of a factor of 1.5-3. The site constraint used in the GIT inversion, however, produces a GIT H/Z ratio approximately equal to one for these two stations. Therefore, the GIT H/Z ratios underestimate the H/V ratio at low frequencies. In Figure 7.27, the comparison between the H/V and the GIT H/Z ratios is shown in the case where the site constraint in the GIT inversion is set to equal the H/V ratio for MLR on the H component and to be one for MLR on the Z component. Therefore, for MLR, the GIT H/Z and H/V ratios are equal. For the other stations, the H/V and GIT H/Z ratios are very close to each other and depict nearly identical shapes. If the H/V ratio at MLR is used as site constraint for the H component, all the site functions of the H component show a little higher amplifications at low frequencies.

A further issue is the different attenuation function for the H and Z component for region 1. By taking the H/V ratio as an estimate of the ratio of site amplification functions for H and Z component, one assumes that both components are subjected to identical attenuation. As presented in Section 7.3, this seems not to be true in the case of Vrancea earthquakes, at least not in region 1. Due to this fact, it is not surprising to still see a slight difference in Figure 7.27 between H/V and GIT H/Z ratios. Note the very good coincidence between H/V and GIT H/Z ratio at station VRI, which is located in region 2 where the difference of the attenuation functions between H and Z component is very small. If, additionally to the usage of the H/V ratio at station MLR as a site constraint, both the H and Z component are corrected with the same attenuation functions in region 1, the H/V and GIT H/Z ratios are exactly matching each other (not shown here). The largest part of the difference, however, is attributable to the site constraint, as Figure 7.27 shows.

These results clearly demonstrate that the H/V ratio is not a good estimate of site amplification in the case of Vrancea earthquakes. An important issue remains to be clarified (which can, however, not be clarified in this work): how are these findings related to the H/V spectral ratios derived from ambient noise data? Two studies of this kind can be cited for the Bucharest area: both Bonjer et al. (1999) and Ziehm (2006) (the latter study using broadband data from the URS project, Ritter et al., 2005) found two peaks in the H/V ratios at frequencies around 0.2 and 0.7-0.8 Hz, and their H/V ratios from ambient noise display values lower than one at frequencies around 10 Hz (which is the maximum frequency they are analyzing). This indicates at least that the strong amplification at high frequencies on the Z component obtained from the GIT inversion may also be reflected to some extent by the H/V

ratios from ambient noise data (at least in Bucharest) and that these might not be representative for the site amplification of the H component either. However, as ambient noise is composed of other wave types (it is usually believed to be dominated by surface waves, Konno and Ohmachi, 1998) than the earthquake data analyzed above, a further interpretation of these issues needs more investigations.

Bonjer et al. (1999) also obtained the peak between 0.7-0.8 Hz in Bucharest computing H/V ratios from Vrancea earthquake data. In the H/V ratios which I computed in this work, the maximum is usually located between 0.5-1 Hz in Bucharest, which corresponds quite well to this peak discussed by the other authors. This peak at around 0.7-0.8 Hz can also be detected for instance in the amplification function for the H component at station BMG in Figure 7.17, even though not very prominent. Therefore, at low frequencies, it seems that features appearing in the H/V ratios in Bucharest are also reflected to some extent in the GIT site amplification function for the H component. However, this is not the case at other stations of the network and, due to the strong amplification at high frequencies (> approximately 2-3 Hz) on the Z component, the H/V ratios are clearly inadequate at high frequencies.

7.6 Comparison to Other Spectral Models and Implications for Ground Motion Simulations

This is not the only existing set of spectral ground motion models for Vrancea earthquakes. It is a well-known property of such an inverse problem that the results also depend upon the parameterization of the problem. Extensive studies on the spectral properties of ground motion from Vrancea earthquakes have also been performed by Sokolov et al. (2004, 2005).

Their approach is however somewhat different. Sokolov et al. (2005) use the H/V ratio from earthquake data as an estimate of site amplification of the H component at eight rock stations which are also included in the dataset used in the GIT above. After removal of this 'site effect', they correct for attenuation along the path using a three-layered $Q(f)$-model which leads to slightly less attenuation than the model derived for region 1 in (7.20). From the results in Section 7.3, this model is clearly inappropriate for stations SIR, VRI and OZU (which are included in their dataset). An additional model parameter, κ, accounts for the remaining high-frequency decay with respect to an ω^{-2} source model. This parameter is the key to understand the main difference between their model and the results of this chapter.

Compared to the results from the GIT in this work, they underestimate the site effect at high frequencies by using the H/V ratio (as the Z component is also amplified), but also strongly underestimate attenuation along the path for high frequencies, especially for stations located in region 2. In summary, without the further model parameter κ accounting for this fact (in the spectral model, the term is $e^{-\pi\kappa f}$), they would strongly overestimate the high-frequency content, as the inappropriateness of the attenuation model for region 2 is a much stronger effect than the high-frequency deficiency from the H/V ratios. Therefore, Sokolov et al. (2005) need very high κ-values in region 2 to fit the observations ($\kappa \sim 0.07$ for SIR, $\kappa \sim 0.04 - 0.07$ for VRI and $\kappa \sim 0.05 - 0.07$ for OZU). In region 1, their $Q(f)$-model is better suited. They also use stress drop values (computed from the corner frequencies) increasing with magnitude. This means that Vrancea earthquakes do not show self-similar scaling, a result in contradiction with my findings.

Sokolov et al. (2004) use the source and attenuation models described in Sokolov et al. (2005) (including an average value for κ, which is however increasing with magnitude – this magnitude dependence

154

in fact counteracts the increase of the stress drop with magnitude) and compute VHR spectra for many Vrancea earthquakes at other stations of the network. The residuals between the observed and VHR spectra are interpreted as site effect. Interestingly, the site response functions for several sites in region 1 that they present look quite similar to the ones obtained from the GIT. Thus, the combination of their source functions, $Q(f)$-model and κ-operator has a similar effect than the combination of the sources and attenuation model derived in this work, even though the parameterization is completely different. Furthermore, they show that it is indeed possible to generate data-consistent stochastic simulations with their model.

Yet, even though both models are able to explain the observed spectra, the key question is the interpretation in terms of physics. Here, the implications of the models are radically different. Whereas the results from the GIT clearly indicate strong lateral heterogeneity in attenuation (with very strong attenuation for stations located in the mountain arc), Sokolov et al. (2004, 2005) do not account for such an effect by using a predefined $Q(f)$-model which does not show this variability. However, they use the κ-term in order to have an additional high-frequency attenuation *ad hoc*. For the rock stations, they use the H/V ratios as an estimate of site response, which I showed to be an inadequate estimate of site amplification. Sokolov et al. (2004, 2005) use stress drops increasing with magnitude, which is in contradiction to the self-similar scaling derived in this work. Thus, if one tries to give a physical interpretation to each of these terms alone, completely different conclusions are reached and yet, it is possible to explain the spectra with both models.

From the point of view of physics, the GIT results are more meaningful, as they have been obtained using a well-defined inversion scheme and without assumptions which are hard to justify. The attenuation characteristics were not assumed to be given by a certain model. Thus, the attenuation correction performed before the second step is certainly in agreement with this specific dataset. For the second step, the only assumption made is the amplification at the rock sites MLR and/or SIR. The H/V ratios are roughly flat for these sites with level unity, which means at least that both the H and Z component are amplified in the same way. In combination with the fact that these are rock sites, assuming unit site response is thus well justified.

In terms of ground motion simulations, the spectral models of Sokolov et al. (2004, 2005) have indeed proven to do very well. Therefore, there is no need to refrain from performing simulations with these parameters. However, they should not be interpreted physically.

7.7 Summary

The results presented in this chapter provide important constraints on the attenuation characteristics beneath Vrancea as well as on the source processes of the intermediate-depth earthquakes. Both the outcome of this study as well as the spectral ratios from Chapter 6.3 indicate that Vrancea earthquakes show to first order self-similar scaling and can be described by an ω^{-2}-model with very high corner frequencies. This indicates large stress release, an issue which is treated in detail in Chapter 6.

For instance, for an $M_W = 4.0$ crustal earthquake, following Brune (1970, 1971), a corner frequency f_c of around 2 Hz would be expected for a stress drop of 10 bar and around 4.5 Hz for a stress drop of 100 bar. In the case of Vrancea earthquakes, f_c ranges around 8-10 Hz for such an event, which would correspond to approximately 1000 bar stress release in Brune's model. However, due to the problems in linking corner frequency to stress drop discussed in Chapter 3, the study of source parameters from Vrancea earthquakes using the EGF method in Chapter 6 is more elucidating than the derivation

of stress release from the corner frequency. What can however be clearly stated is that the corner frequencies for the intermediate-depth Vrancea earthquakes are generally larger by at least a factor of two as compared with crustal events. This is of great importance for stochastic ground motion simulations.

Seismic attenuation in the Carpathians and the surrounding areas depicts strong lateral variations, with very strong attenuation in the epicentral area (and, based on the findings of other authors mentioned above, behind the mountain arc in the Transylvanian basin) and much lower attenuation in the foreland. These differences in attenuation are also of high importance regarding seismic hazard and certainly play a key role in understanding the macroseismic intensity maps of past Vrancea earthquakes.

The site amplification functions obtained show a tendency for rather large amplification at high frequencies and the amplification of the Z component is not even approximately close to unity for most sites, but generally shows very prominent amplification at high frequencies. This is the main reason why the H/V ratios derived from earthquake data (more investigations are needed with respect to the ones derived from ambient noise) do not represent a good estimate of site amplification.

The results from the GIT inversion also constitute a complete set of spectral ground motion models for Vrancea earthquakes. As such, these models can also be used as a basis for stochastic ground motion simulations for future potential Vrancea earthquakes as presented in Chapter 4.2. It is possible with the models derived here to compute synthetic ground motion time series for 'very hard rock' conditions over the entire Romanian territory (by leaving out the site functions). If site effects shall be included in the simulations at a site which was not part of the dataset analyzed here, this site must be classified in some way with respect to the site functions obtained from the GIT.

The comparison of the spectral models derived in this chapter and the ones of Sokolov et al. (2004, 2005) has clearly shown that there is no unique model to explain ground motion spectra. This is of course not unexpected for such an inverse problem. Their results are fine for performing data-consistent ground motion simulations. However, care has to be taken if the model parameters shall be interpreted in terms of physics.

Chapter 8

Summary and Conclusions

In this thesis, the strong motion generation process of Vrancea earthquakes as well as the spectral characteristics of seismic ground motion resulting from these earthquakes have been analyzed. Appropriate 'strong motion generation area' (SMGA, Miyake et al., 2003) source models have been derived using the empirical Green's functions (EGF) approach of Irikura (1983, 1986, 1999) and a genetic algorithm designed to find sets of appropriate solutions to this problem. A novel approach was adopted to find appropriate source models for the large 1977 ($M_W = 7.4$) event, where, in combination with the EGF technique, macroseismic intensity was used as an inversion criterion. The results obtained are highly satisfactory and indicate that this methodology could be a highly interesting tool to investigate the source process of historical earthquakes. Furthermore, the acceleration spectra of Romania-wide recordings of Vrancea earthquakes have been separated into their source, path and site contributions, which represents the basis for stochastic simulations of ground motion anywhere on the Romanian territory. I will now summarize the most relevant results with reference to the respective sections in the thesis.

In Chapter 3, earthquake source parameters and especially stress drop were discussed on a theoretical basis, with a particular emphasis on the relationship between the spectra of seismic waves and these parameters. In fact, one has to distinguish between static and dynamic stress drop. Both of of them are key parameters in seismology, as they provide information on the scaling properties of source parameters (such as source dimensions, slip, rise time) and the (dynamic) stress drop is important in the estimation of strong ground motion, as it influences the high-frequency level of acceleration (Brune, 1970, 1971).

It has become common practice to compute stress drop estimates from the spectra of seismic waves (e.g. Abercrombie, 1995; Abercrombie and Rice, 2005; Allmann and Shearer, 2007) by determining the corner frequency and making use of models such as the one of Brune (1970, 1971) or Madariaga (1976), which provide relations between corner frequency and source dimensions (and hence, stress drop). Yet, as I discussed in Chapter 3.2, these values of stress drop are heavily dependent on the assumptions made in these models. The only directly measurable quantities from the spectra are the seismic moment M_0, which has a clear physical meaning, and the corner frequency f_c, which is, as such, a purely empirical parameter. Nevertheless, the corner frequency is an important parameter, as it enables us for instance to investigate whether earthquakes show self-similar scaling (which can be expressed as $M_0 f_c^3 = constant$, Aki, 1967, and is equivalent to constant stress drop) or not, regardless of the absolute value of stress drop. By analyzing differences of the relation between M_0 and f_c for

different seismogenic zones, the seismic sources of these regions can be directly compared without the necessity to make further model assumptions.

Ground motion simulation techniques, with a particular emphasis on Irikura's (1983, 1986, 1999) empirical Green's functions (EGF) method, have been discussed in Chapter 4. Irikura's technique is based on a simple rectangular source with constant slip and slip velocity, which Miyake et al. (2003) called the 'strong motion generation area' (SMGA). Furthermore, the method is based on the scaling relations among earthquakes (as opposed to the technique of Hutchings, 1991, 1994), and the scaling factor N and stress drop ratio C between the EGF and mainshock (TARGET) can be derived from the spectra. This is, for instance, an exploitation of the above mentioned relation between M_0 and f_c, without linking f_c directly to any source parameter. As I showed in Chapter 4.1, proper estimates of C and N as well as SMGA size, rise time and rupture initiation location are essential in order to compute reasonable simulations.

The latter five SMGA parameters (length L, width W, rise time T_r, rupture initiation point along strike and dip) have been determined for four Vrancea earthquakes by inversion of waveform and macroseismic intensity data in Chapter 6. This is the first study of this type performed for Vrancea earthquakes and the most extensive strong motion database ever available for a source study of these intermediate-depth events was used in this work. The analyzed earthquakes are the two moderate shocks which occurred on October 27, 2004 ($M_W = 5.8$) and May 14, 2005 ($M_W = 5.2$) and the two large events on March 3, 1977 ($M_W = 7.4$) and August 30, 1986 ($M_W = 7.1$). Especially the 1977 earthquake had a disastrous impact on Romanian territory, killing 1570 people and injuring 11300 (Cioflan et al., 2004). The May 30, 1990 ($M_W = 6.9$) earthquake could not be used due to a lack of appropriate EGF earthquakes.

For the 2004, 2005 and 1986 earthquakes (Chapter 6.4.1), enough observed acceleration time histories were available (especially for the 2004 event, a large number of recordings exists) to perform an inversion for the five parameters mentioned above by minimizing the cost (misfit) between observed and simulated acceleration envelopes and displacement waveforms. As the inversion problem is a non-linear one, a genetic algorithm was designed for this purpose (Chapter 5, e.g. Goldberg, 1989; Haupt and Haupt, 1998). The particular focus in the design of the algorithm was that it should be able to find sets of acceptable solutions rather than the 'one and only' optimal solution. This approach is essential in order to evaluate whether the solutions obtained are well constrained or not. The scaling factor N and the stress drop ratio C have been derived from the spectral ratios between TARGET and EGF earthquakes.

Three different ratios of rupture to shear wave velocity were used (v_R/v_S = 0.7, 0.8, 0.9) and the obtained SMGA source models are well constrained for the 2004 and 2005 events. For the 1986 earthquake, the results are ambiguous for v_R/v_S = 0.9, where at least three different lowest cost models with similar cost were found. This non-uniqueness of the solution is probably due to the fact that C and N were difficult to estimate for this TARGET earthquake (see Chapter 6.3), the database is rather sparse as compared for instance with the 2004 event and the azimuthal coverage is not optimal. However, the lowest cost model was found for v_R/v_S = 0.7 (where the lowest cost model is well constrained) and the costs of the models with v_R/v_S = 0.9 are about 10-15% larger, which makes these models less probable.

For the 1977 earthquake, a novel approach to estimate an appropriate SMGA source model was adopted (Chapter 6.4.2). In this case, it was not possible to perform an inversion based on waveforms, as only one strong motion observation exists. Therefore, macroseismic intensity (MSK scale) data were used as an inversion criterion. Using the 2004 earthquake analyzed previously as an EGF,

synthetic acceleration time histories were computed at 33 locations and the instrumental intensity was deduced using the technique of Sokolov (2002) based on the Fourier amplitude spectra. The genetic algorithm was then utilized to minimize the cost between observed and simulated intensity values at these 33 sites. The stress drop ratio C was set to 1, as it was not possible to evaluate it from spectral ratios and this is a reasonable assumption in view of the results obtained for the other events. Furthermore, as the inversion does not include any phase information, the aspect ratio of the SMGA was fixed and two inversions with different aspect ratios were performed.

The inverted SMGA models can explain the observed intensity pattern acceptably well. Moreover, the lowest cost SMGA model is able to explain the observed strong motion record at station Incerc astonishingly well and, as the SMGA size and rise time of the 2004 earthquake are very close to the subfault size and rise time resulting from the intensity based inversion for the 1977 earthquake (remember that the 2004 earthquake was used as EGF for the 1977 one), these results are consistent with each other.

The outcome of this study shows that Vrancea earthquakes are characterized by small strong motion generation areas with very short rise times. Following the interpretation of Miyake et al. (2003), the strong motion generation area is equivalent to an asperity in the stress-free field. Thus, the asperities of Vrancea earthquakes depict high static stress drops (300-1200 bars) and high particle velocities (up to 5 m/s) respectively high dynamic stress drops (around 1 kbar). Crustal earthquakes, on the other hand, show asperity stress drops of about 100 bar (Miyake et al., 2003) and particle velocities lower than 2 m/s (Kanamori, 1994). Hence, the intermediate-depth Vrancea earthquakes are inherently different from typical crustal events in terms of strong motion generation. They show a very efficient high-frequency radiation which has to be taken into account when assessing Romania's seismic hazard.

The approach to use macroseismic intensity information to derive appropriate source models is a promising one. For the 1977 intermediate-depth Vrancea earthquake, the results are very satisfactory. A possible field of application is the determination of appropriate source models for large historical earthquakes. For such events, macroseismic maps can be compiled by using the descriptions of the earthquake effects from historical records (e.g. the earthquake intensity database of the National Geophysical Data Center, http://www.ngdc.noaa.gov/seg/hazard/int_srch.shtml). With the technique used in this thesis, it might be possible to derive source parameters for such earthquakes which could provide insights into the strong motions generated by them. In principle, only an appropriate small earthquake which can be used as an EGF is necessary. Of course, several assumptions have to be made to stabilize the inversion procedure, as done for the 1977 Vrancea event. Therefore, the technique needs further testing, especially in the case of crustal events, and the application to crustal test earthquakes for which source parameters are well known from other studies will reveal how powerful the method is in the crustal case, which is more common than the intermediate-depth one.

Finally, in Chapter 7, the acceleration Fourier amplitude spectra of the S-wave have been analyzed for 55 Vrancea earthquakes at 43 stations spread over Romania. Using the generalized inversion technique (GIT) (e.g. Castro et al., 1990; Parolai et al., 2000, 2004a; Bindi et al., 2006a), the attenuation characteristics beneath Vrancea have been derived in a first step. Therefore, non-parametric attenuation functions have been fitted to the data, which revealed that there is a strong difference in seismic attenuation between the mountain arc and the foreland. This assumption has been verified by performing a synthetic data test. To account for this effect, two separate attenuation functions have been derived for the two regions defined in Chapter 7.3, which revealed that there is approximately one order of magnitude difference in attenuation at high frequencies between these regions. A possible explanation for the effect is provided by the subcrustal zone of weak coupling between the slab and

the crust (Sperner and the CRC 461 Team, 2005), for which some indications are also provided by refraction seismics (Hauser et al., 2001).

These strong lateral variations of seismic attenuation at high frequencies are of extraordinary importance in view of seismic hazard assessment. This was also noted by Popa et al. (2005). For structures sensitive to low-frequency ground motions, such as high-rise buildings or long-span bridges, the hazard is rather uniform over the territory of Romania. Most of these structures are located in the metropolitan area of Bucharest. Within and behind the mountain arc, the hazard for small buildings, which are sensitive to higher frequencies, is much smaller than in the foreland, as the high frequency content is efficiently attenuated. Furthermore, these findings are certainly also a key component in understanding the macroseismic intensity distribution of past earthquakes. The isoseismals separating rather high from rather low intensities follow almost exactly the shape of the mountain arc. This is a clear indication that this attenuation effect might play an important role in that regard.

The site amplification and source spectra derived from the attenuation-corrected data in the second step of the inversion reveal that both the horizontal and vertical component of ground motion show significant amplification effects, especially at higher frequencies. Assuming that the source spectrum of the 2004/10/27 (M_W = 5.8) is known (with a corner frequency of 1.6 Hz), an assumption based on the results of Chapter 6.3, the source functions obtained from the GIT inversion (which are still affected by attenuation over the reference distance) can be corrected for the remaining attenuation effect. The resulting source spectra are in good agreement with the ω^{-2}-model (Brune, 1970, 1971) and depict very high corner frequencies. For instance, an M_W = 4.0 earthquake depicts corner frequencies around 8-10 Hz. These high corner frequencies indicate a very efficient high-frequency radiation and large stress release and corroborate thus the results obtained from the empirical Green's functions simulations in Chapter 6. Furthermore, the trend between corner frequencies and seismic moment roughly indicates self-similar behavior, although the number of large magnitude events in the dataset is of course rather sparse.

A comparison of the H/V ratios computed from the shear wave windows and the site amplification functions obtained by GIT inversion clearly reveal that the H/V ratios are not a good estimate of site amplification on the horizontal component. By computing the ratio of the horizontal to vertical site amplification functions estimated from the GIT, the H/V ratios can be very well reproduced. Due to the large amplification on the vertical component at most stations, the H/V ratios systematically underestimate the amplification at high frequencies.

The spectral ground motion models resulting from this study can be used as a basis for stochastic simulations of ground motions resulting from scenario earthquakes and are thus a valuable contribution in view of seismic hazard assessment for Romania. These models are not unique, as expected for such an inverse problem. Other models with a completely different parameterization of the problem might explain the spectra as well. However, the spectral models in this work have been derived using a well-defined inversion scheme with few constraints that are easily justifiable and the minimum necessary number of model parameters, as with an 'over-parameterized' model, the fit to the data might get better and better, but the physical meaning of these model parameters is questionable.

In summary, this thesis represents a complete study of Vrancea earthquakes and their effects, starting from a detailed investigation of the source processes and ending with an estimate of attenuation and site amplification effects. Understanding all these components is the key to improve the seismic hazard assessment for Romania and represents the first step towards better risk mitigation.

Appendix A

Genetic Algorithm Validation Runs

In order to assess the ability of the genetic algorithm presented in Chapter 5.3 to find a global minimum, several test runs have been performed. Two of these are presented in a bit more detail below.

The test run idea is very simple: using the method of Irikura (1983, 1986, 1999) as presented in Chapter 4.1, I compute synthetic time histories with a set of parameters which I choose randomly. These parameter sets are summarized in Table A.1. To make sure that the algorithm performs identically well with different amounts of data, I shall use the database of EGF-A200211 to compute a synthetic TARGET-A dataset (10 stations) and EGF-D199907 to compute a synthetic TARGET-D dataset (for details on the true TARGET-A and -D events, see Chapter 6). The GA is then used to invert these synthetic records for the parameters characterizing the SMGA: length L, width W, rise time T_r and position of rupture starting location along strike and dip. These five parameters are also the ones evaluated in Chapter 6.

(a) Theoretical TARGET-A		(b) Theoretical TARGET-D	
Parameter	Value	Parameter	Value
length L [km]	2.5	length L [km]	4.0
width W [km]	1.75	width W [km]	3.0
rise time T_r [km]	0.11	rise time T_r [km]	0.15
rupt. init. along strike	1	rupt. init. along strike	1
rupt. init. along dip	4	rupt. init. along dip	2
v_S [km/s]	4.5	v_S [km/s]	4.5
v_R [km/s]	4.0	v_R [km/s]	3.6
N	7	N	3
C	1.9	C	2.1

Table A.1: Parameters of the theoretical TARGET-A (left) and TARGET-D (right) earthquakes computed to perform the genetic algorithm validation runs 1 and 2.

As in the latter chapter, five runs are performed for each validation dataset. Obviously, if the GA works as it should, the results of the inversion must, within the discretization error imposed by the binary coding of the GA, be identical to the ones utilized in the forward modeling of the test datasets and the cost for this lowest cost model should take the value zero. The cost function utilized is the same as given by (6.1).
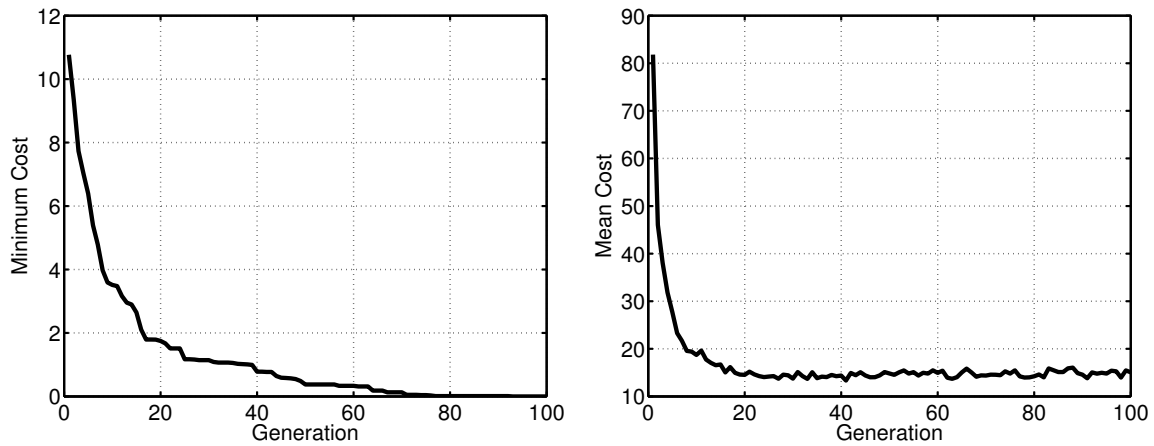
Figure A.1: Convergence plots for the genetic algorithm for validation run 1. Left: Evolution of the minimum cost (misfit) from generation to generation. Right: Evolution of mean cost. The curves shown here represent the evolution of the cost averaged over 5 runs of the algorithm.

The outcome of the inversions is listed in Table A.2 for both test cases. For each run, the first non-zero digit following the decimal point of the cost value is larger than two and thus, the costs can be regarded to be approximately zero.

Validation Run 1	Run	L [km]	W [km]	T_r [s]	Pos. along strike	Pos. along dip	Cost
	1	2.54	1.78	0.11	1 (7)	4 (7)	0.00
	2	2.50	1.73	0.10	1 (7)	4 (7)	0.00
theor. TARGET-A	3	2.51	1.73	0.11	1 (7)	4 (7)	0.00
	4	2.55	1.75	0.11	1 (7)	4 (7)	0.00
	5	2.51	1.72	0.11	1 (7)	4 (7)	0.00
Validation Run 2	Run	L [km]	W [km]	T_r [s]	Pos. along strike	Pos. along dip	Cost
	1	3.98	3.00	0.15	1 (3)	2 (3)	0.00
	2	3.99	3.01	0.15	1 (3)	2 (3)	0.00
theor. TARGET-D	3	3.98	3.01	0.15	1 (3)	2 (3)	0.00
	4	4.00	2.99	0.15	1 (3)	2 (3)	0.00
	5	3.99	2.99	0.15	1 (3)	2 (3)	0.00

Table A.2: Lowest cost models resulting from 5 runs for the validation datasets. Compare the outcome of the inversion with the input parameters summarized in Tables A.1(a) and A.1(b). The number in parentheses close to the position of the rupture initation point along strike and dip is the value of N.

An analysis of the convergence plots averaged over the five runs (Figures A.1 for validation run 1 and A.3 for validation run 2) show that the lowest cost model (with practically zero cost) is found in all cases at the latest in approximately generation 70. Furthermore, the histogram plots of the best 750 solutions found by the algorithm within five runs (Figures A.2 for validation run 1 and A.4 for validation run 2) clearly prove that the GA is indeed able to well constrain the global minimum, if a single one exists. Therefore, it is well suited to tackle the source inversion problem considered in this work.
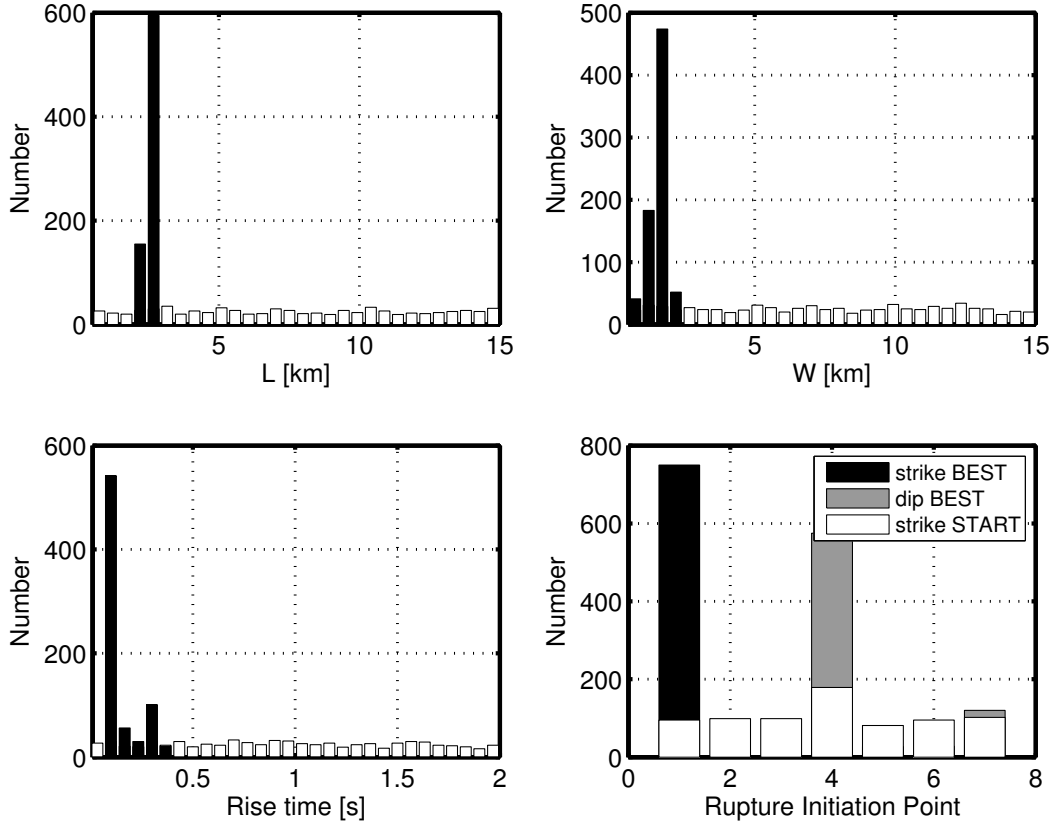
Figure A.2: Histograms of 750 best solutions (150 best from each of 5 runs) for validation run 1. Upper left: SMGA length L [km]. Upper right: SMGA width W [km]. Lower left: Rise time T_r [s]. Lower right: Rupture initiation location along strike (black) and dip (grey) (scaling factor $N = 7$). White bars: Initial sampling of the parameter space when starting the genetic algorithm (150 starting models from each run).
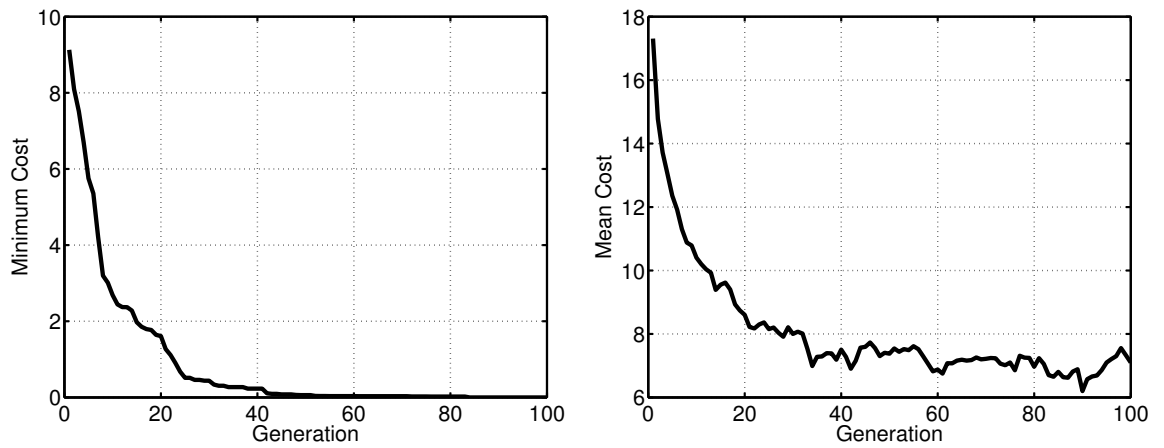
Figure A.3: Convergence plots for the genetic algorithm for validation run 2. Left: Evolution of the minimum cost (misfit) from generation to generation. Right: Evolution of mean cost. The curves shown here represent the evolution of the cost averaged over 5 runs of the algorithm.
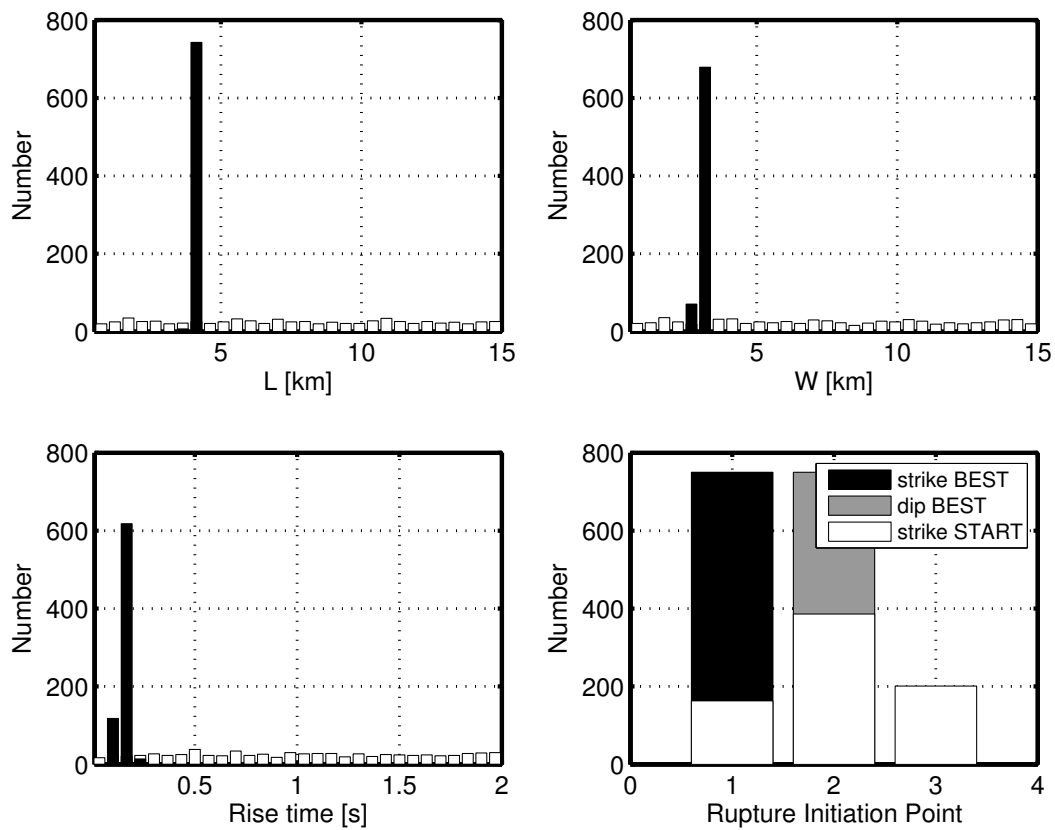
Figure A.4: Histograms of 750 best solutions (150 best from each of 5 runs) for validation run 2. Upper left: SMGA length L [km]. Upper right: SMGA width W [km]. Lower left: Rise time T_r [s]. Lower right: Rupture initiation location along strike (black) and dip (grey) (scaling factor $N = 3$). White bars: Initial sampling of the parameter space when starting the genetic algorithm (150 starting models from each run).

List of Figures

List of Tables

List of Abbreviations

EGF	–	Empirical Green's function
EMS	–	European macroseismic scale
FAS	–	Fourier amplitude spectrum
GA	–	Genetic algorithm
GIT	–	Generalized inversion technique
H	–	Horizontal component (Chapter 7)
H/V	–	Horizontal-to-vertical
JMA	–	Japanese Meteorological Agency
K2	–	recordings obtained with K2 accelerograph
MM	–	Modified Mercalli intensity scale
MSK	–	Medvedev-Spohnheuer-Karnik intensity scale
NE	–	North-East
NIEP	–	National Institute for Earth Physics
NW	–	North-West
PGA	–	Peak ground acceleration
PGD	–	Peak ground displacement
PGV	–	Peak ground velocity
PHA	–	Peak horizontal acceleration
PHV	–	Peak horizontal velocity
rms	–	root-mean-square
SE	–	South-East
SMA-1	–	recordings obtained with SMA-1 accelerograph
SMGA	–	strong motion generation area (see Chapter 4.1)
SN	–	signal-to-noise
SW	–	South-West
TARGET	–	Target (large) earthquake
VHR	–	Very hard rock
Z	–	Vertical component (Chapter 7)

Bibliography

Aagaard, B. T., Heaton, T. H., and Hall, J. F. (2001). Dynamic Earthquake Ruptures in the Presence of Lithostatic Normal Stresses: Implications for Friction Models and Heat Production. *Bull. Seismol. Soc. Am.*, 91:1765–1796.

Abercrombie, R. E. (1995). Earthquake Source Scaling Relationships from -1 to 5 M_L Using Seismograms Recorded at 2.5-km Depth. *J. Geophys. Res.*, 100:24015–24036.

Abercrombie, R. E. and Rice, J. R. (2005). Can Observations of Earthquake Scaling Constrain Slip Weakening? *Geophys. J. Int.*, 162:406–427.

Abrahamson, N. A. and Silva, W. J. (1997). Empirical Response Spectral Attenuation Relations for Shallow Crustal Earthquakes. *Seismol. Res. Lett.*, 68:94–128.

Aki, K. (1967). Scaling Law of Seismic Spectrum. *J. Geophys. Res.*, 72:1217–1231.

Aki, K. and Richards, P. G. (2002). *Quantitative Seismology, Second Edition*. University Science Books, Sausalito, CA.

Allmann, B. P. and Shearer, P. M. (2007). Spatial and Temporal Stress Drop Variations in Small Earthquakes Near Parkfield, California. *J. Geophys. Res.*, 112(B04305), doi:10.1029/2006JB004395.

Anderson, J. G. (2003). Strong-Motion Seismology. In Lee, W., Kanamori, H., Jennings, P., and Kisslinger, C., editors, *International Handbook of Earthquake and Engineering Seismology, Part B*, chapter 57. Elsevier.

Anderson, J. G. and Hough, S. E. (1984). A Model for the Shape of the Fourier Amplitude Spectrum of Acceleration at High Frequencies. *Bull. Seismol. Soc. Am.*, 74:1969–1993.

Andrews, D. J. (1986). Objective Determination of Source Parameters and Similarity of Earthquakes of Different Size. In Das, S., Boatwright, J., and Scholz, C. H., editors, *Earthquake Source Mechanics*. American Geophysical Monograph 37, 259-267.

Aochi, H. and Madariaga, R. (2003). The 1999 Izmit, Turkey, Earthquake: Nonplanar Fault Structure, Dynamic Rupture Process, and Strong Ground Motion. *Bull. Seismol. Soc. Am.*, 93:1249–1266.

Ardeleanu, L., Leydecker, G., Bonjer, K.-P., Busche, H., Kaiser, D., and Schmitt, T. (2005). Probabilistic Seismic Hazard Map for Romania as a Basis for a New Building Code. *Nat. Haz. Earth Sys. Sc.*, 5:679–684.

Atkinson, G. M. and Boore, D. M. (1995). Ground Motion Relations for Eastern North America. *Bull. Seismol. Soc. Am.*, 85:17–30.

Atkinson, G. M. and Silva, W. (1997). An Empirical Study of Earthquake Source Spectra for California Earthquakes. *Bull. Seismol. Soc. Am.*, 87:97–113.

Bard, P.-Y. (1999). Local Effects of Strong Ground Motion: Physical Basis and Estimation Methods in View of Microzonation Studies. In *Proceedings of the Advanced Study Course Seismotectonics and Microzonation Techniques in Earthquake Engineering: Integrated Training in Earthquake Risk Reduction Practices*. Kefallinia.

Benetatos, C. A. and Kiratzi, A. A. (2004). Strong Ground Motion Simulation of Intermediate Depth Earthquakes: the Cases of the 30 May 1990 Vrancea (Romania) and of the 22 January 2002 Karpathos Island (Greece) Earthquakes. *Soil Dyn. and Earth. Eng.*, 24:1–9.

Beresnev, I. A. (2001). What We Can and Cannot Learn about Earthquake Sources from the Spectra of Seismic Waves. *Bull. Seismol. Soc. Am.*, 91:397–400.

Beresnev, I. A. (2002). Source Parameters Observable from the Corner Frequency of Earthquake Spectra. *Bull. Seismol. Soc. Am.*, 92:2047–2048.

Beresnev, I. A. (2003). Uncertainties in Finite-Fault Slip Inversions: To What Extent to Believe? *Bull. Seismol. Soc. Am.*, 93:2445–2458.

Beresnev, I. A. and Atkinson, G. M. (1997). Modeling Finite-Fault Radiation from the ω^n Spectrum. *Bull. Seismol. Soc. Am.*, 87:67–84.

Beresnev, I. A. and Atkinson, G. M. (1998). FINSIM — A FORTRAN Program for Simulating Stochastic Acceleration Time Histories from Finite Faults. *Seismol. Res. Lett.*, 69:27–32.

Bindi, D., Parolai, S., Grosser, H., Milkereit, C., and Karakisa, S. (2006a). Crustal Attenuation Characteristics in Northwestern Turkey in the Range from 1 to 10 Hz. *Bull Seismol. Soc. Am.*, 96:200–214.

Bindi, D., Parolai, S., Grosser, H., Milkereit, C., and Zünbül, S. (2006b). Cumulative Attenuation Along Source-to-Receiver Paths in Northwestern Turkey. *Bull Seismol. Soc. Am.*, 96:188–199.

Boatwright, J. (1980). A Spectral Theory for Circular Seismic Sources; Simple Estimates of Source Dimension, Dynamic Stress Drop, and Radiated Seismic Energy. *Bull. Seismol. Soc. Am.*, 70:1–27.

Boatwright, J. (1984). Seismic Estimates of Stress Release. *J. Geophys. Res.*, 89:6961–6968.

Boatwright, J. (1988). The Seismic Radiation from Composite Models of Faulting. *Bull. Seismol. Soc. Am.*, 78:489–508.

Bonilla, L. F., Steidl, J. H., Lindley, G. T., Tumarkin, A. G., and Archuleta, R. J. (1997). Site Amplification in the San Fernando Valley, California: Variability of Site-Effect Estimation Using the S-wave, Coda and H/V Methods. *Bull. Seismol. Soc. Am.*, 87:710–730.

Bonjer, K.-P. and Grecu, B. (2004). Data Release 1996-2004 of the Vrancea K2 Seismic Network. *One DVD with evt-files*, Bucharest-Karlsruhe December 6.

Bonjer, K.-P., Oncescu, M. C., Driad, L., and Rizescu, M. (1999). A Note on Empirical Site Responses in Bucharest, Romania. In Wenzel, F., Lungu, D., and Novak, O., editors, *Vrancea Earthquakes: Tectonics, Hazard and Risk Mitigation*. Kluwer Academic Publishers, Dordrecht, Netherlands.

Boore, D. M. (1983). Stochastic Simulation of High-Frequency Ground Motions Based on Seismological Models of the Radiated Spectra. *Bull. Seismol. Sol. Am.*, 73:1865–1894.

Boore, D. M. (1986). Short-period P- and S-wave Radiation from Large Earthquakes: Implications for Spectral Scaling Relations. *Bull. Seismol. Soc. Am.*, 76:43–64.

Boore, D. M. (2003). Simulation of Ground Motion Using the Stochastic Method. *Pure Appl. Geophys.*, 160:635–676.

Boore, D. M. and Joyner, W. B. (1981). Peak Horizontal Acceleration and Velocity from Strong-Ground Motion Recordings Including Records from the 1979 Imperial Valley, California, Earthquake. *Bull. Seismol. Soc. Am.*, 71:2011–2038.

Boore, D. M. and Joyner, W. B. (1997). Site Amplifications for Generic Rock Studies. *Bull. Seismol. Soc. Am.*, 87:327–341.

Boore, D. M., Joyner, W. B., and Fumal, T. E. (1997). Equations for Estimating Horizontal Response Spectra and Peak Acceleration from Western North American Earthquakes: A Summary of Recent Work. *Seismol. Res. Lett.*, 68:128–153.

Borcherdt, R. D. (1970). Effects of Local Geology on Ground Motion Near San Francisco Bay. *Bull. Seismol. Soc. Am.*, 60:29–61.

Bour, M. and Cara, M. (1997). Test of a Simple Empirical Green's Function Method on Moderate-Sized Earthquakes. *Bull. Seismol. Soc. Am.*, 87:668–683.

Brune, J. N. (1970). Tectonic Stress and the Spectra of Seismic Shear Waves from Earthquakes. *J. Geophys. Res.*, 75:4997–5009.

Brune, J. N. (1971). Correction. *J. Geophys. Res.*, 76:5002.

Campbell, K. W. (1997). Empirical Near-Source Attenuation Relationships for Horizontal and Vertical Components of Peak Ground Acceleration, Peak Ground Velocity and Pseudo-absolute Acceleration Response Spectra. *Seismol. Res. Lett.*, 68:154–179.

Campbell, K. W. (2003). Strong-Motion Attenuation Relations. In Lee, W., Kanamori, H., Jennings, P., and Kisslinger, C., editors, *International Handbook of Earthquake and Engineering Seismology, Part B*, chapter 60. Elsevier.

Castro, R. R., Anderson, J. G., and Singh, S. K. (1990). Site Response, Attenuation and Source Spectra of S Waves Along the Guerrero, Mexico, Subduction Zone. *Bull. Seismol. Soc. Am.*, 80:1481–1503.

Castro, R. R., Fabriol, H., Bour, M., and Le Brun, B. (2003). Attenuation and Site Effects in the Region of Guadeloupe, Lesser Antilles. *Bull. Seismol. Soc. Am.*, 93:612–626.

Castro, R. R., Franceschina, G., Pacor, F., Bindi, D., and Luzi, L. (2006). Analysis of the Frequency Dependence of the S-wave Radiation Pattern from Local Earthquakes in Central Italy. *Bull. Seismol. Soc. Am.*, 96:415–426.

Castro, R. R., Munguia, L., and Brune, J. N. (1995). Source Spectra and Site Response from P and S Waves from Local Earthquakes in the Oaxaca, Mexico, Subduction Zone. *Bull. Seismol. Soc. Am.*, 85:923–936.

Castro, R. R., Pacor, F., Sala, A., and Petrungaro, C. (1996). S Wave Attenuation and Site Effects in the Region of Friuli, Italy. *J. Geophys. Res.*, 101:22355–22369.

Chen, S.-Z. and Atkinson, G. M. (2002). Global Comparisons of Earthquake Source Spectra. *Bull. Seismol. Soc. Am.*, 92:885–895.

Cioflan, C. O., Apostol, B. F., Moldoveanu, C. L., Panza, G. F., and Marmureanu, G. (2004). Deterministic Approach for the Seismic Microzonation of Bucharest. In Panza, G. F., Paskaleva, I., and Nunziata, C., editors, *Seismic Ground Motion in Large Urban Areas*. volume 161 of Pageoph Topical Volumes.

Coley, D. A. (1999). *An Introduction to Genetic Algorithms for Scientists and Engineers*. World Scientific Publishing, Singapore.

Das, S. and Kostrov, B. V. (1986). Fracture of a Single Asperity on a Finite Fault: a Model for Weak Earthquakes? In Das, S., Boatwright, J., and Scholz, C. H., editors, *Earthquake Source Mechanics*. American Geophysical Monograph 37, 91-96.

Demetrescu, C. and Andreescu, M. (1994). On the Thermal Regime of Some Tectonic Units in a Continental Collision Environment in Romania. *Tectonophysics*, 230:265–276.

Efron, B. and Tibshirani, R. J. (1994). *An Introduction to the Bootstrap*. Chapman & Hall, CRC.

Field, E. H. and Jacob, K. H. (1995). A Comparison and Test of Various Site Response Estimation Techniques Including Three That Are Not Reference-Site Dependent. *Bull. Seismol. Soc. Am.*, 85:1127–1143.

Fuchs, K., Bonjer, K.-P., Bock, G., Cornea, I., Radu, C., Enescu, D., Jianu, D., Nourescu, A., Merkler, G., Moldoveanu, T., and Tudorache, G. (1979). The Romanian Earthquake of March 4, 1977: II. Aftershocks and Migration of Seismic Activity. *Tectonophysics*, 53:225–247.

Furumura, T. and Chen, L. (2005). Parallel Simulation of Strong Ground Motions During Recent and Historical Damaging Earthquakes in Tokyo, Japan. *Parallel Computing*, 31:149–165.

Furumura, T. and Hayakawa, T. (2006). Anomalous Propagation of Long-Period Ground Motions Recorded in Tokyo During the 23 October 2004 Niigata-ken Chuetsu (Mw 6.6) Earthquake, Japan. *Bull. Seismol. Soc. Am.*, submitted.

Furumura, T., Hayakawa, T., Nakamura, M., Koketsu, K., and Baba, T. (2006). Development of Long-Period Ground Motions from Earthquakes Within the Nankai Trough, Japan: Observations and Computer Simulation of the 1944 Tonankai (Mw 8.1) and 2004 SE Off-Kii Peninsula (Mw 7.4) Earthquakes. *Pure Appl. Geophys.*, submitted.

Furumura, T. and Kennett, B. L. N. (2005). Subduction Zone Guided Waves and the Heterogeneity Structure of the Subducted Plate: Intensity Anomalies in Northern Japan. *J. Geophys. Res.*, 110, B10302, doi:10.1029/2004JB003486.

Furumura, T., Koketsu, K., and Wen, K.-L. (2002). Parallel PSM/FDM Hybrid Simulation of Ground Motions from the 1999 Chi-Chi, Taiwan, Earthquake. *Pure Appl. Geophys.*, 159:2133–2146.

Garcia, D., Singh, S. K., Herraiz, M., Ordaz, M., and Pachebo, J. F. (2005). Inslab Earthquakes of Central Mexico: Peak Ground-Motion Parameters and Response Spectra. *Bull. Seismol. Soc. Am.*, 95:2272–2282.

Geller, R. J., Jackson, D. D., Kagan, Y. Y., and Mulargia, F. (1997). Earthquakes Cannot Be Predicted. *Science*, 275:1616–1617.

Goldberg, D. E. (1989). *Genetic Algorithms in Search, Optimization and Machine Learing*. Addison-Wesley, New York.

Gottschämmer, E. (2002). *Kinematic and Dynamic Simulation of Ground Motion: Implications for Seismic Hazard Assessment*. Cuvillier Verlag, Göttingen.

Gottschämmer, E., Wenzel, F., Wust-Bloch, H., and Ben-Avraham, Z. (2002). Earthquake Modeling in the Dead Sea Basin. *Geophys. Res. Lett.*, 29, doi: 10.1029/2001GL013800:8–1–8–4.

Gusev, A., Radulian, M., Rizescu, M., and Panza, G. F. (2002). Source Scaling of Intermediate-Depth Vrancea Earthquakes. *Geophys. J. Int.*, 151:879–889.

Hanks, T. C. (1982). fmax. *Bull. Seismol. Soc. Am.*, 72:1867–1879.

Hanks, T. C. and Johnson, D. A. (1976). Geophysical Assessment of Peak Accelerations. *Bull. Seismol. Soc. Am.*, 66:959–968.

Hanks, T. C. and Kanamori, H. (1979). A Moment Magnitude Scale. *J. Geophys. Res.*, 84:2348–2350.

Hanks, T. C. and McGuire, R. K. (1981). The Character of High-Frequency Strong Ground Motion. *Bull. Seismol. Soc. Am.*, 71:2071–2095.

Hartzell, S. (1979). Analysis of the Bucharest Strong Ground Motion Record for the March 4, 1977 Romanian Earthquake. *Bull. Seismol. Soc. Am.*, 69:513–530.

Hartzell, S. H. (1978). Earthquake Aftershocks as Green's Functions. *Geophys. Res. Lett.*, 5:1–4.

Hartzell, S. H. (1992). Site Response Estimation from Earthquake Data. *Bull. Seismol. Soc. Am.*, 82:2308–2327.

Hartzell, S. H., Leeds, A., Frankel, A., and Michael, J. (1996). Site Response for Urban Los Angeles Using Aftershocks of the Northridge Earthquake. *Bull. Seismol. Soc. Am.*, 86:S168–S192.

Haskell, N. (1966). Total Energy and Energy Spectral Density of Elastic Wave Radiation from Propagating Faults. *Bull. Seismol. Soc. Am.*, 56:125–140.

Haupt, R. L. and Haupt, S. E. (1998). *Practical Genetic Algorithms*. John Wiley & Sons, New York.

Hauser, F., Raileanu, V., Fielitz, W., Bala, A., Prodehl, C., Polonic, G., and Schulze, A. (2001). VRANCEA99 — The Crustal Stucture Beneath the SouthEastern Carpathians and the Moesian Platform from Seismic Refraction Profile in Romania. *Tectonophysics*, 340:233–256.

Hauser, F., Raileanu, V., Fielitz, W., Dinu, C., Landes, M., Bala, A., and Prodehl, C. (2007). Seismic Crustal Structure Between the Transylvanian Basin and the Black Sea, Romania. *Tectonophysics*, 430:1–25.

Heaton, T. (1990). Evidence for and Implications of Self-Healing Pulses of Slip in Earthquake Rupture. *Phys. Earth Planet. Int.*, 64:1–20.

Holland, J. H. (1975). *Adaptation in Natural and Artifical Systems*. The University of Michigan Press, Ann Arbor.

Hutchings, L. (1991). "Prediction" of Strong Ground Motion for the 1989 Loma Prieta Earthquake Using Empirical Green's Functions. *Bull. Seismol. Soc. Am.*, 81:1813–1837.

Hutchings, L. (1994). Kinematic Earthquake Models and Synthesized Ground Motion Using Empirical Green's Functions. *Bull. Seismol. Soc. Am.*, 84:1028–1050.

Hutchings, L. and Wu, F. (1990). Empirical Green's Functions From Small Earthquakes: A Waveform Study of Locally Recorded Aftershocks of the 1971 San Fernando Earthquake. *J. Geophys. Res.*, 95:1187–1214.

Ide, S., Beroza, G. C., and McGuire, J. J. (2005). Imaging Earthquake Source Complexity. In Levander, A. and Nolet, G., editors, *Seismic Earth: Array Analysis of Broadband Seismograms*. Geophysical Monograph Series 157, 117-135.

Irikura, K. (1983). Semi-Empirical Estimation of Strong Ground Motions during Large Earthquakes. *Bull. Dis. Prev. Res. Inst., Kyoto Univ.*, 33, Part 2, No. 298.

Irikura, K. (1986). Prediction of Strong Acceleration Motions Using Empirical Green's Functions. *In: Proceedings of the Seventh Japan Earthquake Engineering Symposium*.

Irikura, K. (1999). Techniques for the Simulation of Strong Ground Motion and Deterministic Seismic Hazard Analysis. In *Proceedings of the Advanced Study Course Seismotectonics and Microzonation Techniques in Earthquake Engineering: Integrated Training in Earthquake Risk Reduction Practices*. Kefallinia.

Ismail-Zadeh, A., Müller, B., and Schubert, G. (2005). Three-dimensional Numerical Modeling of Contemporary Mantle Flow and Tectonic Stress Beneath Earthquake-Prone SouthEastern Carpathians Based on Integrated Analysis of Seismic, Heat Flow and Gravity Data. *Phys. Earth Planet. Int.*, 149:81–98.

Jennings, P. C. (2003). An Introduction to the Earthquake Response of Structures. In Lee, W., Kanamori, H., Jennings, P., and Kisslinger, C., editors, *International Handbook of Earthquake and Engineering Seismology, Part B*, chapter 67. Elsevier.

Joyner, W. B. and Boore, D. M. (1986). On Simulating Large Earthquakes By Greens-Function Addition of Smaller Earthquakes. In Das, S., Boatwright, J., and Scholz, C. H., editors, *Earthquake Source Mechanics*. American Geophysical Monograph 37, 269-274.

Kamae, K. and Irikura, K. (1998). Source Model of the 1995 Hygo-ken Nanbu Earthquake and Simulation of Near-Source Ground Motion. *Bull. Seismol. Soc. Am.*, 88:400–412.

Kamae, K., Irikura, K., and Pitarka, A. (1998). A Technique for Simulating Strong Ground Motion Using Hybrid Green's Function. *Bull. Seismol. Soc. Am.*, 88:357–367.

Kanamori, H. (1994). The Mechanics of Earthquakes. *Ann. Rev. Earth Planet. Sci.*, 22:207–237.

Kanamori, H. and Anderson, D. L. (1975). Theoretical Basis of Some Empirical Relations in Seismology. *Bull. Seismol. Soc. Am.*, 65:1073–1095.

Kanamori, H. and Heaton, T. H. (2000). Microscopic and Macroscopic Physics of Earthquakes. In Rundle, J. B., Turcotte, D. L., and Klein, W., editors, *Geocomplexity and the Physics of Earthquakes*. AGU Geophysical Monograph Series.

Kawase, H. (2003). Site Effects on Strong Ground Motions. In Lee, W., Kanamori, H., Jennings, P., and Kisslinger, C., editors, *International Handbook of Earthquake and Engineering Seismology, Part B*, chapter 61. Elsevier.

Kohrs-Sansorny, C., Courboulex, F., Bour, M., and Deschamps, A. (2005). A Two-Stage Method for Ground-Motion Simulation Using Stochastic Summation of Small Earthquakes. *Bull. Seismol. Soc. Am.*, 95:1387–1400.

Komatitsch, D. (1999). Introduction to the Spectral-Element Method for 3-D Seismic Wave Propagation. *Geophys. J. Int.*, 139:806–822.

Konno, K. and Ohmachi, T. (1998). Ground-Motion Characteristics Estimated from Spectral Ratio between Horizontal and Vertical Components of Microtremor. *Bull. Seismol. Soc. Am.*, 88:228–241.

Kramer, S. L. (1996). *Geotechnical Earthquake Engineering*. Prentice Hall, Upper Saddle River, NJ.

Lay, T. and Wallace, T. C., editors (1995). *Modern Global Seismology*, volume 58 of *International Geophysics Series*. Academic Press.

Lermo, J. and Chavez-Garcia, F. J. (1993). Site Effect Evaluation Using Spectral Ratios with Only One Station. *Bull. Seismol. Soc. Am.*, 83:1574–1594.

Lomax, A. and Snieder, R. (1994). Finding Sets of Acceptable Solutions with a Genetic Algorithm with Application to Surface Wave Group Dispersion in Europe. *Geophys. Res. Lett.*, 21:2617–2620.

Madariaga, R. (1976). Dynamics of an Expanding Circular Fault. *Bull. Seismol. Soc. Am.*, 66:639–666.

Madariaga, R. (1979). On the Relation Between Seismic Moment and Stress Drop in the Presence of Stress and Strength Heterogeneity. *J. Geophys. Res.*, 84:2243–2250.

Mai, P. M. and Beroza, G. C. (2000). Source Scaling Properties from Finite-Fault-Rupture Models. *Bull. Seismol. Soc. Am.*, 90:604–615.

Mai, P. M. and Beroza, G. C. (2002). A Spatial Random Field Model to Characterize Complexity in Earthquake Slip. *J. Geophys. Res.*, 107(B11), 2308, doi:10.1029/2001JB000588.

Mantysniemi, P., Marza, V. I., Kijko, A., and Retief, P. (2003). A New Probabilistic Seismic Hazard Analysis for the Vrancea (Romania) Seismogenic Zone. *Natural Hazards*, 29:371–385.

Martin, M., Wenzel, F., and the CALIXTO working group (2006). High-Resolution Teleseismic Body Wave Tomography Beneath SE-Romania (II): Imaging of a Slab Detachment Scenario. *Geophys. J. Int.*, 164:579–595.

Menke, W. (1989). *Geophysical Data Analysis: Discrete Inverse Theory*. International Geophysics Series, Academic Press.

Miksat, J. (2006). *Earthquake Ground Motion Modelling from Crustal and Intermediate Depth Sources*. PhD thesis, Unversität Karlsruhe (TH), Germany.

Miksat, J., Wenzel, F., and Sokolov, V. (2005). Low Free-Field Accelerations of the 1999 Kocaeli Earthquake? *Pure Appl. Geophys.*, 162:857–874.

Mikumo, T. (1971). Source Process of Deep and Intermediate Earthquakes as Inferred from Long-Period P and S Waveforms. 2. Deep-focus and Intermediate-Depth Earthquakes around Japan. *J. Phys. Earth*, 19:303–320.

Miyake, H., Iwata, T., and Irikura, K. (2001). Estimation of Rupture Propagation Direction and Strong Motion Generation Area from Azimuth and Distance Dependence of Source Amplitude Spectra. *Geophys. Res. Lett.*, 28:2727–2730.

Miyake, H., Iwata, T., and Irikura, K. (2003). Source Characterization for Broadband Ground-Motion Simulations: Kinematic Heterogeneous Source Model and Strong Motion Generation Area. *Bull. Seismol. Soc. Am.*, 93:2531–2545.

Mogi, K. (1968). Development of Aftershock Areas of Great Earthquakes. *Bull. Earthquake Res. Inst. Tokyo Univ.*, 46:175–203.

Moya, A. and Irikura, K. (2003). Estimation of Site Effects and Q Factor Using a Reference Event. *Bull. Seismol. Soc. Am.*, 93:1730–1745.

Murphy, J. R. and O'Brien, J. L. (1977). The Correlation of Peak Ground Acceleration Amplitude with Seismic Intensity and Other Physical Parameters. *Bull. Seismol. Soc. Am.*, 67:877–915.

Nadeau, R. M. and Johnson, L. R. (1998). Seismological Studies at Parkfield VI: Moment Release Rates and Estimates of Source Parameters for Small Repeating Earthquakes. *Bull. Seismol. Soc. Am.*, 88:790–814.

Nakamura, Y. (1989). A Method for Dynamic Characteristics Estimation of Subsurface Using Microtremor on the Ground Surface. *QR Railway Tech. Res. Inst.*, 30:25–33.

Olsen, K. B. (2000). Site Amplification in the Los Angeles Basin from 3D Modeling of Ground Motion. *Bull. Seismol. Soc. Am.*, 90:S77–S94.

Olsen, K. B., Archuleta, R. J., and Matarese, J. R. (1995). Three Dimensional Simulation of a Magnitude 7.75 Earthquake on the San Andreas Fault. *Science*, 270:1628–1632.

Olsen, K. B., Day, S. M., Minster, J. B., Cui, Y., Chourasia, A., Faerman, M., Moore, R., Maechling, P., and Jordan, T. (2006). Strong Shaking in Los Angeles Expected from Southern San Andreas Earthquake. *Geophys. Res. Lett.*, 33, doi: 10.1029/2005GL025472.

Olsen, K. B., Madariaga, R., and Archuleta, R. J. (1997). Three Dimensional Dynamic Simulation of the 1992 Landers Earthquake. *Science*, 278, 834-838.

Oncescu, M. C. (1989). Investigation of a High Stress Drop Earthquake on August 30, 1986 in the Vrancea Region. *Tectonophysics*, 163:35–43.

Oncescu, M. C. and Bonjer, K.-P. (1997). A Note on the Depth Recurrence and Strain Release of Large Vrancea Earthquakes. *Tectonophysics*, 272:291–302.

Oncescu, M. C., Bonjer, K.-P., and Rizescu, M. (1999a). Weak and Strong Ground Motion of Intermediate Depth Earthquakes from the Vrancea Region. In Wenzel, F., Lungu, D., and Novak, O., editors, *Vrancea Earthquakes: Tectonics, Hazard and Risk Mitigation*. Kluwer Academic Publishers, Dordrecht, Netherlands.

Oncescu, M. C., Marza, V. I., Rizescu, M., and Popa, M. (1999b). The Romanian Earthquake Catalogue Between 984-1997. In Wenzel, F., Lungu, D., and Novak, O., editors, *Vrancea Earthquakes: Tectonics, Hazard and Risk Mitigation*. Kluwer Academic Publishers, Dordrecht, Netherlands.

Oth, A., Wenzel, F., and Radulian, M. (2007a). Source Parameters of Intermediate-Depth Vrancea (Romania) Earthquakes from Empirical Green's Functions Modeling. *Tectonophysics*, 438:33–56.

Oth, A., Wenzel, F., Wust-Bloch, H., Gottschämmer, E., and Ben-Avraham, Z. (2007b). Parameterization of a Composite Attenuation Relation for the Dead Sea Area Based On 3-D Modeling of Elastic Wave Propagation. *Pure Appl. Geophys.*, 164:23–37.

Papageorgiou, A. S. and Aki, K. (1983). A Specific Barrier Model for the Quantitative Description of Inhomogeneous Faulting and Prediction of Strong Motion, Part I: Description of the Model. *Bull. Seismol. Soc. Am.*, 73:693–722.

Parolai, S. and Bindi, D. (2004). Influence of Soil-Layer Properties on k Evaluation. *Bull. Seismol. Soc. Am.*, 94:349–356.

Parolai, S., Bindi, D., and Augliera, P. (2000). Application of the Generalized Inversion Technique (GIT) to a Microzonation Study: Numerical Simulations and Comparison with Different Site-Estimation Techniques. *Bull. Seismol. Soc. Am.*, 90:286–297.

Parolai, S., Bindi, D., Baumbach, M., Grosser, H., Milkereit, C., Karakisa, S., and Zünbül, S. (2004a). Comparison of Different Site Response Estimation Techniques Using Aftershocks of the 1999 Izmit Earthquake. *Bull. Seismol. Soc. Am.*, 94:1096–1108.

Parolai, S., Bindi, D., Durukal, E., Grosser, H., and Milkereit, C. (2007). Source Parameters and Seismic Moment-Magnitude Scaling for Northwestern Turkey. *Bull. Seismol. Soc. Am.*, 97:655–660.

Parolai, S., Bindi, D., and Trojani, L. (2001). Site Response for the RSM Seismic Network and Source Parameters in the Central Appenines (Italy). *Pure Appl. Geophys.*, 158:695–715.

Parolai, S., Richwalski, S. M., Milkereit, C., and Bormann, P. (2004b). Assessment of the Stability of the H/V Spectral Ratios from Ambient Noise: Comparison With Earthquake Data in the Cologne Area (Germany). *Tectonophysics*, 390:57–73.

Plenefisch, T. (1996). *Untersuchungen der Spannungsfeldes im Bereich des Rheingrabens mittels der Inversion von Herdflächenlösungen und Abschätzung der bruchspezifischen Reibungsparameter.* PhD thesis, Unversität Karlsruhe (TH), Germany.

Popa, M., Radulian, M., Grecu, B., Popescu, E., and Placinta, A. O. (2005). Attenuation in South-Eastern Carpathians Area: Result of Upper Mantle Inhomogeneity. *Tectonophysics*, 410:235–249.

Prieto, G. A., Shearer, P. M., Vernon, F. L., and Kilb, D. (2004). Earthquake Source Scaling and Self-Similarity Estimation from Stacking P and S Spectra. *J. Geophys. Res.*, 109, B08310, doi: 10.1029/2004JB003084.

Pulido, N., Ojeda, A., Atakan, K., and Kubo, T. (2004). Strong Ground Motion Estimation in the Marmara Sea Region (Turkey) Based on a Scenario Earthquake. *Tectonophysics*, 391:357–374.

Purvance, M. D. and Anderson, J. G. (2003). A Comprehensive Study of the Observed Spectral Decay in Strong-Motion Accelerations Recorded in Guerrero, Mexico. *Bull. Seismol. Soc. Am.*, 93:600–611.

Radu, C., Polonic, G., and Apopei, I. (1979). Macroseismic Field of the March 4, 1977 Vrancea Earthquake. *Tectonophysics*, 53:185–186.

Radu, C., Utale, A., and Winter, V. (1987). The August 30, 1986 Vrancea Earthquake. Seismic Intensity Distribution. *National Institute for Earth Physics Report*, II,A-3.

Radulian, M., Mandrescu, N., Panza, G. F., Popescu, E., and Utale, A. (2000). Characterization of Seismogenic Zones of Romania. In Panza, G. F., Radulian, M., and Trifu, C.-I., editors, *Seismic Hazard of the Circum-Pannonian Region*. Birkhäuser Verlag, Basel, Switzerland.

Räkers, E. and Müller, G. (1982). The Romanian Earthquake of March 4, 1977 III. Improved Focal Model and Moment Determination. *J. Geophys.*, 50:143–150.

Ritter, J. R. R., Balan, S. F., Bonjer, K.-P., Diehl, T., Forbriger, T., Marmureanu, G., Wenzel, F., and Wirth, W. (2005). Broadband Urban Seismology in the Bucharest Metropolitan Area. *Seismol. Res. Lett.*, 76:574–580.

Russo, R. M., Mocanu, V., Radulian, M., Popa, M., and Bonjer, K.-P. (2005). Seismic Attenuation in the Carpathian Bend Zone and Surroundings. *Earth Planet. Sci. Lett.*, 237:695–709.

Sadigh, K., Chang, C. Y., Egan, J. A., Makdisi, F., and Youngs, R. R. (1997). Attenuation Relationships for Shallow Crustal Earthquakes Based on Californian Strong Motion Data. *Seismol. Res. Lett.*, 68:180–189.

Salazar, W., Sardina, V., and de Cortina, J. (2007). A Hybrid Inversion Technique for the Evaluation of Source, Path and Site Effects Employing S-Wave Spectra for Subduction and Upper-Crustal Earthquakes in El Salvador. *Bull. Seismol. Soc. Am.*, 97:208–221.

Sambridge, M. and Drijkoningen, G. (1992). Genetic Algorithms in Seismic Waveform Inversion. *Geophys. J. Int.*, 109:323–342.

Saragoni, G. R. and Hart, G. C. (1974). Simulation of Artifical Earthquakes. *Earthq. Eng. Struct. Dyn.*, 2:249–267.

Sato, T. and Hirawasa, T. (1973). Body Wave Spectra from Propagating Shear Cracks. *J. Phys. Earth*, 21:415–431.

Scherbaum, F., Cotton, F., and Staedtke, H. (2006). The Estimation of Minimum-Misfit Stochastic Models from Empirical Ground-Motion Prediction Equations. *Bull. Seismol. Soc. Am.*, 96:427–445.

Scholz, C. H. (2002). *The Mechanics of Earthquakes and Faulting, 2nd edition*. Cambridge University Press, Cambridge.

Sekiguchi, H. and Iwata, T. (2002). Rupture Process of the 1999 Kocaeli, Turkey, Earthquake Estimated from Strong-Motion Waveforms. *Bull. Seismol. Soc. Am.*, 92:300–311.

Shedlock, K. M., Giardini, D., Grünthal, G., and Zhang, P. (2000). The GSHAP Global Seismic Hazard Map. *Seismol. Res. Lett.*, 71:679–686.

Siddiqqi, J. and Atkinson, G. M. (2002). Ground-Motion Amplification at Rock Sites Across Canada as Determined from the Horizontal-to-Vertical Component Ratio. *Bull. Seismol. Soc. Am.*, 90:877–884.

Sokolov, V., Bonjer, K.-P., Onescu, M., and Rizescu, M. (2005). Hard Rock Spectral Models for Intermediate Depth Vrancea (Romania) Earthquakes. *Bull. Seismol. Soc. Am.*, 95:1749–1765.

Sokolov, V., Bonjer, K.-P., and Wenzel, F. (2004). Accounting for Site Effect in Probabilistic Assessment of Seismic Hazard for Romania and Bucharest: a Case of Deep Seismicity in Vrancea Zone. *Soil Dyn. Earthquake Eng.*, 24:929–947.

Sokolov, V. Y. (2002). Seismic Intensity and Fourier Acceleration Spectra: Revised Relationships. *Earthquake Spectra*, 18:161–187.

Somerville, P., Irikura, K., Graves, R., Sawada, S., Wald, D., Abrahamson, N., Iwasaki, Y., Kagawa, T., Smith, N., and Kowada, A. (1999). Characterizing Crustal Earthquake Slip Models for the Predicition of Strong Ground Motion. *Seismol. Res. Lett.*, 70:59–80.

Somerville, P. G., Smith, N. F., Graves, R. W., and Abrahamson, N. A. (1997). Modification of Empirical Strong Ground Motion Attenuation Relations to Include the Amplitude and Duration Effects of Rupture Directivity. *Seismol. Res. Lett.*, 68:199–222.

Sperner, B., Lorenz, F. P., Bonjer, K.-P., Hettel, S., Müller, B., and Wenzel, F. (2001). Slab Break-off – Abrupt Cut or Gradual Detachment? New Insights from the Vrancea Region (SE Carpathians, Romania). *Terra Nova*, 13:172–179.

Sperner, B. and the CRC 461 Team (2005). Monitoring of Slab Detachment in the Carpathians. In Wenzel, F., editor, *Perspectives in Modern Seismology*. Lecture Notes in Earth Sciences, Vol. 105, Springer Verlag, Berlin.

Stein, S. and Wysession, M. (2003). *An Introduction to Seismology, Earthquakes and Earth Structure*. Blackwell Publishing.

Su, F., Anderson, J. G., and Zeng, Y. (1998). Study of Weak and Strong Ground Motion Including Nonlinearity from the Northridge, California, Earthquake Sequence. *Bull. Seismol. Soc. Am.*, 88:1411–1425.

Suzuki, W. and Iwata, T. (2005a). Source Characteristics of Interplate Earthquakes in Northeast Japan Inferred from the Analysis of Broadband Strong-Motion Records. *Eos Trans. AGU, 86(52), Fall Meet. Suppl.*, Abstract S43A - 1040.

Suzuki, W. and Iwata, T. (2005b). Source Model of the 2005 West off Fukuoka Prefecture Earthquake Estimated from the Empirical Green's Function Simulation of Broadband Strong Motions. *Earth Planets Space*, submitted.

Suzuki, W., Iwata, T., Asano, K., and Yamada, N. (2005). Estimation of the Source Model fort he Foreshock of the 2004 off the Kii Peninsula Earthquakes and Strong Motion Simulation of the Hypothetical Tonankai Earthquake Using the Empirical Green's Function Method. *Earth Planets Space*, 57:345–350.

Takenaka, H., Mamada, Y., and Futamure, H. (2003). Near-Source Effect on Radiation Pattern of High-frequency S waves: Strong SH-SV Mixing Observed from Aftershocks of the 1997 Northwestern Kagoshima, Japan Earthquakes. *Phys. Earth Planet. Int.*, 137:31–43.

Tarantola, A. (1987). *Inverse Problem Theory*. Elsevier, New York.

Theodulidis, N. and Bard, P.-Y. (1995). Horizontal to Vertical Spectral Ratio and Geological Conditions: an Analaysis of Strong Motion Data from Greece and Taiwan. *Soil. Dyn. Earthquake Eng.*, 14:177–197.

Toro, G. R., Abrahamson, N. A., and Schneider, J. F. (1997). Model of Strong Ground Motions from Earthquakes in Central and Eastern North America: Best Estimates and Uncertainties. *Seismol. Res. Lett.*, 68:41–57.

Treml, M. (2000). *Starkbebensynthese mit Empirischen Greenschen Funktionen am Beispiel der Cascadia Subduktionszone*. Diplomarbeit, Universität Fridericiana, Karlsruhe.

Trifu, C.-I. and Oncescu, M. C. (1987). Fault Geometry of August 30, 1986 Vrancea Earthquake. *Annal. Geophys.*, 5B:727–730.

Trifunac, M. D., , and Brady, A. G. (1975). On the Correlation of Seismic Intensity Scales With the Peaks of Recorded Strong Ground Motion. *Bull. Seismol. Soc. Am.*, 65:139–162.

Trifunac, M. D. and Brady, A. G. (1975). A Study of the Duration of Strong Earthquake Ground Motion. *Bull. Seismol. Soc. Am.*, 65:581–626.

Udias, A. (1999). *Principles of Seismology*. Cambridge University Press.

Wald, D. J. and Heaton, T. H. (1994). Spatial and Temporal Distribution of Slip for the 1992 Landers, California, Earthquake. *Bull. Seismol. Soc. Am.*, 84:668–691.

Wald, D. J., Quitoriano, V., Heaton, T. H., and Kanamori, H. (1999). Relationships Between Peak Ground Acceleration, Peak Ground Velocity and Modified Mercalli Intensity in California. *Earthquake Spectra*, 15:557–564.

Wells, D. L. and Coppersmith, K. J. (1994). New Empirical Relations Among Magnitude, Rupture Length, Rupture Width, Rupture Area and Surface Displacement. *Bull. Seismol. Soc. Am.*, 84:974–1002.

Wenzel, F., Lorenz, F. P., Sperner, B., and Oncescu, M. C. (1999). Seismotectonics of the Romanian Vrancea Area. In Wenzel, F., Lungu, D., and Novak, O., editors, *Vrancea Earthquakes: Tectonics, Hazard and Risk Mitigation*. Kluwer Academic Publishers, Dordrecht, Netherlands.

Wyss, M. (1997). Second Round of Evaluations of Proposed Earthquake Precursors. *Pure Appl. Geophys.*, 149:3–16.

Wyss, M. (2001). Why is Earthquake Prediction Research Not Progressing Faster? *Tectonophysics*, 338:217–223.

Ziehm, J. (2006). *Seismisches Monitoring einer Großstadt, Analyse von H/V-Spektralverhältnissen*. Diplomarbeit, Universität Karlsruhe (TH), Germany.

Used hard- and software

This thesis was written on a computer with the operating system Linux (SuSE Linux 10.2) using the word processing package TEX, the macro package LATEX 2_ε, and several extensions. The bibliography was generated with BibTEX.

The empirical Green's functions computations were done using the Fortan code provided by K. Irikura and H. Miyake, which was bound to Matlab (The Mathworks) via a graphical user interface (GUI). The calculation of seismic intensities from acceleration time histories was performed using a Fortran code provided by V. Sokolov. For all other calculations (including the inversions in Chapter 7) and for visualization, the mathematical program Matlab (The MathWorks) and several Fortran codes were used. Schematical figures were constructed with Corel Draw.

Danksagung / Acknowledgment

during his visit at the Geophysical Institute. I learnt a lot about finite differences while I was working with your code and from the e-mail exchange when I was again facing some problem.

Special thanks also to Dr. Hillel Wust-Bloch and Prof. Dr. Zvi Ben-Avraham for taking so kindly care of me during my visit to Tel Aviv in 2006. I had a great time in Israel and hope that our scientific and personal contact will persist in the forthcoming years.

Vielen Dank auch an alle bislang nicht genannten Mitarbeiter des GPI, insbesonders allerdings an Silvia Bachmann für den vielen guten Kaffee und ihre unermüdliche Hilfe bei Dienstreiseangelegenheiten, Monika Hebben (die administratorischen SAFER Leiden und Ihre Hilfe bei diesen Problemen sind nicht vergessen!), Rainer Plockarz (der SAC Experte – hätte ich ihn nicht gehabt, wäre ich manchmal schon am Konvertieren der Formate gescheitert), Petra Knopf (ich weiss nicht, wie oft sie mir bei Rechnerproblemen diversester Art aus der Patsche geholfen hat), Thomas Nadolny, Gaby Bartman und Claudia Payne. Ganz herzlich möchte ich mich auch bei allen bedanken, die es verdient gehabt hätten, hier Erwähnung zu finden, und die ich bedauerlicherweise dann doch irgendwie vergessen habe...

Dir, Jérôme, vielen Dank für die unendlich vielen sowohl philosophisch geprägten als auch manchmal sehr pragmatischen Diskussionen und deine (mittlerweile schon knapp 15 Jahre andauernde) Freundschaft.

Ein ganz großes Dankeschön geht an meine Familie: meine Eltern und meine Oma, dafür dass sie immer an mich geglaubt haben und mich sowohl moralisch wie auch finanziell unterstützt haben. Nicht zu vergessen sind auch meine Geschwister, Jocelyn und Elodie, mit denen ich seit dem Kindesalter (manchmal mehr oder weniger viel) Spaß gehabt habe.

Schließlich und endlich möchte ich mich aber vor allem bei meiner großen moralischen Stütze während meiner gesamten Doktorandenzeit bedanken: meine liebe Annett, Danke für deine unendlich große Geduld und deine aufmunternden Worte, wenn wieder mal irgendetwas nicht ganz nach Plan lief und ich dann meine Uni-Gedanken (was läuft schief mit diesem Programm?) wieder mal mit nach Hause gebracht habe anstatt abzuschalten...

Lebenslauf

Persönliche Daten

Name:	Adrien Pierre Henri Oth
Geburtsdatum:	20. Juli 1980
Nationalität:	luxemburgisch
Geburtsort:	Luxembourg

Schulausbildung

1986 - 1992	École Primaire Luxembourg–Cents & Oberanven
1992 - 1994	Lycée Robert Schuman, Luxembourg
1994 - 1999	Athénée de Luxembourg
08.07.1999	Diplôme de Fin d'Études Secondaires (Abitur)

Hochschulausbildung

1999 - 2005	Studium der Geophysik an der Universität Karlsruhe (TH)
10.02.2005	Diplom
seit Mai 2005	Wissenschaftlicher Mitarbeiter am Geophysikalischen Institut der Universität Karlsruhe (TH)